UNIVERSITÉ DE STRASBOURG

Université de Strasbourg

ECOLE DOCTORALE pcp

Observatoire astronomique de Strasbourg

THÈSE présentée par :

Nicolas LONGEARD

soutenue le : **26 Septembre 2019**

pour obtenir le grade de : **Docteur de l'Université de Strasbourg**

Discipline/ Spécialité : Astrophysique

An in-depth study of the faintest galaxies with dedicated spectroscopy based on the *Pristine* survey.

THÈSE dirigée par :
  Monsieur MARTIN Nicolas   Docteur, Observatoire astronomique de Strasbourg

RAPPORTEURS :
  Monsieur READ Justin   Professeur, University of Surrey
  Monsieur VALLS-GABAUD David   Docteur, Observatoire de Paris, LERMA

AUTRES MEMBRES DU JURY :
  Monsieur FAMAEY Benoît   Docteur, Observatoire astronomique de Strasbourg
  Madame LANÇON Ariane   Professeur, Observatoire astronomique de Strasbourg
  Monsieur MARTIN Nicolas   Docteur, Observatoire astronomique de Strasbourg
  Madame STARKENBURG Else   Docteur, Leibniz-Institut für Astrophysik Potsdam

An in-depth study of the faintest galaxies with dedicated spectroscopy based on the Pristine survey

Nicolas Longeard

Table of contents

List of Figures

List of Figures

List of Figures

List of Figures

List of Publications

First author:

- *Nicolas Longeard, Nicolas Martin, Else Starkenburg, Rodrigo A. Ibata, Michelle L. M. Collins, Marla Geha, Benjamin P. M. Laevens, R. Michael Rich, David S. Aguado, Anke Arentsen, Raymond G. Carlberg, Patrick Côté, Vanessa Hill, Pascale Jablonka, Jonay I. González Hernández, Julio F. Navarro, Rubén Sánchez-Janssen, Eline Tolstoy, Kim A. Venn, Kris Youakim, 2018*: Pristine dwarf galaxy survey - I. A detailed photometric and spectroscopic study of the very metal-poor Draco II satellite (Published, Chapter 3)

- *Nicolas Longeard, Nicolas Martin, Else Starkenburg, Rodrigo A. Ibata, Michelle L. M. Collins, Benjamin P. M. Laevens, Dougal Mackey, R. Michael Rich, David S. Aguado, Anke Arentsen, Pascale Jablonka, Jonay I. González Hernández, Julio F. Navarro, Rubén Sánchez-Janssen, 2019*: The Pristine Dwarf-Galaxy survey - II. In-depth observational study of the faint Milky Way satellite Sagittarius II (Accepted, Chapter 4)

- *Nicolas Longeard, Nicolas Martin, Rodrigo A. Ibata, Michelle L. M. Collins Benjamin P. M. Laevens, Eric Bell, Dougal Mackey, 2019*: Detailed study of the Milky Way globular cluster Laevens 3 (Accepted, Chapter 5)

Contributed work:

- *Federico Sestito, Nicolas Longeard, Nicolas F. Martin, Else Starkenburg, Morgan Fouesneau, Jonay I. González Hernández, Anke Arentsen, Rodrigo Ibata, David S. Aguado, Raymond G. Carlberg, Pascale Jablonka, Julio F. Navarro, Eline Tolstoy, Kim A. Venn, 2019*: Tracing the formation of the Milky Way through ultra metal-poor stars (Accepted, Appendix A)

- *Nicolas F. Martin , Michelle L. M. Collins, Nicolas Longeard and Erik Tollerud, 2019*: Current Velocity Data on Dwarf Galaxy NGC 1052-DF2 do not Constrain it to Lack

Dark Matter (Accepted, Appendix B)

- *David Martínez-Delgado, Eva K. Grebel, Behnam Javanmardi, Walter Boschin, Nicolas Longeard, Julio A. Carballo-Bello, Dmitry Makarov, Michael A. Beasley, Giuseppe Donatiello, Martha P. Haynes, Duncan A. Forbes, Aaron J. Romanowsky, 2018*: Mirach's Goblin: Discovery of a dwarf spheroidal galaxy behind the Andromeda galaxy (Accepted)

- *Else Starkenburg, Nicolas Martin. Kris Youakim, David S. Aguado, Carlos Allende Prieto, Anke Arentsen, Edouard J. Bernard, Piercarlo Bonifacio, Elisabetta Caffau, Raymond G. Carlberg, Morgan Fouesnau, Patrick François, Oliver Franke, Jonay I. González Hernández, Stephen D. J. Gwyn, Vanessa Hill, Rodrigo A. Ibata, Pascale Jablonka, Nicolas Longeard, Alan W. McConnachie, Julio F. Navarro, Rubén Sánchez-Janssen, Eline Tolstoy, Kim A. Venn, 2017*: The Pristine survey - I. Mining the Galaxy for the most metal-poor stars (Accepted)

- *Else Starkenburg, David S. Aguado, Piercarlo Bonifacio, Elisabetta Caffau, Pascale Jablonka, Carmela Lardo, Nicolas Martin, Rubén Sánchez-Janssen, Federico Sestito, Kim Venn, Kris Youakim, Anke Arentsen, Marc Gentile, Jonay I. González Hernández, Collin Kielty, Helmer H. Koppelman, Nicolas Longeard, Eline Tolstoy, Raymond G. Carlberg, Patrick Côté, Morgan Fouesnau, Vanessa Hill, Alan W. McConnachie, Julio F. Navarro, 2018*: The Pristine survey IV: approaching the Galactic metallicity floor with the discovery of an ultra-metal-poor star (Accepted)

- *Boyajian, Tabetha. S.; Alonso, Roi; Ammerman, Alex; Armstrong, David; Asensio Ramos, A.; Barkaoui, K.; Beatty, Thomas G.; Benkhaldoun, Z.; Benni, Paul; Bentley, Rory O.; Berdyugin, Andrei; Berdyugina, Svetlana; Bergeron, Serge; Bieryla, Allyson; Blain, Michaela G.; Capetillo Blanco, Alicia; Bodman, Eva H. L.; Boucher, Anne; Bradley, Mark; Brincat, Stephen M. Brink, Thomas G.; Briol, John; Brown, David J. A.; Budaj, J.; Burdanov, A.; Cale, B.; Aznar Carbo, Miguel; Castillo García, R.; Clark, Wendy J.; Clayton, Geoffrey C.; Clem, James L.; Coker, Phillip H.; Cook, Evan M.; Copperwheat, Chris M.; Curtis, J. L.; Cutri, R. M.; Cseh, B.; Cynamon, C. H.; Daniels, Alex J.; Davenport, James R. A.; Deeg, Hans J.; De Lorenzo, Roberto; de Jaeger, Thomas; Desrosiers, Jean-Bruno; Dolan, John; Dowhos, D. J.; Dubois, Franky; Durkee, R.; Dvorak, Shawn; Easley, Lynn; Edwards, N.; Ellis, Tyler G.; Erdelyi, Emery; Ertel, Steve; Farfán, Rafael. G.; Farihi, J.; Filippenko, Alexei V.; Foxell, Emma; Gandolfi, Davide; Garcia, Faustino; Giddens, F.; Gillon, M.; González-Carballo, Juan-Luis; González-Fernández, C.; González Hernández, J. I.; Graham, Keith A.; Greene, Kenton A.; Gregorio, J.; Hallakoun, Na'ama; Hanyecz, Ottó; Harp, G. R.; Henry, Gregory W.; Herrero, E.; Hildbold, Caleb F.; Hinzel, D.; Holgado, G.;*

Ignácz, Bernadett; Ilyin, Ilya; Ivanov, Valentin D.; Jehin, E.; Jermak, Helen E.; Johnston, Steve; Kafka, S.; Kalup, Csilla; Kardasis, Emmanuel; Kaspi, Shai; Kennedy, Grant M.; Kiefer, F.; Kielty, C. L.; Kessler, Dennis; Kiiskinen, H.; Killestein, T. L.; King, Ronald A.; Kollar, V.; Korhonen, H.; Kotnik, C.; Könyves-Tóth, Réka; Kriskovics, Levente; Krumm, Nathan; Krushinsky, Vadim; Kundra, E.; Lachapelle, Francois-Rene; LaCourse, D.; Lake, P.; Lam, Kristine; Lamb, Gavin P.; Lane, Dave; Lau, Marie Wingyee; Lewin, Pablo; Lintott, Chris; Lisse, Carey; Logie, Ludwig; Longeard, Nicolas; Lopez Villanueva, M.; Whit Ludington, E.; Mainzer, A.; Malo, Lison; Maloney, Chris; Mann, A.; Mantero, A.; Marengo, Massimo; Marchant, Jon; Martínez González, M. J.; Masiero, Joseph R.; Mauerhan, Jon C.; McCormac, James; McNeely, Aaron; Meng, Huan Y. A.; Miller, Mike; Molnar, Lawrence A.; Morales, J. C.; Morris, Brett M.; Muterspaugh, Matthew W.; Nespral, David; Nugent, C. R.; Nugent, Katherine M.; Odasso, A.; O'Keeffe, Derek; Oksanen, A.; O'Meara, John M.; Ordasi, András; Osborn, Hugh; Ott, John J.; Parks, J. R.; Rodriguez Perez, Diego; Petriew, Vance; Pickard, R.; Pál, András; Plavchan, P.; Pollacco, Don; Pozo Nuñez, F.; Pozuelos, F. J.; Rau, Steve; Redfield, Seth; Relles, Howard; Ribas, Ignasi; Richards, Jon; Saario, Joonas L. O.; Safron, Emily J.; Sallai, J. Martin; Sárneczky, Krisztián; Schaefer, Bradley E.; Schumer, Clea F.; Schwartzendruber, Madison; Siegel, Michael H.; Siemion, Andrew P. V.; Simmons, Brooke D.; Simon, Joshua D.; Simón-Díaz, S.; Sitko, Michael L.; Socas-Navarro, Hector; Sódor, Á.; Starkey, Donn; Steele, Iain A.; Stone, Geoff; Strassmeier, Klaus G.; Street, R. A.; Sullivan, Tricia; Suomela, J.; Swift, J. J.; Szabó, Gyula M.; Szabó, Róbert; Szakáts, Róbert; Szalai, Tamás; Tanner, Angelle M.; Toledo-Padrón, B.; Tordai, Tamás; Triaud, Amaury H. M. J.; Turner, Jake D.; Ulowetz, Joseph H.; Urbanik, Marian; Vanaverbeke, Siegfried; Vanderburg, Andrew; Vida, Krisztián; Vietje, Brad P.; Vinkó, József; von Braun, K.; Waagen, Elizabeth O.; Walsh, Dan; Watson, Christopher A.; Weir, R. C.; Wenzel, Klaus; Westendorp Plaza, C.; Williamson, Michael W.; Wright, Jason T.; Wyatt, M. C.; Zheng, WeiKang; Zsidi, Gabriella, 2018: The First Post-Kepler Brightness Dips of KIC 8462852 (Accepted)

Acknowledgements

First of all, I would like to thank my PhD surpervisor, Nicolas Martin. I didn't know where I was going into when I decided to do a PhD, I guess nobody really does, but Nicolas has been there every step of the way. Of course, science-wise, I have learned a lot in three years, and that's mainly thanks to him and his way of "teaching" things. He never seemed to lose patience over anything (maybe that's because he's good at hiding it), and was always here to talk if needed. I'm glad we should be able to work together in the future.

I also have to thank Else Starkenburg, who also played a big role in my PhD. Science-related discussion was always nice, and so is she. She never complained whenever I needed my data reduced, which is great. Furthermore, I would like to thank Rodrigo Ibata who was always interested in my work during our meetings, and had nice suggestions to improve things. And I might have been stuck in Heidelberg if it were not for him. So thank you for that as well.

Obviously, I extend these thanks to the entire crew of the Observatoire Astronomique de Strasbourg. It is a really great work environment, and it is mainly due to the fact that everyone is nice and open to talk there.

I am also grateful to all the people I met during my master's degree: Kanthanakorn (Nu) Noysena, Abderrahmane Bouakline, and Vincent Di Piro on one hand, and the astronomers on the other.

I also thank the fellow (sometimes former) PhD students I met along the way, Guillaume, Jerome, Jeremy, Mathieu, Nicolas (yes, another Nicolas), Jonathan, Joe, Tim, Federico, Guillaume, Julien, François, Khyati, Kris and Anke.

Finally, thank you to my family.

"Good luck exploring the infinite abyss"

Zach Braff, Garden State

Abstract

In the standard cosmological model, dwarf galaxies are faint stellar systems embedded in a massive dark matter halo, and usually orbiting around brighter host galaxies. Because their very existence is linked to the early formation and evolution of galaxies, but also to the fundamental properties of the universe, the study of dwarf galaxies is particularly important. However, as fainter and fainter systems are found, the more dwarf galaxies are difficult to identify, as they start to share the properties of a different type of stellar systems that do not possess any dark matter halo: the globular clusters. To classify a faint satellite as a galaxy, detecting the signature of its dark matter halo is the key. This is done by analysing its dynamical properties and measuring the iron abundance of its star. All these analyses require spectroscopic observations of the dwarf-galaxy candidates. However, the faintness of some of these candidates comes with a lack of giant stars which are in general the target of choice of spectroscopy.

This thesis presents the studies of three faint Milky Way satellites: Draco II (Dra II), Sagittarius II (Sgr II) and Laevens 3 (Lae 3) using deep CFHT/MegaCam broadband photometry and Keck II/DEIMOS multi-object spectroscopy. To overcome the challenge that is the lack of giant stars in these systems, the analyses of Dra II and Sgr II are supplemented with the narrow-band, metallicity-sensitive CaHK photometry from the *Pristine* Survey. Because of its ability to measure the metallicity photometrically, *Pristine* is able to highlight the metal-poor population of the faintest dwarf galaxies with respect to the contamination that represents the stellar halo of the Milky Way. In doing so, the stars belonging to the dwarf-galaxy candidates can be more easily identified in spectroscopic datasets, and the photometric metallicities can even be used to estimate, without any spectroscopy, the metallicity of a given satellite. The size ($r_h = 19^{+4.5}_{-2.6}$ pc), luminosity ($L_V = 180^{+124}_{-72}$ $L_\odot$) and metallicity ($[\mathrm{Fe/H}]^{\mathrm{DraII}}_{\mathrm{photo}} = -2.7 \pm 0.1$ dex) of Dra II place the satellite in the realm of dwarf galaxies. However, its internal dynamics is not constrained tightly enough to prove the existence of a dark matter halo. The same goes for its metallicity dispersion, which is unresolved. The distribution of Dra II-like stars in the field suggests that the satellite is being affected by the tidal effects provoked by the Milky Way. Though its case is not perfectly closed, the properties of Dra II suggest that it is one of the faintest dwarf galaxies known.

Sgr II is a much brighter satellite ($M_V = -5.7 \pm 0.1$ mag) but its nature is not any more straightforward. With a size of $35.5^{+1.4}_{-1.2}$ pc, Sgr II sits in-between the realm of globular

clusters and dwarf galaxies. Its metallicity corresponds to what is expected from a dwarf at this luminosity, and its velocity and metallicity dispersions are hinting at the existence of a dark matter halo. However, the uncertainties on both these properties do not exclude the possibility that Sgr II is a purely baryonic system. Its orbit points at a possible association with the Sgr stream and at the fact that Sgr II may be a former satellite of the Sgr dwarf spheroidal galaxy.

Lae 3, despite its size of ~ 11 pc, is without a doubt a globular cluster. Even though both its velocity and metallicity dispersion are not informative on the nature of the system, its systemic metallicity from spectroscopic observations ($\mathrm{[Fe/H]}^{\mathrm{Lae3}}_{\mathrm{spectro}} = -1.8 \pm 0.1$ dex) confirms that Lae 3 is too metal-rich to be a dwarf galaxy. A careful analysis of its orbit shows that its pericenter is at $40.7^{+5.6}_{-14.7}$ kpc, and therefore that Lae 3 is an outer halo globular cluster.

My thesis highlights the importance of both deep photometric and spectroscopic data, as well as the importance of the *Pristine* Survey in the study of those systems. On a more global scale, the next generation of telescopes and digital surveys will greatly participate to our understanding of the satellites of the Milky Way. It will allow more detailed studies of the systems already known, both with photometry and spectroscopy, as well as lead to the discovery of a variety of new faint and distant satellites.

Introduction 1

1.1   Galaxies in the standard cosmological model

According to the current standard cosmological model, the ΛCDM model, the Universe is composed of ∼ 70 % of dark energy that drives its expansion, ∼ 25 % of Dark Matter (DM), and a mere ∼ 5 % for the baryonic matter (Planck Collaboration et al., 2016). Minuscule fluctuations (over- and underdensities) in the matter distribution of the very early Universe slowly grew over time under the effect of gravity to form DM halos. These halos, again through the action of gravity, attracted the gas and formed denser regions. Because they allowed for these dense environments to form, massive enough halos indirectly triggered the formation of stars that would themselves assemble to produce galaxies. Careful studies of the Cosmic Microwave Background, the first light of the Universe, suggest that small structures, i.e. the smallest, least massive halos, should have been the first to form. These halos then proceeded to continue accreting gas, but also to merge with one another, and their gas and stellar contents along with them, forming larger and larger structures, finally ending up as the galaxies that we are able to observe today (White & Rees 1978, Mo, van den Bosch & White 2010). Some of these halos, however, did not follow this path completely and did not undergo enough mergers to form massive galaxies such as our own, or even larger. This did not prevent them from accreting gas and form stellar systems. Thus, the ΛCDM model predicts that most galaxies should come up in groups, with a massive central galaxies, and less massive, fainter ones orbiting around them.

Therefore, galaxies are a direct consequence of the underlying properties of the Universe. In being so, the cosmological parameters that describe the behaviour of the Universe from the dawn of time can be inferred and constrained by studying them. This also includes the hope of understanding the nature and properties of the elusive DM particle, that still up to now, escapes our insight (Bertone, Hooper & Silk 2005, Geringer-Sameth, Koushiappas & Walker 2015). Reversing these statements, it is fair to say that an accurate and complete description of the fundamental cosmological and physical properties of the Universe should, in principle, be able to predict the different features observable when pointing our telescopes at the sky. Several attempts have been made over the years to model the Universe, and in particular Local Group-like environnements, through numerical simulations such as the

Aquarius (Springel et al. 2008, see Figure 1.1), the Illustris (Vogelsberger et al., 2014) or the Evolution and Assembly of GaLaxies and their Environments (EAGLE, Schaye et al. 2015) projects. These extremely computationally expensive and complex attempts to reproduce the various features of the Universe have lead to the raise of several discrepancies with observations, thus pointing out at some potential weaknesses in the classical ΛCDM framework.

The standard cosmological model predicts that clumps of DM should come at all masses, from extremely large ones through the hierarchical growth of structures discussed above, to very low-mass, starless halos. Hundreds of subhalos with enough mass to trigger the birth of stars and galaxy formation should be observed in our Local environnement (Figure 1.1), but we barely discovered several decades of smaller satellite galaxies orbiting the Milky Way (MW) within its virial radius (Tollerud et al., 2008). Of course, our view of the MW neighbourhood is perfectible on many accounts, and other fainter and/or more distant systems will probably be discovered in the future (Hargis, Willman & Peter, 2014), but it will probably not be enough to account for the entire predicted population of galaxies in simulations. This is often referred to as the "Missing Satellites Problem" (Klypin et al., 1999). Moreover, the most massive halos of MW satellites known today are less massive that the ones observed in simulations, otherwise known as the "Too-Big-To-Fail" problem (Boylan-Kolchin, Bullock & Kaplinghat, 2011). In addition to these abundance issues, the very distribution of dark matter in the center of galaxies is a point of tension between observations and simulations, as ΛCDM predicts a denser distribution (a "cusp") than what can be actually observed in most galaxies (a "core") through a careful examination of their rotation curves. (Flores & Primack 1994, McGaugh, Rubin & de Blok 2001, Simon et al. 2005, Navarro et al. 2010, Read, Walker & Steger 2018). Furthermore, the possible anisotropy in the distribution of MW satellites, contrarily to an isotropic/prolate one, could cast an even larger shadow on our standard cosmological model (Pawlowski, McGaugh & Jerjen, 2015). Indeed, dwarf galaxies seem to be distributed anisotropically in the sky and be confined within a "plane of satellites" (Lynden-Bell 1976, Lynden-Bell & Lynden-Bell 1995). A configuration that may not expected in the standard cosmological model (Metz, Kroupa & Jerjen, 2007) but is observed both for the MW and the Andromeda galaxy, though this claim is quite disputed. For M 31, there is even evidence of dwarf galaxies forming a "thin", rotationnaly-supported disk (Ibata et al., 2013).

Several hypothesis within ΛCDM already exist to address these various problems. Baryonic feedback could influence the dark matter density in dwarf galaxies. Especially extremely energetic events such as supernovae that could redistribute the central dark matter, and therefore making the dark matter halo central density less cuspy (Navarro, Eke & Frenk 1996, Read & Gilmore 2005, Oñorbe et al. 2015, Read, Agertz & Collins 2016). This feedback is however not expected to produce cores for all mass regime and could become inefficient in low-mass systems. When it comes to the lack of satellites in the low-luminosity regime, external processes may well be the answer, such as the UV feedback that could simply shut off the star formation in the least massive halos (Sawala et al., 2016). Another example, in the high-mass regime, is the work of Read & Erkal (2019) who use a novel technique to
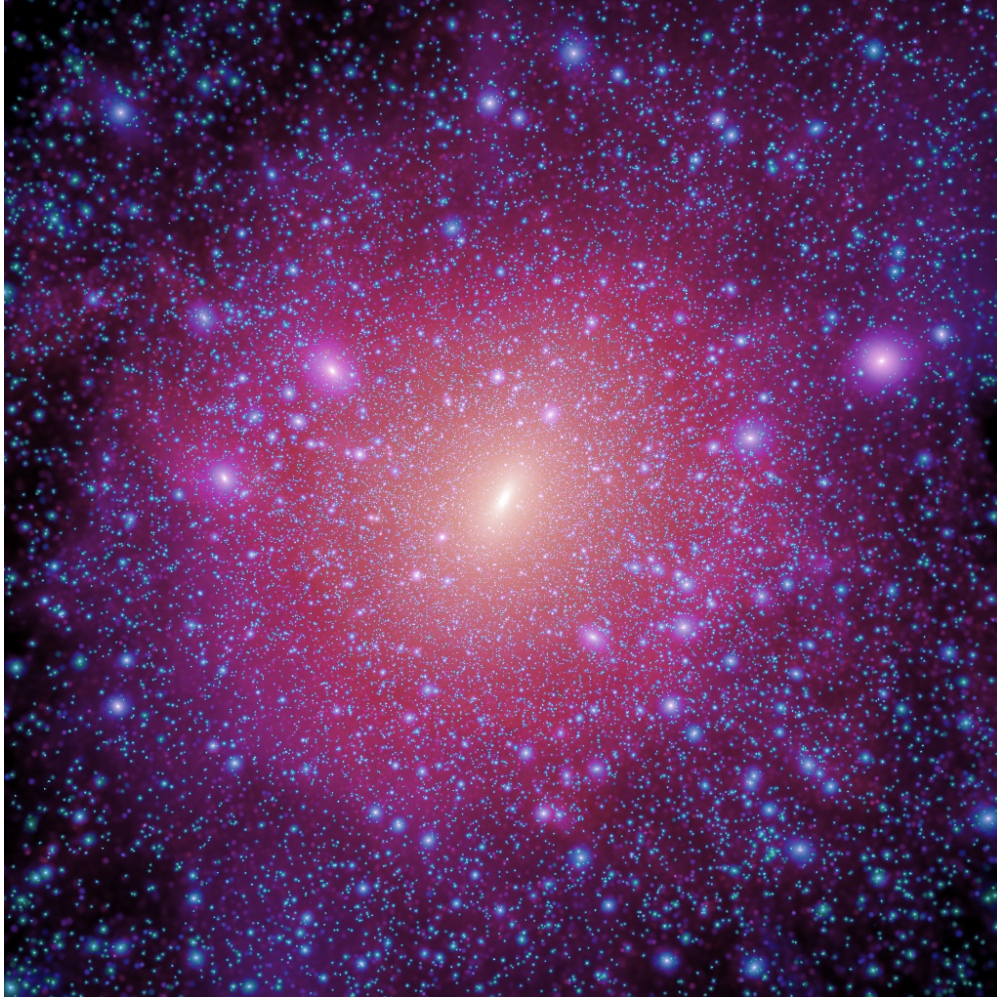
Figure 1.1: Dark matter simulation from the Aquarius simulation (Springel et al., 2008) for a MW-like halo. Such a simulation shows how diverse and numerous the dark matter sub-structures populate the local environment according to the ΛCDM model.

estimate M_{200}, the dark matter halo mass of a galaxy. This method consists into abundance matching M_{200} with the mean star formation rate of these systems, $< \mathrm{SFR} >$, instead of using the stellar mass M_*. Read & Erkal (2019) conclude that, within 280 kpc and above a mass of $10^9 \mathrm{M}_\odot$, the cumulative number of dark matter halo observed around the MW is consistent with the predictions of ΛCDM. For the "plane of satellites", it has been argued that such a behaviour can be reproduced in cosmological simulations and that the configuration of the MW and its satellites is simply an outlier in a large sample of possible configurations of subhalos (Kang et al. 2005, Zentner et al. 2005) or just the result of an observational bias.

Most of these issues show the importance of both the census of dwarf galaxies of the MW and establishing their properties with accuracy. While the brightest systems in our neighbourhood have been extensively studied for years, a lot of fainter galaxies still awaits

discovery and/or to be understood. Doing so would bring a lot more data points to the table, since faint satellites are more numerous than bright ones, as well as confronting the predictions of ΛCDM with observations in a whole new regime, given that cosmological simulations are able to continue pushing back numerical limits and reach the resolution needed to model faint stellar systems. These faint satellites, called "dwarf galaxies" according to the definition of Bullock & Boylan-Kolchin (2017), are not only useful for their close link to cosmology-related tensions. Generally speaking, galaxies owe their existence, not only to DM halos, but also to all kind of physical processes, from the heating/cooling of gas, to the processes that trigger the formation of stars. The hierarchical formation of structures automatically implies that faint, least massive galaxies formed first, and were therefore not heavily polluted by supernovae (Bland-Hawthorn et al. 2010, Ji, Frebel & Bromm 2015). As such, they can be seen as unique laboratories of the properties of stars and gas in the early Universe. This peculiarity of faint dwarfs also means that they can be really important to study the various possible pathways and the contribution of the different astrophysical events occurring in a galaxy (Type I and II supernovae, neutron star mergers, etc.) leading to the formation of certain chemical elements (Ji et al. 2016a, Ji et al. 2019). Their high sensitivity to environmemental effects, because of their lower mass, also makes them excellent candidates to recreate the history of our cosmic neighbourhood and understand how external processes can affect the formation and the evolution of galaxies (Kirby et al., 2014).

Faint galaxies are therefore a key to both near-field cosmology and stellar/galaxy formation and evolution. The rest of this Introduction will be focused on them. First, I will detail the main outlines of the discovery of MW satellites in section 1.2. Then, the complexity of identifying galaxies in the faint regime, and the various tools to do so, will be detailed in section 1.3. Finally, in chapter 2, I will describe the main characteristics of the *Pristine* Survey and its usefulness in the study of the faint MW satellites.

1.2   A brief history of the discovery of faint structures around the MW

The brightest objects in the Local Group, the Triangulum galaxy, Andromeda and our own MW are not its only inhabitants. On a clear night and in a nice star-hunting location, any pair of eyes could spot extended objects contrasting with the hesitant spotlights of the stars of the MW. For example, the distant galaxies that are the Large and Small Magellanic Clouds (LMC and SMC respectively), among many other celestial objects, have been known for centuries. However, the faintest ones eluded our careful study of the night sky for a long time. The 20th century is a milestone regarding astronomers' knowledge of our celestial neighbourhood. In 1938, Shapley was the first to discover smaller, faint galaxies, invisible to the naked eye, yet orbiting around the MW (Shapley, 1938a). That is, only around 20 years after astronomers realised that most extended objects were true extragalactic objects. Those satellites, Sculptor (Scl) and Fornax (Fnx), sitting at around 90 kpc of the MW, were only the first in a list that would only grow longer and more diverse over the course of history. Alike Scl and Fnx, the discovery of most satellite galaxies in the subsequent decades until
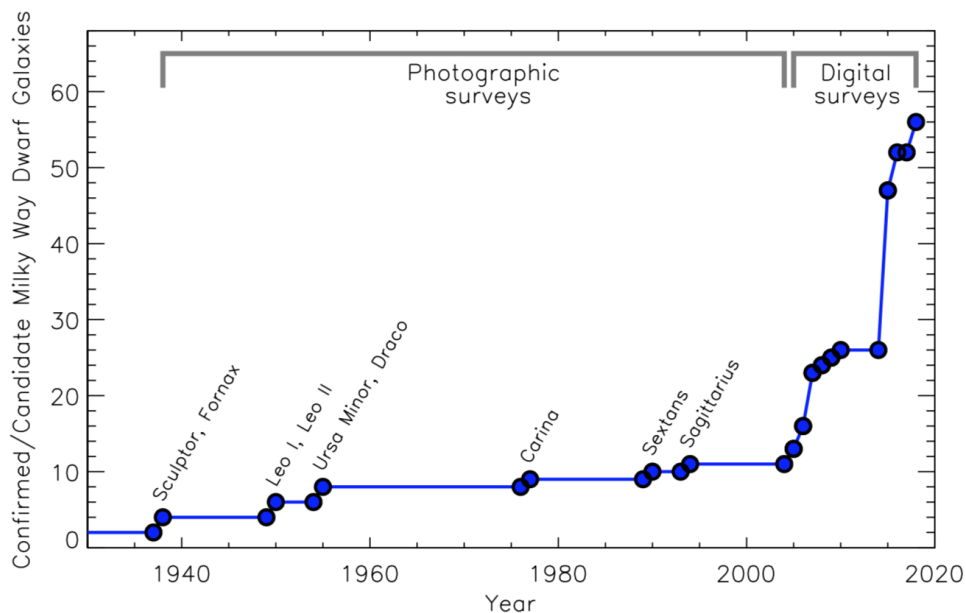
Figure 1.2: Number of MW satellite galaxies discovered as a function of time (Simon, 2019). This illustrates the revolution engaged by the large digital photometric surveys. In just a few years, the abundance of galaxies known in the vicinity of the MW exploded, starting from 2005 and the beginning of the SDSS era.

2004 were done by the careful, visual inspection of photographic plates. These 8 satellites, Carina, Draco, Fornax Leo I, Leo II, Sextans, Sculptor and Ursa Minor, are now denominated as "classical dwarf spheroidal" galaxies, or "dSphs".

However, the field was revolutionised in 2005 with the Sloan Digital Sky Survey (York et al., 2000, SDSS). Because of its depth, large coverage and accurate star-galaxy separation algorithms, the number of MW satellite galaxies discovered in only two years was the same as in the previous seven decades (Ursa Major, Willman et al. 2005b, Canes Venatici, Zucker et al. 2006b, Bootes I, Belokurov et al. 2006, Leo T, Irwin et al. 2007). This effort was quickly followed by other large digital photometric surveys. The Dark Energy Survey (The Dark Energy Survey Collaboration, 2005, DES) or the Panoramic Survey Telescope and Rapid Response System (Chambers et al., 2016, PS1) both unveiled fainter and more distant satellites, down to the hundred of solar luminosities, i.e. ∼ 1500 times less luminous than Draco or Ursa Minor, the less luminous satellites galaxies known prior to SDSS (Drlica-Wagner et al. 2015, Laevens et al. 2014 ,Laevens et al. 2015a, Luque et al. 2016, Martin et al. 2016c). The rapid evolution of the number of satellite discovered is illustrated in Figure 1.2, while Figure 1.3 shows how much the morphology of galaxies that we are able to detect changed in only two decades. The MW is, of course, not the only one under careful scrutiny, as the number of satellite galaxies around M31 drastically rose with the Pan-Andromeda Archeological Survey (PAndAS, McConnachie et al. 2009, Martin et al. 2013, McConnachie et al. 2018).

Even now, the hunt goes on, with the recent discoveries of Cetus III (Homma et al., 2018)
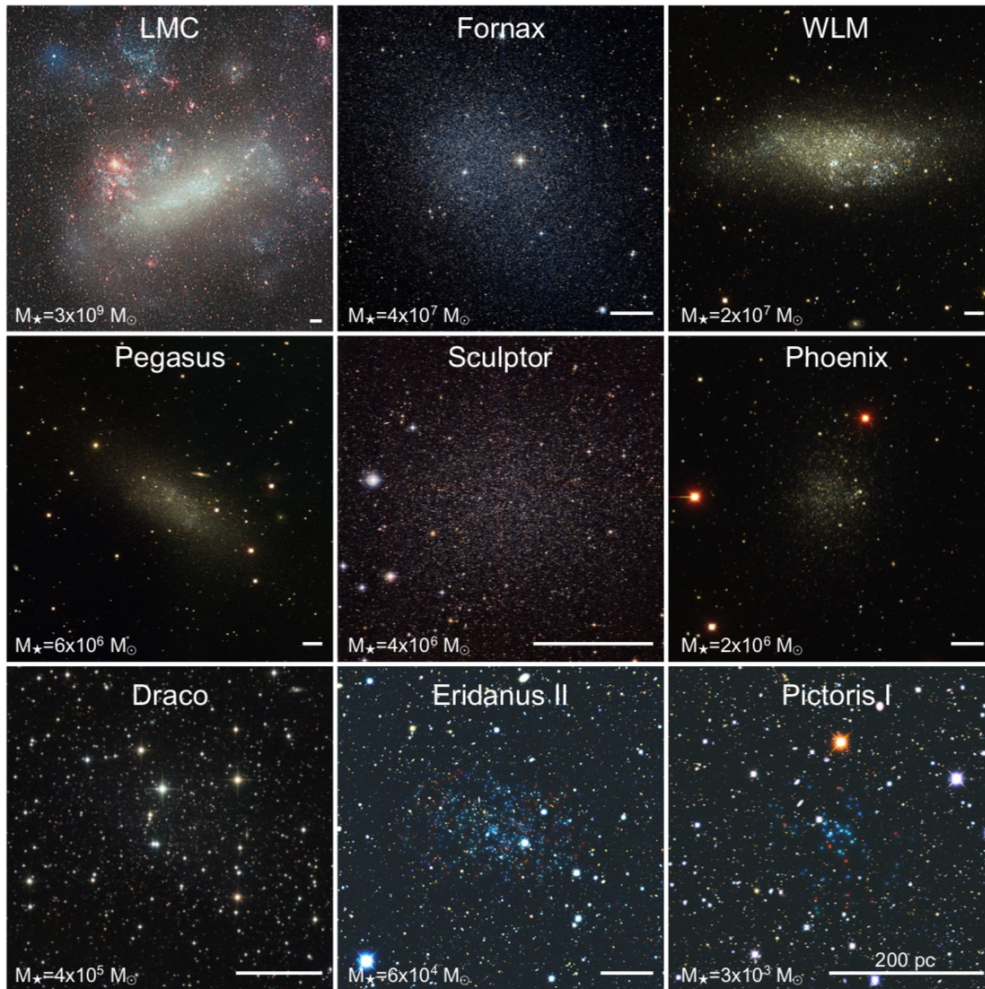
Figure 1.3: Images of galaxies of decreasing mass, from the top left to the bottom right (Bullock & Boylan-Kolchin 2017 and references therein). Most of them are satellites of the MW. Only WLM and Phoenix are independent, dwarf irregular galaxies. The name of each galaxy is displayed at the top center of each panel, while their stellar mass is shown in the bottom-left corner. Large photometric surveys clearly allowed astronomers to enter a new era of MW satellite detection, as the difference between bright galaxies such as the LMC and very faint ones, such as Pictoris I, is stunning.

or Bootes IV (Homma et al., 2019) from the Hyper Suprime-Cam (HSC) Subaru Strategic Program (SSP). This quest for low surface brightness systems not only results in the finding of faint, small-sized (a few tens of parsecs) objects, but also allows for the discovery of bright yet extremely extended satellites such as Antlia 2 (Torrealba et al., 2019).

1.3 What makes a galaxy ?

Whether we consider bright satellite galaxies such as the Sgr dSph, ($M_V \sim -13.5$ mag) or the faint Segue 1 ($M_V \sim -1.3$ mag), one of their fundamental properties is their age. Using the dark-matter central densities of several dwarfs, Strigari et al. (2008) showed that they have started to form stars very early, at a redshift ~ 12, i.e. a mere 100 million years after the Big Bang. Deep *HST* observations from Orban et al. (2008) showed that contrarily to the bright satellites of the MW, which continued to form stars for several Gyr, the star formation history of fainter ones ($M_V < -6$ mag) is much shorter. Once more, *HST* observations, combined with theoretical populations models and sometimes supplemented by spectroscopy, showed that in the faint regime, satellites formed the vast majority, if not all, their stars in the first 2-3 Gyr (Brown et al. 2012, Brown et al. 2014).

However, diving deeper and deeper into these relics of the earliest times of the Universe challenged our view of the very nature of galaxies. Figure 1.4 shows the absolute magnitude and half-light radius of most MW globular clusters and dwarf galaxies, as circles and squares respectively, the dwarfs being colour-coded by their epoch of discovery. The galaxies discovered prior to the SDSS era, in large blue squares, form a distinct population to that of the globular clusters shown as small black dots. For example, a galaxy like Draco has an absolute magnitude of ~ -8.8 mag and a half-light radius of ~ 200 pc (Martin, de Jong & Rix, 2008). NGC 5904 is a globular cluster at roughly the same luminosity. However, its half-light radius is only 4 pc (Harris, 2010). The galaxy/cluster classification, before the large digital photometric surveys era, was therefore quite straightforward if one knew the fundamental, structural properties of a given system, and in particular its physical size, as proposed, for example, by Tammann (1994). Figure 1.4 shows that the distinction between galaxy and clusters in the absolute magnitude-half-light radius plane becomes less and less clear as one ventures into the faint regime of satellites.

The right panel of Figure 1.4 displays the absolute magnitude with respect to their systemic metallicity and shows that dwarfs follow a relation in this parameter space, represented as a solid black line according to Kirby et al. (2013b). The dashed line show the scatter of this metallicity-luminosity relation. Once more, if the brightest systems form a separate group from clusters, it is not true when adventuring into the faint regime. The sparseness of the globular clusters in the M_V-[Fe/H] plane allows many of them to be compatible with the relation of Kirby et al. (2013b). As such, it is more of a useful tool to identify a satellite as not being a dwarf rather than confirming it is one. One could argue that no cluster has been yet identified as being more metal-poor than [Fe/H] < -2.5 dex, indicating that faint systems below this limit are dwarfs, but in the same way as galaxies, the census of clusters is still incomplete. Moreover, some dwarf galaxies below this metallicity limit are still candidates
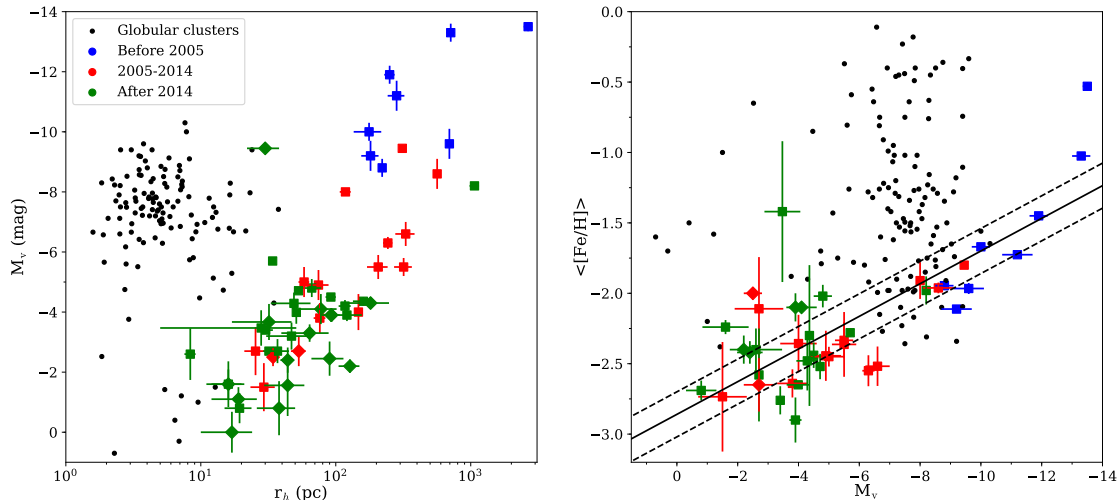
Figure 1.4: Size and absolute magnitude of most globular clusters (black circles), dwarf galaxies (coloured squares) and dwarf-galaxy candidates (coloured diamonds) orbiting around the MW known to this day. For the galaxies, we also indicate if they have been discovered prior to the beginning of the SDSS era, i.e. before 2005 (blue), between 2005 and 2014 (red) or after 2014 (green). The properties of the brightest galaxies, discovered first, are clearly separated from those of the bulk of clusters. Uncertainties are only reported for dwarfs and dwarf candidates. As one goes into the faint regime of galaxies, the frontier between those and clusters starts to blur. 124 globular clusters are presented here. The properties of 116 of them were extracted from Harris (1996) catalog, revised in 2010. For the remaining ones (Kim 1, Kim 2, Kim 3, Laevens 1, Balbinot 1, Munoz 1 and SMASH 1) parameters of the discovery publications were used (Kim & Jerjen (2015a), Kim et al. (2015), Kim et al. (2016), Laevens et al. (2014), Balbinot et al. (2013), Muñoz et al. (2012) and Martin et al. (2016c)). Globular cluster metallicity spread measurements are taken from Willman & Strader (2012) and references therein: Carretta et al. (2006, 2007, 2009b, 2011), Cohen et al. (2010), Gratton et al. (2007), Johnson & Pilachowski (2010), and Marino et al. (2011). McConnachie (2012) and Willman & Strader (2012) are used to compile the properties of the dwarf galaxies represented here. The 35 dwarf galaxies represented here are: Aquarius II (Torrealba et al., 2016b), Bootes I (Belokurov et al., 2006; Norris et al., 2010), Canes Venatici I (Zucker et al., 2006b), Canes Venatici II (Sakamoto & Hasegawa, 2006), Carina (Cannon, Hawarden & Tritton, 1977), Carina II (Torrealba et al., 2018), Colomba I (Drlica-Wagner et al., 2015), Coma Berenices, Hercules, Leo IV and Segue I (Belokurov et al., 2007), Crater II (Torrealba et al., 2016a), Draco and Ursa Minor (Wilson, 1955), Eridanus II (Bechtol et al., 2015; Conn et al., 2018; Koposov et al., 2015b), Fornax (Shapley, 1938b), Grus I (Koposov et al., 2015a), Hydra II (Martin et al., 2015), Hydrus I (Koposov et al., 2018), Leo I and Leo II (Harrington & Wilson, 1950), Leo V (Belokurov et al., 2008), Leo T (Irwin et al., 2007), Phoenix II (Bechtol et al. 2015, Pisces II (Belokurov et al., 2010), Reticulum II and Horologium I (Koposov et al., 2015a), Sagittarius (Ibata, Gilmore & Irwin, 1994), Sextans (Irwin et al., 1990), Sculptor (Shapley, 1938a), Triangulum II (Laevens et al., 2015b), Tucana II (Bechtol et al., 2015), Ursa Major I (Willman et al., 2005b), Ursa Major II (Zucker et al., 2006a), Willman I (Willman et al., 2005a). Their metallicity and metallicity spreads were drawn from Caldwell et al. (2017), Fritz et al. (2019), Kirby et al. (2008), Kirby et al. (2010), Kirby et al. (2017), Li et al. (2018), Martin et al. (2016b), Norris et al. (2010), Walker et al. (2016), Willman et al. (2011). The dwarf galaxy candidates discovered recently and shown on this figure are Bootes II (Koch & Rich, 2014), Carina III, Cetus III (Homma et al., 2018), DES1 (Luque et al., 2016; Conn et al., 2018), DESJ0225+0304 (Luque et al., 2017), Horologium II (Kim & Jerjen, 2015b), Pegasus III (Kim & Jerjen, 2015a),Koposov et al. 2015a), Pictor I (Bechtol et al., 2015), Pictor II (Drlica-Wagner et al., 2016), Segue 2(Belokurov et al., 2009), the discoveries of Drlica-Wagner et al. (2015) that await confirmation: Cet II, Gru II, Indus II, Ret III, Tuc III, Tuc IV and Tuc V, and Virgo I (Homma et al., 2016)

only, and could well turned out to be clusters.

With the increasing number of identifications of faint, ambiguous satellites came the necessity to come back to what is commonly used as the definition of a galaxy: they reside at the center of DM haloes, while star clusters are purely baryonic systems (Mateo 1998, Simon et al. 2011, Tollerud et al. 2011). This definition, however, only makes sense in a "dark-matter compatible" cosmological framework. In an attempt to come up with a less exclusive characterisation, Willman & Strader (2012) proposed a description of galaxies that does not need DM or the lack thereof, by defining them as a "gravitationally bound collection of stars whose properties cannot be explained by a combination of baryons and Newton's laws of gravity". Since we placed ourselves in a ΛCDM Universe in this thesis, classifying faint satellites as galaxies revolves around proving the existence of a DM halo. Of course, this is not an easy task, as one of the fundamental property of DM in a ΛCDM is that it does not interact with light or with baryonic matter. However, the mass of a halo should impact the properties of the galaxy embedded in it on multiple levels, therefore allowing us to detect and probe the halo in an indirect manner.

1.3.1 The dynamical properties of dwarf galaxies

Rather immediately, this context provides a reasonable explanation to the significant discrepancy in size between bright dwarf galaxies and clusters ($M_V \geq -6$) illustrated in Figure 1.4. The extra mass brought by the halo allows a galaxy to be more extended while maintaining its integrity and remaining a gravitationally bound system. Here, the term "size" is used to refer to the half-light radius of a stellar system, i.e. the radius that emcompasses half of the system's luminosity. For dwarf galaxies and clusters, exponential, King and Plummer profiles are commonly used as they are all able to adequately model the distribution of their stars on the de-projected sky. In the very faint regime where the size does not necessarily suffice, other tracers of the underlying DM halo are needed. The internal dynamics of any stellar system should be impacted by its mass. Richstone & Tremaine (1986) showed that for a fixed mass-to-light ratio, the central velocity dispersion of a stellar system should indeed depend on the size and surface brightness of the object, assuming that it is in dynamical equilibrium. Walker et al. (2009) and Wolf et al. (2010) tackle the problem slightly differently and provide a way to estimate the mass of a stellar system enclosed within one half-light radius, using its observed velocity dispersion. Assuming that the satellite is in dynamical equilibrium and that its velocity dispersion profile is flat near the half-light radius, the relation of Wolf et al. (2010) is

$$M_{\frac{1}{2}} = 930 \, \sigma_{\mathrm{v}}^2 \, r_{\frac{1}{2}}, \tag{1.1}$$

with σ_{v} the stellar velocity dispersion in km s^{-1} and $r_{\frac{1}{2}}$ the 2D projected half-light radius in parsec. The resulting half-light mass $M_{\frac{1}{2}}$ is in solar masses. For old stellar populations, one can also introduce the luminosity (in solar luminosities) in this equation by taking into account that the ratio of mass to light in old, metal-poor stellar populations is of the order of 2 (McLaughlin & van der Marel, 2005). This procedure has the advantage to replace the

mass by a "direct" observable quantity, here, the luminosity. In doing so, the equation can be reversed into the following

$$\sigma_v^{\text{baryonic}} = \sqrt{\frac{2L_{\frac{1}{2}}}{930r_{\frac{1}{2}}}} \tag{1.2}$$

and the stellar velocity dispersion of a purely baryonic system can be predicted once its size and luminosity are both measured.

In the regime of faint MW satellites, Kleyna et al. (2005) were the first to undertake such an endeavour, with Ursa Major I (UMa I) discovered by Willman et al. (2005b). UMa I has a luminosity of ~ 9600 $L_\odot$ and a half-light radius of ~ 319 pc, which, using Equation 1.2, would translate into a velocity dispersion of ~ 0.2 km s^{-1} if the satellite were purely baryonic. Using the 10-meter Keck telescope and the High Resolution Echelle Spectrometer (HIRES), Kleyna et al. (2005) identified five stars members of UMa I and constrained the velocity dispersion of the satellite to be $\sigma_v = 9.3^{+11.7}_{-1.2}$ km s^{-1}. This measurement was later refined by Martin et al. (2007) and Simon & Geha (2007), giving respectively $\sigma_v = 6.5^{+2.0}_{-1.4}$ km s^{-1} and $\sigma_v = 7.6 \pm 1.0$ km s^{-1} based on a sample of 14 and 39 stars. Undoubtably, the motion of UMa I's stars is not driven by its stellar content alone, even more so since no faint galaxy orbiting around the MW shows traces of HI gas (Grcevich & Putman, 2009). Using equation 1.1, it is straightforward to show that there is roughly 200 times more mass in UMa I than what its stars can possibly account for, a mass associated, in our standard cosmological model, to a underlying DM halo.

The study of Kleyna et al. (2005) was quickly followed by a similar one performed on Boötes I (Boo I) by Muñoz et al. (2006), finding a velocity dispersion of $\sigma_v = 6.6 \pm 2.3$ km s^{-1} (vs. ~ 0.4 km s^{-1} if purely baryonic). Boo I would later reveal itself to be a complex system in that regard, as its velocity dispersion is not correctly modelled by one single population, but by the combination of two dynamically different populations, a "cold" one ($\sigma_v^{\text{cold}} = 2.4^{+0.9}_{-0.5}$ km s^{-1}) and a "hot" one ($\sigma_v^{\text{hot}} \sim 9$ km s^{-1}), as shown by Koposov et al. (2011). If the question of two distinct stellar populations spatially, chemically and dynamically in Boo I remains unclear to this day, the dwarf is nevertheless another example of a system for which the dynamical mass is much more important than its stellar one. The inference of the stellar velocity dispersion of several other systems exploded in the following years (Boo I, UMa II and Willman I for Martin et al. 2007, Canes Venatici I and II, Coma Berenices, Hercules, Leo IV and T for Simon & Geha 2007, Segue 1 for Geha et al. 2009) or with the Dwarf galaxy Abundances and Radial-velocities Team (DART) survey (Tolstoy et al., 2006). The importance of the mass-to-light ratio of stellar systems as an indicator of the nature of a stellar system is strengthened by its robustness against tidal interactions. Indeed, any hope of robustly classifying stellar systems around massive hosts would be somewhat thin, should this ratio be extremely sensitive to tidal forces. Peñarrubia, Navarro & McConnachie (2008) show that the impact of tidal stripping on the denomination of a galaxy is limited, as the mass-to-light ratio should remain high in those systems. If the dark matter halo is cuspy, a tidal stripping event could event increase this ratio as the stellar component of the system
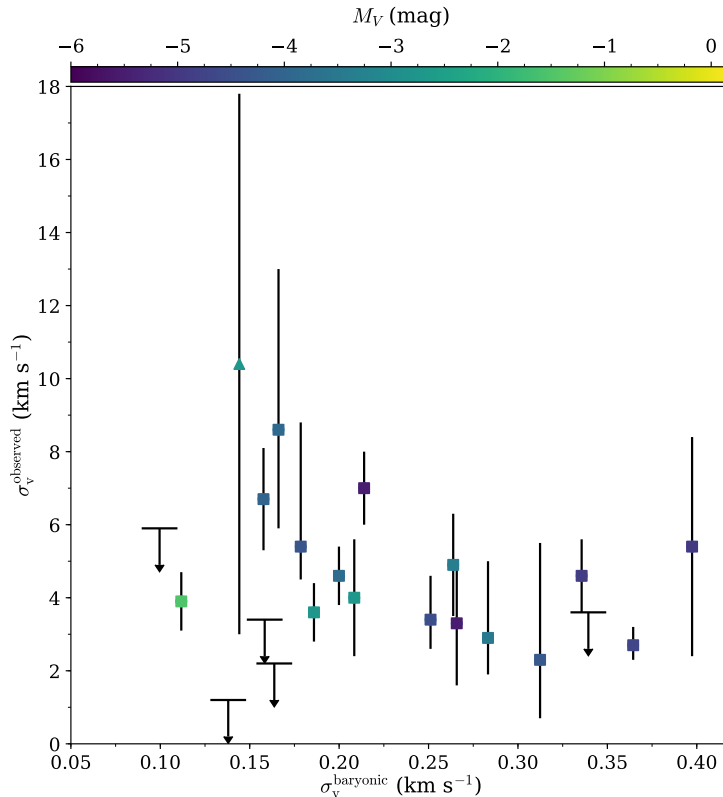
Figure 1.5: Comparison between the expected purely baryonic velocity dispersion on the x-axis and the observed one from spectroscopic observations on the y-axis for all faint satellite galaxies ($M_V \geq -6$ mag) of the MW. Confirmed dwarf galaxies are represented as squares, dwarf-galaxy candidates as triangles. They are colour-coded according to their absolute magnitude. The observed velocity dispersion is at least ten times larger than the baryonic one for most systems. In this plot, a few satellites have a limited, unresolved dispersion: Dra II, Hydra II, Seg 2, Tri II and Tucana III. For this reason, they are reported here as 90 per cent confidence level upper limits.

should be stripped before the cusp, while the dark component should remain almost intact. Of course, these considerations only holds in cases where the stripping is not extreme and does not completely destroy the galaxy.

However, studying the dynamics of a faint satellite has its limits. In that regard, the important example to cite when discussing the chase for measuring the dynamical mass of galaxy is the one of Segue 2. (Kirby et al., 2013a). For the second time, another step in the study of faint systems was reached, as Kirby et al. (2013a) were unable to resolve the velocity dispersion of the faint satellite ($M_V \sim -2$ mag) but only put an upper limit with $\sigma_v < 2.6$ km s^{-1} at the 95 % confidence limit. Other systems with a velocity dispersion too low to actually be measured with the data at hand soon started to pile up after Segue 2 (Martin et al. 2016a, Kirby et al. 2017, Simon et al. 2017, Longeard et al. 2018, Fritz et al. 2019). Several reasons are in play to explain the increasing difficulty to measure the dynamical mass of faint satellites. The first of those is that some dwarf galaxies in the extremely

faint regime will be dynamically colder than brighter dwarfs while still being DM dominated because their stellar mass should scale with their halo mass (even though the stellar mass is sensitive to tidal interactions and the quenching of star formation). As shown in Figure 1.5, the estimated $\sigma_{\rm v}^{\rm baryonic}$ is extremely low in most cases (< 0.4 km s^{-1}) for known satellites with $M_V \geq -6$ mag. Therefore, an observed velocity dispersion of the order of 1-2 km s^{-1} would still indicate the presence of a fairly massive DM halo. This order of magnitude is also the one that is typically cited as the individual uncertainty measurements on the velocities of stars in these systems. For more distant/fainter galaxy candidates, these observational uncertainties can even be slightly higher for most stars in a given dataset. A straightforward way to overcome this issue would be to have enough statistics, i.e. identify enough stars members of a given system. In that regard, the use of multi-object spectroscopy has been essential over the last decades to establish velocity dispersion profiles in bright dwarfs and find several members in very faint systems drowned in the Galactic contamination (Wilkinson et al. 2004, Battaglia et al. 2007, Kirby, Simon & Cohen 2015, Martin et al. 2016a). However, with the remarkable faintness and/or distance of the dwarfs studied also comes a critical lack of the Red Giant Branch and Horizontal Branch (HB) stars, which considerably reduces the number of stars actually members of the dwarfs that can be observed and identified with a reasonable time spent at the telescope. An extreme example is the satellite Draco II (see Chapter 3). Theoretical simulations of the colour-magnitude diagram (CMD) of this faint dwarf-galaxy candidate ($M_V \sim -0.8$ mag) show that in ~ 80 per cent of cases, Dra II should not have any RGB star at all. This is backed up by both Martin et al. (2016a) and Longeard et al. (2018) who fail to identify even one RGB or HB star belonging to the system, despite two different spectroscopic runs and 57 CMD-selected stars observed in the vicinity of the satellite.

Using the internal dynamics of a system comes with other caveats. Unidentified binary stars can also be an issue and can artificially inflate the velocity dispersion of faint systems with extremely low expected velocity dispersions (McConnachie & Côté 2010, Bradford et al. 2011). On that aspect, Koposov et al. (2011) finds, in Boo I, a binary star for which the radial velocity varies in a matter of days.

Binaries are not the only way to inflate the velocity dispersion of a stellar system. Earlier on, I mentionned that the velocity dispersion should be robust against tidal interactions. However, it is still theoretically possible that a tidal disruption event affecting a globular cluster can cause stellar remnants to accumulate at the core and inflate the observed dispersion. Even though extreme cases of tidal stripping already known do not show such an effect (Palomar 5, Dehnen et al. 2004). Finally, it is important to point out that Equation 1.2 only probes the system's dark matter halo up to its half-light radius, and within the prior hypothesis of dynamical equilibrium. For all these reasons, other tracers of the presence of an underlying DM halo are needed to face these observational challenges.

1.3.2 Metallicity properties

Theoretically, the dynamics and size of a galaxy should not be the only properties impacted by the presence of a massive DM component. In any stellar system, the chemical enrichment is sustained by stellar evolution, whether it is by the fusion of lighter elements in stars themselves during their lifetime or at a later, violent stage of evolution (Alpher, Bethe & Gamow, 1948). Iron holds a peculiar place in astronomy as it is the first element that stars are unable to fuse, due to its low binding energy. The intra-galactic medium is then enriched by supernovae (SNe) that produce heavier elements. The next generation of stars will be formed with this gas and be more metal-rich than the last one. This basic picture provides a direct understanding of the possible consequences of the existence of a massive DM halo in a galaxy. SNe enrich the gas of a system, but the extreme violence of such events can also lower its gas content, consequently preventing the stellar system from forming new stars (Tassis et al. 2003, Marcolini et al. 2006, Hopkins, Quataert & Murray 2012). Therefore, the metallicity should correlate with the ability of a given system to retain its gas and shield it against SNe winds. The large mass brought by the dark component of a galaxy (and therefore its deeper gravitational well) is perfectly adequate for this task. Alternatively, or additionally, the Star Formation Rate (SFR), a property linked to the mass of a galaxy (Magrini et al., 2012), can have a role to play. An effective star formation process would enable the possibility to achieve higher metallicities before the SNe start expelling most of the gas. The possibilities of a steeper Initial Mass Function (IMF) for the dwarfs' stellar populations (Gennaro et al., 2018) or a dilution of metals in a pristine gas also have to be considered. The question of which effect actually drives the metallicity properties of a stellar system, or if it is the result of a complex interplay between said effects is still not fully answered, but the importance of the mass of a galaxy, and in particular the extra mass brought by its dark component on its abundance patterns is clear. Measuring these abundances, and in particular the metallicity, should therefore be a priority in the context of faint systems.

The most straightforward and convenient method to access the metallicity is photometry, through a careful comparison of the morphology of observed CMDs with theoretical ones, or with empirical ones build from well-described, bright systems (Bernard et al., 2014). The pattern formed by a stellar population depends on its characteristics, from the steepness of the Main Sequence Turn-Off (MSTO) to the location of the Horizontal Branch (HB). The main caveat of this method is the age-metallicity degeneracy which prevents from estimating the metallicity of a stellar population if its age is not known. Large uncertainties on the distance can also be an additional issue, even though its impact is limited as it only results in a shift of the CMD model that we wish to compare with the observed one. Fortunately, the efforts carried out by the community to infer the dynamical properties of those objects using spectroscopy, detailed in the previous subsection, also enabled to access to the properties of their stellar populations, although several methods have been used over the years with the use of Iron lines directly, a Calcium triplet calibration, or combinations of weak lines (Kirby et al. 2010, Koch & Rich 2014).

Nonetheless, all this work slowly led to painting a large picture of the metallicity properties

of the satellites of the MW, shown in the right panel of Figure 1.4. The latter highlights the peculiarity of dwarf galaxies compared to clusters, as brighter/more massive galaxies are more metal-rich than their faintest/less massive cousins. It is also interesting to note that this relation still holds for central galaxies such as the MW or M 31, which belong to a mass regime not shown in the plot, and that even the dwarf galaxies of M 31 follow a similar trend (Collins et al. 2013, Collins et al. 2017). The scatter of this relation, shown as dashed lines, can have numerous causes, from the stochasticity of the stellar evolution (Revaz & Jablonka, 2018) or of the DM halo, to environmental effects such as tidal interactions. The larger scattering of dwarfs and dwarf candidates at the faint-end of the luminosity regime can be intriguing but could simply be caused by larger uncertainties on the metallicity measurements. Two obvious outliers can be spotted in Figure 1.4: Grus I ($M_V \sim -3.5$ mag, [Fe/H] ~ -1.4 dex) and the Sagittarius Dwarf Spheroidal (Sgr dSph, $M_V \sim -13.5$ mag, [Fe/H] ~ -0.5 dex). In the case of Grus I, only seven stars identified as members of the system have a metallicity measurement. Out of those, four are reported as more metal-rich than [Fe/H] > -1.4 dex (Walker et al., 2016). This suggests that some contaminating, foreground stars may be wrongfully identified as members of Grus I. In addition to this consideration, the uncertainties on Grus I's metallicity are quite large. The case of the Sgr dSph is different: the system is extremely bright and its properties are known with a great precision. However, the dwarf is giving birth to the largest stellar stream in the sky, the Sgr stream, and is therefore being heavily stripped. Tidal stripping should not affect the metallicity of a given stellar population (unless that population is spatially segregated) but can considerably change its luminosity, which can cause a horizontal shift in the luminosity-metallicity plane.

However, if a velocity dispersion much higher than implied by the baryonic content of a given system is convincing enough to prove its galaxy nature (unless evidence of extreme tidal stripping), the luminosity-metallicity relation of galaxies is not a diagnostic tool in itself. The properties of globular clusters are diverse enough so that they can overlap with the relation in many cases, especially in the range of $-10 < M_V < -6$ mag. Nonetheless, it can be a powerful argument when taken the other way around, to prove that an extended stellar system is not a galaxy, considering how well most galaxies are compatible with the relation. The case of the Sgr dSph, however, shows that some cases may be ambiguous when considering tidally stripped galaxy, which can consequently occupy "exotic" locations in the diagram. Going back to the progenitor's properties of a stripped galaxy is not straightforward. Confirming that the galaxy was stripped is already a challenge since tidal debris are extremely low surface brightness features that cannot always be detected. A high ellipticity and/or tidal tails are easier to detect, but they are not necessarily the proof of a tidal stripping because a) such features can appear at the very beginning of the tidal interactions, when no material has yet been stripped, or b) because they can simply be artefact of the sampling of stars on the sky for very faint systems (Martin, de Jong & Rix 2008, Muñoz, Geha & Willman 2010).

The physical reason behind the luminosity-metallicity relation has other important consequences on the chemical properties of galaxies. If the dark matter halo is massive enough to
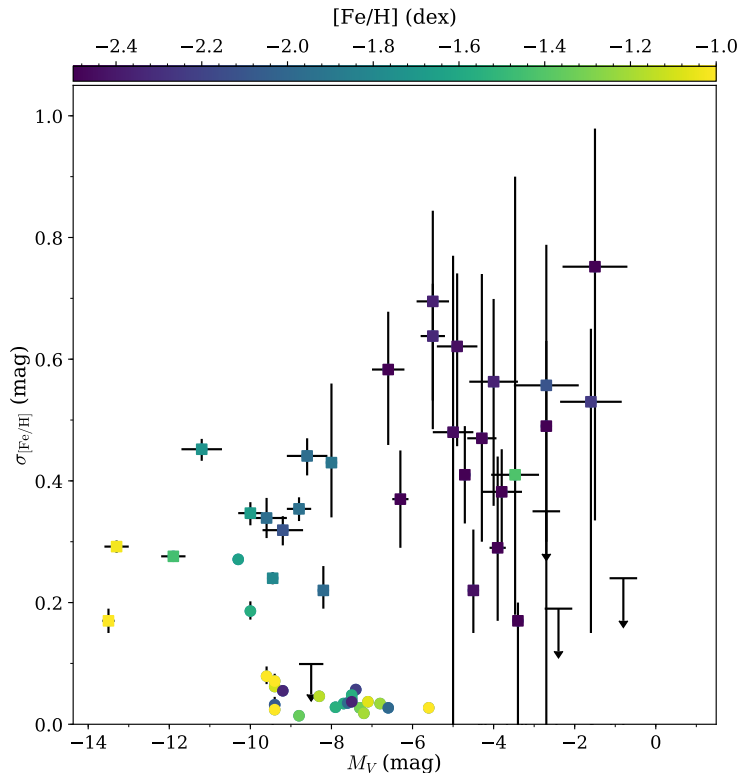
Figure 1.6: Metallicity dispersion vs. absolute magnitude for the dwarf galaxies, candidates and globular clusters (circles), colour-coded by their systemic metallicity. The only stellar clusters with a significant metallicity dispersion are very bright. Some of them, such as Omega Centauri, are suspected to be the remnants of tidally disrupted dwarf galaxies (Bellazzini et al., 2008; Carretta et al., 2010), a picture strengthened by the recent discovery of the Fimbulthul stream originating from the cluster (Ibata et al., 2019).

retain supernovae ejecta and gas, causing an iron enrichment with mass, it also implies that these satellites should host multiple stellar populations (Baumgardt, Kroupa & Parmentier, 2008). This property is often referred to as the "metallicity dispersion" or "metallicity spread" in the literature. Webster, Sutherland & Bland-Hawthorn (2014) showed this effect in their simulations , and constrained the dark matter halo of a system to have a mass of $\sim 10^7$ $M_\odot$ to be able to retain gas against SNe explosions and continue forming stars. However, this picture is made more complex by the fact that the location of the exploding SNe is crucial. While a SNe at the center of a system will have a huge impact on its gas content, most of the energy of a SNe in the ouskirt will be lost and not affect significantly the gas of the system. It remains clear that a significant metallicity enrichment is linked to the mass of a satellite, and therefore to the dark component of a faint dwarf galaxy. The locations of satellites of the MW in the absolute magnitude-metallicity dispersion plane is shown in the right panel of Figure 1.4. The group of globular clusters stands out as most of them have a very limited metallicity dispersion. However, for the brightest ones, a significant metallicity dispersion

can be measured. Omega Centauri is a perfect example with a dispersion of $\sigma_{[Fe/H]} \sim 0.3$ dex. The existence of a few clusters at $M_V \leq -10$ mag showing clear signs of hosting several stellar populations is expected for very bright and therefore massive satellites for which their stellar mass is enough to retain their gas. For these systems, classification is not an issue, they belong to the luminosity regime of satellites where classification is straightforward based on their size. When looking at fainter clusters with $M_V \geq -10$ mag, $\sigma_{[Fe/H]}$ quickly drops down to a few centh of dex or upper limits only.

For dwarf galaxies, the picture is radically different: they show signs of chemical enrichment at all magnitudes. However, the same issue than kinematics starts to arise in the very faint regime, as constraints on the metallicity dispersion are less and less tight. Some dwarf-galaxy candidates (Dra II, Hya II, Seg 2, Tri II and Tuc III) only have upper limits at the 90 per cent confidence level. This is once more a direct consequence of the hardship of building reasonably-sized samples of member stars for a lot of faint satellites. Therefore, most of the Metallicity Distribution Functions (MDFs) of those faint satellites, which are invaluable pieces of informations to constrain galaxy formation and stellar evolution models, are not known. The picture painted by Figure 1.5 is interesting and informative, even if there is a vast disparity in both the sizes of the samples used to determine the metallicity properties, the methods used (Iron lines or calibration based on Calcium triplet, mainly) and the models chosen to describe the MDFs. Nonetheless, a well-constrained, resolved $\sigma_{[Fe/H]}$ is a powerful tool to discriminate between clusters and galaxies in the faint regime.

1.3.3   A note on chemical history and pattern

Iron abundance is not the only element that have been looked at with careful scrutiny over the years. Because of their old age and low mass relatively to the MW, dwarf galaxies were suspected to hold important clues about stellar populations in the early Universe and their evolution over cosmic time. To reveal these clues, diving deeper into the chemical composition of a dwarf's stars and characterise in great detail their abundances in various elements was needed. Indeed, because elements in a stellar population are formed through a wide variety of processes (stellar nucleosynthesis, Type I and II supernovae, etc.), studying their abundance can tell us more about the interplay of these very different formation paths in building the stellar systems that we observed today. For example, the group called α elements, composed of Oxygen, Magnesium, Titanium, Silicon and Calcium, are extremely useful. While the last three mainly form in the explosions caused by the Type II Supernovae (SNII), O and Mg usually form in massive stars. The $[\alpha/Fe]$ abundance ratio can only be enhanced by SNII, i.e. by the explosion of massive stars in supernovae occuring shortly after star formation (Tinsley, 1979). This ratio decreases as soon as SNIa (mass transfer in a binary system) starts to drive the stellar evolution and keep producing iron without much α elements. Therefore, $[\alpha/Fe]$ is often used as a tracer of the star formation timescale in stellar systems (Tolstoy, Hill & Tosi, 2009). Neutron-capture elements such as Barium are divided in two groups (slow s- and rapid r- process) and are also able to trace the star formation history of a system. However, measuring these abundances in faint dwarfs was only
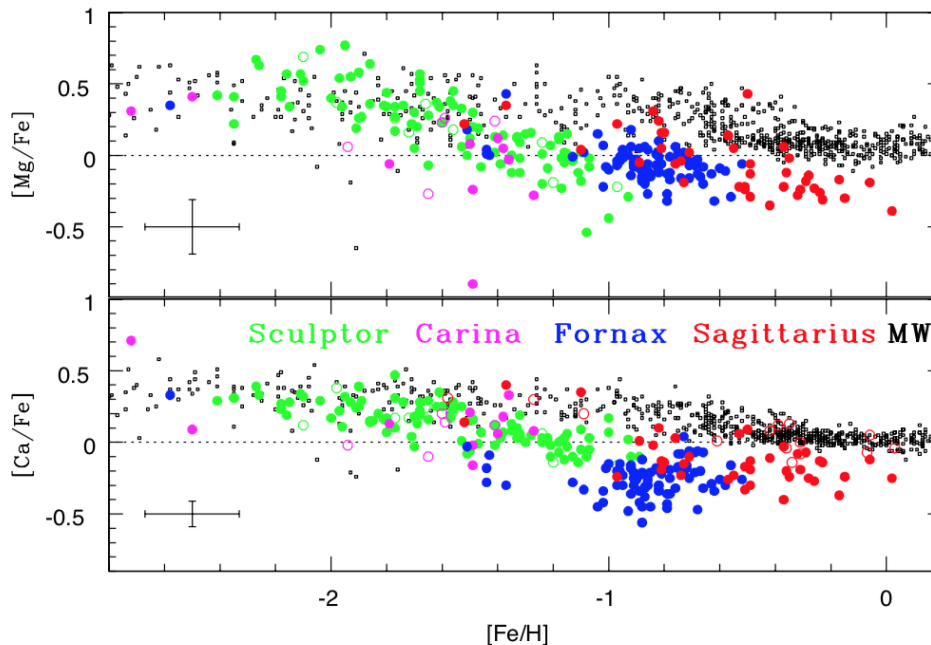
Figure 1.7: Figure from Tolstoy, Hill & Tosi (2009) representing the abundances of individual stars for Magnesium (top panel) and Calcium (bottom panel) with respect to their metallicities. These stars belong to four different dwarf galaxies: Sculptor (green), Carina (magenta), Fornax (blue) and Sagittarius (red), and to the MW halo stars for comparison (black). The abundances of the dwarfs match those of the MW stars in the metal-poor end, but ends up being quite different when going into a more metal-rich regime ([Fe/H] > −1.0 dex). Furthermore, we can see in the top panel a sudden change in trend at a metallicity [Fe/H]∼ −1.8 dex. Such a feature, called a "knee", marks the moment where the enrichment of the galaxy by SNIa started to take over the one by SNII. Though less visible in the three other galaxies represented because of the small number of stars in the metal-poor end of the plot, one can still notice that this knee is not located at the same metallicity for each system, and for the MW.

made possible thanks to the emergence of 8-10 meters class telescope in the mid 90's, with telescopes such as the Keck (1993) or the Very Large Telescope (VLT, 1998) and equipped with high-resolution spectrographs.

The first to carry such a endeavour was Shetrone, Bolte & Stetson (1998) with the Keck telescope and HIRES. They measured abundances for Ba and Ca for four stars in Draco, as well as their metallicities. Other studies followed over the years (Bonifacio et al. 2000, Shetrone, Côté & Sargent 2001, Geisler et al. 2005, Monaco et al. 2005, Koch et al. 2008a) for Draco (Dra), Carina (Car), Fornax (Fnx), Sculptor (Scl), Sextans (Sex), the Sgr dSph and UMi. The first results showed that the [α/Fe] abundance ratio of these bright dwarfs resemble the one of the MW halo at low metallicity, and start to differ when going into the more metal-rich regime. This is shown in Figure 1.7. In this plot, the [Mg/Fe] ratio for Scl highlights a very important feature. This ratio is steady in the metal-poor regime, but at [Fe/H] ∼ −1.8 dex, [Mg/Fe] starts to decrease while metallicity increases. This feature is known as the "knee" and marks the metallicity, and therefore the moment when SNIa
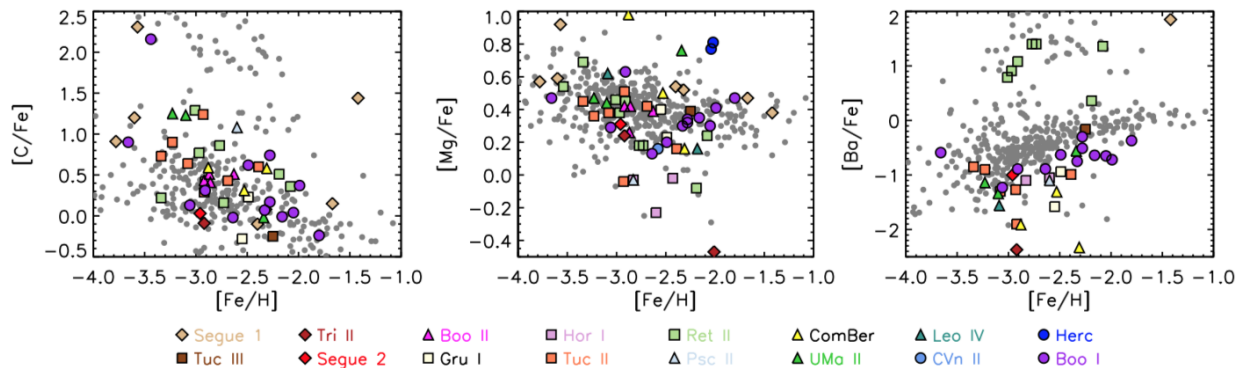
Figure 1.8: Figure from Simon (2019) representing the abundances of individual stars for Carbon (left panel), Magnesium (middle panel) and Barium (right panel) with respect to their metallicities. These stars are colour-coded according to the dwarf galaxy they belong to among the sixteen shown here as a legend at the bottom. A sample of MW halo stars is shown in grey.

began to prevail over SNII in the enrichment process of the dwarf galaxy, implying that the metal-poor component of Scl formed over less than 1 Gyr. Interestingly enough, the location of the knee in Scl is consistent with the two kinematically different population detected in the system (Battaglia et al., 2007). Figure 1.7 shows that the location of this knee is different in each dwarf, as well as in the MW, hinting at different star formation histories and ability to self-enrich (Kirby, Martin & Finlator, 2011). For example, the knee of the Sgr dSph is at [Fe/H] ~ -1.0 dex, showing that the star formation timescale of the system was significantly higher than the one of Scl. The study of neutron-capture elements also goes in this direction, showing that dwarf galaxies must have enriched on a shorter timescale than the MW halo, and the large scatter of their abundances compared to α elements in dwarfs suggests that the processes giving birth to these neutron-capture elements are rarer events. This example illustrates quite well how the stellar population of these faint stellar systems can help in understanding and constraining stellar evolution.

For the very faint regime ($M_V \sim -6$ and greater), this type of studies began with the analysis of two RGB stars in Hercules (Koch et al., 2008b), followed by Frebel et al. (2010) in UMa II and Coma Berenices. This effort has continued over the years to reach about 50 stars in 16 different faint dwarfs that have been observed with high-resolution, and their chemical abundances passed under careful scrutiny. This sample is shown in Figure 1.8. Although we went from 2 RGB to 50 stars in ten years, a lot of work and telescope time is still needed to have a clear picture of the chemical histories and patterns of the dwarf galaxies of the MW. Indeed, among these 50 stars, 13 are members of Boo I only, 7 belong to Ret II and 6 to Seg I. In other words, three dwarf galaxies represent ~ 50 per cent of the whole sample of stars with known abundances. On the opposite, Tuc III and Seg 2 only have 1 star represented here. Therefore, the chemical patterns of the dwarf galaxy population as
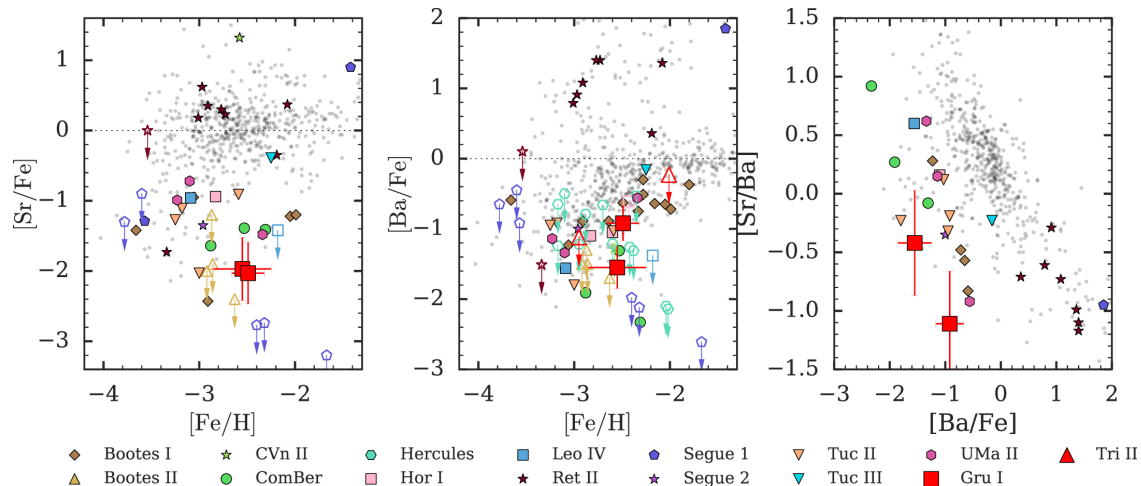
Figure 1.9: Plot taken from Ji et al. (2019) showing the abundances of Sr and Ba in 15 different faint dwarf galaxies. Boo I, Her and Seg 1 represent most of the sample. The grey dots represent the same abundances, but for halo stars. Clearly, the abundances of these r-process elements is quite different for most satellites compared to the halo stars. The picture is still complex, as some systems exhibit a MW-like behaviour, such as Seg 2, especially with [Sr/Fe].

a whole are still rather poorly sampled.

Nonetheless, some interesting conclusions can still be drawn from these data. Vargas et al. (2013) reported the abundances of 7 dwarf galaxies to study the behaviour of the $[\alpha/\text{Fe}]$ abundance ratio with respect to the metallicity of their stars. Most of the systems taken independently do not have enough data for us to draw any conclusion. However, combining the abundances of all the dwarfs' stars together,"as if" they belong to the same system, suggests that the knee is located around $[\text{Fe/H}] \sim -2.3$ dex and therefore a star formation of about 100 Myr. All faint dwarf galaxies have similar chemical patterns, although there are some exceptions. Seg 1, for example, does not show any clear sign of decrease in $[\alpha/Fe]$ abundance ratio, thus implying that the star formation must have been longer. Moreover, the MW halo Extremely Metal-Poor stars (EMPs) are a close match to the ones of dwarfs for all elements up to the iron-peak, such as illustrated with C and Mg in Figure 1.8. This is already an interesting observation since it implies that evolutionary pathways, at least up to the synthesis of Iron, must be quite similar for the faintest, least massive systems and for their central host galaxy such as the MW. However, heavier, neutron-capture elements abundances are quite peculiar in dwarfs, as is shown with Ba in the right panel of Figure 1.8: while Seg 1 and Ret II are extremely enriched in Ba, the other faint systems are slightly depleted of Ba compared to the MW stars. Ji et al. (2016a) further showed that Ba was no exception and that most of the stars of Ret II was also heavily enriched in Eu, another r-process element. This observation is quite important for stellar evolution models. Because only Ret II is significantly enriched in Ba and Eu but not particularly massive compared to other galaxies of the same luminosities, it must imply that only a rare event can cause such a boost, but that it must not be the only formation path as those elements are still found

in less abundance in all dwarfs (recent examples include Ishigaki et al. 2014 for Boo I and Chiti et al. 2018 for Tuc II).

Chemical patterns in globular clusters have also been studied extensively. In particular, their r-process elements abundances match those of the MW halo stars (Pritzl, Venn & Irwin 2005, Gratton, Carretta & Bragaglia 2012) very well. Therefore, Ji et al. (2019) propose that this criterion could be used to identify galaxies for extremely faint systems using the examples of Gru I and Tri II, as shown in Figure 1.9. Tri II already has a confirmed metallicity dispersion ($\sigma_{[Fe/H]} = 0.53^{+0.12}_{-0.38}$ dex) despite having only an upper limit on its σ_v. The case of Gru I is more straightforward, with both a velocity and metallicity dispersion indicating that the satellite is a galaxy. Ji et al. (2019) finds that the two stars of Gru I and the one of Tri II with a sufficient S/N to obtain abundances show signs of lack in r-process, neutron-capture elements. This is even clearer for the Sr abundances of the Gru I stars that are located ∼ 2 dex below the distribution of MW halo stars. High-resolution spectroscopy is time-consuming and requires that low/medium-resolution have been carried out first to identify certain members, and the examples of Ret II and Seg 1 show that the composition of faint dwarf galaxies can be quite complex and that not all of them follow the same chemical patterns. However, with the increasing size of the sample of extremely faint systems' stars observed at high-resolution, it is more and more convincing that the chemical composition of stellar systems can give away clues about their nature.

1.3.4   A note on orbits

The orbital properties of satellites can have a significant impact on their structural properties and kinematics, notably through tidal stripping if they come too close of their massive host galaxy (Peñarrubia, Navarro & McConnachie, 2008). Furthermore, their stellar populations can also be affected by ram-pressure stripping (Grcevich & Putman, 2009). This mechanism is the removal of the gas of a system that dives into the potential of its host, sub-consequently quenching its star formation (Tolstoy, Hill & Tosi, 2009), and it has been suggested for years that ram-pressure stripping has affected the star formation of the dwarf galaxies of the MW (Gatto et al., 2013). Of course, the luminosity (and mass) of a satellite can be dramatically changed by tidal forces, and there is no better example of this than the Sgr dSph that paints a large portion of the sky with its stars.

As explained in section 1.1, galaxies seems to be regrouping in the sky under a "Vast Polar Structure" (VPOS), a plane containing most identified dwarfs of the MW (Pawlowski, McGaugh & Jerjen, 2015). This is illustrated in the left panel of Figure 1.10. Such a repartition of dwarf galaxies is not per se a prediction of the ΛCDM model. If, in addition to that, it is showed that satellites are coherently rotating around the MW, as some pieces of evidence may suggest for M 31 (Ibata et al., 2013), the tension with ΛCDM would be even greater. Prove that such a plane is rotating requires to have knowledge of the individual orbits of each systems.

For all these reasons, knowledge of the orbits of dwarf galaxies and clusters around the MW is of first importance. However, this does not come without challenges. Ideally, to predict an orbit, the first element one needs would be the knowledge of the central galaxy's
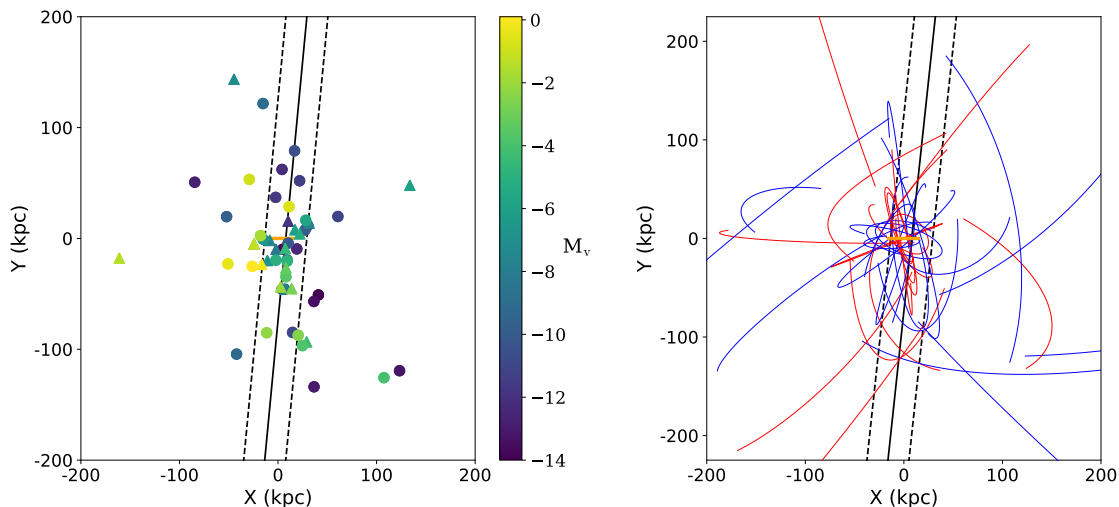
Figure 1.10: *Left Panel*: Locations of the MW dwarf galaxies (dots) and dwarf-galaxy candidates (triangles) in galactic coordinates. The colour scheme corresponds to the absolute magnitude. The solid and dashed lines correspond respectively to the "VPOS+new-4" and its corresponding RMS from Pawlowski, McGaugh & Jerjen (2015). The orange line shows the MW disc, with a chosen radius of 15 kpc. *Right Panel*: Orbits over 2 Gyr for all confirmed dwarfs with proper motion, radial velocity and distance measurements in the literature. All proper motions are taken from Fritz et al. (2018), Gaia Collaboration et al. (2018b) and Simon (2018). Prograde orbits are shown in red, while retrograde are shown in blue.

gravitational potential inside which the satellite is evolving. This is currently not known to this day, although it represents a busy and diverse field of research. Among the methods employed, the extensive search for streams is promising as they are direct witnesses of the violent behaviour of the MW tidal field (Malhan & Ibata, 2019). Thomas et al. (2018) use the Blue Horizontal Branch (BHB) stars to trace the density profile of the halo. If more constraints are placed over the years, the precise distribution of the various MW components and their respective masses is still debated. But even if it were, the other element needed is each of the three dimensional components of the satellite's velocity: the line-of-sight velocity given by spectroscopy, and the tangential velocity deduced from its proper motion. If the first "only" requires one observation, proper motions are more challenging to obtain since several observations over a large period of time are needed.

Very early in astronomy, the need to understand the motion of stars was clear. The first measurement of proper motion of stars in a cluster was undertaken more than one century ago. For 18 different star clusters and more than a thousand stars, Barnard (1931) carefully tried to detect a motion on photographic plates from observations spanning from 1898 to 1922. Only two stars had a measurable proper motion, both in the globular cluster M92. The study was used thirty years later by Kadla (1972) to deduce the proper motions of 106 stars. Rees (1992) took over and deduced the tangential motions of 300 stars, over 88 years of observations. These numbers illustrate quite well the hardship of having a full understanding of the motion of stars. The first major event in the field of observational galaxy dynamics

is the launch of the HIgh Precision PARallax Satellite (Hipparcos) space mission (Perryman et al., 1997). With an astrometry precise down to the milli-arcsecond, Hipparcos provided for its first catalog the proper motion of more than 118.000 stars. This was followed by the the Tycho catalogs, for a final sample of more than 2.5 million stars (Høg et al., 2000). van Leeuwen (2009), for example, use the Hipparcos catalog to derive the motion and distance of twenty globular clusters. But more important than the numbers themselves, Hipparcos was decisive as it provided something invaluable for astrometry and sky motion: an absolute reference frame based on background quasars and galaxies. In parallel, the Hubble Space Telescope (HST) was also providing good astrometry (~ 0.5 mas) and was therefore used to derive proper motions to study the MW and its surroundings (McNamara, Harrison & Anderson 2003, McLaughlin et al. 2006, Lépine et al. 2011) and even beyond with M 31 (Sohn, Anderson & van der Marel, 2012). A lot of important and diverse science cases have been covered by the HST proper motions, some of them being summarized by the HST PROper MOtion (HSTPROMO) paper (van der Marel et al., 2014). Astronomy has come a long way since the examination of photographic plates over decades just to obtain two proper motions measurements. However, the biggest leap was still to come with the spiritual successor of Hipparcos. The satellite Gaia was launched in 2013 and scanned the entire sky for five years before providing more than 1.3 billion proper motion measurements for our Galaxy and its satellites with its second Data Release (Gaia Collaboration et al., 2018a).

Immediately, the number of dwarf galaxies and globular clusters with a proper motion measurement, and therefore a constrained orbit rose in a formidable way (Gaia Collaboration et al. 2018b, Fritz et al. 2018, Kallivayalil et al. 2018, Massari & Helmi 2018, Simon 2018, Pace & Li 2019). The orbits of confirmed dwarf galaxies are shown in the right panel of Figure 1.10, along with one of the plane of satellites proposed by Pawlowski, McGaugh & Jerjen (2015). However, for the faintest of them, constraints on the proper motion can be weak. For example, the uncertainties on the proper motions of Aqu II and Boo II as derived by Fritz et al. (2018) are respectively of the order of ~ 0.5 mas yr^{-1} and ~ 0.4 mas yr^{-1}. This translates into large uncertainties on the tangential velocity (resp. 244^{+242}_{-174} and 379^{+79}_{-70} km s^{-1}). Associated with uncertainties on the distance and radial velocity, this can lead to a large variety of different allowed orbits. Only the favoured proper motions, radial velocities and distances are used to derive the orbits presented in Figure 1.10, but one has to keep in mind that this picture is not definitive, especially for faint and/or distant satellites. Nonetheless, these orbital properties bring invaluable pieces of information. The first straightforward result is the fact that most dwarf galaxies' orbits tend to be more eccentric than that of clusters. Moreover, the majority of dwarf galaxies are very close to their pericenter (less than 5 kpc). This indicates that an observational bias probably exists in our current census of the MW satellites because we are overall only able to find those lying as close as they can possibly be on their respective orbits. If such a bias exists, it must mean than a lot of satellites currently sitting further away on their orbits still await to be discovered with better instruments and telescopes. The origin of some systems were also uncovered by their orbital properties. Most dwarfs' orbits display a large inclination, which could be the sign of a filamentary infall instead of an isotropic one (Libeskind et al., 2005). Some satellites,

such as Eri III, Phoenix II, Hor I, Car II, Car III and Hyi I, have properties matching those of the Magellanic Clouds, hinting that they formed there before being accreted by the MW (Jethwa, Erkal & Belokurov 2016, Kallivayalil et al. 2018). Due to the faintness of some of these systems, these conclusions need to be strengthen by putting better constrains on their motions.

Because most dwarf galaxies have an eccentric orbit, several of them are (or were in the past) dangerously close to the MW and could have been tidally affected by its gravitational potential. Tuc III, a significant outlier with respect to the luminosity-metallicity relation developed in section 1.3.2, is one of those "endangered" satellites, which could (partially) explain its peculiar location on the [Fe/H]-M_V plane. The very low surface brightness satellite of Crater II ($r_h \sim 1066$ pc, $M_V \sim -8.2$ mag) can also be explained by its orbit. The satellite is extremely extended compared to others with a similar luminosity, such as Sextans ($r_h \sim 456$ pc, $M_V \sim -9.0$ mag) or CVn I ($r_h \sim 437$ pc, $M_V \sim -8.7$ mag). This large size could be the sign that the tidal field of the MW is currently ripping the dwarf apart and is therefore enlarging it. Even more so since Crater II is found to probably have experienced several passages at its pericenter, given its relatively small period of ~ 2 Gyr (Sanders, Evans & Dehnen 2018, Fu, Simon & Alarcón Jara 2019).

If Gaia showed that the dwarf galaxies' orbits are not all confined within a very thin plane, Fritz et al. (2018) find that out of the 23 satellites in their sample, 17 orbit along the VPOS, but they do not seem to do so in a coherent fashion. The right panel of Figure 1.10 contains 32 orbits and show that there is still a non-negligible fraction of satellites that do not follow the VPOS, especially the most distant ones. Those which are confined within the polar structure are not necessarily rotating together. Furthermore, by integrating orbits with three different MW mass, Fritz et al. (2018) propose that a "high-mass" MW ($\sim 1.6 \times 10^{12}$ $M_\odot$) can better explain the orbits of the dwarfs, compared to a low-mass one ($\sim 0.8 \times 10^{12}$ $M_\odot$) because a lighter MW would imply that a substantial fraction of the satellites would escape the MW and/or are lying outside its virial radius. As stated earlier, the mass of the MW is still a heavily debated subject, but this high-mass MW is compatible with other recent studies using the dynamics of the MW globular clusters or its streams (Küpper et al. 2015, Malhan & Ibata 2019, Vasiliev 2019, Watkins et al. 2019).

In this first chapter, we saw that a complete characterisation of the faintest satellites is needed to understand their nature and being able to listen to the stories they can tell us about the properties of the stellar and galaxy formation, the properties of the MW and of the Universe. The photometric and structural properties are the foundations, as they can tell us if the satellite is too extended, or too small, to be a galaxy, or a cluster, given its luminosity, especially in the brighter regime of MW satellites. In the faint regime ($M_V > -6$ mag), dynamical and metallicity properties are crucial: they are the indirect witnesses of the dark matter content of a galaxy. They also allow us to identify member stars of these systems that will later be extremely useful to be scrutinised at high-resolution to look for peculiar chemical patterns, or as a way to more reliably infer the proper motion and hence the orbit of the satellite. However, as we explained in section 1.3.1 and 1.3.2, finding member stars

of dwarf galaxies is becoming increasingly difficult as most observations focus on RGB stars that are lacking in faint/distant systems. Even with multi-object spectroscopy, which allows to follow spectroscopically several dozens of targets in one exposure, it still is an extremely time-consuming method that does not always give a large enough number of members that will allow to constrain the dynamics and metallicity (and its dispersion) of the system.

Therefore, to efficiently study the faintest dwarf galaxies and dwarf-galaxy candidates of the MW, one needs a method of selecting *a priori* the stars that have a higher probability of being associated with these systems, in order to focus the spectroscopic investigations on these stars specifically. This method would also be able to identify member stars *a posteriori* in cases where the *a priori* selection was not performed, and where the foreground contamination is significant. In section 1.3.2, we explained that in the faint regime of satellites, dwarf galaxies are overall more metal-poor than the MW disc and halo stars. Therefore, the hunt for faint dwarf galaxy stars can simply be associated to a hunt for very metal-poor stars ($[Fe/H] < -2.0$ dex) with photometry. Such an endeavour is made possible by the *Pristine* survey.

The Pristine survey

2.1   History and motivation for the creation of the *Pristine* Survey

Since stars are enriched through the successive life and death of their predecessors, the ones with the lowest metal content should be the oldest. They would therefore provide a unique way to probe the earliest times of the Universe, providing pieces of information about the birth of galaxies, as well as stellar formation and evolution. And of course, as explained in the previous chapter, dwarf galaxies fainter than $M_V > -8$ mag should be mostly populated by very metal-poor stars, as shown by the luminosity-metallicity relation of Kirby et al. (2013b) and confirmed by the various spectroscopic inquiries of those satellites in recent years. Therefore, detecting and studying those metal-poor stars is extremely important.

It would be surprising today (but maybe not quite impossible) to be able to observe the very first generation of stars (Population III) because they were most likely very massive (Abel, Bryan & Norman, 2000), and therefore had a short life, of the order of a few million years (Hirano et al. 2014, Stacy & Bromm 2014, Magg et al. 2018). However, Pop II and Pop I stars are still observable nowadays. Finding extremely metal-poor stars (EMPs, [Fe/H] ≤ -3.0 dex) among the hundreds of million of stars that our MW hosts looks like a "needle in a haystack" kind of problem. Indeed, the chance of blindly finding an EMP star is of $1/2000$ for stars with $14 < V < 18$ mag based on the Besançon model (Robin et al., 2003). This probability even decreases dramatically for lower metallicities. Therefore, blind spectroscopic observations do not intuitively seem to be the optimal road to follow, even though large spectroscopic surveys have allowed the detection of metal-poor stars over the last decades, such as with the Sloan Extension for Galactic Understanding and Exploration (Yanny et al., 2009, SEGUE), the Baryonic Oscillations Spectroscopic Survey (Dawson et al., 2013, BOSS), the RAdial Velocity Experiment (Steinmetz et al., 2006, RAVE) with 43 EMPs discovered, or the Large Sky Area Multi-Object Spectroscopic Telescope (LAMOST, Cui et al. 2012, Zhao et al. 2012). However, their primary objective was not necessarily to find such objects, which is the main reason why these surveys did not perform this task very efficiently.

A significant fraction of EMPs to this day are the result of two projects: the HK survey (Beers, Preston & Shectman 1985, Beers, Preston & Shectman 1992) and the Hambourg/ESO Survey (HES, Wisotzki et al. 2000, Christlieb, Wisotzki & Graßhoff 2002). The HK survey used an objective-prism and a narrow-band interference filter to cover ~ 7000

deg^2 for the hunt of metal-poor stars. It is interesting to mention that these ~ 7000 deg^2 were covered with 300 plates and inspected visually with a microscope, which contrasts enormously with the large spectroscopic surveys mentionned above. It is on the basis of the observed strengths of the CaII doublet lines H and K that the metal-poor candidates were selected for spectroscopic follow-up. With this method, the HK survey discovered ~ 1000 very metal-poor stars and ~ 100 EMP stars for a limiting B-magnitude of 15.5. The HES, also based on an objective prism, covered more than ~ 8000 deg^2 roughly two magnitudes deeper. Once more, the selection of metal-poor candidates was based on the strength of the CaII H and K doublet lines. However, the broad spectral range of the HES (3200 to 5200 angstroms) allowed for the measurement of the $B-V$ colour of stars. This particularity is important because the CaII H&K doublet lines, at a fixed metallicity, varies with the temperature and therefore the colour of a given star. Because of this, the HES was able to perform a reliable selection, leading to the identification of hundreds of EMPs in the MW and several Ultra Metal-Poor (UMP) stars (Beers & Christlieb, 2005).

If these two surveys gave outstanding results, their limiting magnitudes was a problem, mainly because they did not probe the MW halo in depth. Therefore, the next logical step in the search for metal-poor stars was to switch to surveys that could determine the metallicity of all stars in a field of view with photometry only. Several examples of broadband photometry being used to this end exist in the literature. For example, Ivezić et al. (2008) used $\sim 60,000$ stars with a spectroscopic metallicity measurement in SEGUE to build a relation between colours using the broadband u, g and r of the SDSS and their SEGUE metallicity for stars brighter than $g \sim 19.5$ mag. This work was mostly possible because of the SDSS u-band, which contains a lot of metal lines and therefore most of the metallicity information, even though its acquisition can be challenging because of the opacity of the sky in this spectral region. Ivezić et al. (2008) used this relation to compute the photometric metallicity of millions of stars in the Data Release 6 of SDSS to study the metallicity distribution of stars in some regions of the MW. In the near future, the Canadian-France Imaging Survey (Ibata et al., 2017, CFIS) will also take advantage of the possibilities offered by their u-band filter to map the northern high-galactic latitudes. Another similar project is the work of Schlaufman & Casey (2014) who combined the optical bands from the AAVSO Photometric All-Sky Survey (Henden et al., 2009, APASS), the near and med-infrared photometry of the Two Micron All-Sky Survey (Skrutskie et al., 2006, 2MASS) and the Wide-Field Infrared Survey Explorer (Wright et al., 2010, WISE) to identify 11,916 metal-poor stars. Among those, 3.8 per cent were EMPs and about a third between the range $-3.0 <$[Fe/H]< -2.0 dex. However, these surveys often have trouble yielding reliable results for stars more metal-poor than -2.5 dex, and/or are limited to bright targets. The work of Schlaufman & Casey (2014), for example, is only going down to $V \sim 14$ mag, and is therefore not probing the MW halo in depth, let alone the satellites of the MW.

One of the most notable attempt for the systematic hunt for metal-poor stars with photometry is the one of the SkyMapper Survey (Keller et al. 2007, Wolf et al. 2018). While studies like Ivezić et al. (2008) and Schlaufman & Casey (2014) used broadband photometry of one or several pre-existing surveys, and combined them to extract some metallicity

information, Skymapper used a 1.3 meters telescope to observe the southern sky with *ugriz* filters (slightly different from the "usual" ones from the SDSS), but more importantly with a specific, intermediate-band filter covering the spectral region between 367 and 398 nm. The spectral region of this filter contains the metallicity-sensitive CaII H&K doublet. One of the most important result of the SkyMapper survey is the finding of the most-iron poor star known to this day, poetically named SMSS J031300.36-670839.3, also known as the "Keller star" (Keller et al., 2014). The spectrum of the Keller star shows no iron lines, and only has an upper limit on its metallicity, with [Fe/H] < -7.1 dex (< -6.5 dex according to Nordlander et al. 2017). Therefore, this star may be the result of a single supernova enrichment. As a side note, it is interesting to mention that, while SMSS J031300.36-670839.3 is the most iron-poor star ever discovered to this day, it is not the most metal-poor one. The "Caffau star" (Caffau et al., 2011) has a metallicity of [Fe/H] $= -5.0$ dex, but contrary to the Keller star, is not severely enhanced in carbon. Nonetheless, the efforts of the SkyMapper team, not only with the Keller star, but with other studies, such as the findings of metal-poor stars in the bulge (Howes et al., 2015) has proven the usefulness and efficiency of large photometric, narrow-bands surveys designed to look for the oldest stellar relics of the Universe. But these efforts are solely being focused on the southern sky at the moment. For this reason, another photometric survey designed to accurately measure the metallicity with photometry of stars both in the MW and its faintest satellites in the northern hemisphere was created: the *Pristine* survey.

2.2 Characteristics of the *Pristine* survey and its Ca H&K filter

The *Pristine* survey (Starkenburg et al., 2017, S17) is a photometric survey led by Dr. Else Starkenburg (Leibniz-Institut für Astrophysik Potsdam) and Dr. Nicolas Martin (Observatoire Astronomique de Strasbourg). It is designed to find and study metal-poor stars individually, but also the various substructures composed of these old stellar populations both in the Galactic halo and beyond, such as the faint dwarf galaxies orbiting around the MW. *Pristine* uses the MegaCam (MC) wide-field imager based in the Canada France Hawai Telescope (Boulade et al., 2003, CFHT). As of July 2019, the *Pristine* survey has already observed more than $6,000$ deg^2. The entire footprint is shown in Figure 2.1 and was chosen to overlap with the SDSS. This overlapping is important because it provides broadband photometry, and therefore a temperature proxy with the $(g-i)$ colour, for all the stars in the survey. Spectroscopic metallicities from SDSS/SEGUE, for a fraction of stars in *Pristine*, are also needed to calibrate the *Pristine* model, as detailed in section 2.3. Furthermore, this footprint also includes 22 dwarf galaxies and dwarf-galaxy candidates, a portion of the Sgr stream, several globular clusters and streams, and a fraction of the bulge with the *Pristine* Inner Galaxy Survey (PIGS, Arentsen et al. 2019).

The core of the project resides in its narrow-band filter centred on the metallicity-sensitive Ca H&K doublet lines, and covers the spectral range between 3900 and 4000 angstroms. Most of the survey is run with 2×100 second subexposures, reaching $g_0 \sim 20.0 - 21.0$ for red giants and main sequence stars, respectively. Figure 2.2 illustrates the sensitivity of
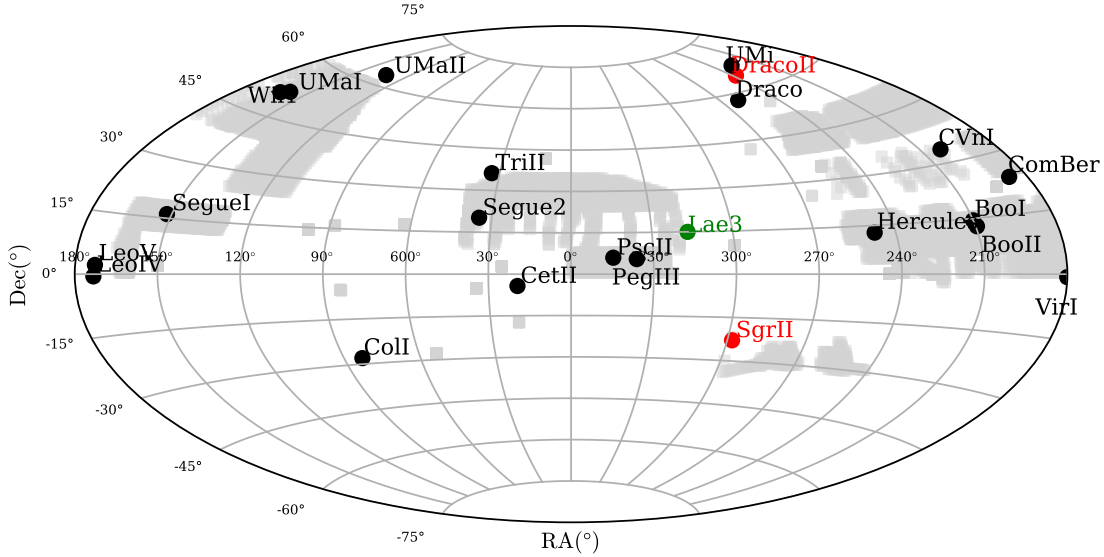
Figure 2.1: Footprint of the *Pristine* Survey as of July 2019, superimposed with the locations of all 22 dwarf galaxies and dwarf-galaxy candidates observed by *Pristine* on the sky. The main *Pristine* footprint is shown in grey. The two satellites in red, Dra II and Sgr II, have deeper *g* and *i* MegaCam/CFHT broadband photometry and *CaHK*. The studies of these two systems are detailed in Chapters 3 and 4. The remaining ones, in black, have shallower *CaHK* and their broadband comes from large photometric surveys (SDSS or PS1). Lae 3, an outer halo globular cluster which is the main focus of Chapter 5, is shown in green, even though it is not in *Pristine*.

the *Pristine* filter with respect to the main properties of a star. Synthetic spectra of giant stars with different effective temperatures, surface gravities and metallicities, simulated with the Model Atmospheres in Radiative and Convective Scheme (MARCS) and TURBOSPEC-TRUM (Gustafsson et al., 2008), are superimposed with the *Pristine* filter. In each panel, the only difference between the spectra is their metallicity. Figure 2.2 demonstrates that the flux received by the *Pristine* filter will decrease as a function of the metallicity, for a fixed effective temperature and surface gravity. This flux is transformed into a magnitude denoted as "*CaHK*" in the rest of this thesis, and therefore contains the metallicity information that we are interested in. Since the *Pristine* survey has the ambition to observe large areas of the northern sky to identify metal-poor stars, it is interesting to wonder how its filter compares with respect to the SkyMapper filter, which has a similar aim, but in the south. This comparison is shown in Figure 2.3. The synthetic spectra of two EMP stars are shown in this figure. They differ only by their carbon and nitrogen abundances: the star represented by the black spectrum is enhanced by 2 dex in nitrogen and carbon compared to the one represented by the blue line. Since the SkyMapper filter is much wider than the *Pristine* filter and is not centred on the Ca doublet, the flux it receives is sensitive to the metallicity, but also to the strong molecular features found in C and N enhanced stars. The *Pristine* filter, on the other hand, encompasses the CaII doublet tightly and is therefore far less subject to the leakage of features others than the CaII H&K doublet. In contrast
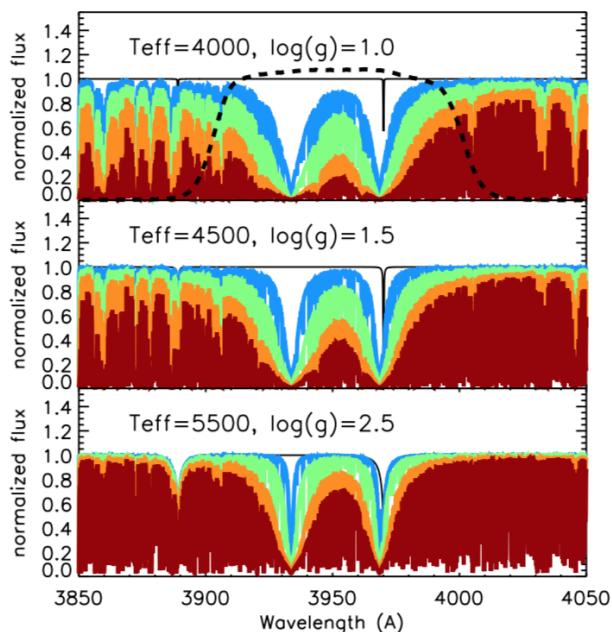
Figure 2.2: Plot from S17 illustrating the sensitivity of the *Pristine* Ca H&K filter for different stellar parameters. Each panel shows the synthetic spectra of a giant star simulated from MARCS stellar atmosphere and TURBOSPECTRUM with a fixed temperature and surface gravity, but with varying metallicities: a solar [Fe/H] in red, [Fe/H] = −1.0 dex in orange, [Fe/H] = −2.0 dex in green and [Fe/H] = −3.0 dex in blue. A spectrum with only hydrogen is shown as a solid black line. The effective temperature and the surface gravity vary with each panel.
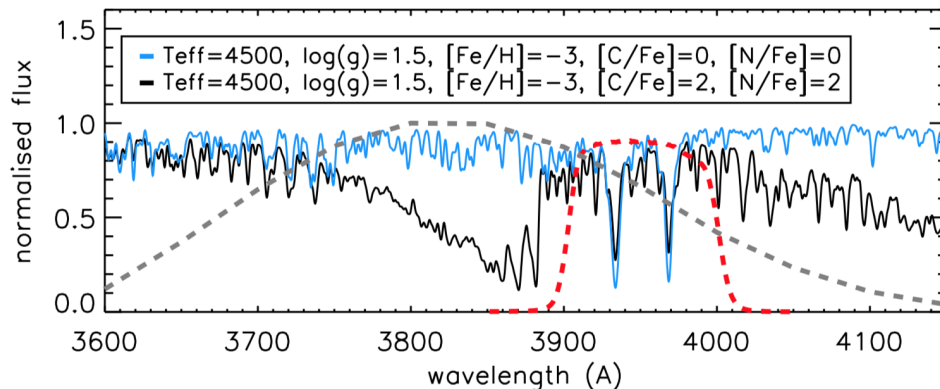
Figure 2.3: Plot from S17 representing the *Pristine* CaHK filter in red and the SkyMapper intermediate-band filter in grey. Two different synthetic spectra of giant stars are shown in black and blue, with the same effective temperature, surface gravity and metallicity, but with different carbon and nitrogen abundances. The black spectrum is enhanced in C and N by two dex. This figure shows the discriminative power of *Pristine* as the narrowness of the *Pristine* filter allows to probe more specifically the CaII H&K doublet lines without being much influenced by unwanted, strong molecular features existing in the C and N enhanced star in black.

with the other surveys dedicated to the hunt for metal-poor stars, *Pristine* does not classify metal-poor and metal-rich stars in a "binary" manner, but quantitatively assign a metallicity to each star in its footprint.

2.3   The *Pristine* model: calibration and results

To link the *CaHK* photometry to a metallicity measurement, S17 use $\sim 17{,}500$ stars in common between the *Pristine* footprint and the SDSS, which provides both their broadband *ugriz* photometry and their spectroscopic metallicities (with the SEGUE1 and SEGUE2 surveys). A cascade of cuts are applied to clean this sample. To ensure that the SEGUE spectroscopic metallicities are robust, S17 discards all stars for which the uncertainty on $[\mathrm{Fe/H}]_{\mathrm{SEGUE}}$ is greater than 0.2 dex, and the ones with an uncertainty on the radial velocity greater than 10 km s^{-1}. Only stars with a spectroscopic S/N of 25 in SEGUE or above over the spectral range between 400 and 800 nm are selected. Very hot stars ($T_{\mathrm{eff}} < 7000$ K) do not make the cut. Then, all the stars identified as non-point sources by the photometric reduction pipeline, the Cambridge Astronomical Survey Unit pipeline (CASU, Irwin & Lewis 2001) and by the SDSS are discarded. Then, all stars identified as variables in PS1 (Hernitschek et al., 2016) are discarded. S17 get rid of white dwarfs by keeping all the stars with $(u - g)_0 > 0.6$ (Lokhorst et al., 2016). Finally, a selection of cool, metal-poor stars from the dwarf galaxy Boo I studied with spectroscopy over the years complements the metal-poor end of the sample. In the end, the final calibration sample contains more than 7,000 stars and is shown in the "*Pristine* colour-colour diagram" of Figure 2.4. This diagram is the key to the *Pristine* survey. On the x-axis is the usual $(g - i)_0$ temperature proxy. The y-axis is the dimension containing the photometric metallicity information as it combines the g and i bands with *CaHK*. We saw in Figure 2.2 that at a fixed temperature and surface gravity, the *CaHK* depends on the metallicity of a star. Therefore, since the *Pristine* colour-colour diagram contains a temperature proxy on the x-axis and the *CaHK* on the y-axis, the stars represented in this diagram should be distributed according to their metallicity. The colour-scheme of the figure, representing the spectroscopic metallicities of the sample from the SEGUE surveys, shows that it is the case: more "metal-rich" stars with a $[\mathrm{Fe/H}] \sim 0.0$ dex, in red, are located at the bottom of the diagram. Then, the metallicity gradually decreases as we venture towards the upper part of the colour-colour diagram.

It is from this diagram that the *Pristine* model is calibrated by S17. First, the colour-colour space is binned with 0.025 wide bins, and the spectroscopic metallicities of all stars in a given bin are averaged. This is not done blindly, but through a 2σ clipping procedure in order to weed out the contamination in the bins. Some of the bins don't have any star, especially in the very metal-poor regime. Therefore, those empty bins are assigned with the value of their closest neighbour. At a fixed temperature, i.e. a fixed $(g - i)_0$, the calibration is also forced to have a monotonic behaviour, i.e. a lower metallicity when the $CaHK_0 - g_0 - 1.5(g - i)_0$ colour is lower. Such a behaviour is expected, but due to the contamination and low-number statistics in some bins, is not always the case in practice for the calibration sample. Any star located above the no metals line (determined from synthetic spectra) are assigned a
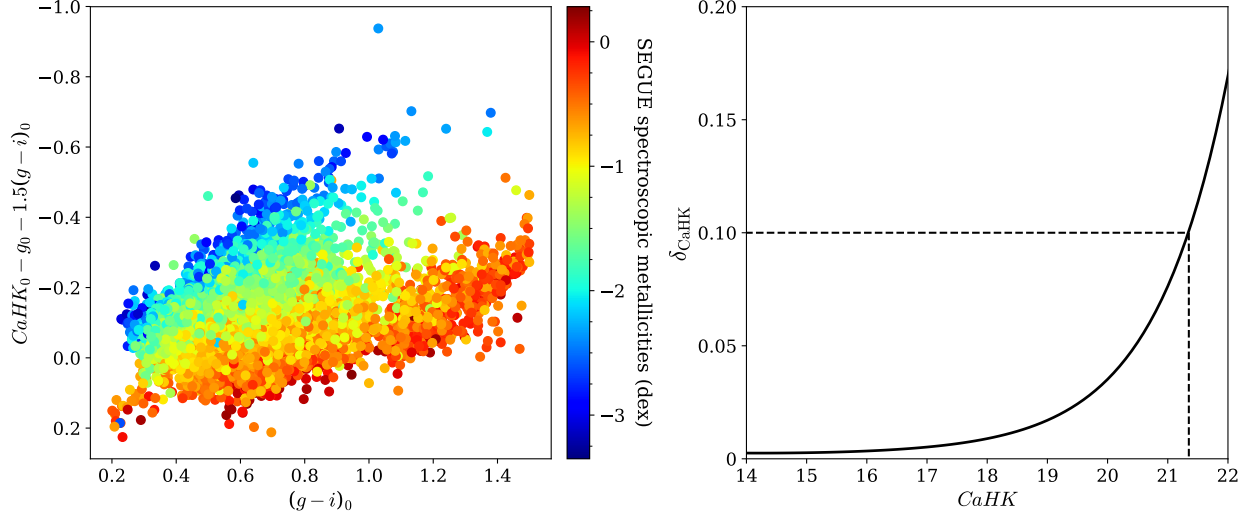
Figure 2.4: *Left panel: Pristine* colour-colour plot. The x-axis displays the $(g-i)_0$ temperature proxy, while the y-axis contains the photometric metallicity information, with the *CaHK* magnitude. Stars are colour-coded according to their spectroscopic metallicities from the SEGUE survey. The discriminative power of the *Pristine* filter is illustrated here: stars with solar metallicities lie at the bottom of the diagram, and the metallicity gradually decreases upwards. The photometric metallicity of any star can therefore be inferred by knowing its location on the diagram. *Right panel:* Typical uncertainties on the *CaHK* for a 2 deg^2 region representative of the main survey. The quality criterion used to calibrate the *Pristine* model is indicated with the dashed black lines. We reach $\delta_{\mathrm{CaHK}} \sim 0.1$ at $CaHK \sim 21.3$ mag.)

photometric metallicity of -4.0 dex. Finally, the grid model is smoothed with a 2 pixels wide Gaussian kernel. It is important to note that, at a fixed effective temperature, the difference of colour on the y-axis between two stars with different metallicities decreases as we go towards the metal-poor regime. In other words, the discriminative power of *Pristine* becomes less important at lower metallicities. The final *Pristine* model is a grid that can transform any set of $(CaHK_0,g_0,i_0)$ into a photometric metallicity, called "[Fe/H]$_{\mathrm{CaHK}}$" in the rest of the text.

One important quantity assigned to all stars in *Pristine* is their probability to have a metallicity below -2.5 dex. It is computed through a $10,000$-iteration Monte Carlo procedure. Let us consider a star with a set of $(CaHK_0,g_0,i_0)$ and their associated photometric uncertainties $(\delta_{\mathrm{CaHK}},\delta_g,\delta_i)$. During the j-th iteration of the Monte Carlo, each magnitude will be randomly drawn from a Gaussian of mean $(CaHK_0,g_0,i_0)$ and standard deviation $(\delta_{\mathrm{CaHK}},\delta_g,\delta_i)$. These new $(CaHK_0^j,g_0^j,i_0^j)$ place the star at a certain position in the *Pristine* grid model, which yields a photometric metallicity [Fe/H]$_{\mathrm{CaHK}}^j$. The probability of the star to have a metallicity below -2.5 dex is then simply determined by the fraction of iterations for which the star was indeed assigned a photometric metallicity below -2.5 dex.

Once the model is calibrated, the photometric metallicities of the stars in the calibration sample are determined, and compared to their spectroscopic counterparts in order to assess
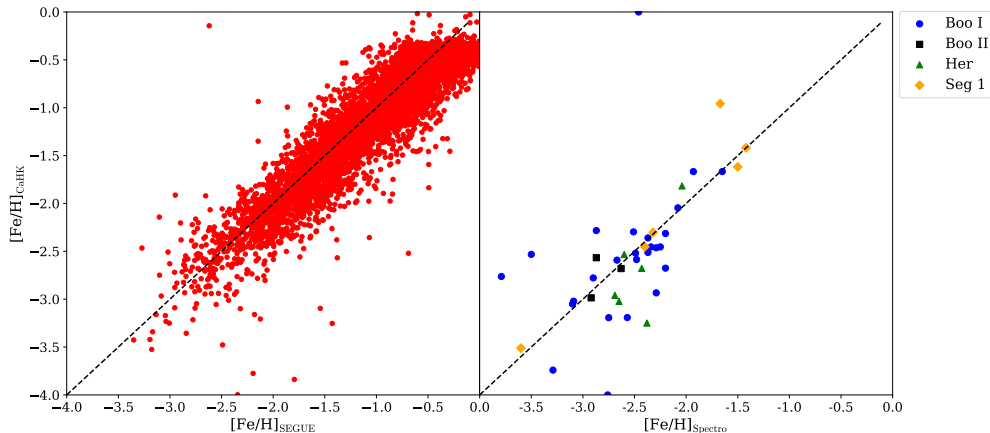
Figure 2.5: Performances of the *Pristine* survey. *Left panel:* Plot adopted from S17 comparing the SEGUE spectroscopic metallicities on the x-axis and the *Pristine* photometric metallicities on the y-axis. The black dashed line shows the 1:1 ratio. *Pristine* performs very well, even in the low-metallicity regime, with a standard deviation of 0.22 dex and a small bias of −0.08 dex over the entire sample. *Right panel:* Comparison between the spectroscopic (x-axis) and photometric (y-axis) metallicities for member stars of four dwarf galaxies: Boo I, Boo II, Her and Seg 1. Only stars with $\delta_{\mathrm{CaHK}} < 0.1$ are shown. Contrarily to the left panel, this sample is inhomogeneous as different instruments, resolutions and techniques used to infer the spectroscopic metallicities are represented here in the same plot. However, the performances of *Pristine* are still very satisfying.

the performances of *Pristine*. The left panel of Figure 2.5 shows the comparison between the photometric metallicities and the spectroscopic SEGUE metallicities. *Pristine* performs very well: the difference $[\mathrm{Fe/H}]_{\mathrm{CaHK}} - [\mathrm{Fe/H}]_{\mathrm{SEGUE}}$ is computed for all stars and modelled with a Gaussian. The best Gaussian fit yields a mean of −0.08 dex and a standard deviation of 0.22 dex. This indicates that there is a tight relation between the photometric and spectroscopic metallicities, but also that the *Pristine* model tends to infer a $[\mathrm{Fe/H}]_{\mathrm{CaHK}}$ that is slightly more metal-poor than the $[\mathrm{Fe/H}]_{\mathrm{SEGUE}}$. However, this systematic effect is small. It is important to note that this bias of −0.08 dex is an estimation over the entire metallicity range, but the left panel of Figure 2.5 hints that it increases in the low-metallicity regime. The right panel of Figure 2.5 shows that the relation between $[\mathrm{Fe/H}]_{\mathrm{CaHK}}$ and $[\mathrm{Fe/H}]_{\mathrm{SEGUE}}$ holds very well for very metal-poor stars in four faint dwarf galaxies: Boo I, Boo II, Her and Seg 1, for which the spectroscopic metallicities were inferred by different instruments and techniques. S17 also demonstrate that no significant systematic effect appear on the photometric metallicities when considering stars at very different galactic latitudes/longitudes.

The search for metal-poor stars conducted by the *Pristine* team started with a follow-up campaign at the Roque de los Muchachos observatory. Stars chosen as targets are the ones identified as promising metal-poor candidates based on their probability to have a metallicity below −2.5 dex in *Pristine*. The medium-resolution spectra of 205 stars were obtained using the Intermediate Dispersion Spectrograph (IDS, with a resolution of 3333 at 4500 angstroms) on the Isaac Newton Telescope (INT). In order to reach a magnitude of

$V = 17$ mag, a fraction of the 205 stars were obtained using the William Herschel Telescope (WHT) and its Intermediate dispersion Spectrograph and Imaging System (ISIS). Youakim et al. (2017) use this spectroscopic sample to assess qualitatively, and in more details, the ability of *Pristine* to find metal-poor stars and measure their metallicity. To do so, Y17 start to clean the sample in the same way as S17. First of all, all the stars identified as non-point sources, variables or white dwarfs are discarded according to the same criteria as S17. The stars falling outside the regions where the *Pristine* calibration is defined in the *Pristine* colour-colour diagram, or outside the range $(0.25 < (g-i)_0 < 1.5)$ are also discarded. The final sample includes 149 stars.

The spectroscopic metallicities are also derived by the collaboration, with the FERRE code (Allende Prieto et al. 2006, Aguado et al. 2017), for all stars with a minimum S/N of 10. The comparison between the two methods showed that the *Pristine* survey has a success rate of $\sim 22\%$ at identifying EMPs. In other words, 22% of the 46 stars identified as EMPs with *Pristine* are confirmed EMPs with spectroscopy. This number is confirmed by Aguado et al. (2019) who find a 23% success rate for an enlarged spectroscopic sample of 1008 stars. The fraction of EMPs compared with the entire spectroscopic sample (of 149 stars) is 17%. Since the best metal-poor candidates were observed first, one cannot consider than the rate of 17% can be applied to the entire *Pristine* survey. In order to have the rate of identified EMPs over the entire footprint, the spectroscopic sample is divided into ranges of photometric metallicities, and the relative fraction of EMP stars confirmed with FERRE in each range is computed. These relative fractions are then rescaled to the entire sample. This procedure yields a frequency of 1/800 EMP stars in *Pristine* (1,25%). The Besançon model predicts that roughly 1/2000 stars in the Galactic halo in the magnitude range of the 149 *Pristine* sample, i.e. $14 < V < 18$, should have a metallicity below -3.0 dex (0.05%).

When comparing the performances of *Pristine* to other works, the results of the survey are very satisfying. For example, Schlaufman & Casey (2014) report that $3.8^{+1.3}_{-1.1}\%$ of their sample are EMPs, and $32.0^{+3.0}_{-2.9}\%$ have a spectroscopic metallicity comprised between -3.0 and -2.0 dex, based on the high-resolution spectroscopic follow-up of their sample. These rates are lower than the ones reported by *Pristine*, with respectively 17 and 76%. Schörck et al. (2009), who compile the recovery rates of the HES survey, report a 7% EMP stars recovery rate from their best-selected sample, and 4% for the entire survey. This contrasts with the 17% rate of *Pristine*.

The *Pristine* survey excels at finding metal-poor stars, and based on the statistics from Youakim et al. (2017) and the 6,000 deg^2 footprint, thousands of EMP and ~ 60 UMP stars should be discovered by *Pristine*, for stars with $V < 18$. An exciting possibility would be to extend this limiting magnitude, which would probe the MW halo much deeper and would result in the finding of even more UMP stars. Of course, individual follow-up of all the interesting metal-poor candidates in the *Pristine* survey is not possible. In order to make the best of *Pristine*, upcoming large spectroscopic surveys, such as the William Herschel Telescope Enhanced Area Explorer (Dalton, 2016, WEAVE), the 4-meter Multi-Object Spectroscopic Telescope (de Jong et al., 2016, 4MOST) or the MaunaKea Spectroscopic Explorer (The MSE Science Team et al., 2019, MSE) will play a important role. Among those, *Pristine*
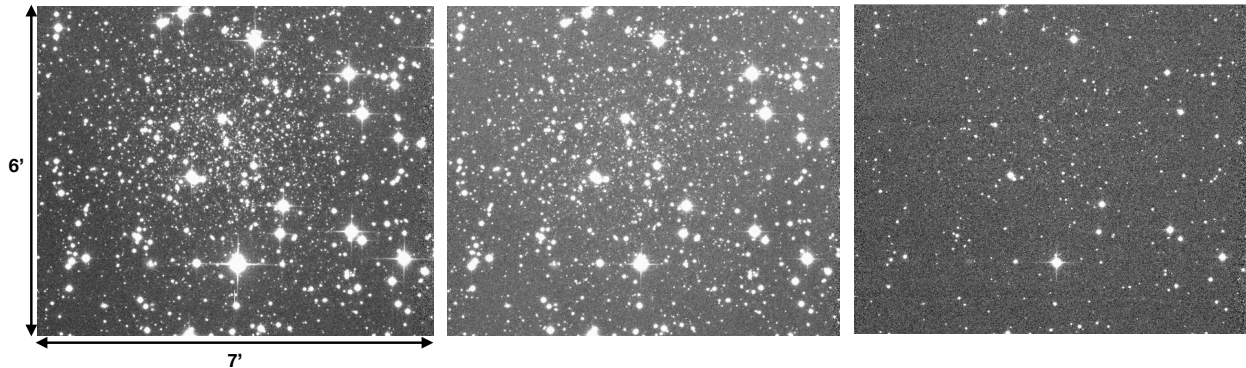
Figure 2.6: Images of the dwarf-galaxy candidate Sgr II (α_0 = 298.16628°, δ_0 = −22.89633°) with the MC/CFHT in the g (left panel), i (middle panel) and $CaHK$ bands (right panel). These images illustrate the shallowness of the $CaHK$ observations with respect to the broadband photometry.

already has a MoU with WEAVE.

2.4   Application to dwarf galaxies

The previous section demonstrates the power of the *Pristine* survey to identify metal-poor stars, but also to estimate their metallicity with a satisfying accuracy. Therefore, *Pristine* is extremely useful for the study of dwarf galaxies. In addition to the four faint dwarf galaxies in the main footprint, *Pristine* also specifically observed 18 dwarfs and dwarf candidates outside of this footprint. The locations of all the stellar systems observed in *Pristine* are shown in Figure 2.1. Thanks to the location of the CFHT, six low-declination systems ($\delta < -30°$) are observed in *Pristine*. All the satellites represented in black in Figure 2.1 have broadband photometry from SDSS and/or PS1, and the $CaHK$ observations from the *Pristine* survey. The two dwarf-galaxy candidates Dra II and Sgr II, represented in red, have gone through a special treatment. Both systems have been observed with deep MC/CFHT g_{MC} and i_{MC} broadband photometry and $CaHK$ observations deeper than the main survey. For these two fields, the integration time is of 3×700 s for g_{MC}, 5×500 s for i_{MC} and 3×705 s for the $CaHK$ (vs. 2×100s for the main survey), reaching $g_{MC} \sim 25.0$ and $CaHK \sim 23.0$ mag. For illustrative purposes, images of the Sgr II field in the three bands, centred on the satellite, are shown in Figure 2.6. Those two satellites are the ones I studied extensively during my PhD (Chapters 3 and 4).

As I explained in great length in the first chapter, the main challenge of the characterisation and study of the faint/distant MW dwarf-galaxy candidates is the low number of the spectroscopically-confirmed members. This directly impacts the metallicity and dynamical properties of the studied systems, which are not very well constrained. The proper motion can also be impacted and the resulting orbits can be so diverse that they bring little to no information to the table. However, the *Pristine* survey can be of great service to alleviate these problems. The $CaHK$ observations can be applied to faint systems and can allow us to
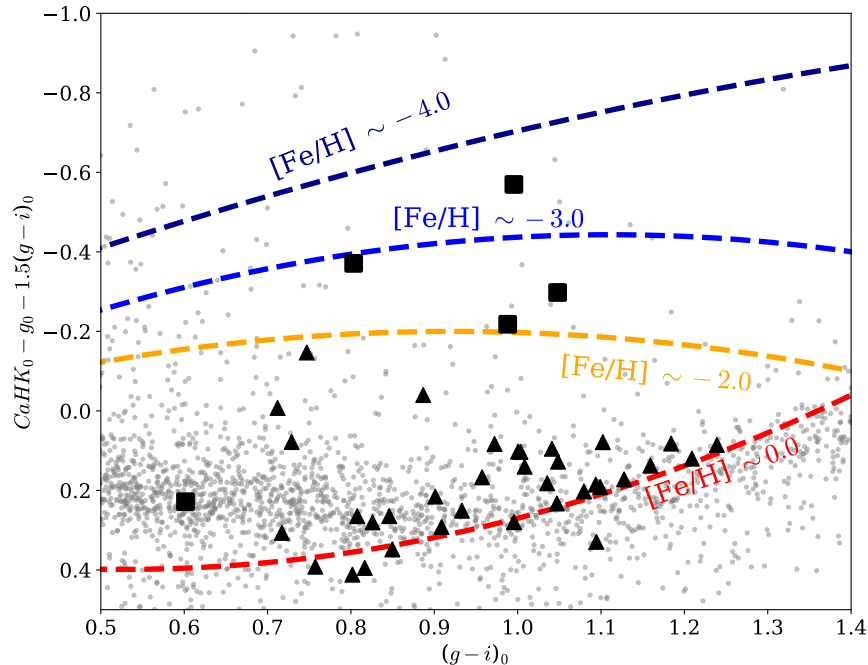
Figure 2.7: *Pristine* colour-colour diagram of a 1 deg² region centred on Col I. Grey dots represent field stars. Black markers represent the spectroscopic observations of Fritz et al. (2019). Triangles are stars identified as contaminants, while the squares show the location of the dwarf member stars on the diagram. Four iso-metallicity lines are shown here, from [Fe/H]$_{\rm CaHK}$ = −4.0 dex (dark blue) to a solar photometric metallicity in red. Four out of the five members are identified as metal-poor by *Pristine*, while the rest form a separate group of more metal-rich stars.

immediately detect the metal-poor stars in an entire field of view. Since dwarf galaxies are populated with metal-poor stars, *Pristine* is able to highlight their stellar populations from the more metal-rich stars of the foreground MW halo and disc. This is perfectly illustrated with the example of the recently discovered, faint and distant satellite (M_V = −4.2±0.2 mag, $d_\odot$ = 183±10 kpc) Colomba I (Drlica-Wagner et al., 2015, Col I). The dwarf-galaxy candidate has been observed with spectroscopy (Fritz et al., 2019, F19) using the Fibre Large Array Multi Element Spectrograph (FLAMES) on the VLT. Figure 2.7 shows the locations of all the targets observed by F19 for this system in the *Pristine* colour-colour diagram that discriminates stars based on their metallicity. For clarity, iso-metallicity lines are superimposed to the diagram. F19 selected their 39 targets with respect to their proximity to the Col I center as defined in Drlica-Wagner et al. (2015), but also to their locations in the CMD. Figure 2.7 discriminates the FLAMES targets in two groups: the 5 stars identified as members by F19 in black squares (using their line-of-sight velocities and proper motions in Gaia), and the contaminants represented as black triangles. In the *Pristine* colour-colour diagram, 4 out of 5 of the member stars appear as significantly more metal-poor than the rest of the spectroscopic sample, since they are located between the −2.0 and −4.0 dex iso-metallicity lines, respectively in orange and dark blue. In this diagram, the entire contamination is

easily identified, with most of them following the red iso-metallicity line at $[\mathrm{Fe/H}]_{\mathrm{CaHK}} \sim 0.0$ dex. Only one of the members also lies in the more metal-rich regime, which could indicate a misidentification of the star as a member or a significant metallicity gradient in Col I. Either way, the Figure 2.7 shows how powerful *Pristine* can be when applied to the study of faint satellites, because of its ability to efficiently weed out the "metal-rich" contamination of the MW.

Throughout these two introductory chapters, we saw what was the main properties of the faintest dwarf galaxies and the challenges faced by the astronomers who try to unveil their mysteries. A combination of deep photometric and spectroscopic data is crucial to understand these elusive satellites, and the useful contribution that the *Pristine* survey can bring in this field has been demonstrated. All of this will be combined and used in the three following chapters, where I will present the three first author publications I have written during my PhD. All three aim at understanding the nature of three different MW satellites, Dra II (Chapter 3), Sgr II (Chapter 4) and Lae 3 (Chapter 5) and constraining their properties. The first one is published, while the other two are accepted for publication.

Chapter 6 summarises my PhD work and move on to the exciting perspectives and potential that the *Pristine* survey and future telescopes hold in the study of faint satellites.

In Appendices A and B, I present two papers that I significantly contributed to, respectively on the dynamics of all the known UMP stars of the MW led by Federico Sestito, and on the proper statistical determination of the velocity dispersion of the NGC1052-DF2 galaxy led by Nicolas Martin.

A detailed photometric and spectroscopic study
of the very metal-poor Draco II satellite

3
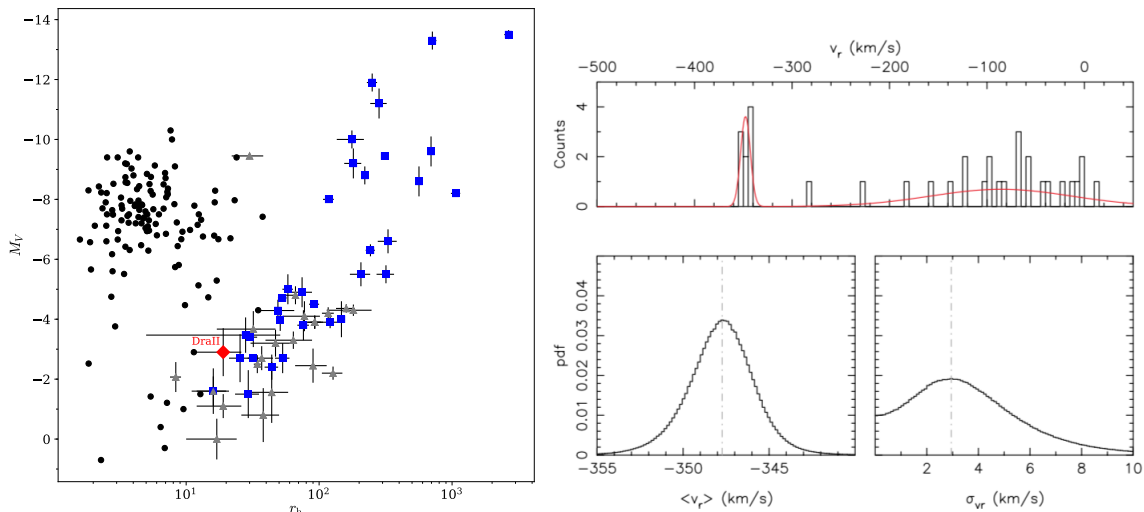
Figure 3.1: *Left plot*: Half-light radius (x-axis) and absolute magnitude (y-axis) of globular clusters (black dots), confirmed (blue squares) and candidate dwarf galaxies (grey triangles). Dra II is represented as a red diamond, with the $r_{\rm h}$ and M_V shown here both taken from L15. In this parameter space, Dra II occupies a location corresponding to dwarf galaxies. However, it was in 2015 the faintest galaxy candidate known, and was therefore extremely interesting to study. *Right plot*: Plot from M16 representing the radial velocities histogram of the 34 stars observed in M16. The red line corresponds to the best model to describe Dra II and the contamination populations. The lower panels correspond to the PDFs of the systemic velocity (left) and velocity dispersion (right) of Dra II. Although the favoured $\sigma_{\rm vr}$ hints at the existence of a dark matter halo, the PDF flattens in the lower regime, making it impossible to conclude about the nature of the system.

This chapter presents my study on the faint MW satellite Dra II. The satellite was discovered in 2015 by Laevens et al. (2015a, L15) using a detection algorithm to find statistically significant stellar overdensities in the PS1 data. The surface brightness of Dra II places the satellite close to the detection limit of the algorithm.

Dra II was immediately identified as a faint and interesting system. L15 already noticed the peculiarity of Dra II's population that did not have any obvious HB/RGB features in its CMD. Therefore, the age (~ 12 Gyr), metallicity (~ -2.2 dex) and distance modulus (16.9 ± 0.3 mag) of the system, determined at the time by fitting, by eye, an isochrone on

the main sequence of the satellite, were only crude estimates. L15 pointed out the need for deep photometry and spectroscopy to determine the nature of the system. Its size ($r_h = 19^{+8}_{-6}$ pc) and luminosity ($L = 10^{3.1\pm0.4}$ $L_\odot$) placed the satellite closer to the properties of dwarf galaxies, although Dra II was not very different from a few globular clusters such as Kim 2 or Eri III. The location of Dra II in the size-absolute magnitude plane at the time of its discovery, is shown in Figure 3.1.

A spectroscopic study was performed a year later by Martin et al. (2016a, M16) using the DEep Imaging Multi-Object Spectrograph (DEIMOS) with the Keck II telescope on Mauna Kea. The radial velocities of 34 stars in the vicinity of Dra II were measured, and their distribution is shown in the upper panel of Figure 3.2. Dra II was found to be highly recessional, with a systemic heliocentric velocity of $-347.6^{+1.7}_{-1.8}$ km s^{-1}. However, its velocity dispersion σ_{vr} revealed itself to be much more challenging to measure. For a satellite of the size and luminosity of Dra II as derived by L15, the expected σ_{vr} in the purely baryonic scenario, i.e. if the system was a globular cluster, would be of the order of 0.3 km s^{-1}. M16 measured a dispersion of 2.9 ± 2.1 km s^{-1}. If this value excludes the baryonic case at 1σ, the PDF of σ_{vr}, represented in the lower right panel of Figure 3.2, flattened all the way to zero, therefore not statistically excluding the possibility of a very low or large dispersion. Hence, it was not possible to determine the nature of Dra II from the dynamical properties of the satellite alone.

M16 were able to identify nine stars members of Dra II. However, it is quite exceptional to notice that none of these members were brighter than $i \sim 18.5$ mag. If L15 managed to identify, by eye, a promising group of stars that might be part of the RGB of Dra II in the CMD, M16 showed that they were in fact foreground contaminants, and were not able to identify one single giant star in the satellite. This lack of RGB stars has a direct consequence on the ability to measure the metallicity properties of Dra II. First, the calibration used by M16, based on the calcium triplet lines, is calibrated for giant stars, even though Leaman (2012) showed that it can be applied for sub-RGB stars. Moreover, the lack of giants also means that most stars do not have a spectrum with a good enough signal-to-noise ratio (S/N ~ 10) to infer their metallicities. In order to go as far as possible with the spectroscopic sample at hand, M16 first compared qualitatively the spectrum of the four highest S/N members with a metal-poor star ([Fe/H] ~ -2.1 dex) of the globular cluster NGC 2419, and noticed that in the Dra II stars, the Ca triplet lines were significantly weaker than the cluster star, indicating that its metallicity is lower. The caveat of this analysis is the fact that the NGC 2149 is a giant ($M_i = -0.6$ mag), while the four Dra II stars are sub-giants ($M_i \sim +2.0$ mag). Therefore, weaker lines in the Dra II members are expected. M16 then compared the aspects of the calcium triplets of the four highest S/N stars in Dra II and showed that, even for stars with roughly the same colour and magnitude, their triplets looked different enough to suspect that they do not have the same metallicity. This suggested a metallicity dispersion in the satellite. The main conclusions of this study was that the velocity dispersion was not constrained enough to assert the presence of a dark matter halo. Hints of a metallicity dispersion existed but were only suggested by a qualitative analysis of the spectra of four members stars of the system. M16 pointed out the need to

have both deeper photometry and more spectroscopic data to constrain all these parameters.

Therefore, deep g and i photometry were obtained with MegaCam on the CFHT, as well as another set of spectroscopic observations using Keck II/DEIMOS. Dra II was also observed with the CaHK filter of the *Pristine* survey. Using all these data, I conducted a study that resulted in my first paper, presented hereafter (Longeard et al., 2018). This study aims at exploiting the deep MegaCam photometry to refine the structural properties and the distance of the satellite, the spectroscopy to resolve the velocity dispersion of the satellite, and the photometric metallicities provided by *Pristine* to select member stars for both a better determination of the dynamical properties of Dra II and to infer, for the first time, the metallicity properties of the satellite. The Gaia Data Release 2 (DR2) also allows to determine the orbit of Dra II. Combining all these properties, I attempt to determine the nature of Dra II.

Pristine dwarf galaxy survey – I. A detailed photometric and spectroscopic study of the very metal-poor Draco II satellite

Nicolas Longeard,[1]★ Nicolas Martin,[1,2]★ Else Starkenburg,[3] Rodrigo A. Ibata,[1]
Michelle L. M. Collins,[4,6] Marla Geha,[6] Benjamin P. M. Laevens,[5] R. Michael Rich,[7]
David S. Aguado,[8,9] Anke Arentsen,[3] Raymond G. Carlberg,[10] Patrick Côté,[11]
Vanessa Hill,[12] Pascale Jablonka,[13,14] Jonay I. González Hernández,[8,9]
Julio F. Navarro,[15] Rubén Sánchez-Janssen,[11,16] Eline Tolstoy,[17]
Kim A. Venn[15] and Kris Youakim[3]

[1]*Université de Strasbourg, CNRS, Observatoire astronomique de Strasbourg, UMR 7550, F-67000 Strasbourg, France*
[2]*Max-Planck-Institut für Astronomie, Königstuhl 17, D-69117 Heidelberg, Germany*
[3]*Leibniz Institute for Astrophysics Potsdam (AIP), An der Sternwarte 16, D-14482 Potsdam, Germany*
[4]*Department of Physics, University of Surrey, Guildford, GU2 7XH, Surrey, UK*
[5]*Institute of Astrophysics, Pontificia Universidad Católica de Chile, Av. Vicua Mackenna 4860, 7820436 Macul, Santiago, Chile*
[6]*Department of Astronomy, Yale University, New Haven, CT 06520, USA*
[7]*University of California Los Angeles, Department of Physics & Astronomy, Los Angeles, CA, USA*
[8]*Instituto de Astrofisica de Canarias, Via Lactea, E-38205 La Laguna, Tenerife, Spain*
[9]*Universidad de La Laguna, Departamento de Astrofisica, E-38206 La Laguna, Tenerife, Spain*
[10]*Department of Astronomy & Astrophysics, University of Toronto, Toronto, ON M5S 3H4, Canada*
[11]*NRC Herzberg Astronomy and Astrophysics, 5071 West Saanich Road, Victoria, BC V9E 2E7, Canada*
[12]*Laboratoire Lagrange, Université de Nice Sophia-Antipolis, Observatoire de la Côte d'Azur, CNRS, Bd de l'Observatoire, CS 34229,
F-06304 Nice cedex 4, France*
[13]*GEPI, Observatoire de Paris, PSL Research University, CNRS, Place Jules Janssen, F-92190 Meudon, France*
[14]*Laboratoire d'astrophysique, École Polytechnique Fédérale de Lausanne (EPFL), Observatoire, CH-1290 Versoix, Switzerland*
[15]*Department of Physics and Astronomy, University of Victoria, PO Box 3055, STN CSC, Victoria BC V8W 3P6, Canada*
[16]*ISTFC UK Astronomy Technology Centre, Royal Observatory, Blackford Hill, Edinburgh, EH9 3HJ, UK*
[17]*Kapteyn Astronomical Institute, University of Groningen, Landleven 12, NL-9747AD Groningen, the Netherlands*

ABSTRACT

We present a detailed study of the faint Milky Way satellite Draco II (Dra II) from deep CFHT/MegaCam broad-band g and i photometry and narrow-band metallicity-sensitive CaHK observations, along with follow-up Keck II/DEIMOS multi-object spectroscopy. Forward modelling of the deep photometry allows us to refine the structural and photometric properties of Dra II: the distribution of stars in colour–magnitude space implies Dra II is old (13.5 ± 0.5 Gyr), very metal-poor, very faint ($L_V = 180^{+124}_{-72}\,L_\odot$), and at a distance $d = 21.5 \pm 0.4$ kpc. The narrow-band, metallicity-sensitive CaHK Pristine photometry confirms this very low metallicity ([Fe/H] $= -2.7 \pm 0.1$ dex). Even though our study benefits from a doubling of the spectroscopic sample size compared to previous investigations, the velocity dispersion of the system is still only marginally resolved ($\sigma_{vr} < 5.9$ km s^{-1} at the 95 per cent confidence level) and confirms that Dra II is a dynamically cold stellar system with a large recessional velocity ($\langle v_r \rangle = -342.5^{+1.1}_{-1.2}$ km s^{-1}). We further show that the spectroscopically confirmed members of Dra II have a mean proper motion of $(\mu_\alpha^*, \mu_\delta) = (1.26 \pm 0.27, 0.94 \pm 0.28)$ mas/yr in the Gaia DR2 data, which translates to an orbit with a pericentre and an apocentre of $21.3^{+0.7}_{-1.0}$ and $153.8^{+56.7}_{-34.7}$ kpc, respectively. Taken altogether, these properties favour the scenario of Dra II being a potentially disrupting dwarf galaxy. The low-significance extra-tidal features we map around the satellite tentatively support this scenario.

Key words: galaxies: dwarf – galaxies: individual: Draco II – Local Group.

★ E-mail: nicolas.longeard@astro.unistra.fr (NL); nicolas.martin@astro.unistra.fr (NM)

1 INTRODUCTION

During the last decades, important photometric surveys such as the Sloan Digital Sky Survey (SDSS York et al. 2000), the Panoramic Survey Telescope And Rapid Response System, Pan-STARRS1 (PS1; Chambers et al. 2016), or the Dark Energy Survey (DES; The Dark Energy Survey Collaboration 2005) have led to the discovery of dozens of Milky Way satellites. Some of these systems are extremely faint (e.g. Belokurov et al. 2007; Bechtol et al. 2015; Drlica-Wagner et al. 2015; Kim et al. 2015; Koposov et al. 2015b; Laevens et al. 2015; Martin et al. 2015), but studying them is important in order to better constrain the low-mass end of the galaxy mass function (Koposov et al. 2009). Moreover, systems confirmed to be dwarf galaxies are thought to be among the most dark matter dominated systems in the Universe, potentially making them one of the best locations to test the standard cosmological model ΛCDM (e.g. Bullock & Boylan-Kolchin 2017).

However, the distinction between dwarf galaxies and globular clusters can be challenging (e.g. Willman & Strader 2012; Laevens et al. 2014) yet crucial. In the ΛCDM model, dwarf galaxies are located in massive dark matter halos. Thus, they have deep potential wells that can leave a trail of indirect observational evidence. For instance, they are more extended for a given luminosity, which explains the low surface brightness nature of those systems and why deep photometric surveys were needed to reveal their existence. Dwarf galaxies are overall dynamically hot (i.e. their velocity dispersion is larger than that implied by the mass stored in their baryons alone, e.g. Martin et al. 2007; Simon & Geha 2007), thus implying the presence of a much higher mass than can be estimated from their stars alone, while the typical velocity dispersion for faint clusters is of order tenths of km s^{-1}. Dwarf galaxies also share a few chemical properties: they are overall more metal-poor than old globular clusters with the same luminosity, and show evidence of a large metallicity spread, which indicates that the system has undergone chemical enrichment (Willman & Strader 2012; Kirby et al. 2013). This is a strong indirect evidence for the presence of a dark matter halo as the deeper potential well of dwarf galaxies allows them to retain their gas more efficiently against supernovae winds and shields them against re-ionization, therefore allowing for the formation of successive stellar populations through time, despite early star formation truncation (e.g. Brown et al. 2014). On the contrary, most Milky Way globular clusters show very low metallicity dispersion with $\sigma_{\rm [Fe/H]} < 0.1$ (Willman & Strader 2012 and references therein). The few clusters with significant enrichment, such as ω Cen, are massive systems and even thought to be dwarf galaxy remnants (Bellazzini et al. 2008; Carretta et al. 2010).

As the detection of fainter satellites enabled by deeper and deeper surveys continues, the line between dwarf galaxies and globular clusters becomes blurred. For this reason, dwarf galaxy candidates have to be studied thoroughly: deep observations in both photometry and spectroscopy are needed to constrain the main chemical and structural properties of a given system.

Draco II (Dra II) is a Milky Way satellite discovered by Laevens et al. (2015) in the Pan-STARRS1 3π survey. At the time of its discovery, the satellite was found to be compact (half-light radius $r_h = 19^{+8}_{-6}$ pc). Martin et al. (2016a) carried out the spectroscopic follow-up of Dra II and inferred a marginally resolved velocity dispersion of $\sigma_{vr} = 2.9 \pm 2.1$ km s^{-1}. Visual comparison of spectra of the few brightest Dra II member stars suggested that the satellite could be metal-poor ([Fe/H] < −2.1) and could exhibit a metallicity spread. Martin et al. (2016a) tentatively favoured Dra II being a dwarf galaxy, but pointed out that the velocity dispersion of the system is only marginally resolved. Furthermore, no bright giant stars ($g < 19$) were identified as Dra II members, making the estimate of the chemical properties of the satellite challenging. Due to the particular faintness of the satellite, and the small number of bright members, kinematic evidence for a DM halo was limited.

In this work, we re-analyse Dra II and present a detailed study of its properties based on deep photometric observations obtained with the Megacam wide-field imager on the Canada–France–Hawaii Telescope (CFHT; Boulade et al. 2003) and Keck II/DEIMOS spectroscopy (Faber et al. 2003) that complements the sample of Martin et al. (2016a). In particular, we include here novel narrow-band photometry that focuses on the metallicity-sensitive CaHK doublet. We use these observations, which are part of a specific dwarf galaxy programme within the larger Pristine survey (Starkenburg et al. 2017), to identify the metal-poor Dra II stars and estimate the metallicity and metallicity dispersion of the system.

The paper is arranged as follows: Section 2 describes the observations and data of both our photometry and spectroscopy; Section 3 focuses on the analysis of the deep broad-band g and i photometry to infer the structural and photometric properties of Dra II; Section 4 specifically centres on the study of the narrow-band CaHK observations to derive the metallicity and metallicity dispersion of the system; and Section 5 revises the multi-object spectroscopic study of Dra II. The paper concludes with a discussion and conclusions in Section 6.

2 OBSERVATIONS AND DATA

2.1 Photometry

The photometry used in this paper was observed with the wide-field imager MegaCam on CFHT. It consists of deep, broad-band observations with $g_{\rm MC}$ (487 nm) and $i_{\rm MC}$ (770 nm) MegaCam filters and narrow-band observations with the new narrow-band CaHK Pristine filter that focuses on the metallicity-sensitive Calcium H&K lines. This is the same filter that is used by the Pristine survey (Starkenburg et al. 2017) to build a metallicity map of the Milky Way halo and search for the most metal-poor stars in the Galaxy. The data for Dra II, which were observed before the official start of the Pristine survey, are now folded into a dedicated effort by the Pristine collaboration to observe all northern, faint Milky Way dwarf galaxies or dwarf galaxy candidates with this filter (the Pristine dwarf galaxy survey).

Observations were conducted in service mode by the CFHT staff during the night of 2016 April 5 during conditions of good seeing (∼0.5–0.7 arcsec). Multiple sub-exposures were observed in each band to better address CCD defects and facilitate cosmic ray removal. Exposure times amounted to 3 × 700 s, 5 × 500 s, and 3 × 705 s in the $g_{\rm MC}$, $i_{\rm MC}$, and CaHK bands, respectively. After retrieval from the CFHT archive, the images are processed with a version of the Cambridge Astronomical Survey Unit pipeline (Irwin & Lewis 2001), which is specifically tailored to MegaCam data. We refer the reader to Ibata et al. (2014) for more details. The astrometric solution is derived using the catalogue of Pan-STARRS1 stars (PS1; Chambers et al. 2016) that are located in the field and have uncertainties on the $g_{\rm P1}$ PS1 photometry lower than 0.1 mag. The astrometric solution is good at the ∼0.1 arcsec level.

MegaCam $g_{\rm MC}$ and $i_{\rm MC}$ bands are then transformed onto the PS1 photometric system by using the PS1 $g_{\rm P1}$ and $i_{\rm P1}$ catalogues. Unsaturated MegaCam point sources are cross identified with PS1 sources having photometric uncertainties below 0.05 mag. To derive the colour equations between the instrumental and PS1 magnitudes,
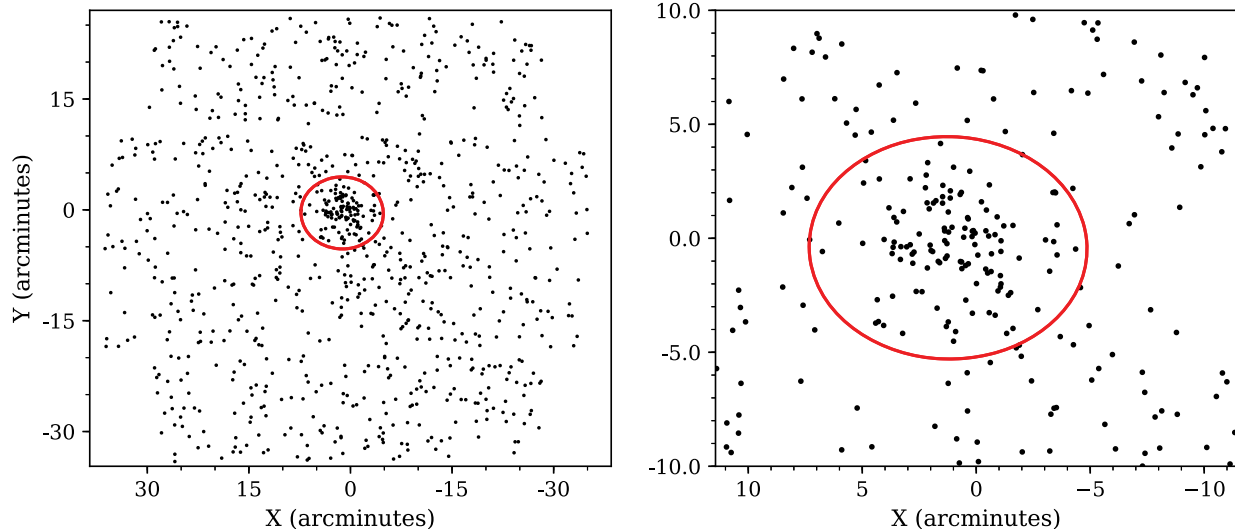
Figure 1. Left-hand panel: Distribution of MegaCam stars corresponding to a Dra II-like stellar population, centred on the system. The mask selecting Dra II-like stars only is shown in Fig. 2. The red line represents the two half-light radii ($r_h \sim 3.0'$, $\epsilon \sim 0.23$) region of Dra II based on the favoured model found in Section 3. Right-hand panel: Magnified view of the central region.

we performed a second-order polynomial fit. We find

$$g_{\mathrm{MC}} - g_{\mathrm{P1}} = a_0^g x^2 + a_1^g x + a_2^g,$$
$$i_{\mathrm{MC}} - i_{\mathrm{P1}} = a_0^i x^2 + a_1^i x + a_2^i,$$

with $x \equiv g_{\mathrm{MC}} - i_{\mathrm{MC}}$. The calibration yields $a_0^g = -0.0208 \pm 0.0021$, $a_1^g = 0.0626 \pm 0.0051$, $a_2^g = 3.5304 \pm 0.0052$ for the g band and $a_0^i = -0.0235 \pm 0.0019$, $a_1^i = -0.0235 \pm 0.0048$, $a_2^i = 4.2369 \pm 0.0047$ for the i band. The uncertainties on the polynomials coefficients are propagated into the photometric uncertainties. For clarity, we drop the P1 subscripts in the rest of the text.

The narrow-band CaHK photometry is processed following the treatment presented in the paper describing the Pristine survey and includes specific calibration steps to deal with variations in the photometry as a function of the position in the field of view (Starkenburg et al. 2017). The Pristine model that translates ($CaHK$, g, i) into [Fe/H] is recalculated for the PS1 photometric system and applied to the Draco II photometry.

All MegaCam magnitudes are dereddened following Schlegel, Finkbeiner & Davis (1998) and using the extinction coefficients from Schlafly & Finkbeiner (2011), but it is worth noting that Dra II is located in a low extinction area of the sky, with a median $E(B - V)$ of 0.018 mag. We rely on the CASU flags to isolate point sources. The MegaCam photometry are deeper than the original PS1 photometry that enabled the discovery of Dra II but this means that the MegaCam data saturate for magnitudes brighter than $i \sim 17.7$. For this reason, we complement the MegaCam data set with the PS1 photometry for magnitudes brighter than this limit. Finally, we clean the sample from stars for which the information on either of the two broad-bands is missing, we discard stars with photometric uncertainties larger than 0.2 mag in either of the two bands, and we further discard faint sources with $g < 24.5$. This latter cut removes regions of the colour–magnitude diagram (CMD) for which the star/galaxy separation becomes inefficient and the data are contaminated by a large number of background compact galaxies.

The final photometric sample comprises 12 638 stars with broadband photometry, out of which 3 238 also have good quality CaHK magnitudes. The spacial distribution of a fraction of this sample, composed only of Dra II-like stars, is shown in the left-hand panel

of Fig. 1, where the system is clearly visible as a compact stellar overdensity.

2.2 Spectroscopy

Dra II was observed during two different runs using the Deep Extragalactic Imaging Multi-Object Spectrograph (DEIMOS) in multi-object spectroscopy mode: a first mask was observed in 2015 and was the focus of the study presented by Martin et al. (2016a) whilst the second run was observed a year later on 2016 September 4. We used our group's standard set-up for these observations, employing the OG550 filter, the 1200 lines mm^{-1} grating and a central wavelength of 7800 Å. This results in a FWHM resolution at our central wavelength of $\sim$1.3 Å, and covers a wavelength range of $\sim$6500–9000 Å. Such a set-up allows us to well-resolve the Ca II triplet lines at $\sim$8500 Å. These strong absorption features are used to measure the line-of-sight velocities of our observed stars. The mask was observed for 1 h, split into 3 × 1200 s exposures.

Stars were selected for targeting using the colour–magnitude diagram for Dra II and they were given a priority for observation based on their distance from a fiducial isochrone, which highlighted the main sequence turn-off (MSTO), sub-giant and red giant branch of Dra II. We then designed a slitmask using the IRAF DSIMULATOR software package provided by Keck Observatories. In total, 96 stars were selected for observation, and 73 of these targets returned spectra of sufficiently high signal to noise (S/N) such that a velocity could be measured using the pipeline detailed in Ibata et al. (2011) and Martin et al. (2016a). All stars with a signal-over-noise ratio below 3.0 or a velocity uncertainty greater than 15 km s^{-1} were finally discarded. Heliocentric velocities and equivalent widths from stars observed twice are transformed into one single measurement by computing the weighted mean and uncertainties from the two independent velocity measurements. We do not investigate the potential binarity of Dra II stars in great detail as the low signal-over-noise of the spectra translate into typical velocity uncertainties in the range 5–15 km s^{-1}, which can make the detection of any variability challenging. Martin et al. (2016a) presented a spectroscopic study of Dra II using the 2015 data set, however, the heliocentric velocities of the 2015 stars in this work are slightly different: using the usual
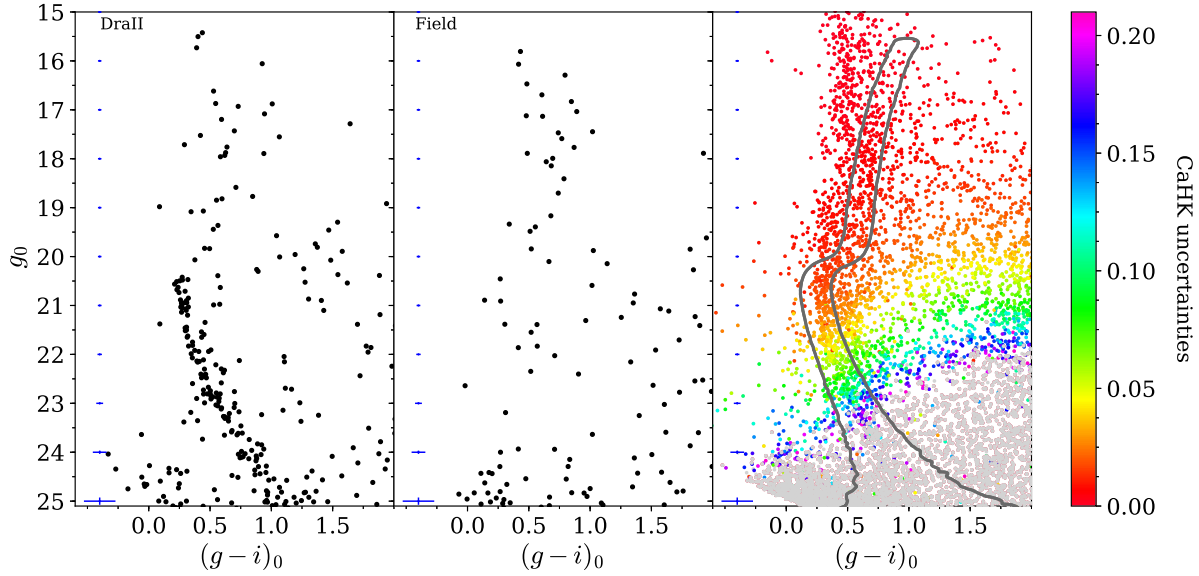
Figure 2. Left-hand panel: CMD of stars within two half-light radii ($r_h \sim 3.0'$) of the Dra II centroid. The main sequence of Dra II clearly stands out and points towards an old and metal-poor stellar population. The satellite seems to have very few, if any, giant stars. The photometric uncertainties in the g band and $g - i$ colour are shown every magnitude on the left of each panel. Middle panel: The field CMD obtained within a similarly sized region $\sim$25 arcmin away from Dra II centroid. Right-hand panel: CMD of all stars in the photometric data set, colour-coded according to the *CaHK* photometric uncertainties. Stars coloured in grey have *CaHK* uncertainties above 0.2. The CaHK is clearly shallower than the broad-band g and i photometry. Finally, the mask selecting only Dra II-like stellar population is shown in solid, dark-grey line.

method of the Ibata et al. (2011) pipeline to derive the velocities, the average difference of the 2015 and 2016 velocities is not 0 km s^{-1} as expected, but is shifted of a few km s^{-1}. These effects appear when the velocities are derived through a non-flexible, but suppos-edly more precise method in the pipeline of Ibata et al. (2011), that was used in the paper of Martin et al. (2016a). In this work, using a slightly less precise, but more flexible method of the same pipeline to extract the velocities, we are able to get rid of these systemat-ics and find the expected mean difference in velocities for all stars observed twice of 0 km s^{-1}.

3 BROAD-BAND PHOTOMETRY ANALYSIS

The CMD of Dra II for sources within two half-light radii ($2r_h$, see below) is presented in Fig. 2 (left-hand panel). For comparison, the CMD of a field region of the same coverage but selected in the outskirts of the MegaCam field of view is shown in the middle-left panel. The main sequence observed in the Dra II CMD is consistent with an old and metal-poor stellar population (see below) as origi-nally pointed out by Laevens et al. (2015), but the MegaCam data is much deeper and traces the main sequence of the system more than three magnitudes below the turn-off. The exquisite MegaCam CMD is highlighted by the narrowness of this sequence. The 50 per cent completeness of the data in the g band is reached at $g = 25.2$ mag and $i = 23.9$ mag. We confirm that the main sequence of Dra II contains very few stars brighter than the turn-off and that the satel-lite is particularly faint. Anticipating on the spectroscopic analysis presented below, the right-hand panel of Fig. 15 highlights stars with radial velocity measurements. Likely Dra II members appear in red with $v_r \sim -345$ km s^{-1}. With these velocities, it is possible to isolate a handful of potential Dra II stars just above the turn-off. We find no bright RGB stars and no horizontal branch stars in the system.

3.1 Structural and CMD analysis

We take advantage of the deep MegaCam data and of the better sampling of the system to revisit the structural analysis performed by Laevens et al. (2015). The analysis is based heavily on the algorithm presented in Martin, de Jong & Rix (2008) and Martin et al. (2016b) and we separately infer the CMD-properties of Dra II. Altogether, we aim to estimate the structural properties of the system (the coordinate offsets of the centroid from the literature values, X_0 and Y_0, the half-light radius along the major axis, r_h, the ellipticity,[1] ϵ, the position angle of the major axis east of north, θ, and the number of stars within the MegaCam data, $N*$), along with its distance modulus $m - M$, Age A, metallicity [Fe/H]$_{\text{CMD}}$, and abundance in α elements [α/Fe].

For any star k in our sample, the pieces of information used at this stage are the coordinates of the star X_k and Y_k, pro-jected on the sky on the plane tangent to Dra II's centroid, and the MegaCam magnitudes, g_k and i_k. For clarity, we de-fine $\vec{d}_k^{\,sp} \equiv \{X_k, Y_k\}$ and $\vec{d}_k^{\,CMD} \equiv \{g_k, i_k\}$. The suite of parame-ters we aim to infer is divided into a set of structural parameters $\mathcal{P}_{\text{sp}} \equiv \{X_0, Y_0, r_h, \epsilon, \theta, N^*, \eta_{\text{sp}}\}$ and a set of CMD-related parame-ters, $\mathcal{P}_{\text{CMD}} \equiv \{m - M, A, [\text{Fe/H}]_{\text{CMD}}, [\alpha/Fe], \eta_{\text{CMD}}\}$, with η_{sp} and η_{CMD} the fractions of Dra II stars in the spacial and CMD data sets. Following these definitions and keeping in mind that any star could be a Dra II star or a field star that belongs to the Milky Way con-tamination, we can express the spacial likelihood of star k as

$$\ell_{\text{sp}}^{\text{tot}}(\vec{d}_{k,\text{sp}}|\mathcal{P}_{\text{sp}}) = \eta_{\text{sp}}\ell_{\text{sp}}^{\text{DraII}}(\vec{d}_{k,\text{sp}}|\mathcal{P}_{\text{sp}}) + (1 - \eta_{\text{sp}})\ell_{\text{sp}}^{\text{MW}}(\vec{d}_{k,\text{sp}}), \quad (1)$$

where $\ell_{\text{sp}}^{\text{DraII}}$ and $\ell_{\text{sp}}^{\text{MW}}$ are the spacial likelihoods of star k in the Dra II or the field-contamination models, respectively.

---

[1]The ellipticity is defined as $\epsilon = 1 - \frac{a}{b}$, with a and b the major and minor axes of the ellipse, respectively.

We follow Martin et al. (2016b) and assume that Dra II stars follow an exponential radial density profile whereas the field contamination is taken to be flat over the MegaCam field of view. However, and contrary to Martin et al. (2016b), we assume $N*$ is a parameter to be determined by the normalization. For this reason, the formalism is slightly different here. The radial density profile of the system is expressed as

$$\rho_{\mathrm{dwarf}}(r) = \frac{1.68^2}{2\pi r_{h^2}(1-\epsilon)} \exp(-1.68\frac{r}{r_h}), \tag{2}$$

with r the elliptical radius, which relates to projected sky coordinates (x, y) via

$$r = \left[\left(\frac{1}{1-\epsilon}((X - X_0)\cos\theta - (Y - Y_0)\sin\theta) \right)^2 \right.$$
$$\left. + \left((X - X_0)\sin\theta + (Y - Y_0)\cos\theta \right)^2 \right]^{1/2}. \tag{3}$$

The spacial likelihood of the Dra II component of the model is then simply

$$\ell_{\mathrm{sp}}^{\mathrm{DraII}}(X_k, Y_k) = \frac{\rho_{\mathrm{dwarf}}(r)}{\int_{\mathcal{A}} \rho_{\mathrm{dwarf}}(r)\mathrm{d}\mathcal{A}}, \tag{4}$$

where $\mathcal{A}$ is the area of the sky over which the analysis is conducted.

The spacial likelihood of the Milky Way contamination model is much simpler and, with our assumption that it is constant, we simply have

$$\ell_{\mathrm{sp}}^{\mathrm{MW}} = \frac{1}{\int_{\mathrm{d}}\mathcal{A}}. \tag{5}$$

Similarly, one can express the total CMD likelihood as followed :

$$\ell_{\mathrm{CMD}}^{\mathrm{tot}}(\vec{d}_{k,\mathrm{CMD}}|\mathcal{P}_{\mathrm{CMD}}) = \eta_{\mathrm{CMD}}\ell_{\mathrm{CMD}}^{\mathrm{DraII}}(\vec{d}_{k,\mathrm{CMD}}|\mathcal{P}_{\mathrm{CMD}})$$
$$+ (1 - \eta_{\mathrm{CMD}})\ell_{\mathrm{CMD}}^{\mathrm{MW}}(\vec{d}_{k,\mathrm{CMD}}), \tag{6}$$

where $\ell_{\mathrm{CMD}}^{\mathrm{DraII}}$ and $\ell_{\mathrm{CMD}}^{\mathrm{MW}}$ are the CMD likelihoods of star k in the Dra II or the field-contamination models, respectively.

To build the CMD models, we rely on a set of isochrones for Dra II and build an empirical model for the field contamination. We base our CMD model of Dra II, $\ell_{\mathrm{CMD}}^{\mathrm{DraII}}$, on a set of Dartmouth isochrones and luminosity functions[2] (Dotter et al. 2008) calculated for the PS1 photometric system. For a given set of CMD parameters $\mathcal{P}_{\mathrm{CMD}}$, we download the isochrone and luminosity function (LF) of the stellar population of this age A, metallicity [Fe/H]$_{\mathrm{CMD}}$, and α abundance [α/Fe], and shift it by the distance modulus $m - M$. Since the isochrones and LFs provided by the Darmouth library are not continuous but discrete tracks, they are linearly splined. The isochrones are then weighted according to their associated LF. At this stage, each isochrone is a continuous track in CMD space with a 'height' equal to the luminosity function along it. We then generate a CMD PDF of where the system stars are likely to be located by simply convolving this track with the photometric uncertainties. With this formalism, we implicitly assume that Dra II contains a single stellar population and any intrinsic spread in the properties of the system will generate wider posterior PDFs. However, as isochrones pile up towards the blue in the metal-poor end regime ([Fe/H] <-1.4), only significant metallicity or age gradients would affect our results. Finally, the colour–magnitude space over which the PDF is calculated is implemented with pixel sizes of 0.01 mag on the side, so we further convolve the resulting PDF

[2] http://stellar.dartmouth.edu/models/webtools.html
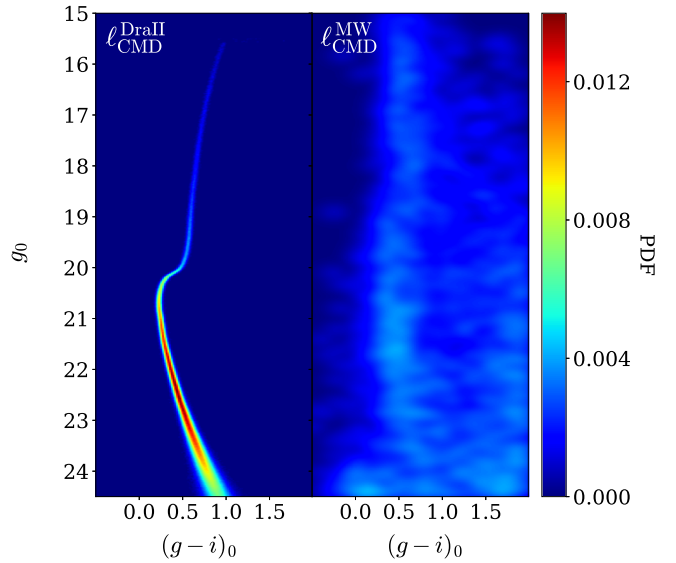
Figure 3. Left-hand panel: Likelihood of the stellar population favoured by our model (*A*: 13.5 Gyr, [Fe/H]$_{\mathrm{CMD}} = -2.4$, [α/Fe] $= 0.6$ and a distance modulus of 16.67). It is constructed from a theoretical isochrone weighted by its luminosity function, convolved by the typical Megacam photometric uncertainties, and finally weighted by the complteness in g_0 and i_0. Right-hand panel: Likelihood of the contamination stars. The maximum density for the left-hand panel is far greater than for the background likelihood on the right so the two are represented with a square-root colour scale.

by a Gaussian of dispersion 0.01 mag to avoid aliasing issues in our representation of the PDF. Since this PDF is supposed to describe the observed Dra II features of the CMD, the completeness of the data needs to be taken into account, therefore, each track is weighted by the product of the completenesses in g_0 and i_0. This completeness is computed following the model built by Martin et al. (2016b) on similar MegaCam data, simply shifted to the appropriate reference median magnitude (the median magnitude of all stars in our photometry with photometric uncertainties between 0.09 and 0.11). The final step normalizes this PDF to unity so it is properly defined. An example of the resulting model is shown in the left-hand panel of Fig. 3 for the specific set of parameters $\mathcal{P}_{\mathrm{CMD}} = \{m - M = 16.67, A = 13.5\,\mathrm{Gyr}, [\mathrm{Fe/H}]_{\mathrm{CMD}} = -2.4, [\alpha/\mathrm{Fe}] = +0.6\}$.

The model for $\ell_{\mathrm{CMD}}^{\mathrm{MW}}$ is built empirically from the CMD position of field stars in the MegaCam data. We select all stars beyond $5r_h$ and bin them in CMD space. Each bin has a width of 0.01 mag along both the magnitude and the colour directions. In order to diminish the amount of shot noise in the resulting binned CMD, we further smooth it with a Gaussian kernel of width 0.1 mag in both dimensions. The resulting smoothed CMD is presented in Fig. 3 after its normalization so it is a properly defined PDF.

With the model being entirely defined, we can now focus on the inference on the model's parameters. Since the structural side of the analysis can be biased by the presence of the chip gaps visible in Fig. 1, they are accounted for by constructing a binary mask correcting the effective area of the field. From the N_{tot} stars present in this region, the spacial likelihood $\mathcal{L}_{\mathrm{sp}}$ (resp. for the CMD) of a given model is

$$\mathcal{L}_{\mathrm{sp}}\left(\{\vec{d}_{k,\mathrm{sp}}\}|\mathcal{P}_{\mathrm{sp}}\right) = \prod_{k=1}^{N_{\mathrm{tot}}} \ell_{\mathrm{sp}}^{\mathrm{tot}}\left(\vec{d}_{k,\mathrm{sp}}|\mathcal{P}_{\mathrm{sp}}\right) \tag{7}$$

Table 1. Inferred properties of Dra II.

Parameter	Unit	Prior	Favoured model	Uncertainties
RA α	deg	–	238.174	± 0.005
DEC δ	deg	–	+64.579	± 0.006
r_h	arcmin	>0	3.0	$^{+0.7}_{-0.5}$
r_h	pc		19.0	$^{+4.5}_{-2.6}$
θ	deg	[0,180]	76	$^{+22}_{-32}$
ϵ	–	>0	0.23	± 0.15
Distance modulus	mag	[16.3,17.1]	16.67	± 0.05
Distance	kpc		21.5	± 0.4
Age	Gyr	[10,13.5]	13.5	± 0.5
[Fe/H]	dex	–	−2.7	± 0.1
$\sigma_{[Fe/H]}$	dex	>0	Unresolved	<0.24 dex at 95%
[α/Fe]	dex	[0.0,0.6]	0.6	>0.4 at 89%
L_V	$L_\odot$	>0	180	$^{+124}_{-72}$
M_V	mag	–	−0.8	$^{+0.4}_{-1.0}$
μ_0	mag arcsec^{-2}	–	28.1	± 0.7
$<v_r>$	km s^{-1}	–	−342.5	$^{+1.1}_{-1.2}$
$<v_r>_{gsr}$	km s^{-1}	–	−172.0	$^{+1.1}_{-1.2}$
σ_{vr}	km s^{-1}	> 0	Unresolved	< 5.9 km s^{-1} at 95%
μ_α^*	mas yr^{-1}	–	0.54	± 0.27
μ_δ	mas yr^{-1}	–	0.94	± 0.28

and the posterior probability we are after is, trivially,

$$P_{sp}\left(\mathcal{P}_{sp}|\{\vec{d}_{k,sp}\}\right) \propto \mathcal{L}_{sp}\left(\{\vec{d}_{k,sp}\}|\mathcal{P}_{sp}\right) P_{sp}(\mathcal{P}_{sp}), \qquad (8)$$

with $P_{sp}(\mathcal{P}_{sp})$ the combined prior on the model parameters. These priors are listed in Table 1 and are chosen to be uniform for an old stellar population, with distance and structural parameters loosely close to the favoured parameters according to Laevens et al. (2015). Anticipating on Section 4, the systemic metallicity of the satellite is found to be $\langle[Fe/H]_{DraII}^{CaHK}\rangle = -2.7 \pm 0.1$ dex using the narrow-band, CaHK photometry. This result is used as a Gaussian prior to the CMD analysis.

In order to build the posterior N-dimensional distribution function, we devised our own Markov Chain Monte Carlo code based on a Metropolis–Hastings algorithm (Hastings 1970). To ensure convergence, we aim for an acceptance ratio of ∼25 per cent and run the algorithm for a few million iterations. Convergence is not an issue for this large number of iterations. Finally, for the CMD analysis, we restrict ourselves to a specific region of the CMD: a visual inspection of the Dra II main sequence in Fig. 2 shows that all stars outside $-0.5 < (g - i)_0 < 2.0$ are contaminants. For this reason, there is no need to take them into account in our analysis, and the following CMD and structural analyses are performed only with stars with $15 < g_0 < 24.5$, and $-0.5 < (g - i)_0 < 2.0$. The resulting 2D marginalized PDFs are presented in Fig. 4 for spacial and Fig. 5 for CMD parameters.

Our results are compatible with the ones presented by Laevens et al. (2015) in the discovery paper of Dra II. From the deeper MegaCam data, we confirm the half-light radius of the satellite to be $r_h = 3.0^{+0.7}_{-0.5}$ arcmin (versus $2.7^{+1.0}_{-0.8}$ arcmin before). Overall, the deeper MegaCam data allows for better constraints with smaller uncertainties on all parameters. The use of a Plummer profile instead of an exponential profile yields similar results. The radial profile of the favoured spacial model is presented in Fig. 8.

The CMD part of the analysis yields a robust distance estimate ($m - M = 16.67 \pm 0.05$ mag; or a heliocentric distance $d = 21.5 \pm 0.4$ kpc) that is slightly smaller than the one proposed by Laevens et al. (2015), who estimated a distance modulus of ∼16.9 by eye. The favoured isochrone also corresponds to a stellar population of

$A = 13.5 \pm 0.5$ Gyr, [Fe/H]$_{CMD} = -2.40 \pm 0.05$ dex, and [α/Fe] $= +0.6$ dex. The 1D PDFs of the CMD parameters are shown in Fig. 5, while Fig. 6 shows that this stellar population is a good description of the features in the CMD of Dra II and of the stars identified as members of the satellite through a spectroscopic study (see Section 5). The choice of showing only 1D PDFs for the CMD inference is purely aesthetic: each parameter is chosen over a grid that can have large steps (e.g. [α/Fe] is chosen over a grid with 0.2 dex step), which does not give representative or aesthetically pleasing 2D contours. It is however important to note that there is no clear correlation between the CMD parameters.

The alpha-abundance ratio of the favoured model is to be taken with caution as it reaches the limits of the [α/Fe] range allowed by this set of isochrones. The alpha abundance of 0.6 found above is high but not totally unrealistic for a dwarf galaxy: Vargas et al. (2013) shows that faint Milky Way dwarf galaxies such as Segue 1 ($M_V \sim -1.5$) are compatible with this result. Another fit was performed using a uniform prior in [α/Fe] over the range [0.0,0.4] to test the analysis without reaching the end of the alpha abundance grid. This does not significantly change our results.

To investigate the impact of the choice of the completeness model used, the favoured CMD and spacial model are used to simulate a Dra II-like population. The analysis is then performed three more times: one time with our actual completeness model, and two other times using the completeness model shifted by ± 0.5 mag, respectively. The results of these analyses are all consistent within the uncertainties, showing that the impact of the completeness model is limited and that it does not significantly affect our results.

The systemic metallicity of the satellite appears consistent with the luminosity–metallicity relation for DGs and with the analysis previously proposed by Martin et al. (2016a) in a qualitative analysis of their spectra. We repeat the Calcium-triplet equivalent-width analysis of Martin et al. (2016a) for the three low-RGB stars with S/N >10 that used the Starkenburg et al. (2010) relation. It is worth pointing out that this relation is calibrated for RGB stars. However, Leaman et al. (2013) implies that it can be applied to stars 2 mag below the RGB and give consistent results. The analysis yields a systemic metallicity for Dra II of [Fe/H]$_{spectro} = -2.43^{+0.41}_{-0.82}$ dex,
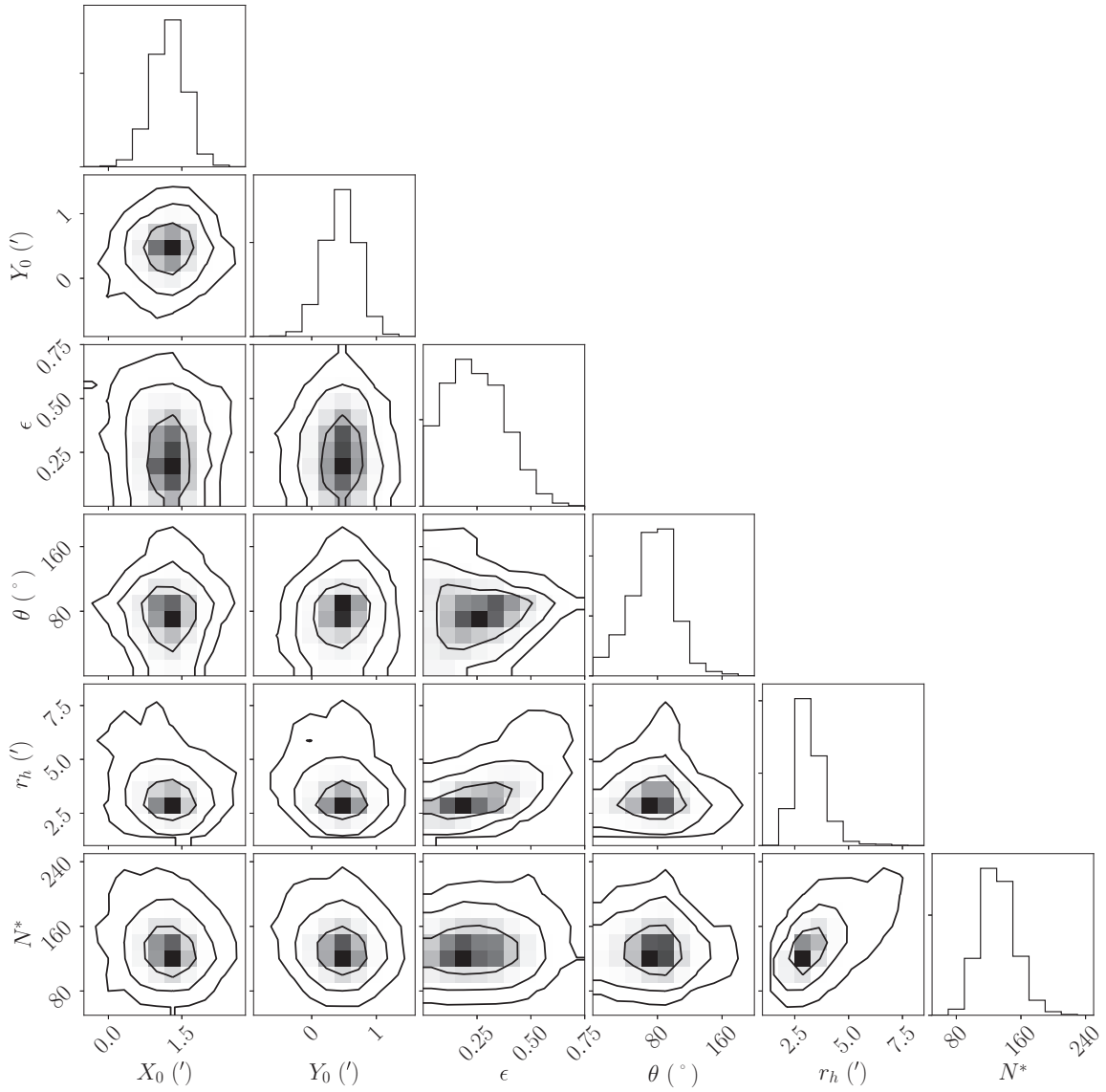
Figure 4. 1D and 2D posterior PDFs of the structural parameters of Dra II, inferred using the method described in Section 3.1. Contours correspond to the usual 1σ, 2σ, and 3σ confidence intervals in the case of a 2D Gaussian.
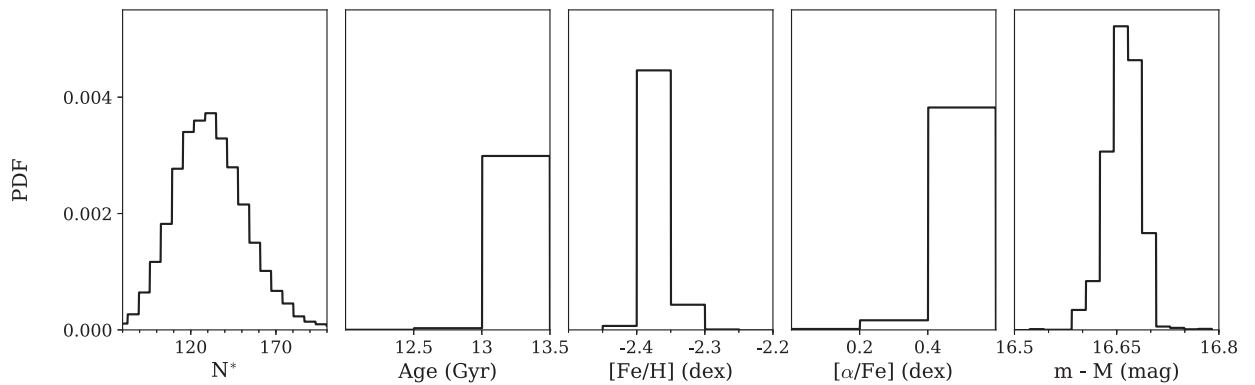
Figure 5. 1D PDFs of the CMD parameters of Dra II.
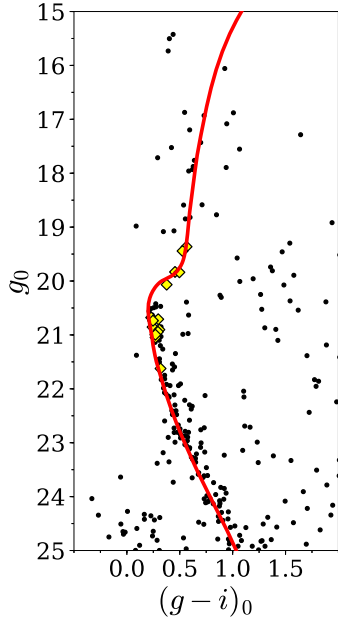
Figure 6. CMD of stars within $2r_h$ of Dra II's centroid, along with the favoured isochrone found in Section 3.1, corresponding to a stellar population of $13.5^{+0.5}_{-1.0}$ Gyr, [Fe/H]$_{CMD} = -2.40 \pm 0.05$ dex and [α/Fe] $= +0.6$ dex. Stars confirmed as spectroscopic members in Section 5 are represented as yellow diamonds.

which is compatible with our CMD analysis. Due to the lack of bright member stars (the brightest used in this analysis has $g_0 = 18.8$), it is challenging to obtain tight constrains on the spectroscopic metallicity of the satellite.

As a sanity check, the main sequence of Dra II can be compared to the fiducials of old and metal-poor globular clusters constructed by Bernard et al. (2014). A few of those fiducials are overlaid on the CMD of Dra II in Fig. 7. From this figure, fiducials in the metallicity ranges $-2.4 <$ [Fe/H] < -2.0 and $-1.8 <$ [Fe/H] < -1.4 provide good visual match to the Dra II features and its spectroscopically confirmed members (determined in Section 5 below and highlighted in yellow in the figure). The most metal-poor fiducials, however, provide a better match for stars with $P_{mem} > 0.01$ brighter than $g_0 = 19$ mag. Although this does not give any precise quantitative information on the metallicity of Dra II, it confirms the metallicity measured from the CMD-fitting procedure and from spectroscopy.

Our spacial and CMD models can be used to estimate the Dra II membership for each star by computing the ratio of the satellite likelihood, $\mathcal{L}_{DraII}(\vec{d})$, over the total likelihood $\mathcal{L}_{DraII}(\vec{d}) + \mathcal{L}_{MW}$. These membership probabilities are reported in Table 1 for all stars in the spectroscopic sample. The membership probability can also be used to draw the density map of the Dra II-like stellar population. The field is binned with intervals of width 0.5 arcmin in both X and Y. For each bin, we count the density of stars. The map is further convolved with a Gaussian kernel of 2 arcmin. To identify potential structures, the distribution of background pixels, i.e. pixels located further than $4.0r_h$, is fitted with a gamma distribution. Pixels with a density within the upper 68, 95, and 99.85 per cent of the total background pixels distribution are represented with magenta, pink, and white contours in Fig. 9. This map tentatively reveals the existence of an extended Dra II-like structure over the field of view, consistent with the orientation of the major axis of the satellite. This hint of extra-tidal features could be the sign that Dra II could be tidal disrupting. The orbit of Dra II we infer in Section 6 is consistent
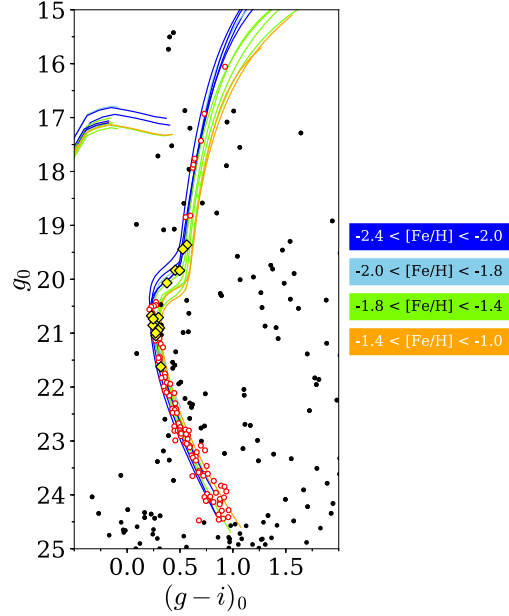
Figure 7. CMD of stars within two half-light radii of Dra II centroid. Several metal-poor globular cluster fiducials from Bernard et al. (2014) are represented and colour-coded by metallicity ranges. Red circled dots are stars with a Dra II membership probability greater than 1 per cent. Yellow diamonds are Dra II members confirmed by spectroscopy. The fiducials that best represent the Dra II CMD features are the blue ones, with a metallicity range $-2.4 <$ [Fe/H] < -2.0.
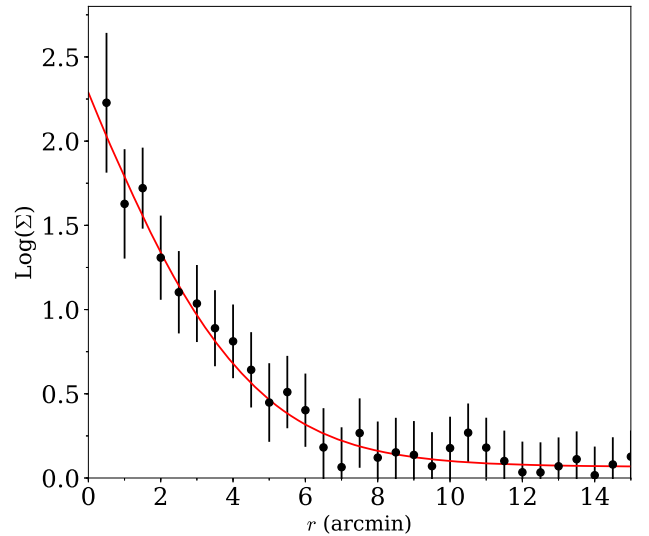
Figure 8. Comparison of the favoured exponential radial density profile (red solid line) with the binned data in elliptical annuli following the favoured structural model (dots). The error bars represents Poisson uncertainties on the number count of each annulus. r is the elliptical radius.

with the direction of these potential tails. We stress that this needs to be confirmed with a spectroscopic search for members in these regions.

Finally, we investigate the presence of mass segregation within the system as this phenomenon can occur in globular clusters, but not in dwarf galaxies, and could therefore be used as a diagnostic for the nature of the satellite (Kim et al. 2015). The stellar population models provided by the Darmouth library give an estimate
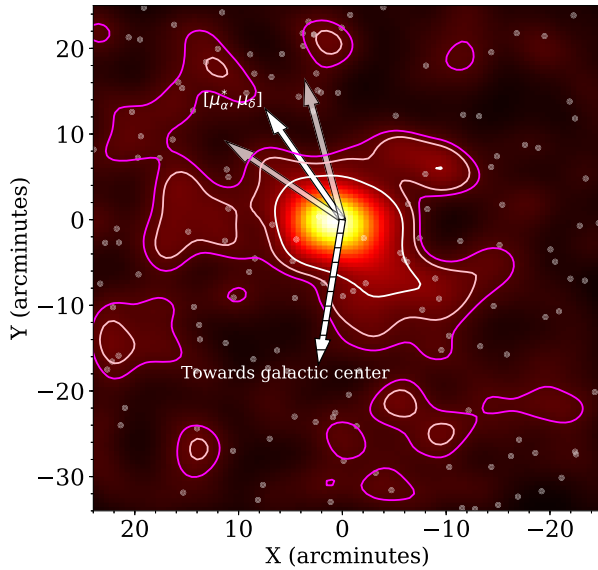
Figure 9. On-sky density plot of the full field of view for all stars with $\mathcal{P}_{\mathrm{mem}} \geq 0.01$, smoothed using a 2 arcmin Gaussian kernel. Regions with a density within the upper 68, 95, and 99.85 per cent of the background pixels distribution are shown with magenta, pink, and white contours, respectively. The dashed arrow shows the direction towards the Galactic centre. The upper white arrow shows the favoured proper motion vector $\vec{\mu} = [\mu_\alpha^{*,\mathrm{DraII}}, \mu_\delta^{\mathrm{DraII}}]$ (see Section 6 for more details), while the uncertainties on this vector are shown as the two shaded arrows. Transparent white dots represent bright stars ($g_0 < 17$) over the field.

of the mass of a given star following these isochrones. Using this piece of information, each star within $3r_h$ is associated with its most likely mass by comparison with the favoured isochrone. This subsample is then separated into three mass ranges (0.5–0.6M$_\odot$, 0.6–0.7M$_\odot$, and 0.7–0.8M$_\odot$). The cumulative number of stars in each mass range with respect to their radial distance to Dra II is finally computed. This procedure is repeated for stars with a membership probability above 1, 35, and 50 per cent, respectively, to investigate the potential effect of the contamination on the analysis. The results are shown in Fig. 10 for the 35 per cent case. This analysis gives no conclusive evidence of mass segregation in the satellite. Choosing a membership probability threshold of 1 and 50 per cent does not change significantly the results.

3.2 Luminosity and absolute magnitude M_V

We rely on the method presented in Martin et al. (2016a) to determine the total luminosity of the satellite: this method uses the PDFs on the stellar population of Dra II and on the number of stars within the MegaCam data, N_*, to infer the total luminosity of the system. Therefore, it does not correspond to the sum of the fluxes of all stars seemingly members of Dra II in the observed CMD, but it can be seen as a statistical determination of the luminosity of a system with the structural and CMD properties of Dra II.

At every iteration in the procedure, we randomly draw a target N_j^* value from the N_* PDF, as well as a set of stellar parameters $(A_j, [\alpha/\mathrm{Fe}]_j, [\mathrm{Fe/H}]_{\mathrm{CMD},j}, (m-M)_j)$ from the PDFs obtained through the inference of Section 3.1. CMD stars are then simulated according to the j-th stellar population. The probability to draw a star at a given magnitude g_0 is given by the luminosity function. For each simulated star, its colour $(g-i)_0$ and magnitude g_0 are checked. If they fall within the CMD box used to perform the fit
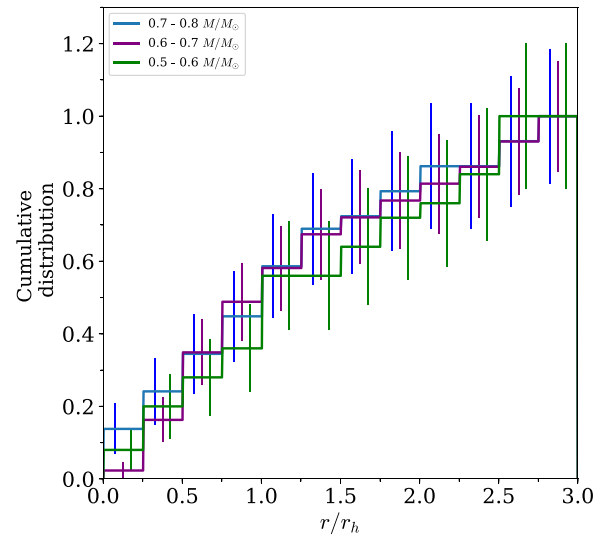
Figure 10. Normalized cumulative number of stars from 0 to 3 half-light radii, for three mass intervals: 0.8–0.7 M$_\odot$ (blue), 0.7–0.6 M$_\odot$ (purple), and 0.6–0.5 M$_\odot$ (green). The analysis is performed for all stars with a CMD membership probability above 35 per cent.
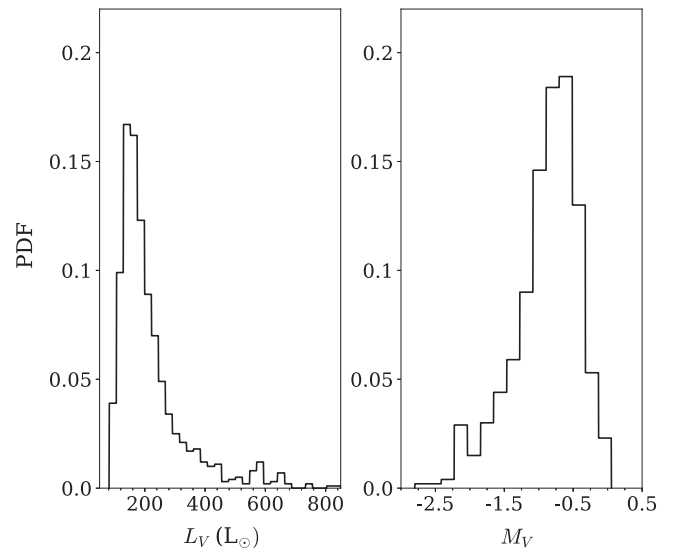
Figure 11. PDFs of the V-band luminosity (left-hand panel) and absolute magnitude (right-hand panel) of Dra II. The system is particularly faint, with a favoured luminosity of only $L_V = 180^{+124}_{-72} \mathrm{L}_\odot$.

in the previous section, it is flagged. The simulated star is then independently checked against the completeness of the data in both g and i. The g and i values are then converted into a V magnitude using the colour equations presented in Tonry et al. (2012). Once the number of flagged simulated stars is equal to N_j^*, the flux of all stars, flagged or not, is summed to yield the total luminosity, $L_{V,j}$, of that realization of the satellite. Those luminosity values are then converted into absolute magnitudes, $M_{V,j}$. Repeating this exercise several thousands of times yields the PDFs presented in Fig. 11.

From this analysis, Dra II emerges as a very faint satellite, with a luminosity of only $L_V = 180^{+124}_{-72}$ L$_\odot$, corresponding to an absolute magnitude of $M_V = -0.8^{+0.4}_{-1.0}$ mag. The satellite has a surface brightness of $\mu_0 = 28.1 \pm 0.7$ mag arcsec^{-2}, comparable to the Milky Way satellites with the lowest surface brightness. Shifting the

completeness model by ± 0.5 mag does not significantly change the inferred luminosity. Most of the simulated CMDs contain no RGB star much brighter than the turn-off, which is compatible with the absence of confirmed RGB stars brighter than $g_0 = 19.3$ in our spectroscopic sample (Fig. 7 and Table A1 for the member list) and with the observed CMD. This value is however significantly fainter than the one of Laevens et al. (2015), who found a luminosity of $1259^{+1903}_{-758}\,L_\odot$. Two possible explanations for this difference can be proposed. First, the photometry at hand in 2015 is 2 mag shallower than ours, thus only reaching the bright end of the main sequence of Dra II. Finally, a small fraction of our simulated CMDs still predicts the existence of an RGB star in the satellite that could lead to a significant increase in luminosity. This is illustrated by the bright tail up to 800 $L_\odot$ in the left-hand panel of Fig. 11, which is only due to the existence of one or two giant stars in a small fraction of our simulated CMDs. One bright star ($g < 16$) in Dra II would potentially be enough to solve the discrepancy between Laevens et al. (2015) and this work. However, recent spectroscopic investigations of bright Dra II candidates did not lead to the identification of any additional member with $g < 17$. Therefore, the discrepancy found regarding the luminosity must be caused by an overestimation of the additional overall number of stars by Laevens et al. (2015), driven by shallower and noisier data.

4 NARROW-BAND CAHK ANALYSIS

The Pristine survey (Starkenburg et al. 2017) combines CFHT narrow-band CaHK photometry with broad-band colours, typically $g - i$, to infer photometric metallicities (hereafter [Fe/H]$_{\mathrm{CaHK}}$). A specific set of Pristine observations aims at observing all known northern Milky Way dwarf galaxy (or dwarf galaxy candidate) with $M_V > -9.0$. These images are much deeper than the usual Pristine observations (1-h versus 100-s integrations) but remain shallower than the broad-band g and i photometry described in Section 3. Reliable CaHK photometry, i.e. with *CaHK* uncertainty below 0.1, is achieved down to $g \sim 23.0$.

In Fig. 12, we show the typical colour–colour space used by the Pristine collaboration, for which stars with [Fe/H] ~ -1 or lower reside in the bottom part of the panel and more metal-poor stars towards the top. Comparison via models and calibration onto thousands of stars in common with the Segue spectroscopic survey allow us to assign a [Fe/H]$_{\mathrm{CaHK}}$ value to all these stars (Starkenburg et al. 2017; Youakim et al. 2017). Two iso-metallicity sequences of, respectively, [Fe/H] $= -3.5$ (green-dashed line) and [Fe/H] $= -1.8$ (red-dashed line) are shown in the figure for illustration purposes. In the figure, we also highlight stars that are part of our DEIMOS spectroscopic sample that will be discussed in the next section. The group of likely Dra II members at $v_r \sim -345\,\mathrm{km\,s^{-1}}$ mainly clumps along a low-metallicity sequence that is compatible with the low metallicity inferred from the broad-band photometry.

The Starkenburg et al. (2017) Pristine metallicity model tends to slightly underestimate the metallicity at the low-metallicity end. Therefore, before turning to the Dra II CaHK data, we first estimate and correct for this bias when determining a [Fe/H]$_{\mathrm{CaHK}}$. We use the same catalogue Starkenburg et al. (2017) used to build their (*CaHK*, g, i) to [Fe/H]$_{\mathrm{CaHK}}$ model, with the same quality criteria on the Pristine photometry and SEGUE/SDSS spectra. We bin this sample of 3999 stars into 0.2 dex bins in metallicity for stars in the interval $-4.0 <$ [Fe/H]$_{\mathrm{CaHK}} < -1.0$. For each of these bins, we determine the median value of both [Fe/H]$_{\mathrm{SEGUE}}$ and [Fe/H]$_{\mathrm{CaHK}}$. The bias is then defined as the difference between these two values. This set of values is then fitted with a third-order polynomial to
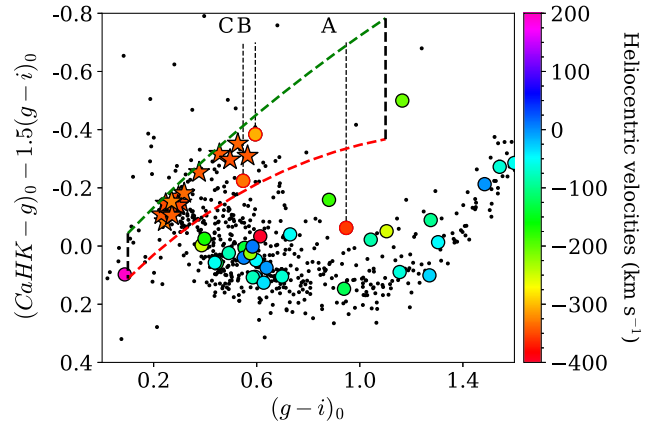
Figure 12. Pristine colour–colour diagram. The usual temperature proxy $(g - i)_0$ is represented on the *x*-axis while the metallicity information is carried by the $(CaHK - g) - 1.5*(g - i)$ colour shown on the *y*-axis (see Starkenburg et al. 2017). Stars observed spectroscopically that pass the *CaHK* quality cut, i.e. an uncertainty on the *CaHK* photometry below 0.1, are colour-coded according to their heliocentric velocities. Small black dots are field stars and form a clear stellar locus of more metal-rich stars ([Fe/H] ~ -1 or above) while more metal-poor stars are located towards above this sequence. Two iso-metallicity sequences with [Fe/H] $= -3.5$ and [Fe/H] $= -1.8$ are shown as green and red-dashed lines, respectively. Most stars compatible with the velocity of Dra II (red–orange) are located between these two sequences, and form a distinct, more metal-poor population than the rest of the spectroscopic sample made of more metal-rich halo and disc stars. The black dashed lines show a colour cut of $0.1 < (g - i)_0 < 1.1$, which is applied to discard potential foreground dwarfs. A, B, and C are the three stars close to the Dra II velocity peak that were discarded using the CaHK and CMD cuts (see the text for more detail).
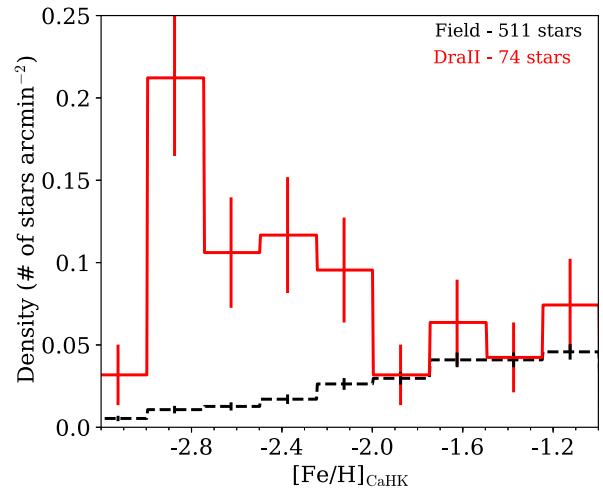
Figure 13. Area-normalized metallicity distribution for all stars within $2r_h$ (solid red line). The same histogram is also shown for all field stars, i.e. stars outside $5r_h$ (black-dashed line). Dra II members are clearly responsible for an overdensity of stars around [Fe/H] ~ -2.8 in the red distribution.

model the metallicity bias throughout the whole metallicity range. This bias is, at most, of ~ 0.2 dex at [Fe/H] $\lesssim -2.0$.

For every star in the Dra II sample with uncertainties on the CaHK magnitude below 0.1, we first apply the model of Starkenburg et al. (2017) to infer a photometric metallicity, which we then correct for the bias modelled above. The area-normalized metallicity distribution for stars within $2r_h$ of Dra II is shown in red in Fig. 13. For comparison, the black-dashed histogram shows the

same distribution but for field stars, i.e. for all stars outside $5r_h$. Dra II stars stand out quite prominently as a significantly metal-poor overdensity compared to the field contamination. A lot of stars in the figure appear to be at the same photometric metallicity around -3.0. However, the calibration of the Pristine model becomes unreliable at $[Fe/H]_{CaHK} \sim -3.0$. The high number of stars at ~ -3.0 stars is probably a consequence of this.

Using Pristine metallicities, we want to infer both the mean metallicity of the system, $\langle [Fe/H]_{DraII}^{CaHK} \rangle$, and its dispersion $\sigma_{[Fe/H]}$. In order to do so, we assume that the distribution of photometric metallicities in the Dra II sample corresponds to a Gaussian-distributed Dra II population and a contamination model $\mathcal{L}_{bkg}$, which is constructed empirically from the field data outside a $5r_h$ radius. The metallicity distribution of this contamination sample is binned, then smoothed with a Gaussian kernel of 0.1 dex to account for poor number counts in some metallicity bins. Finally, we assume the following metallicity distribution model:

$$\mathcal{L}(\{[Fe/H]_{CaHK,k}, \delta_{[Fe/H],k}\} | \langle [Fe/H]_{DraII}^{CaHK} \rangle, \sigma_{[Fe/H]})$$
$$= \prod_k G([Fe/H]_{CaHK,k} | \langle [Fe/H]_{DraII}^{CaHK} \rangle, \sigma_k)$$
$$+ \mathcal{L}_{bkg}([Fe/H]_{CaHK,k}), \qquad (9)$$

with $G(x|\mu, \sigma)$ the value of a Gaussian distribution of mean μ and dispersion σ evaluated for x, $\delta_{[Fe/H],k}$ the uncertainty on the photometric metallicity of star k, and $\sigma_k = \sqrt{\sigma_{[Fe/H]}^2 + \delta_{[Fe/H],k}^2}$.

The inference analysis yields the 2D joined PDF of $\langle [Fe/H]_{DraII}^{CaHK} \rangle$ and $\sigma_{[Fe/H]}$ presented in Fig. 14. The metallicity of the system is found to be $\langle [Fe/H]_{DraII}^{CaHK} \rangle = -2.7 \pm 0.1$ dex, with a metallicity dispersion lower than 0.24 dex at the 95 per cent confidence level. The favoured systemic metallicity confirms that Dra II is significantly metal-poor. The fraction of Dra II stars favoured by the analysis is $\eta \sim 0.6$, corresponding to a total of 41 stars. The metallicity dispersion of the satellite cannot be resolved with this data set. Performing the analysis using an asymmetrical Gaussian does not change significantly change our results.

In order to validate our inference based on the CaHK metallicities, the same analysis is performed on the Pristine data of two metal-poor globular clusters, M15 and M92. Globular clusters are crucial in this case as their metallicity dispersion is expected to be too small to be resolved using purely photometric metallicities and they are a good test of the quality of our constraints on $\sigma_{[Fe/H]}$. Carretta et al. (2009a, C09) and Carretta et al. (2009b, C09b) showed that both clusters have a similar spectroscopic metallicity, with $[Fe/H]_{C09b} = -2.34 \pm 0.06$ dex for M15 and $[Fe/H]_{C09} = -2.35 \pm 0.05$ dex for M92, as well as metallicity dispersions around ~ 0.05. The application of our inference model to the globular cluster Pristine data sets yields $[Fe/H]_{M15} = -2.32 \pm 0.04$ dex and $[Fe/H]_{M92} = -2.38 \pm 0.05$ dex, compatible with the values of C09. As expected, the inferred metallicity dispersions are unresolved for both clusters, as can be seen with the coloured contours in Fig. 14. The favoured models yields 43 stars for M15 and 25 stars for M92, comparable to the 41 stars studied in Dra II.

The inference on the metallicity mean and dispersion for the two globular clusters is as expected and yields confidence that the CaHK metallicities are reliable. We therefore conclude that Dra II is indeed a very metal-poor satellite and we further note that despite similar numbers of member stars in the three systems, the Dra II metallicity dispersion PDF is wider than that of the clusters, which may hint at a larger metallicity dispersion for Dra II.

5 SPECTROSCOPIC ANALYSIS

We now investigate the dynamical properties of the satellite using our spectroscopic data, for which the processing was detailed in Section 2.2. Examples of spectra can be found in fig. 4 of Martin et al. (2016a), who display four spectra of our 2015 run that are representative of the whole data set since the 2016 spectroscopic observations were performed under similar conditions and have similar quality. Their spacial and CMD distribution are shown in Fig. 15. The histograms of heliocentric velocities for our 2015 and 2016 runs combined are shown in the middle panel of Fig. 16.

Dra II stars clearly stand out in Fig. 16 as they form a peak around -345 km s^{-1}, as was already pointed out by Martin et al. (2016a) in their initial analysis of the 2015 data set. A broader distribution around ~ -45 km s^{-1} corresponds to stars from the Milky Way disc while Milky Way halo stars are responsible for the sparsely distributed velocities throughout the range shown here. In order to better constrain the dynamical properties of the system, one has to isolate Dra II members as well as possible. Particular care should be taken when handling the contamination by Milky Way halo stars that are distributed within a broad velocity range that includes the systemic velocity of the satellite. For this reason, it would not be surprising to find a few contaminating stars in the vicinity of the velocity peak of Dra II. In particular, one can also notice the existence of two slight outliers around the Dra II velocity peak, noted stars A and B. It is quite challenging to know whether those stars are bona fide members based only on their kinematic properties. This is a common problem when dealing with such faint systems for which only a handful of members are confirmed: the velocity dispersion and systemic velocity can be biased by slight outliers that are in fact not members (McConnachie & Côté 2010).

Pristine CaHK photometry can be very useful to clean the spectroscopic sample as the Dra II stellar population is very metal-poor, as shown in Section 3.1. All Dra II members are too faint to yield reliable spectroscopic metallicities but it is expected that they can be disentangled from Milky Way contaminants by using the CaHK photometric metallicities described in the previous section.

The Pristine colour–colour diagram presented in Fig. 12 highlights the location of stars with heliocentric velocities, which are colour-coded according to those. As mentioned before, the metal-rich stars from the disc form a clear stellar locus at the bottom of the panel, whereas metal-poor stars are always located above this locus. The two iso-metallicity sequences that bracket the metallicity peak visible in Fig. 13, with $[Fe/H] = -3.5$ and $[Fe/H] = -1.8$, are represented by the green- and red-dashed line, respectively. As expected, stars with velocities compatible with the systemic velocity of Dra II (red–orange) are clearly isolated from the metal-rich, foreground contamination from the Milky Way. Most of the other stars from the spectroscopic sample lie in or close to the metal-rich stellar locus. To help discriminate between Dra II stars and the contamination in our spectroscopic sample, we isolate stars with good CaHK photometry ($\delta_{CaHK} < 0.1$), metallicity uncertainties below 0.3 dex, and, following Fig. 13, with $-3.5 < [Fe/H]_{CaHK} < -1.8$. Further applying a CMD-cut along the favoured isochrone of Section 3.1 yields the cleaned velocity sample that is presented in the bottom panel of Fig. 16. It is obvious that the combined CaHK and CMD information has significantly cleaned the velocity distribution, leaving only highly probable Dra II stars. As a result, star A is clearly not a member: not only is it far from the Dra II sequence in the CMD, but it is
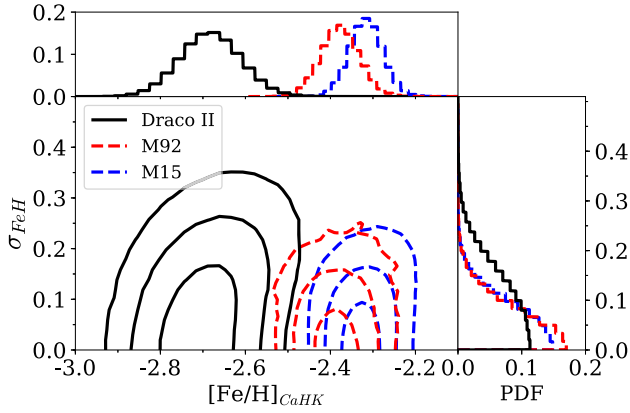
Figure 14. 2D joined PDFs of the systemic CaHK metallicity and its associated dispersion for Dra II (black) and the globular clusters M15 and M92 (blue and red-dashed line, respectively). The marginalized 1D PDFs are shown in the top and right-hand panels for the two parameters. The contours represent the usual 1σ, 2σ, and 3σ confidence intervals in the case of a 2D Gaussian distribution.

also far too metal-rich to belong to the system. Star B seems to be at the appropriate photometric metallicity to be a Dra II member but is offset from the Dra II main sequence by 0.1 mag in the CMD. This location corresponds to a part of the CMD where one might expect to find Dra II binary stars (Romani & Weinberg 1991), which could mean that this star is a Dra II member in a binary star and therefore not reliable for the velocity analysis. We also conservatively discard star C for the same reason, even though it falls within the Dra II velocity peak. Keeping star C or discarding it does not change our results on the velocity properties of Dra II. Including B in the sam-

Figure 16. Top panel: Radial distances to the centroid of Dra II versus heliocentric velocities for all stars in our spectroscopic sample. Black-filled markers represent the remaining spectroscopic population after the CaHK and CMD cuts were applied. They are considered as dynamical members of the system. Middle panel: Histogram of the heliocentric velocities in the spectroscopic sample. Bottom panel: Histogram of velocities for dynamical member stars only, obtained by discarding stars that do not come out as metal-poor through the CaHK model detailed in Section 4 (Fig. 12), as well as stars that are not compatible with our favoured CMD model (section 3). They correspond to the black-filled markers in the top panel.

ple also has no significant impact as its velocity uncertainty is large ($\sim 15\,\mathrm{km\,s^{-1}}$).

In order to derive the systemic velocity and velocity dispersion of Dra II from this clean sample, we follow the framework of

Figure 15. Left-hand panel: Magnified view of the central region showing the spacial distribution of the spectroscopic sample. Stars observed spectroscopically are represented by large dots colour-coded according to their heliocentric velocities. Diamonds and triangles correspond to stars observed in 2015 and 2016, respectively, while squares correspond to stars observed both in 2015 and 2016. Some of the stars observed spectroscopically do not overlap small black dots as those correspond only to Dra II like population and do not represent the full photometric data set. Right-hand panel: Distribution of the spectroscopic sample in the CMD within two half-light radii of Dra II. Stars lying on the Dra II main sequence, in red-orange, are likely members of the system. Some of the stars with velocity measurements are located further away than 2 half-light radii and thus do not also appear as small dots.

Figure 17. Marginalized PDFs for the Dra II systemic velocity (left-hand panel) and velocity dispersion (right-hand panel). The system is dynamically cold, with a marginally resolved velocity dispersion. We constrain the velocity dispersion to be lower than 5.9 km s^{-1} at the 95 per cent confidence level (dashed vertical line).

Martin et al. (2018) and assume stars are normally distributed. The likelihood function is therefore

$$\mathcal{L}(\{v_{r,k}, \delta_{v,k}\}|\langle v_r\rangle, \sigma_v) = \prod_k G(v_{r,k}|\langle v_r\rangle, \sigma_k), \qquad (10)$$

with $G(x|\mu, \sigma)$ the value of a Gaussian distribution of mean μ and dispersion σ evaluated on x, $\delta_{v,k}$ the uncertainty on the photometric metallicity of star k and $\sigma_k = \sqrt{\sigma_v^2 + \delta_{v,k}^2 + \delta_{v,sys}^2}$, $\delta_{v,sys}$ is the systematic uncertainty floor tied to DEIMOS observations. Here, we use the value determined by Martin et al. (2016a; $\delta_{v,sys} = 2.3$ km s^{-1}), which is compatible with the value we determine from the few stars in common between the Dra II 2015 and 2016 samples.

The resulting 1D PDFs of the velocity dispersion and systemic velocity are shown in Fig. 17. These updated results do not change significantly from those presented by Martin et al. (2016a), despite our slightly larger sample and the removal of dubious members by using the CaHK photometric metallicities. The velocity dispersion of Dra II is only marginally resolved, whereas the inferred systemic velocity is $\langle v_r\rangle = -342.5^{+1.1}_{-1.2}$ km s^{-1}. Assuming a mass-to-light (M/L) ratio of two typical of MW globular clusters (McLaughlin & van der Marel 2005), a Dra II-like GC with a size of ~19 pc and absolute magnitude of ~−0.8 mag is expected to have a velocity dispersion of the order of ~0.25 km s^{-1} if it is in equilibrium and unaffected by binaries, using the relation of Walker et al. (2009). Therefore, even with a dispersion as small as ~1 km s^{-1}, Dra II would still possess a significant amount of DM but, unfortunately, the radial velocities of the 14 members do not constrain the M/L ratio of the satellite.

6 GAIA DR2 PROPER MOTIONS AND ORBIT

To determine the orbit of Dra II, we extract the proper motions (PMs) of all stars within half a degree from Dra II's centroid in the Gaia Data Release 2 (Gaia Collaboration et al. 2018a). A cross-match between the 14 identified member stars in Section 5 is then performed, resulting in 10 members with a PM measurement. The
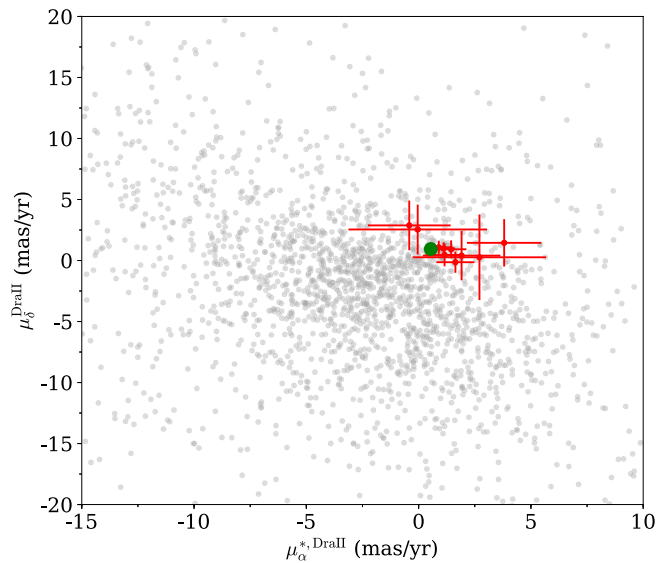
Figure 18. PMs in RA and DEC, for field stars (grey) and 10 Dra II dynamical members (red). The mean proper motion of the satellite is represented as a large green dot.

PMs of the 10 Dra II members are shown in red in Fig. 18. The uncertainty-weighted PM of Dra II yields $\mu_\alpha^{*,\mathrm{DraII}} = \mu_\alpha^{\mathrm{DraII}}\cos(\delta) = 1.26 \pm 0.27$ mas yr^{-1} and $\mu_\delta^{\mathrm{DraII}} = 0.94 \pm 0.28$ mas yr^{-1}, and is shown in Fig. 18 as the large, green dot. These measurements take into account the systematic error of 0.035 mas yr^{-1} on the PMs for dSph as shown by Gaia Collaboration et al. (2018b). However, if we instead choose the systematic error presented in that paper for the GCs, our results do not change given the measured uncertainties on $\mu_\alpha^{*,\mathrm{DraII}}$ and $\mu_\delta^{\mathrm{DraII}}$.

These measurements can be used to put constraints on the orbit of the satellite. To do so, we rely on the GALPY package (Bovy 2015). The MW potential chosen to integrate Dra II orbit is the so-called 'MWPotential14' defined within GALPY, constituted of three components: a power-law, exponentially cut-off bulge, a Miyamoto-Nagai potential disk, and a Navarro-Frenk-White DM halo. A more massive halo is chosen for this analysis, with a mass of 1.2×10^{12} M$_\odot$ (vs. 0.8×10^{12} M$_\odot$ for the halo used in MWPotential14). We integrate 1000 orbits backwards and forwards over 6 Gyr, each time by randomly drawing a position, distance, radial velocity, and PMs from their corresponding PDFs, and extract for each realization the apocentre, pericentre, and ellipticity. The orbit of the favoured model (i.e. favoured position, distance, radial velocity, and PMs) is shown in Fig. 19 in the X–Y, X–Z, and Y–Z planes, and colour-coded by time. Five random realizations of the orbit are also shown in this figure as partially transparent, grey lines.

This analysis yields a pericentre of $21.3^{+0.7}_{-1.0}$ kpc, an apocentre of $153.8^{+56.7}_{-34.7}$ kpc and an ellipticity of $0.77^{+0.08}_{-0.06}$. Dra II seems to be on a quasi-perpendicular orbit with respect to the disk of the MW. Our orbit is compatible with the one of Simon (2018), though they favour a slightly larger apocenter due to their choice of a light MW (0.8×10^{12} M$_\odot$). This is confirmed by the analysis of Fritz et al. (2018), whose results are also consistent with ours. Our larger sample nevertheless provides a more stringent constraint on the orbit of Dra II. The fairly elliptical orbit and the small pericentre we infer appear compatible with the idea that the satellite has been severely affected by tides and could explain the low surface brightness features seen in Fig. 9 that roughly align with the PM vector.
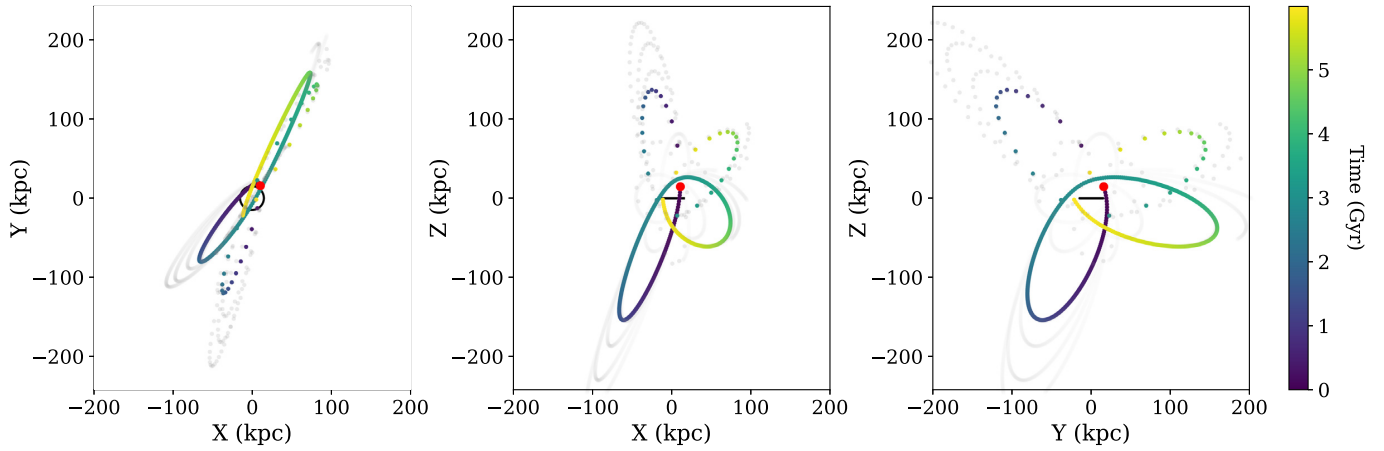
Figure 19. Projections of the orbit of Dra II on the X–Y, X–Z, and Y–Z planes backwards and forwards over 6.0 Gyr. Six orbits are shown here: the one based on the favoured position, distance, radial velocity and PMs of the satellite, and five others using random realizations of those parameters, as slightly transparent, grey lines. The median orbit is colour-coded according to the time elapsed since present day, in Gyr. Dotted lines represent the backwards-integrated orbits. The current position of Dra II is indicated with a red dot, while the MW disk is shown in black, with a chosen radius of 15 kpc.

7 SUMMARY AND DISCUSSION

In this paper, we present an analysis of our deep MegaCam/CFHT broad-band *g* and *i* photometry of Dra II, combined with narrow-band CaHK photometry from a specific sub-program of the Pristine survey that focuses on all northern sky dwarf galaxy candidates. We also present an analysis of the extension of our multi-object spectroscopy observed with Keck II/DEIMOS.

We estimate the structural parameters of Dra II and infer properties that are compatible with the previous study of the satellite by Laevens et al. (2015) albeit with smaller uncertainties: the system has a half-light radius of $r_h = 19.0^{+4.5}_{-2.6}$ pc and is remarkably faint ($L_V = 180^{+124}_{-72} L_\odot$). Based on the CMD information of the observed stars, we confirm that Dra II hosts an old stellar population with an age of 13.5 ± 0.5 Gyr, a metallicity $[Fe/H]_{CMD} = -2.40 \pm 0.05$ dex, $[\alpha/Fe] = +0.6$ dex, and a distance modulus of $m - M = 16.67 \pm 0.05$ mag. Using the Pristine photometry, we were able to find an estimate of the metallicity of Dra II with $\langle [Fe/H]^{CaHK}_{DraII} \rangle = -2.7 \pm 0.1$ dex. This inference is confirmed by the analysis of three Dra II spectroscopic members, which yields $[Fe/H]_{spectro} = -2.43^{+0.41}_{-0.82}$ dex. The metallicity derived from the three different techniques are therefore all consistent. However, the isochrone fitting procedure is limited by the model grid, for which the lowest metallicity is -2.45 dex. Three low-RGB stars were used to derive the spectroscopic metallicity of the satellite using the Calcium triplet relation of Starkenburg et al. (2010). However, this relation is calibrated for RGB stars, though Leaman et al. (2013) shows that it can give consistent results when applied to stars 2 mag fainter. We therefore favour the systemic metallicity inferred by the CaHK technique as it does not suffer from these limitations. The metallicity dispersion of Dra II is only marginally resolved for both the spectroscopic and CaHK procedures. Similarly, applying the same technique to the two old and metal-poor globular clusters M15 and M92 yields no measurable metallicity dispersion, in line with expectations for globular clusters. Finally, we combined the CaHK and broad-band information with our DEIMOS spectroscopy to isolate 14 likely member stars. This sample is used to derive a systemic velocity of $\langle v_r \rangle = -342.5^{+1.1}_{-1.2}$ km s^{-1} and a marginally resolved velocity dispersion, confirming that Dra II is a particularly cold system. Finally, using the Data Release 2 of Gaia, we use 10 Dra II member stars to characterize the orbit of the system: the

apocentre and pericentre are found to be $153.8^{+56.7}_{-34.7}$ kpc and $21.3^{+0.7}_{-1.0}$ kpc, respectively.

Despite the deep photometry studied here and the additional spectroscopy, the derived properties of Dra II are still challenging to interpret and the nature of the system remains uncertain. Dra II is placed in the general context of Milky Way satellites in Fig. 20 and, below, we discuss two broad scenarios: whether Dra II is a globular cluster or a dwarf galaxy.

7.1 Is Dra II a globular cluster?

Fig. 20 (top-right panel) shows Dra II does not present any clearly constrained dispersion in metallicity, in contrast to confirmed dwarf galaxies. Similarly, dwarf galaxies tend to be dynamically hot whereas the spectroscopic analysis of 14 Dra II members only yields a marginally resolved velocity dispersion. These two properties are compatible with the globular cluster hypothesis.

The globular cluster scenario does not come without difficulties, though. In particular, if the system contains no dark matter, its potential well is entirely determined by its very few stars. Using the formalism of Innanen, Harris & Webbink (1983), the instantaneous tidal radius r_t of a Milky Way satellite of mass $M_{cluster}$ at a distance of R, is given by

$$r_t = 0.43 \left(\frac{M_{cluster}}{M_{MW}} \right)^{1/3} R, \tag{11}$$

with M_{MW} the mass of the Milky Way enclosed within that radius R.

Using Dra II's galactocentric distance ($R \sim 23.5$ kpc) and a cluster mass of $360 M_\odot$, obtained from the measured luminosity of Dra II and assuming a mass-to-light ratio of 2 (Bell & de Jong 2001), the tidal radius of Dra II is then a mere ~ 10 pc, i.e. much smaller than the extent of a system with a measured half-light radius of $19.0^{+4.5}_{-2.6}$ pc. We would then be observing Dra II just as it is being destroyed by the Milky Way's tides and, likely, on its final passage around the Galaxy. It would mean that we are observing Dra II during a unique and short-lived moment of its lifetime, and would be a way to explain the relatively high size of the satellite compared to globular clusters of similar faintness : Kim 1 ($r_h \sim 7$ pc), Kim 3 (r_h
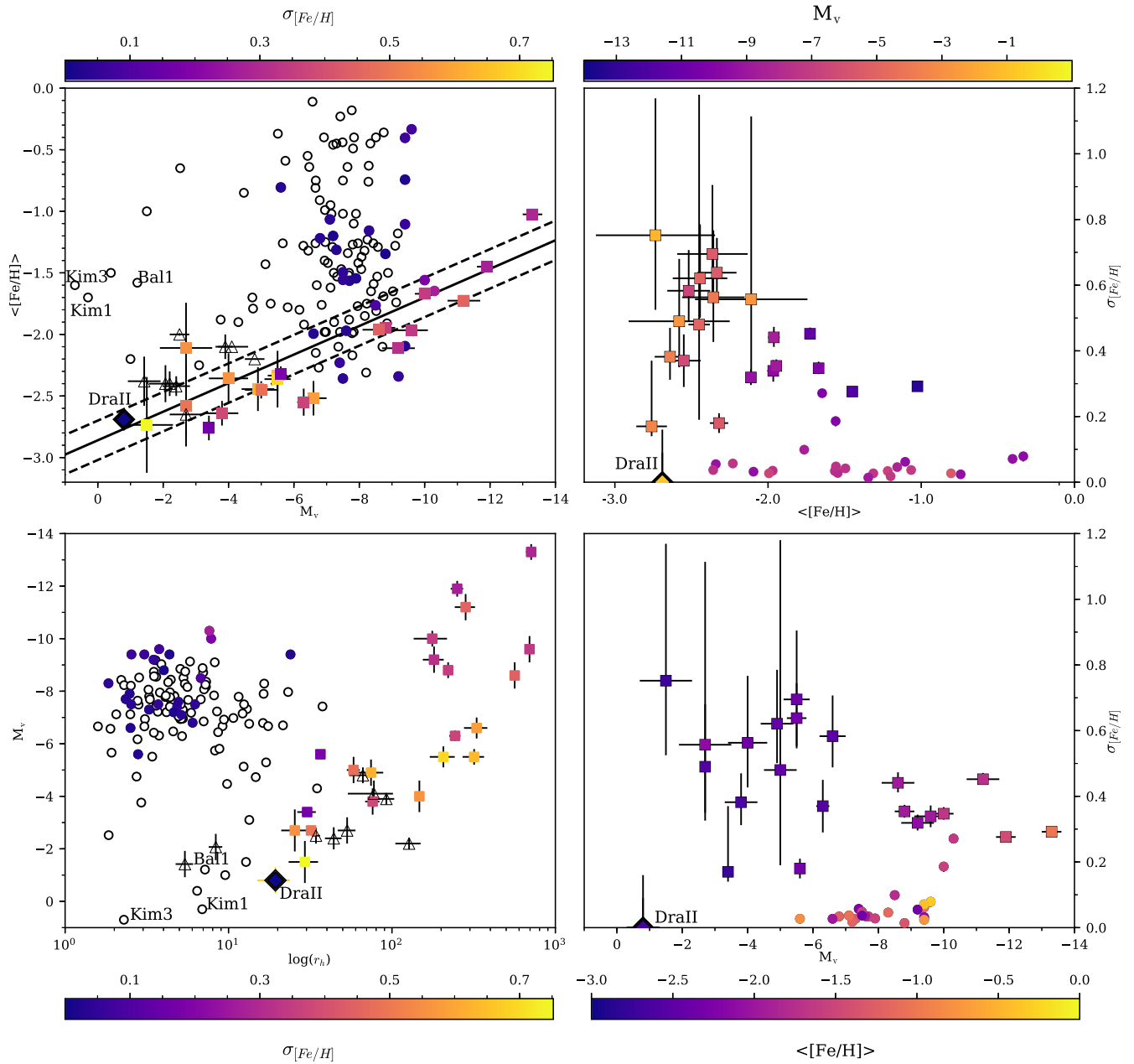
Figure 20. Comparison of Dra II with other GCs and dwarf galaxies of the Milky Way. Squares represent dwarf galaxies while circles represent globular clusters, and the diamond corresponds to Dra II. Triangles stand for recently discovered dwarf galaxy candidates that await confirmation. Hollow markers correspond to systems for which no metallicity dispersion measurement can be found in the literature. The solid line in the top-left panel corresponds to the luminosity–metallicity relation of Kirby et al. (2013) for dwarf spheroidals and dwarf irregulars. Dashed lines represent the RMS about this relation, also taken from Kirby et al. (2013). Among the 123 globular clusters presented here, the properties of 116 were extracted from Harris (1996) catalogue, revised in 2010. For the remaining ones (Kim 1, Kim 2, Kim 3, Laevens 1, Balbinot 1, Munoz 1 and SMASH 1) parameters of the discovery publications were used (Kim & Jerjen 2015; Kim et al. 2015; Kim et al. 2016; Laevens et al. 2014; Balbinot et al. 2013; Muñoz et al. 2012; and Martin et al. 2016c). Globular cluster metallicity spread measurements are taken from Willman & Strader (2012) and references therein: Carretta et al. (2006, 2007, 2009b, 2011), Cohen et al. (2010), Gratton et al. (2007), Johnson & Pilachowski (2010), and Marino et al. (2011). McConnachie (2012) and Willman & Strader (2012) are used to compile the properties of the dwarf galaxies represented here. The 18 dwarf galaxies represented here are: Bootes I (Belokurov et al. 2006; Norris et al. 2010), Canes Venatici I (Zucker et al. 2006b), Canes Venatici II (Sakamoto & Hasegawa 2006), Coma Berinices, Hercules, Leo IV and Segue I (Belokurov et al. 2007), Draco and Ursa Minor (Wilson 1955), Fornax (Shapley 1938b), Leo I and Leo II (Harrington & Wilson 1950), Pisces II (Belokurov et al. 2010), Sculptor (Shapley 1938a), Sextans (Irwin et al. 1990), Ursa Major I (Willman et al. 2005b), Ursa Major II (Zucker et al. 2006a), Willman I (Willman et al. 2005a). Their metallicity and metallicity spreads were drawn from Kirby et al. (2008), Kirby et al. (2010), Norris et al. (2010), Willman et al. (2011). The dwarf galaxy candidates discovered recently and shown on this figure are Bootes II (Koch & Rich 2014), DES1 (Luque et al. 2016; Conn et al. 2018), Eridanus III (Bechtol et al. 2015; Conn et al. 2018; Koposov et al. 2015b), Hyades II (Martin et al. 2015), Pegasus III (Kim & Jerjen 2015), Reticulum II and Horologium I (Koposov et al. 2015a), Segue II (Belokurov et al. 2009), and the most significant candidates of Drlica-Wagner et al. (2015) : Gru II, Tuc III, and Tuc IV.

$\sim$ 2 pc) and Bal 1 ($r_h \sim$ 7 pc) discovered recently (Koposov et al. 2007; Luque et al. 2016; Martin et al. 2016c; Conn et al. 2018).

Finally, the absence of any sign of mass segregation, which could occur in self-gravity dominated systems such as globular clusters (Kim et al. 2015), could also cast doubt on the globular cluster nature of Dra II, even though the existence of mass segregation, especially in a GC possibly in the midst of disruption, is not certain.

7.2 Is Dra II one of the faintest dwarf galaxies?

The top-left panel of Fig. 20 showcases that Milky Way dwarf galaxies follow a reasonably well-defined luminosity–metallicity relation (see also e.g. Kirby et al. 2013). For an extremely faint stellar system like Dra II, one would expect its metallicity to be very low ([Fe/H] ~ -2.5) if it were a dwarf galaxy, which is compatible with our results using independently the CaHK photometry ([Fe/H]$_{\text{CaHK}}$ $= -2.7 \pm 0.1$ dex) and spectroscopy of three low-RGB member stars ([Fe/H]$_{\text{spectro}} = -2.43^{+0.41}_{-0.82}$ dex). Given the scatter and possible stochastic effects of the metallicity–luminosity relation of dwarf galaxies (Revaz & Jablonka 2018), Dra II is entirely compatible with this relation. Moreover, Dra II has a size larger than the vast majority of known Milky Way globular clusters and, in particular, it is several times more extended than GCs of roughly the same luminosity and metallicity, as mentioned in the last section (bottom-left panel of Fig. 20).

The inference on the metallicity dispersion of the satellite was performed through the spectroscopic analysis of 3 low-RGB member stars, and a new technique using the photometric CaHK metallicities of 41 stars. Though both methods do not resolve a significant metallicity dispersion, the final results do not rule it out for the system, because of the faintness and low number of the stars used in both analyses. Similarly, the velocity dispersion PDF of Dra II does not rule out a dynamical mass higher than expected from a globular cluster: if we use the Walker et al. (2009) equation (4) to estimate the dynamical mass, assuming a mass-to-light ratio of 2 that is typical for globular clusters (Bell & de Jong 2001), and the luminosity and half-light radius inferred in this work, a Dra II-like globular cluster should have a velocity dispersion around $\sim$0.25 km s^{-1}. It is therefore challenging to determine whether the satellite has a higher dynamical mass than traced by its stars alone, as even a velocity dispersion of the order of 1 km s^{-1} would indicate that Dra II has a DM halo.

Fig. 9 highlights that there might be extended tidal structures around Dra II, consistent with the proper motion vector and the major-axis of the satellite. Its metallicity is still compatible with brighter dwarf galaxies following the metallicity–luminosity relation. Moreover, Peñarrubia, Navarro & McConnachie (2008) showed that the velocity dispersion of a disrupted dwarf galaxy tends be lower than the original progenitor, consistent with the fact that Dra II appears to be dynamically cold. Could Dra II then be the final remnant of a brighter dwarf galaxy that lost 90 per cent of its mass through tidal interactions with the Milky Way? Such a disruption would not be surprising given the orbit of the satellite, with a pericentre of $21.3^{+0.7}_{-1.0}$ kpc.

7.3 Conclusion

The properties of Draco II tend to indicate that the satellite is a potentially disrupting dwarf galaxy, which could explain its total luminosity, metallicity, size, and relatively low velocity dispersion. The orbit of the satellite, constrained with Gaia PMs, shows that the satellite is very likely to be affected by tidal processes, which

is backed up by potential tidal structures observed in the field. However, the impossibility, with our current data set, to constrain the metallicity dispersion of Dra II casts a doubt of the nature of the satellite, which might well be a globular cluster observed at the very end of its disruption process. Even though challenging, obtaining high-S/N spectra of the faint main-sequence stars of Dra II currently provides the only hope of unravelling the mystery still surrounding Dra II.

REFERENCES

Balbinot E. et al., 2013, ApJ, 767, 101
Bechtol K. et al., 2015, ApJ, 807, 50
Bell E. F., de Jong R. S., 2001, ApJ, 550, 212
Bellazzini M. et al., 2008, AJ, 136, 1147
Belokurov V. et al., 2006, ApJ, 647, L111
Belokurov V. et al., 2007, ApJ, 654, 897
Belokurov V. et al., 2009, MNRAS, 397, 1748
Belokurov V. et al., 2010, ApJ, 712, L103
Bernard E. J. et al., 2014, MNRAS, 442, 2999
Boulade O. et al., 2003, 4841, 72
Bovy J., 2015, ApJS, 216, 29
Brown T. M. et al., 2014, 85, 493
Bullock J. S., Boylan-Kolchin M., 2017, ARA&A, 55, 343
Carretta E., Bragaglia A., Gratton R. G., Leone F., Recio-Blanco A., Lu-
    catello S., 2006, A&A, 450, 523
Carretta E. et al., 2007, A&A, 464, 967
Carretta E., Bragaglia A., Gratton R., D'Orazi V., Lucatello S., 2009a, A&A,
    508, 695
Carretta E. et al., 2009b, A&A, 505, 117
Carretta E. et al., 2010, ApJ, 714, L7
Carretta E., Lucatello S., Gratton R. G., Bragaglia A., D'Orazi V., 2011,
    A&A, 533, A69
Chambers K. C. et al., 2016, preprint (arXiv:e-prints)
Cohen J. G., Kirby E. N., Simon J. D., Geha M., 2010, ApJ, 725, 288
Conn B. C., Jerjen H., Kim D., Schirmer M., 2018, ApJ, 852, 68
Dotter A., Chaboyer B., Jevremović D., Kostov V., Baron E., Ferguson J.
    W., 2008, ApJS, 178, 89
Drlica-Wagner A. et al., 2015, ApJ, 813, 109
Faber S. M. et al., 2003, 4841, 1657
Fritz T. K., Battaglia G., Pawlowski M. S., Kallivayalil N., van der Marel
    R., Sohn T. S., Brook C., Besla G., 2018, preprint (arXiv:e-prints)
Gaia Collaboration, Brown A. G. A., Vallenari A., Prusti T., de Bruijne J. H.
    J., Babusiaux C., Bailer-Jones C. A. L., 2018a, preprint (arXiv:e-prints)
Helmi A., Babusiaux C., Koppelman H. H., Massari D., Veljanoski J.,
    Brown A. G. A., 2018b, preprint (arXiv:e-prints)
Gratton R. G. et al., 2007, A&A, 464, 953
Harrington R. G., Wilson A. G., 1950, PASP, 62, 118
Harris W. E., 1996, AJ, 112, 1487
Hastings W. K., 1970, Biometrika, 57, 97
Ibata R., Sollima A., Nipoti C., Bellazzini M., Chapman S. C., Dalessandro
    E., 2011, ApJ, 738, 186
Ibata R. A. et al., 2014, ApJ, 780, 128
Innanen K. A., Harris W. E., Webbink R. F., 1983, AJ, 88, 338
Irwin M., Lewis J., 2001, New Astron. Rev., 45, 105
Irwin M. J., Bunclark P. S., Bridgeland M. T., McMahon R. G., 1990,
    MNRAS, 244, 16P
Johnson C. I., Pilachowski C. A., 2010, ApJ, 722, 1373
Kim D., Jerjen H., 2015, ApJ, 799, 73
Kim D., Jerjen H., Milone A. P., Mackey D., Da Costa G. S., 2015, ApJ,
    803, 63
Kim D., Jerjen H., Mackey D., Da Costa G. S., Milone A. P., 2016, ApJ,
    820, 119
Kirby E. N., Simon J. D., Geha M., Guhathakurta P., Frebel A., 2008, ApJ,
    685, L43
Kirby E. N. et al., 2010, ApJS, 191, 352
Kirby E. N., Cohen J. G., Guhathakurta P., Cheng L., Bullock J. S., Gallazzi
    A., 2013, ApJ, 779, 102
Koch A., Rich R. M., 2014, ApJ, 794, 89

Koposov S. et al., 2007, ApJ, 669, 337
Koposov S. E., Yoo J., Rix H.-W., Weinberg D. H., Macciò A. V., Escudé J.
    M., 2009, ApJ, 696, 2179
Koposov S. E., Belokurov V., Torrealba G., Evans N. W., 2015a, ApJ, 805,
    130
Koposov S. E. et al., 2015b, ApJ, 811, 62
Laevens B. P. M. et al., 2014, ApJ, 786, L3
Laevens B. P. M. et al., 2015, ApJ, 813, 44
Leaman R. et al., 2013, ApJ, 767, 131
Luque E. et al., 2016, MNRAS, 458, 603
Marino A. F. et al., 2011, A&A, 532, A8
Martin N. F., Ibata R. A., Chapman S. C., Irwin M., Lewis G. F., 2007,
    MNRAS, 380, 281
Martin N. F., de Jong J. T. A., Rix H.-W., 2008, ApJ, 684, 1075
Martin N. F. et al., 2015, ApJ, 804, L5
Martin N. F. et al., 2016a, MNRAS, 458, L59
Martin N. F. et al., 2016b, ApJ, 833, 167
Martin N. F. et al., 2016c, ApJ, 830, L10
Martin N. F., Collins M. L. M., Longeard N., Tollerud E., 2018, ApJ, 859,
    L5
McConnachie A. W., 2012, AJ, 144, 4
McConnachie A. W., Côté P., 2010, ApJ, 722, L209
McLaughlin D. E., van der Marel R. P., 2005, ApJS, 161, 304
Muñoz R. R., Geha M., Côté P., Vargas L. C., Santana F. A., Stetson P.,
    Simon J. D., Djorgovski S. G., 2012, ApJ, 753, L15
Norris J. E., Wyse R. F. G., Gilmore G., Yong D., Frebel A., Wilkinson M.
    I., Belokurov V., Zucker D. B., 2010, ApJ, 723, 1632
Peñarrubia J., Navarro J. F., McConnachie A. W., 2008, ApJ, 673, 226
Revaz Y., Jablonka P., 2018, preprint (arXiv:e-prints)
Romani R. W., Weinberg M. D., 1991, in Janes K., ed., ASP Conf. Ser. Vol.
    13. The Formation and Evolution of Star Clusters, Astron. Soc. Pac.,
    San Francisco, p. 443
Sakamoto T., Hasegawa T., 2006, ApJ, 653, L29
Schlafly E. F., Finkbeiner D. P., 2011, ApJ, 737, 103
Schlegel D. J., Finkbeiner D. P., Davis M., 1998, ApJ, 500, 525
Shapley H., 1938a, Harv. Coll. Obs. Bull., 908, 1
Shapley H., 1938b, Nature, 142, 715
Simon J. D., 2018, preprint (arXiv:e-prints)
Simon J. D., Geha M., 2007, ApJ, 670, 313
Starkenburg E. et al., 2010, A&A, 513, A34
Starkenburg E. et al., 2017, MNRAS, 471, 2587
The Dark Energy Survey Collaboration, 2005, preprint (arXiv:e-prints)
Tonry J. L. et al., 2012, ApJ, 750, 99
Vargas L. C., Geha M., Kirby E. N., Simon J. D., 2013, ApJ, 767,
    134
Walker M. G., Mateo M., Olszewski E. W., Peñarrubia J., Wyn Evans N.,
    Gilmore G., 2009, ApJ, 704, 1274
Willman B., Strader J., 2012, AJ, 144, 76
Willman B. et al., 2005a, AJ, 129, 2692
Willman B. et al., 2005b, ApJ, 626, L85
Willman B., Geha M., Strader J., Strigari L. E., Simon J. D., Kirby E., Ho
    N., Warres A., 2011, AJ, 142, 128
Wilson A. G., 1955, PASP, 67, 27
York D. G. et al., 2000, AJ, 120, 1579
Youakim K. et al., 2017, MNRAS, 472, 2963
Zucker D. B. et al., 2006a, ApJ, 650, L41
Zucker D. B. et al., 2006b, ApJ, 643, L103

APPENDIX A

Table A1. Properties of our spectroscopic sample. Stars A, B, and C have a radial velocity of, respectively, −356.4, −306.2, and −330.5 km s⁻¹ and are indicated in the column 'Member'.

RA (deg)	DEC (deg)	g_0	i_0	$CaHK$	v_r (km s⁻¹)	μ_α^* (mas yr⁻¹)	μ_δ (mas yr⁻¹)	S/N	[Fe/H]$_\mathrm{CaHK}$	P_mem	Member	Time
238.34537500	+64.57397222	19.07 ± 0.01	18.62 ± 0.01	19.95 ± 0.01	−125.8 ± 1.3 −125.0 ± 1.5 −129.3 ± 2.9	−4.44 ± 0.45	−4.02 ± 0.47	23.2	–	0.00	N	Averaged 2015 2016
238.50220833	+64.58488889	20.05 ± 0.01	19.66 ± 0.01	20.78 ± 0.01	−244.0 ± 3.1	−4.27 ± 0.86	0.74 ± 0.93	9.9	−1.03 ± 0.15	0.37	N	2016
238.48954167	+64.58458333	20.59 ± 0.01	19.98 ± 0.01	21.63 ± 0.03	−411.9 ± 5.2	−2.84 ± 1.44	−5.55 ± 1.24	6.9	−1.07 ± 0.13	0.00	N	2016
238.46962500	+64.61827778	20.85 ± 0.01	20.61 ± 0.01	21.28 ± 0.02	−328.4 ± 8.8	−0.04 ± 3.08	2.54 ± 2.04	4.6	−2.50 ± 0.46	0.88	Y	2016
238.13162500	+64.56455556	18.85 ± 0.01	18.29 ± 0.01	19.83 ± 0.01	−137.2 ± 1.7	−7.08 ± 0.32	1.52 ± 0.33	25.6	–	0.03	N	2016
238.32470833	+64.59466667	18.98 ± 0.01	18.89 ± 0.01	19.36 ± 0.01	194.0 ± 8.1	33.07 ± 0.47	42.0 ± 0.46	17.5	–	0.00	N	2016
238.29208333	+64.56011111	19.36 ± 0.01	18.80 ± 0.01	20.05 ± 0.01	−340.6 ± 0.9 −340.6 ± 1.1 −343.7 ± 1.5	1.11 ± 0.50	0.99 ± 0.49	20.5	−2.42 ± 0.17	0.86	Y	Averaged 2015 2016
238.22750000	+64.57172222	19.83 ± 0.01	19.38 ± 0.01	20.35 ± 0.01	−341.9 ± 1.7 −338.3 ± 2.8 −344.1 ± 2.2	1.64 ± 0.85	−0.14 ± 0.87	17.3	−2.93 ± 0.23	0.18	Y	Averaged 2015 2016
238.17570833	+64.57013889	19.84 ± 0.01	19.34 ± 0.01	20.44 ± 0.01	−346.9 ± 1.6 −345.1 ± 2.6 −348.0 ± 2.0	1.45 ± 0.68	0.92 ± 0.73	15.1	−2.57 ± 0.22	0.83	Y	Averaged 2015 2016
238.22337500	+64.55341667	20.07 ± 0.01	19.69 ± 0.01	20.53 ± 0.01	−341.9 ± 2.2 −341.0 ± 2.5 −345.4 ± 4.9	1.15 ± 0.84	0.46 ± 0.93	13.3	−2.93 ± 0.23	0.93	Y	Averaged 2015 2016
238.07675000	+64.59608333	20.52 ± 0.01	19.25 ± 0.01	22.50 ± 0.05	−95.9 ± 2.2 −94.2 ± 3.2 −97.6 ± 3.1	0.09 ± 0.73	−7.85 ± 0.80	13.2	–	0.00	N	Averaged 2015 2016
238.21795833	+64.59575000	20.68 ± 0.01	20.45 ± 0.01	21.06 ± 0.02	−343.5 ± 4.6 −343.6 ± 14.0 −343.5 ± 4.9	3.81 ± 1.66	1.45 ± 1.94	7.7	−2.77 ± 0.31	0.99	Y	Averaged 2015 2016
238.19866667	+64.54908333	20.71 ± 0.01	20.41 ± 0.01	21.13 ± 0.02	−347.5 ± 4.8	1.91 ± 1.73	0.40 ± 2.02	7.0	−2.72 ± 0.38	0.14	Y	2016
238.15762500	+64.54386111	20.74 ± 0.01	20.49 ± 0.01	21.11 ± 0.02	−346.1 ± 6.9	−0.42 ± 1.84	2.88 ± 2.03	7.2	−2.91 ± 0.30	0.98	Y	2016
238.29766667	+64.58597222	20.90 ± 0.01	20.59 ± 0.01	21.36 ± 0.02	−349.7 ± 6.2	–	–	6.6	−2.41 ± 0.44	0.20	Y	2016
238.22362500	+64.56244444	20.94 ± 0.01	20.65 ± 0.01	21.39 ± 0.02	−349.7 ± 5.5	–	–	6.6	−2.48 ± 0.38	0.87	Y	2016
238.25691667	+64.54466667	21.05 ± 0.01	20.78 ± 0.01	21.50 ± 0.02	−340.0 ± 8.4	–	–	5.4	−2.49 ± 0.39	0.98	Y	2016
238.18845833	+64.58144444	21.62 ± 0.01	21.31 ± 0.01	22.07 ± 0.03	−336.3 ± 12.8	–	–	3.6	−2.76 ± 0.46	0.99	Y	2016
238.27908333	+64.56091667	22.71 ± 0.02	21.55 ± 0.01	24.11 ± 0.17	−206.3 ± 5.4	–	–	3.3	−2.35 ± 0.60	0.00	N	2016
238.00450000	+64.55847222	18.82 ± 0.01	18.22 ± 0.01	19.91 ± 0.01	−47.2 ± 1.6	1.63 ± 0.30	−2.54 ± 0.33	25.9	–	0.39	N	2016
238.00004167	+64.57619444	20.37 ± 0.01	18.83 ± 0.01	22.56 ± 0.05	−66.7 ± 2.2	−1.79 ± 0.53	−10.54 ± 0.53	21.6	–	0.00	N	2016
238.05320833	+64.52075000	20.87 ± 0.01	19.56 ± 0.01	22.96 ± 0.07	−47.4 ± 3.4	−6.80 ± 0.98	−2.43 ± 0.97	12.8	–	0.00	N	2016
238.05975000	+64.55613889	22.04 ± 0.01	20.94 ± 0.01	23.80 ± 0.15	−253.1 ± 7.1	–	–	5.7	–	0.00	N	2016
238.52529167	+64.59861111	16.73 ± 0.01	16.18 ± 0.01	17.74 ± 0.0	3.6 ± 0.9	−7.16 ± 0.09	−6.06 ± 0.09	65.4	–	0.00	N	2016
238.39033333	+64.63200000	17.60 ± 0.01	16.33 ± 0.01	19.75 ± 0.01	−30.9 ± 1.2	−4.37 ± 0.10	−2.53 ± 0.10	52.8	–	0.00	N	2016

Table A1 – *continued*

RA (deg)	DEC (deg)	g_0	i_0	CaHK	v_r (km s^{-1})	μ_α^* (mas yr^{-1})	μ_δ (mas yr^{-1})	S/N	[Fe/H]$_{CaHK}$	P_{mem}	Member	Time
238.34487500	+64.58811111	17.20 ± 0.01	16.60 ± 0.01	18.34 ± 0.0	−41.8 ± 1.2	−6.68 ± 0.13	14.34 ± 0.14	57.4	–	0.00	N	2016
238.27975000	+64.55630556	16.93 ± 0.01	16.20 ± 0.01	18.13 ± 0.0	−52.0 ± 1.0	−13.07 ± 0.19	−0.92 ± 0.17	66.4	−1.12 ± 0.09	0.21	N	2016
238.23100000	+64.59677778	17.76 ± 0.01	17.12 ± 0.01	18.94 ± 0.0	−4.1 ± 0.9	0.92 ± 0.16	−2.94 ± 0.16	47.7	–	0.11	N	2016
238.11125000	+64.57577778	17.43 ± 0.01	16.73 ± 0.01	18.73 ± 0.0	−68.8 ± 0.9	−4.60 ± 0.12	−2.21 ± 0.13	50.4	–	0.56	N	2016
238.01183333	+64.53602778	17.96 ± 0.01	17.37 ± 0.01	19.09 ± 0.01	−76.7 ± 1.3	−0.77 ± 0.18	−3.42 ± 0.18	37.8	–	0.00	N	2016
238.5645417	+64.50524722	19.00 ± 0.01	18.42 ± 0.01	20.03 ± 0.01	−225.2 ± 2.3	−2.14 ± 0.38	−0.71 ± 0.41	5.5	–	0.02	N	2015
238.51061250	+64.55532500	19.88 ± 0.01	18.28 ± 0.01	22.15 ± 0.04	−53.2 ± 1.5	6.87 ± 0.40	−6.51 ± 0.42	6.3	–	0.00	N	2015
238.54619167	+64.52975556	20.39 ± 0.01	19.99 ± 0.01	21.11 ± 0.02	−165.9 ± 8.8	−2.78 ± 1.73	−0.87 ± 1.18	3.0	−1.15 ± 0.13	0.00	N	2015
238.55823750	+64.56613611	21.74 ± 0.01	20.00 ± 0.01	23.83 ± 0.14	−39.9 ± 4.7	−3.41 ± 2.63	−4.42 ± 2.37	5.4	–	0.00	N	2015
238.41302083	+64.57990000	22.32 ± 0.01	21.37 ± 0.01	23.82 ± 0.14	−356.4 ± 5.5	–	–	3.1	−1.34 ± 0.53	0.00	N	2015
238.42835417	+64.57927222	22.41 ± 0.01	21.81 ± 0.02	23.06 ± 0.07	−306.2 ± 14.9	–	–	3.3	−2.68 ± 0.63	0.00	N	2015
238.15138333	+64.60540000	19.44 ± 0.01	18.92 ± 0.01	20.03 ± 0.01	−337.6 ± 2.7	0.90 ± 0.52	1.08 ± 0.54	4.1	−2.82 ± 0.24	0.03	Y	2015
238.22609167	+64.59788333	19.57 ± 0.01	18.53 ± 0.01	21.26 ± 0.02	−84.5 ± 1.6	−1.76 ± 0.45	−1.74 ± 0.46	8.6	–	0.00	N	2015
238.21103333	+64.57847778	20.07 ± 0.01	18.59 ± 0.01	22.24 ± 0.04	−3.5 ± 1.6	−3.22 ± 0.53	−13.88 ± 0.55	6.7	–	0.00	N	2015
238.20966667	+64.61985278	20.26 ± 0.01	19.38 ± 0.01	21.58 ± 0.02	−182.3 ± 4.9	−6.00 ± 0.88	3.11 ± 0.98	20.7	−1.62 ± 0.13	0.00	N	2015
238.25460417	+64.54189167	20.63 ± 0.01	20.05 ± 0.01	21.66 ± 0.03	9.4 ± 4.2	−5.38 ± 1.27	2.03 ± 1.44	3.6	−1.02 ± 0.15	0.00	N	2015
238.28841250	+64.58997500	21.39 ± 0.01	19.68 ± 0.01	23.71 ± 0.12	−61.7 ± 2.3	−8.05 ± 1.42	1.98 ± 1.49	5.1	–	0.00	N	2015
238.18912917	+64.55407222	22.21 ± 0.01	21.67 ± 0.02	22.96 ± 0.07	−330.5 ± 5.5	–	–	3.6	−2.53 ± 0.51	0.00	N	2015
238.03618333	+64.57617500	21.00 ± 0.01	20.73 ± 0.01	21.40 ± 0.02	−325.7 ± 8.9	2.71 ± 2.97	0.26 ± 3.51	3.1	−2.90 ± 0.33	0.95	Y	2015
238.51431587	+64.57347835	17.98 ± 0.01	17.49 ± 0.01	18.89 ± 0.0	−79.9 ± 1.1	−6.51 ± 0.19	0.49 ± 0.20	13.1	–	0.00	N	2015
238.49718375	+64.51780965	18.14 ± 0.01	16.31 ± 0.01	20.26 ± 0.01	−11.9 ± 1.1	−68.75 ± 0.13	−42.7 ± 0.13	14.7	–	0.00	N	2015
238.43973971	+64.56761491	18.07 ± 0.01	16.91 ± 0.01	20.04 ± 0.01	−64.2 ± 1.3	6.83 ± 0.17	−6.09 ± 0.17	15.1	–	0.00	N	2015
238.21533400	+64.60644630	15.42 ± 0.01	14.99 ± 0.01	16.29 ± 0.0	−54.3 ± 1.1	−14.42 ± 0.05	−5.44 ± 0.05	96.1	–	0.00	N	2015
238.18480597	+64.61537726	17.88 ± 0.01	17.25 ± 0.01	19.09 ± 0.01	−35.1 ± 1.3	−5.66 ± 0.17	−4.63 ± 0.17	25.8	–	0.03	N	2015
238.12209840	+64.60199650	18.92 ± 0.01	16.98 ± 0.01	21.15 ± 0.02	−0.9 ± 1.2	−1.69 ± 0.20	11.09 ± 0.20	8.9	–	0.00	N	2015
238.11487862	+64.60882637	17.89 ± 0.01	16.96 ± 0.01	19.60 ± 0.01	−123.9 ± 1.2	4.81 ± 0.15	−22.05 ± 0.15	11.8	–	0.00	N	2015

This paper has been typeset from a T$_{\!E}$X/L^{A}T$_{\!E}$X file prepared by the author.

In-depth observational study of the faint Milky Way satellite Sagittarius II
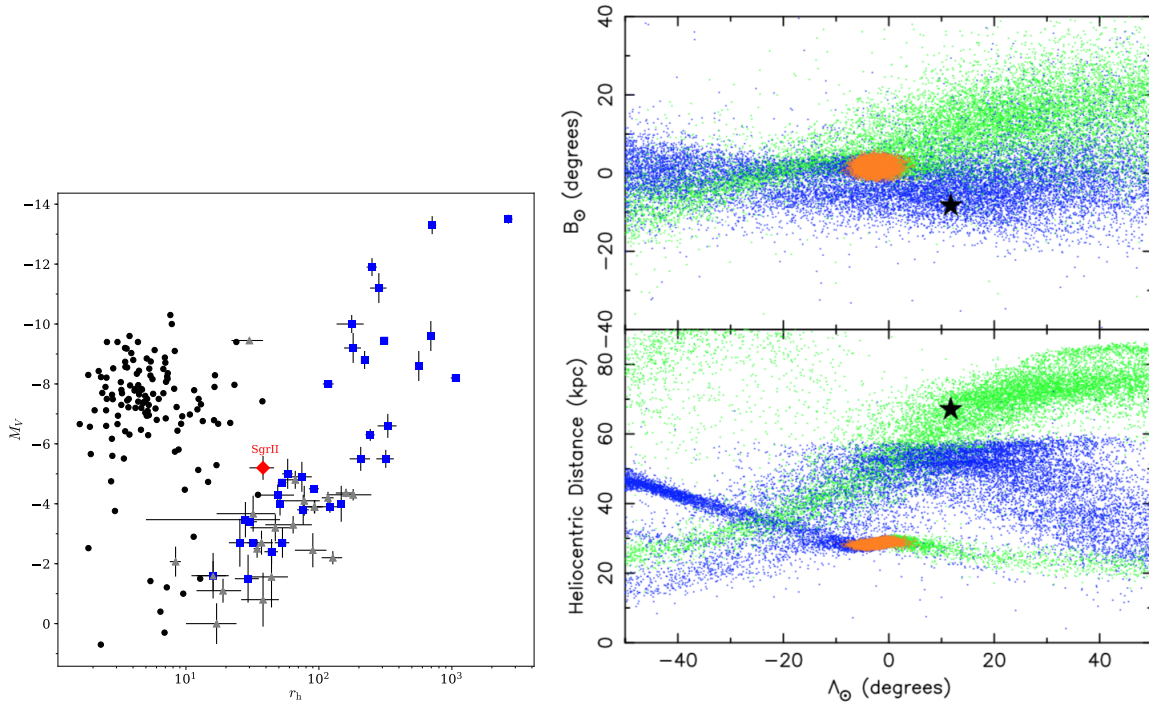
Figure 4.1: *Left plot*: Same plot as Figure 3.1, for Sgr II. Sgr II is represented as a red diamond, with the r_h and M_V shown here both taken from L15. It occupies a peculiar location on this diagram as it is located between the "band" typical of dwarf galaxies, and the group populated by most clusters. At the time of its discovery, Sgr II was therefore a intriguing satellite. *Right plot*: Plot from L15. The upper panel indicates the location of Sgr II (black star) in the Sgr stream coordinates ($\Lambda_\odot$,$B_\odot$), superimposed with the N-body simulation of the stream from Law & Majewski (2010). Green dots represent the stars of the trailing arm, and blue dots the ones of the leading arm. The Sgr dSph is represented in orange. The lower panel shows $\Lambda_\odot$ vs. heliocentric distance for the Sgr stream simulation and Sgr II. The satellite's location and distance from L15 were compatible with the trailing arm of the stream.

This chapter presents my study on the faint MW satellite Sagittarius II (Sgr II), which was also discovered in 2015 by L15. Sgr II was immediately found to be quite different from Dra II, much brighter ($M_V = -5.2 \pm 0.4$ mag) and more distant ($d = 67 \pm 5$ kpc). All the main

features of a stellar population were found in Sgr II, with a prominent RGB and 13 HB stars that were used to estimate the distance of the satellite, based on the method of Deason, Belokurov & Evans (2011). L15 also noticed the presence of a few probable blue stragglers (BS). These peculiar stars are often associated to mass transfer or direct collision in a binary system, and are typically known to populate old and dense environnements. And indeed, L15 found a half-light radius of 38^{+8}_{-7} pc, which placed the satellite in a very peculiar location in the r_h-M_V plane shown in Figure 4.1, being both smaller than the dwarf galaxies of similar luminosities (CVn II, $M_V \sim -5.17 \pm 0.32$ mag, $r_h \sim 71 \pm 11$ pc; Leo IV, $M_V \sim -4.99 \pm 0.26$ mag, $r_h \sim 114 \pm 13$ pc) while still being larger than the vast majority of globular clusters. The blue HB of Sgr II, uncommon among outer halo globular clusters, and its size, made L15 think that the system was a compact dwarf galaxy. However, a spectroscopic confirmation is still required to confirm this assertion.

Spectroscopy is also required to address another interesting aspect of Sgr II first mentionned by L15: its possible association with the Sgr stream. Figure 4.2 shows the location of Sgr II in the Sgr stream reference frame and its distance, as determined by L15, and compares it with the ones of the stream, based on a simulation from Law & Majewski (2010). L15 noticed that both the location and the distance of Sgr II are compatible with this large structure, and more specifically, could be tied to the part of the trailing arm that was stripped from the stream 3 Gyr ago. To confirm that the two systems are on similar orbits, L15 pointed out that a measurement of the radial velocity of the system, and ideally of its orbital properties, were crucial.

The following paper, now accepted for publication in MNRAS, details the results of my study concerning Sgr II, using deep photometry from MegaCam, *Pristine* and three spectroscopic runs from Keck II/DEIMOS.

The Pristine Dwarf-Galaxy survey − II. In-depth observational study of the faint Milky Way satellite Sagittarius II

Nicolas Longeard[1], Nicolas Martin[1,2], Else Starkenburg[3], Rodrigo A. Ibata[1],
Michelle L. M. Collins[4,6], Benjamin P. M. Laevens[5], Dougal Mackey[7], R. Michael Rich [8] ,
David S. Aguado[9], Anke Arentsen[3], Pascale Jablonka[10,11],
Jonay I. González Hernández[12,13], Julio F. Navarro[14], Rubén Sánchez-Janssen[15,16]

[1] *Université de Strasbourg, CNRS, Observatoire astronomique de Strasbourg, UMR 7550, F-67000 Strasbourg, France*
[2] *Max-Planck-Institut für Astronomy, Königstuhl 17, D-69117, Heidelberg, Germany*
[3] *Leibniz Institute for Astrophysics Potsdam (AIP), An der Sternwarte 16, 14482 Potsdam, Germany*
[4] *Department of Physics, University of Surrey, Guildford, GU2 7XH, Surrey, UK*
[5] *Institute of Astrophysics, Pontificia Universidad Católica de Chile, Av. Vicua Mackenna 4860, 7820436 Macul, Santiago, Chile*
[6] *Department of Astronomy, Yale University, New Haven, CT 06520, USA*
[7] *Research School of Astronomy and Astrophysics, Australian National University, Canberra, ACT 2611, Australia*
[8] *University of California Los Angeles, Department of Physics & Astronomy, Los Angeles, CA, USA*
[9] *Institute of Astronomy, University of Cambridge, Madingley Road, Cambridge CB3 0HA, UK*
[10] *GEPI, Observatoire de Paris, PSL Research University, CNRS, Place Jules Janssen, 92190 Meudon, France*
[11] *Laboratoire d'astrophysique, École Polytechnique Fédérale de Lausanne (EPFL), Observatoire, 1290 Versoix, Switzerland*
[12] *Instituto de Astrofisica de Canarias, Via Lactea, 38205 La Laguna, Tenerife, Spain*
[13] *Universidad de La Laguna, Departamento de Astrofisica, 38206 La Laguna, Tenerife, Spain*
[14] *Dept. of Physics and Astronomy, University of Victoria, P.O. Box 3055, STN CSC, Victoria BC V8W 3P6, Canada*
[15] *NRC Herzberg Astronomy and Astrophysics, 5071 West Saanich Road, Victoria, BC V9E 2E7, Canada*
[16] *Royal Observatory Edinburgh, Blackford Hill, Edinburgh, EH9 3HJ, UK*

8 August 2019

ABSTRACT

We present an extensive study of the Sagittarius II (Sgr II) stellar system using MegaCam g and i photometry, narrow-band, metallicity-sensitive Calcium H&K doublet photometry and Keck II/DEIMOS multi-object spectroscopy. We derive and refine the Sgr II structural and stellar properties inferred at the time of its discovery. The colour-magnitude diagram implies Sgr II is old (12.0 ± 0.5 Gyr) and metal poor. The CaHK photometry confirms the metal-poor nature of the satellite ([Fe/H] $_{\rm CaHK} = -2.32 \pm 0.04$ dex) and suggests that Sgr II hosts more than one single stellar population ($\sigma^{\rm CaHK}_{\rm [FeH]} = 0.11^{+0.05}_{-0.03}$ dex). Using the Ca infrared triplet measured from our highest signal-to-noise spectra, we confirm the metallicity and dispersion inferred from the Pristine photometric metallicities ([Fe/H]$_{\rm spectro} = -2.23 \pm 0.05$ dex, $\sigma^{\rm spectro}_{\rm [Fe/H]} = 0.10^{+0.06}_{-0.04}$ dex). The velocity dispersion of the system is found to be $\sigma_v = 2.7^{+1.3}_{-1.0}$ km s^{-1} after excluding two potential binary stars. Sgr II's metallicity and absolute magnitude (M$_V = -5.7 \pm 0.1$ mag) place the system on the luminosity-metallicity relation of the Milky Way dwarf galaxies despite its small size. The low but resolved metallicity and velocity dispersions paint the picture of a slightly dark-matter-dominated satellite ($M/L = 23.0^{+32.8}_{-23.0}$ M$_\odot$ L$_\odot^{-1}$). Furthermore, using the *Gaia* Data Release 2, we constrain the orbit of the satellite and find an apocenter of $118.4^{+28.4}_{-23.7}$ kpc and a pericenter of $54.8^{+3.3}_{-6.1}$ kpc. The orbit of Sgr II is consistent with the trailing arm of the Sgr stream and indicates that it is possibly a satellite of the Sgr dSph that was tidally stripped from the dwarf's influence.

Key words: galaxy: Dwarf – Local Group – object: Sagittarius II, Sagittarius stream

1 INTRODUCTION

During the history of the Universe, structures such as galaxies form hierarchically. Therefore, dwarf galaxies (DGs) are particularly old and metal-poor systems and targets of choice to study the history of the local universe. They are systems spanning a wide range of masses and luminosity. Bright dwarf galaxies such as Sculptor (Shapley 1938b), Draco (Wilson 1955), or Sextans (Irwin et al. 1990) have been known for decades (Mateo 1998), but the extensive search for new dwarf galaxies over the last twenty years revealed fainter systems (Martin et al. 2006, Belokurov et al. 2007, Zucker et al. 2006b). Still, our knowledge of the Milky Way satellites remains incomplete. The recent discoveries of several of those faint galaxy candidates with $M_V > -4$ (Willman et al. 2005a; Belokurov et al. 2007; Drlica-Wagner et al. 2015; Laevens et al. 2015b; Luque et al. 2016) are promising as they might well bring new perspectives to near-field cosmology (Bullock & Boylan-Kolchin 2017).

The study of these nearby small-scale structures can allow one to explore various problematics in astrophysics, from the faint-end of the galaxy luminosity function (Koposov et al. 2009) to the validity of cosmological models. Therefore, DGs are important cosmological probes (Pawlowski et al. 2017; Tulin & Yu 2017) as the comparison of their observed properties with the predictions made by current ΛCDM models leads to some discrepancies that we have to understand in order to constrain and refine our cosmological models. For example, the number of faint satellites, their distribution in the sky, as well as their stellar masses and mass profiles are still in tensions with ΛCDM (Boylan-Kolchin, Bullock & Kaplinghat 2011, Navarro et al. 2010, Pawlowski, McGaugh & Jerjen 2015). DGs are also thought to be among the most dark matter (DM hereafter) dominated systems in the universe (Wolf et al. 2010) and could be useful for the detection of the elusive DM particle through self-annihilation processes (Bertone, Hooper & Silk 2005; Geringer-Sameth, Koushiappas & Walker 2015).

However, using faint dwarf galaxies as cosmological probes can be challenging as their exceptional faintness comes with observational challenges. The overall properties and/or even the very nature of the recently discovered systems can sometimes be puzzling as the distinction between galaxy and globular cluster is difficult to make (e.g., Conn et al. 2018, Longeard et al. 2018). Therefore, only the combined efforts of deep photometric surveys, such as the Dark Energy Survey (The Dark Energy Survey Collaboration 2005, DES), the Panoramic Survey Telescope and Rapid Response System (Chambers et al. 2016, PS1), or the Sloan Digital Sky Survey (York et al. 2000, SDSS), and spectroscopic observations can hope to improve our understanding on the faint-end of the luminosity function and the history of the Milky Way (MW).

In this context, we present here the study of the MW satellite Sagittarius II (Sgr II), discovered by Laevens et al. (2015a, hereafter L15) in PS1, where it was identified as an old (12.5 Gyr) and metal-poor ([Fe/H] = -2.20 dex) dwarf-galaxy candidate. L15 noticed that Sgr II had a peculiar location on the sky: its position and distance were found to be consistent with the predictions of models for the Sagittarius stream (Law & Majewski 2010). They concluded that this satellite might actually have been a satellite of the bright Sagittarius dwarf galaxy discovered by Ibata, Gilmore & Irwin (1994), deposited in the MW's halo as its host is being tidally destroyed. However, spectroscopic observations were still needed at the time to dynamically tie the stream and Sgr II, as well as confirming the galaxy nature of the satellite. Sgr II was also recently studied by Mutlu-Pakdil et al. (2018, M18) with Magellan/MegaCam photometry and they confirmed the structural properties inferred by L15. Furthermore, using both blue horizontal branch stars (BHBs) and a CMD-fitting technique, they constrained it to host an old (13.5 Gyr), metal-poor ([Fe/H] $= -2.2$ dex) stellar population, with an alpha abundance ratio of α/Fe $= 0.4$ dex, and a distance modulus $m - M = 19.2 \pm 0.2$ mag. Moreover, they found a half-light radius of 32 ± 1.0 pc, and an absolute magnitude of $M_V = -5.2 \pm 0.1$ mag. Based on all these photometric properties, M18 concluded that the system is likely a globular cluster, and compared the satellite to several extended clusters of M31 associated to known streams, in the same way that Sgr II is suspected to be linked to the Sgr stream. However, M18 emphasised the importance of a spectroscopic study to confirm their conclusion.

In this work, we present a thorough analysis of the stellar, structural, and orbital properties of Sgr II using deep broadband photometry from the Canadian-France-Hawaii Telescope (CFHT) MegaCam (MC) imager in the context of the Pristine survey. The Pristine survey uses a narrow-band filter centred on the metallicity-sensitive Ca H&K doublet (Starkenburg et al. 2017) to identify metal-poor stars and estimate their metallicity using pure photometry. Keck II/DEIMOS spectroscopy are additionally used to constrain the system's metallicity and kinematics. Finally, combined with the *Gaia* Data Release 2, we constrain the orbital properties of the satellite.

2 OBSERVATIONS AND DATA

2.1 Photometry

Our photometry consists of deep broadband g_{MC} and i_{MC} observations as well as narrow-band observations with the CaHK filter centred on the metallicity-sensitive Calcium H&K doublet. Sgr II was observed using the wide-field imager MegaCam on the CFHT (Boulade et al. 2003). The CaHK photometry is part of a larger survey called Pristine (Starkenburg et al. 2017).

Observations were conducted in service mode by the CFHT staff during the night of July, 2nd, 2016 under good seeing conditions ($\sim 0.4''$). The integration times are of 3×700 s in g_{MC}, 5×500 s in i_{MC} and 3×705 s in $CaHK$. We refer the reader to L18 for the details of the MegaCam data reduction. The star/galaxy separation is done using the Cambridge Astronomical Survey Unit (Irwin & Lewis 2001) pipeline flags, which also indicate saturated sources. The MegaCam photometry is calibrated onto the PS1 photometric system following the same procedure as in L18: a cross-identification of all unsaturated point sources with photometric uncertainties below 0.05 mag in both catalogs is performed. The difference $g_{MC} - g_{PS1}$ (respectively $i_{MC} - i_{PS1}$) is expressed as a function of the colour $g_{MC} - i_{MC}$. We then fit a third-order polynomial to translate MC photometry into PS1 through a 3σ clipping procedure. The coefficients

of the polynomials to transform (g_{MC}, i_{MC}) into (g_{PS1}, i_{PS1}) in this work are different from those in L18 because the uncalibrated color $g_{MC} - i_{MC}$ differs. We define $x \equiv g_{MC} - i_{MC}$ and obtain:

$$g_{MC} - g_{P1} = a_0^g x^2 + a_1^g x + a_2^g,$$
$$i_{MC} - i_{P1} = a_0^i x^2 + a_1^i x + a_2^i.$$

The calibration coefficients are: $a_0^g = -0.0162 \pm 0.0046$, $a_1^g = 0.0906 \pm 0.0029$, $a_2^g = -0.0696 \pm 0.0016$ for the g band and $a_0^i = -0.0117 \pm 0.0032$, $a_1^i = 0.0058 \pm 0.0022$, $a_2^i = -0.1359 \pm 0.0010$ for the i band. All uncertainties on the polynomials coefficients are propagated into the photometric uncertainties.

All stars saturated in the MC photometry, filtered during the calibration process, are taken directly from PS1 and added to the final catalog, for a total of 83,355 stars. This catalog is finally dereddened using the dust map from Schlegel, Finkbeiner & Davis (1998) and the extinction coefficients from Schlafly & Finkbeiner (2011). In the rest of the text, we use the combined catalogue and the PS or MC subscripts are dropped. The 50 per cent completeness of the data is reached at $g_0 \sim 24.2$ and $i_0 \sim 23.4$ mag.

2.2 Spectroscopy

Spectroscopic follow-up observations of Sgr II were obtained with Keck and the Deep Extragalactic Imaging Multi-Object Spectrograph (DEIMOS) (Faber et al. 2003). Similarly to L18, the standard set-up was used here with the OG550 filter and the 1200 lines mm^{-1} grating. The wavelength range goes from 6500 to 9000 Å, for a resolution of ~ 8500 Å. "Mask 1" was observed on 2015-09-12 and re-observed on 2015-09-18 (97 stars) and "mask 2" on the 2015-09-08 (110 stars). Mask 2 was designed to be perpendicular to the other two in order to probe potential Sgr II members further away in the South/North direction (Figure 1). Stars observed spectroscopically were selected based on their distance from the Sgr II population in the CMD as identified by Laevens et al. (2015a). The velocities were derived by selecting a slitmask in the package IRAF SIMULATOR provided by the Keck Observatories, and the pipeline of Ibata et al. (2011). The latter compares a template created from the Calcium II triplet features at rest added to a continuous stellar spectrum with the observed spectra to fit for the doppler shift with a Monte Carlo Markov Chain (Hastings 1970, MCMC) algorithm. This MCMC procedure gives a Probability Distribution Function (PDF) of the radial velocity, from which the velocity uncertainty is measured. The typical velocity uncertainty of our data is of order ~ 3 km s^{-1} at S/N= 12.

All stars with a signal-to-noise ratio (S/N) below 3 or with a velocity uncertainty greater than 15 km s^{-1} are discarded, resulting in a final spectroscopic sample of 118 stars. Following the procedure described in (Simon & Geha 2007) and using the 47 stars observed at least twice and that pass the S/N and velocity uncertainty cuts, we assess the systematics in our sample, including the wavelength calibration uncertainty, and find a negligible bias of 0.4 ± 1.3 km s^{-1} and a systematic uncertainty floor of $\delta_{thr} = 1.8^{+0.3}_{-0.2}$ km s^{-1}. The heliocentric velocities of the stars observed more than once

are combined by taking the mean of all available quantities weighted by the inverse of their respective velocity uncertainties. The same procedure is followed for the equivalent widths of the Ca triplet.

Finally, the existence of binaries in the sample is investigated for all stars with multiple velocity measurements. To do so, we define the quantity μ such that

$$\mu = \frac{v_{r,l} - v_{r,m}}{\sqrt{\delta_{vr,l}^2 + \delta_{vr,m}^2 + 2\delta_{thr}^2}},$$

with $v_{r,l}$ (resp. for $v_{r,m}$) the heliocentric velocity of a star in mask l (resp. mask m), and $\delta_{vr,l}$ (resp. $\delta_{vr,m}$) the uncertainty on this measurement. If μ is greater than 2.5 (a '2.5σ deviation' between the two velocity measurements), the star is considered as a potential binary and flagged accordingly. Two stars are identified as such through this procedure, with differences in velocities of 21.46 ± 6.75 km s^{-1} and 25.07 ± 7.91 km s^{-1}. This variation over one week is large but has been observed before in the dwarf galaxy Bootes I (Koposov et al. 2011).

3 BROADBAND PHOTOMETRY ANALYSIS

We present the one square degree field centred on Sgr II together with the spatial distribution of stars observed with spectroscopy in Figure 1.

The colour-magnitude diagram (CMD) of all stars within two half-light radii ($r_h \sim 1.7'$) of the system is shown in the left panel of Figure 2, along with the spectroscopically observed stars. The CMD of the same areal coverage but selected in the outskirts of the MegaCam field of view is represented as a comparison in the middle panel. The main sequence (MS) and main sequence turn-off (MSTO) of Sgr II are very well defined thanks to the depth of the MegaCam data, and corresponds to an old (> 12 Gyr) and very metal-poor ([Fe/H] < -2.0) population. A few blue stragglers can be seen in the satellite. Sgr II also hosts a few blue horizontal branch stars at $g_0 \sim 19.7$.

The BHB stars are useful as they are good distance tracers (Deason, Belokurov & Evans 2011, D11) so we start by using them to measure the distance to Sgr II. Two out of the three BHBs that were observed with spectroscopy are not compatible with the systemic velocity of Sgr II (see section 5). They are therefore discarded. The remaining 10 BHBs' g_0 and r_0 are calibrated onto the SDSS photometry according to the colour equations of Tonry et al. (2012). Relation (7) of D11 that allows to find the absolute magnitude of BHBs only holds for stars in the colour interval $-0.25 < (g - r)_{0,SDSS} < 0.0$. For this reason, another star is rejected from the sample. Using this relation for the nine remaining stars yields $M_g = 0.47 \pm 0.02$ mag and a median distance modulus of $(m - M)_{BHB} = 19.19 \pm 0.10$ mag or 68.8 ± 3.0 kpc.

3.1 Structural and CMD fitting

We use our MC photometry to refine the structural properties of Sgr II previously studied by L15 and M18 and determine its main stellar properties through a CMD and spatial
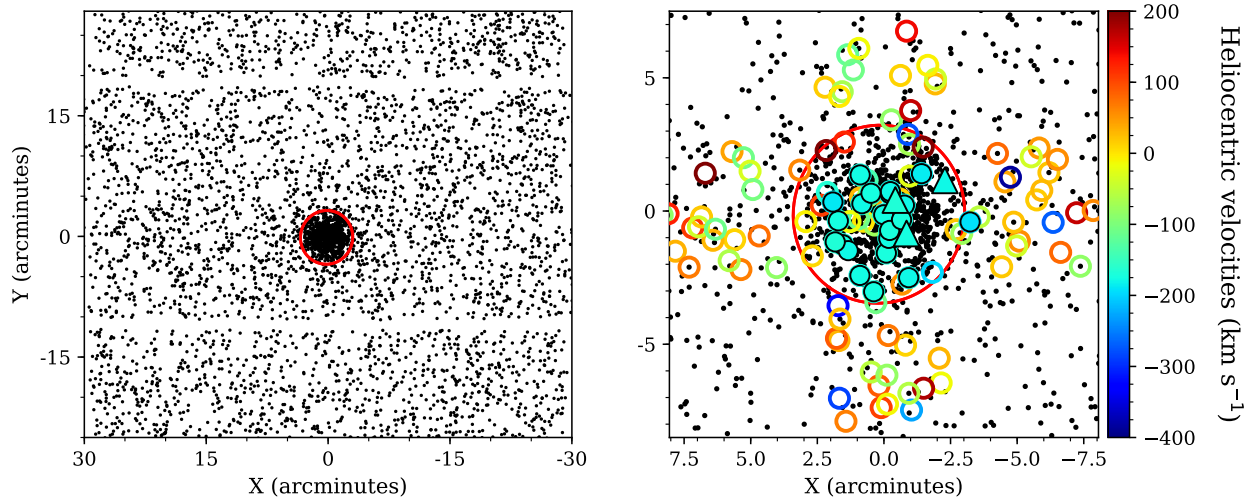
Figure 1. *Left panel:* Spatial distribution of Sgr II-like stars, i.e. stars with a CMD probability membership of 10 per cent or higher. The field is centred on ($\alpha_0 = 298.16628°, \delta_0 = -22.89633°$). The red contour defines the two half-light radii ($r_h \sim 1.7'$) of the satellite. *Right panel:* Close-up on the central region, with stars observed spectroscopically are colour-coded according to their heliocentric velocities. Filled circles represent stars spectroscopically confirmed as Sgr II members, while filled triangles represent Sgr II HB stars in the spectroscopic data set.
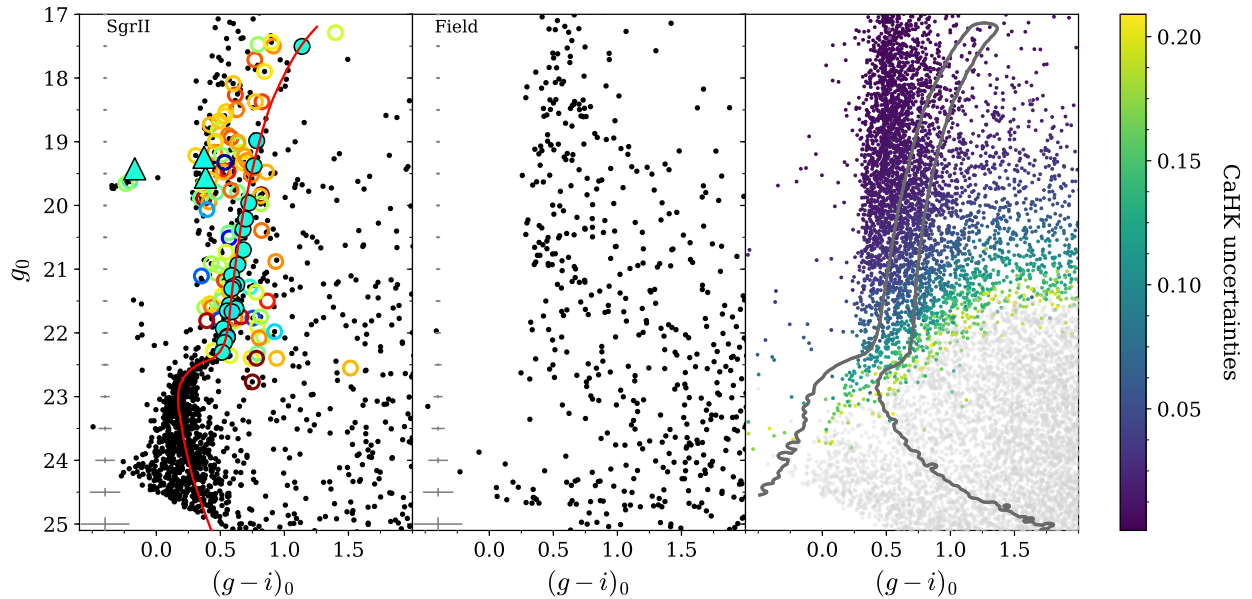
Figure 2. *Left panel:* CMD within two r_h of Sgr II. Its old (> 10 Gyr) and metal-poor ([Fe/H] < -2.2) stellar population clearly stands out. One can notice the presence of a few blue stragglers in the system around $g_0 \sim 22.0$, as well as the Sgr II horizontal branch. Stars observed with spectroscopy are shown with coloured circles. The colour scheme used in this panel is the same as the one in Figure 1. The filled ones represent the confirmed spectroscopic members. Filled triangles show the location, in the CMD, of HB stars in the spectroscopic data set. The favoured isochrone for Sgr II, obtained in section 3, is shown as a solid red line (12 Gyr, [Fe/H] = -2.35 dex, α/Fe = 0 dex, $m - M = 19.32$ mag). *Middle panel:* CMD of the field for an equivalent are centred on (X= -12, Y= -12) arcminutes. *Right panel:* Photometric uncertainties for the $CaHK$ band. The grey contours show the mask used to select the Sgr II-like population showed in the spatial distribution of Figure 1.

distribution fitting procedure. The formalism of this analysis is detailed in Martin et al. (2016a) and L18. Though the main steps will be briefly detailed below, we refer the reader to these two references for more details. Six structural parameters are inferred from our analysis: the centroid offsets along the X and Y axes with respect to the centre coordinates of the literature, x_0 and y_0, the ellipticity ϵ [1], the half-light radius r_h, the position angle θ, and the number of stars N^* of the satellite. These structural properties are gathered in a parameter set noted $\mathcal{P}_{\mathrm{spac}} \equiv \{x_0, y_0, \epsilon, r_h, \theta, N^*\}$.

We then define the CMD parameters derived by our CMD fitting procedure: the age of the satellite A, the systemic metallicity $[\mathrm{Fe/H}]_{\mathrm{CMD}}$, the $[\alpha/\mathrm{Fe}]$ abundance ratio, the distance modulus $m - M$, and η the fraction of Sgr II stars with respect to the total number of stars in the field chosen for the analysis. We regroup these properties into the set $\mathcal{P}_{\mathrm{CMD}} \equiv \{A, [\mathrm{Fe/H}]_{CMD}, [\alpha/\mathrm{Fe}], m - M, \eta\}$

For a given star k, we consider its following properties: its g_k and i_k magnitudes, and its position offset from the center coordinates of the literature, X_k and Y_k. These four properties are gathered into one set $\vec{d_k} = \{X_k, Y_k, g_k, i_k\}$.

The Sgr II radial density, ρ_{dwarf}, is modelled by the following exponential radial profile:

$$\rho_{\mathrm{dwarf}}(r) = \frac{1.68^2}{2\pi r_h^2 (1-\epsilon)} \exp(-\frac{1.68r}{r_h}), \qquad (1)$$

with r the elliptical radius, which can be expressed using the projected sky coordinates (x, y) as

$$r = \left(\left(\frac{1}{1-\epsilon} \big((x - x_0) \cos\theta - (y - y_0)\sin\theta \big) \right)^2 \right.$$
$$\left. + \big((x - x_0)\sin\theta + (y - y_0)\cos\theta \big)^2 \right)^{1/2}. \qquad (2)$$

For the k-th star, the spatial likelihood can then simply be written as

$$\ell_{\mathrm{sp}}^{\mathrm{SgrII}}(X_k, Y_k) = \frac{\rho_{\mathrm{dwarf}}(r)}{\int_S \rho_{\mathrm{dwarf}}(r)dS}, \qquad (3)$$

where S in the area of the sky over which the analysis is conducted.

The spatial likelihood of the Milky Way foreground contamination is assumed flat over the field of view, which yields

$$\ell_{\mathrm{sp}}^{\mathrm{MW}} = \frac{1}{\int dS}. \qquad (4)$$

The CMD likelihood function ℓ_{CMD} is built from the sum of two models: one for the foreground, $\ell_{\mathrm{CMD}}^{\mathrm{MW}}$, constructed empirically from the field CMD, and one to describe the Sgr II population taken as a single stellar population, and called $\ell_{\mathrm{CMD}}^{\mathrm{SgrII}}$. The foreground contamination model is built by selecting all stars outside $5r_h$ of the system centre and binning their distribution on the CMD. This distribution is smoothed by a gaussian kernel in both colour and

[1] The ellipticity is defined as 1 - $\frac{a}{b}$, with a and b the major and minor axis extent of the system.

magnitude of a width of 0.1 in an attempt to limit the effects of shot noise. $\ell_{\mathrm{CMD}}^{\mathrm{SgrII}}$ is generated using a range of Darmouth isochrones (Dotter et al. 2008). We choose isochrones of different $[\mathrm{Fe/H}]_{\mathrm{CMD}}$, A, $[\alpha/\mathrm{Fe}]$, and distance modulus $m - M$. The priors on each parameters are reported in Table 1. To build the PDF of a given stellar population, we simulate the CMD of a population of several million stars, based on its isochrone, luminosity function and photometric uncertainty at a given (g_0, i_0). To avoid aliasing effects, especially at the bright end of our models where the photometric uncertainties are unrealistically low, we add 0.01 in quadrature to the photometric uncertainties. Finally, each PDF is degraded by the completeness of the data, estimated following the method of Martin et al. (2016a).

The structural and CMD parameters are gathered into a single set $\mathcal{P} \equiv \{A, [\mathrm{Fe/H}], [\alpha/\mathrm{Fe}], \mu, \epsilon, r_h, x_0, y_0, \theta, \eta\}$. At the distance of Sgr II, the tip of the Red Giant Branch (RGB) is expected to be located at $g_0 \sim 17.0$. Furthermore, misidentified background galaxies start to pollute our photometry below $g_0 \sim 25.0$. The fit does not take into account the horizontal branch stars as these are poorly modelled by the theoretical stellar population models. Therefore, the analysis is restricted in a specific CMD box defined with the following cuts: $-0.2 < g_0 - i_0 < 1.2$ and $17.0 < g_0 < 25.0$. CMD and spatial properties are fitted at the same time through our own MCMC algorithm by maximising the likelihood of the following model:

$$\mathcal{L}_{tot} = \sum_{k=1}^{N} \ell_{tot}(\vec{d_k}|\mathcal{P}) = \eta\ell_{\mathrm{SgrII}}(\vec{d_k}|\mathcal{P}) + (1-\eta)\ell_{\mathrm{MW}}(\vec{d_k}), \quad (5)$$

with

$$\ell_{\mathrm{SgrII}}(\vec{d_k}|\mathcal{P}) = \ell_{\mathrm{CMD}}^{\mathrm{SgrII}}(g_k, i_k|\mathcal{P}_{\mathrm{CMD}})\ell_{\mathrm{sp}}^{\mathrm{SgrII}}(X_k, Y_k|\mathcal{P}_{\mathrm{spac}}) \quad (6)$$
$$\ell_{\mathrm{MW}} = \ell_{\mathrm{CMD}}^{\mathrm{MW}}(g_k, i_k)\ell_{\mathrm{sp}}^{\mathrm{MW}}(X_k, Y_k). \quad (7)$$

Finally, the distance to Sgr II is constrained using a Gaussian prior based on the distance modulus derived from the median absolute magnitude of the BHBs in the first paragraph of section 3 ($m - M = 19.19 \pm 0.10$ mag). A Gaussian prior on the metallicity of the satellite is also applied and comes directly from the combination of the spectroscopic and CaHK metallicity measurements detailed in the sections 4 and 5 respectively ($[\mathrm{Fe/H}]_{\mathrm{SgrII}} = -2.28 \pm 0.03$ dex). The inference of each parameter of $\mathcal{P}$ is summed up in Table 1, and the 2D PDFs are shown in Figure 3.

The best-fit isochrone is shown as the red PDFs in Figure 3. Sgr II is found to be significantly old and metal-poor with an age of 12.0 ± 0.5 Gyr population along with a systemic metallicity of -2.35 ± 0.05 dex. Furthermore, the alpha abundance of this isochrone is solar ($[\alpha/\mathrm{Fe}] = 0.0$), though we caution the reader about reading too much into this parameter given the roughness of the $[\alpha/\mathrm{Fe}]$ abundance ratio grid. Finally, the favoured distance modulus is $\mu = 19.32^{+0.03}_{-0.02}$ mag, and corresponds to a physical distance of $73.1^{+1.1}_{-0.7}$ kpc. We compare these results by performing the fit without the BHBs or the spectroscopic metallicity priors. For this case, the PDFs are shown in black in Figure 3. The inferences of all the parameters are compatible: the stellar population is here found to be older (12.5 ± 0.5 Gyr) and the metallicity reaches the lower edge of the metallicity grid. In

Table 1. Properties of Sgr II.

Parameter	Unit	Prior	Favoured model	Uncertainties
Right ascension (ICRS) α	degrees	—	298.16628	± 0.001
Declination (ICRS) δ	degrees	—	-22.89633	± 0.001
l	degrees	—	18.93203	± 0.001
b	degrees	—	-22.89461	± 0.001
r_h	arcmin	> 0	1.7	± 0.05
r_h	pc		35.5	$^{+1.4}_{-1.2}$
θ	degrees	[0,180]	103	$^{+28}_{-17}$
ϵ	—	$[0, 1]$	0.0	< 0.12 at the 95% CL
Distance modulus	mag	[18.90,19.45]	19.32	$^{+0.03}_{-0.02}$
Distance	kpc		73.1	$^{+1.1}_{-0.7}$
A	Gyr	[9,13.5]	12.0	± 0.5
[Fe/H]	dex	[-2.4,-1.5]	-2.28	± 0.03
[α/Fe]	dex	[-0.2,0.6]	0.0	± 0.2
log(Luminosity)	—	> 0	4.20	± 0.1
M_V	mag	—	-5.7	± 0.1
μ_0	mag arcsec^{-2}	—	24.7	± 0.2
$< v_r >$	km s^{-1}	—	-177.3	± 1.2
σ_{vr}	km s^{-1}	> 0	2.7	$^{+1.3}_{-1.0}$
μ_α^*	mas yr^{-1}	—	-0.65	$^{+0.08}_{-0.10}$
μ_δ	mas yr^{-1}	—	-0.88	± 0.12
Apocenter	kpc	—	118.4	$^{+28.4}_{-23.7}$
Pericenter	kpc	—	54.8	$^{+3.3}_{-6.1}$
$\epsilon_{\rm orbit}$	—	> 0	0.44	± 0.01
U	km s^{-1}	—	0.4	$^{+14.1}_{-19.5}$
V	km s^{-1}	—	-366.5	$^{+27.3}_{-42.8}$
W	km s^{-1}	—	160.3	$^{+26.3}_{-19.9}$
L_z	km s^{-1} kpc	—	6292	$^{+2236}_{-1899}$
E	km^2 s^{-2}	—	17159	$^{+10213}_{-3120}$

this case, the analysis only gives an upper limit on the metallicity of [Fe/H] $= -2.45$ dex. The distance modulus is found to be $m - M = 19.35 \pm 0.05$ mag. All structural properties are perfectly compatible with L15 and M18. Sgr II is consistent with being spherical ($\epsilon < 0.12$ at the 95% confidence limit) and has a size of $r_h = 1.70 \pm 0.05$ arcminutes, translating into a physical half-light radius of $35.5 ^{+1.4}_{-1.2}$ pc. All the main properties of Sgr II are summarised in Table 1.

Finally, we investigate the presence of RR Lyrae in the field by cross-identifying the PS1 RR Lyrae catalog of Sesar et al. (2017, S17) with our photometry. Three RR Lyrae are found in the vicinity of Sgr II. Two of these have similar distance modulii, as inferred from S17 (18.73 and 18.85 mag). However, the resulting distances are discrepant from both our BHB and CMD fitting analyses by 0.5 mag (roughly 10 kpc in physical distance). To confirm the distance modulus of Sgr II, we compare the CMD of the satellite with fiducials of MW globular clusters in PS1 (Bernard et al. 2014) in Figure 4. In this plot, all fiducials are dereddened and their distance modulii are corrected to correspond to the mean RR Lyrae distance ($m - M = 18.79$ mag) in the left panel, and to our favoured model for Sgr II ($m - M = 19.32 \pm 0.03$ mag) in the right one. For the RR Lyrae distance, the features of Sgr II are well reproduced by the light green fiducials with a metallicity between -1.8 and -1.4 dex. The spectroscopic members shown as yellow diamonds also follow nicely the light green tracks. At the favoured model distance, the dark

blue, more metal-poor fiducials are a better description of the CMD of the satellite and its members. However, both the CaHK photometry and the spectroscopy (see section 4 and 5) show that Sgr II is very metal-poor ([Fe/H] ~ -2.3 dex). Therefore, the distance found from the RR Lyrae is clearly not that of Sgr II. A plausible origin for these two stars might just be the Sgr stream, as shown in section 6.

Another distance measurement based on RR Lyrae in the Sgr II field has recently been proposed by Joo et al. (2019, J19). Using their own method, they find a distance modulus of 19.03 ± 0.10 mag using five RR Lyrae. After investigations, we found three RR Lyrae in common between the catalog of S17 and J19. Only one of those is a RRab star with a reliable distance measurement in S17 of $m - M \sim 18.85$ mag. It appears that distance modulus inferences between the two catalogs do not agree with each other. One of the source of disagreement could lie in the extinction used, which is twice as large in the catalog of S17. This issue is also raised by J19. Repeating the CMD and structural analysis with this $m - M$ also yields compatible results in terms of size and luminosity, while the satellite is found older is this case (13.5 ± 0.5 Gyr). Nonetheless, reproducing Figure 4 with this other distance modulus measurement still does not reproduce the different features of the CMD of Sgr II well, especially the BHB. We therefore favour our distance modulus inference for the rest of this work.
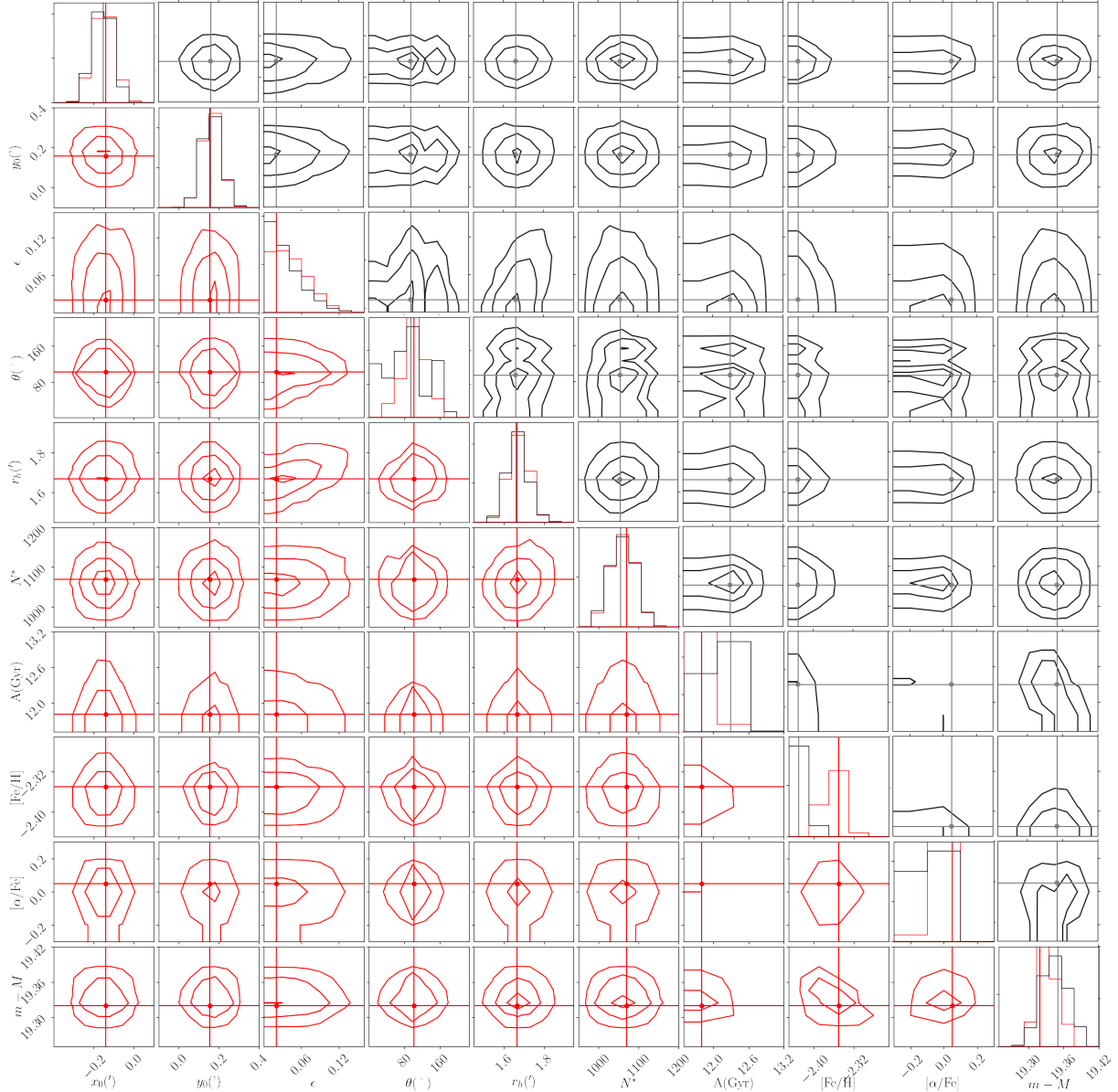
Figure 3. One and two-dimensional PDFs of the structural and CMD properties of Sgr II, inferred using the method described in section 3.1. Red lines correspond to the favoured inference, using both the distance prior based on BHBs and the metallicity prior from the spectroscopy, while the black contours show the case without any prior. These contours are defined as the usual 1, 2 and 3σ confidence intervals in the 2D, gaussian case. This figure shows that using the distance and metallicity priors has a limited impact on our final results. The structural properties remains unchanged in both cases and indicates that Sgr II is spherical with a half-light radius of ~ 1.7 arcminutes. The CMD properties are consistent and show that the satellite is old, metal-poor, and more distant than previously estimated by Laevens et al. (2015a) (~ 73.1 kpc).

3.2 Luminosity

The luminosity, absolute magnitude, and surface brightness of Sgr II are derived using the formalism of Martin et al. (2016a). The first step consists in drawing a set of parameters denoted j from the final multi-dimensional PDF obtained through the analysis of section 3.1. These parameters are the number of stars N_j^*, an age A_j, the metallicity

$[Fe/H]_j^{CMD}$, the alpha abundance ratio $[\alpha/Fe]_j$, and the distance modulus $(m - M)_j$. A CMD of the j-th stellar population is then simulated. For each simulated star, we ensure that its location in the colour-magnitude diagram falls in the CMD box used to perform the structural and CMD fit ($-0.2 < g_0 - i_0 < 1.2$ and $17.0 < g_0 < 25.0$). Furthermore, a completeness test is performed: the completeness of
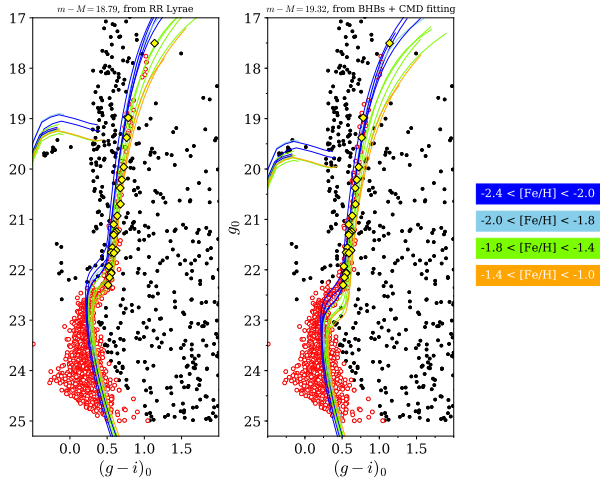
Figure 4. CMDs within two half-light radii of Sgr II overplotted with the fiducials of MW globular clusters from Bernard et al. (2014) shifted at two different distance modulii, the one inferred from the RR Lyrae in the field ($m - M = 18.79$ mag) on the left, and from the BHBs and CMD fitting on the right ($m-M = 19.32$ mag). Stars with a Sgr II membership probability greater than ten per cent from the broadband photometry analysis are shown as red circles. Spectroscopically confirmed members of Sgr II are shown as yellow diamonds. The fiducials are separated in metallicity bins, from the most metal-poor in dark blue to the most metal-rich available in orange.

the survey is first estimated at the colour and magnitude of the simulated star. Then, two random numbers a and b between 0 and 1 are drawn: if the completenesses of the star in both g and i is greater than these numbers, it is flagged. When the number of flagged stars reaches N_j^*, the fluxes of all simulated stars, flagged or not, are summed, which gives the luminosity L_j of the satellite for the j-th iteration. This procedure is repeated a thousand times in order to correctly sample the PDFs.

The 1D marginalised PDFs of Sgr II's luminosity and absolute magnitude M_V are represented in Figure 5. The final favoured parameters are reported in Table 1. The luminosity of the satellite is inferred to be $\log(L_V) = 4.2 \pm 0.1$. This measurement is in agreement with both L15 and M18 ($\log(L_V) = 4.1 \pm 0.1$). Finally, we obtain a surface brightness of $S_0 = 24.7 \pm 0.2$ mag arcsec^{-2}.

4 NARROW-BAND CAHK PHOTOMETRY ANALYSIS

Our CaHK photometry is provided by the Pristine Survey that uses a narrow-band filter centred on the metallicity-sensitive Calcium H&K doublet lines. Therefore, the flux received in this filter depends on the metallicity of the observed stars. By combining the $CaHK_0$ magnitudes with the broadband g_0 and i_0 photometry, the photometric metallicity of each star can be estimated. More details on the Pristine survey and the model used to transform $(CaHK_0, g_0, i_0)$ into a photometric metallicity can be found in Starkenburg et al. (2017). Pristine observations are shallower than our
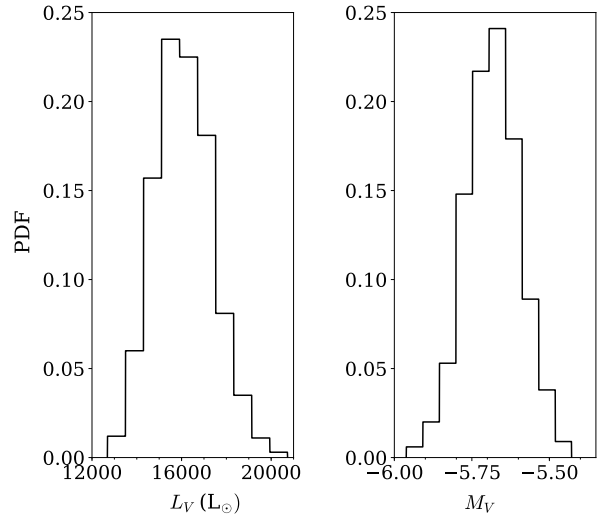
Figure 5. PDFs of the Sgr II luminosity and absolute magnitude. The favoured luminosity of the satellite is $log(L_V) = 4.2 \pm 0.1$, corresponding to an absolute magnitude of $M_V = -5.7 \pm 0.1$ mag.
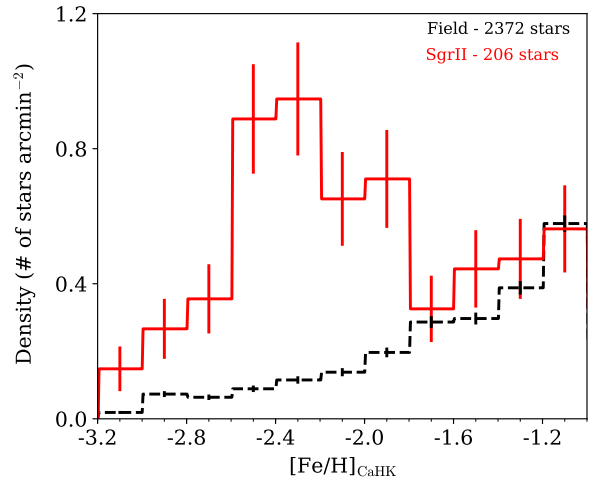
Figure 6. Normalised distribution of Pristine photometric metallicities for all stars within $2r_h$ (solid red line). The same histogram is also shown for all field stars, i.e. stars outside $5r_h$ (black dashed line). Sgr II clearly peaks at [Fe/H]$_{CaHK} \sim -2.3$ dex, while no such overdensity exists for the field distribution.

broadband g and i photometry (right panel of Figure 2) and therefore can only be used to estimate the photometric metallicity [Fe/H]$_{CaHK}$ of stars in our field down to $g_0 \sim 23$ mag. This limit corresponds to a $CaHK$ photometric uncertainty of ~ 0.1 mag. Above this value, the resulting photometric metallicities are less reliable.

Starkenburg et al. (2017) shows that the Pristine metallicities are slightly biased low as we go toward the metal-poor end of the calibration model. Therefore, we repeat the procedure presented in L18 and we first correct for this effect

by binning in metallicity the sample used by Starkenburg et al. (2017), which provides both the SDSS spectroscopic metallicity and the Pristine photometric metallicity for several thousands stars. For each bin, the median difference between the SDSS and Pristine metallicities is computed. This procedure yields the bias as a function of the photometric metallicity, which is used to correct our whole Sgr II metallicity catalog. All stars with $[\text{Fe/H}]_{\text{CaHK}} < -4.0$ or $[\text{Fe/H}]_{\text{CaHK}} > -1.0$ are discarded as our Pristine model is not reliable for those stars (Youakim et al. 2017). This choice does not affect the analysis as the systemic metallicity of Sgr II is well within this range. Stars with a large uncertainty in the $CaHK$ photometry ($\delta_{\text{CaHK}} > 0.1$) are rejected. All remaining stars within $2r_h$ are selected and their photometric metallicity distribution function (MDF) is shown in Figure 6 as the solid red line. The distribution of all field stars within $5r_h < r < 12r_h$ is shown as the black dashed line for comparison.

The red histogram of Sgr II stars stands out clearly in Figure 6, with a pronounced peak around $[\text{Fe/H}]_{\text{CaHK}} \sim -2.3$ dex that does not exist in the MDF of the field stars in black. To derive Sgr II's metallicity properties, we assume that the population present inside 2r_h (corresponding to 206 stars) in Figure 6 can be modelled as the sum of the foreground MDF and a normally distributed photometric metallicity population associated with Sgr II stars. This assumption seems legitimate as the metallicity distribution at the metal-rich end of the red histogram in Figure 6 overlaps well with the black distribution, thus implying that the underlying foreground contamination MDF is comparable over the field of view.

The Sgr II stellar population metallicity distribution is assumed to be normally distributed, with a mean $[\text{Fe/H}]_{\text{CaHK}}^{\text{SgrII}}$ and a standard deviation of $\sigma = \sqrt{(\delta[Fe/H]_k^{\text{CaHK}})^2 + (\sigma_{[\text{Fe/H}]}^{\text{CaHK}})^2}$, for which $\sigma_{[\text{Fe/H}]}^{\text{CaHK}}$ is the intrinsic metallicity dispersion of Sgr II and $\delta[Fe/H]_k^{\text{CaHK}}$ the uncertainty on the photometric metallicity of the k-th star. The likelihood model for the MW contaminating stars is built by interpolating the $[\text{Fe/H}]_{\text{CaHK}}$ MDF of all stars outside 5r_h. This model is then smoothed by a gaussian kernel of 0.2 dex to account for poor statistics in some metallicity bins. The fit is performed through the same MCMC algorithm used previously, and we marginalise over the foreground contamination model. At each iteration, we randomly draw a photometric metallicity for all stars in the contamination subsample. To do so, we assume that the value of $[\text{Fe/H}]_{\text{CaHK}}$ given by the Pristine pipeline is the mean of a normal distribution, for which the uncertainty on this value, $\delta[Fe/H]^{\text{CaHK}}$, is the standard deviation. At each iteration, a new photometric metallicity is then generated for each star in the foreground contamination, thereby accounting for the uncertainty on $[\text{Fe/H}]_{\text{CaHK}}$. Then, the procedure to build the foreground contamination model described above is repeated. In doing so, the analysis takes into account the overall uncertainty of the field MDF.

The 39, 88 and 95 % volume intervals on the final 2D posterior PDF, corresponding to the 1,2 and 3σ confidence levels for the 2D gaussian case, are shown as black solid lines in Figure 7. We measure a significant, non-zero metallicity spread in Sgr II, with $\sigma_{[\text{Fe/H}]}^{\text{sgr}} = 0.11_{-0.03}^{+0.05}$ dex and find it to be particularly metal-poor ($[\text{Fe/H}]_{\text{CaHK}}^{\text{SgrII}} = -2.32 \pm 0.04$ dex),
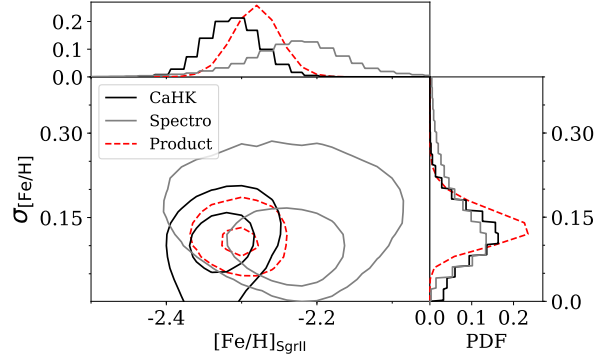
Figure 7. Two-dimensional joint PDFs of the systemic metallicity and dispersion for Sgr II using the photometric CaHK metallicities (black) and the individual spectroscopic metallicities of member stars (grey). These two independent measurements are combined to give the final PDF shown as the dashed red line. The contours represent the 39, 88 and 95 % volume intervals. The associated one-dimensional marginalised PDFs for all cases are shown in the upper and right panels. Both methods are in agreement and shows that Sgr II has a small but measurable metallicity dispersion.

in agreement with the stellar population inferred through the CMD fitting. To ensure that this inference is not caused by any systematic effect, the same analysis was done in L18 with two metal-poor globular clusters in the Pristine footprint, M92 and M15. The systemic metallicities of both clusters were found to be compatible with their previous estimates using spectroscopic data. Furthermore, their metallicity dispersions were unresolved, in agreement with previous studies, showing that the technique does not seem to be affected by a systematic effect.

5 SPECTROSCOPIC ANALYSIS

5.1 Velocity properties

The systemic velocity and velocity dispersion are derived using the deep spectroscopic observations of the system, by following the procedure detailed in section 2.2. The heliocentric velocity distributions of each individual mask are shown in the top three panels of Figure 8. The three spectroscopic runs are combined to obtain the global velocity distribution shown in the fourth panel. Figure 8 only shows the stars with a velocity between -400 and $0\,\text{km s}^{-1}$ in order to have a clearer histogram in the velocity range of interest. For this reason, only 67 stars are shown in the fourth panel of the figure, but the full spectroscopic sample contains 118 stars in total. We present the radial distance of each star with respect to their radial velocities in Figure 9 and the full dataset is detailed in Table 2.

The velocity peak of Sgr II stands out at around $-177\,\text{km s}^{-1}$ while contaminating MW stars are distributed sparsely all over the velocity space and can be located in the vicinity of the Sgr II velocity peak. Because of the small number of stars in the Sgr II population, the velocity properties can be polluted by the contamination. Ideally, those
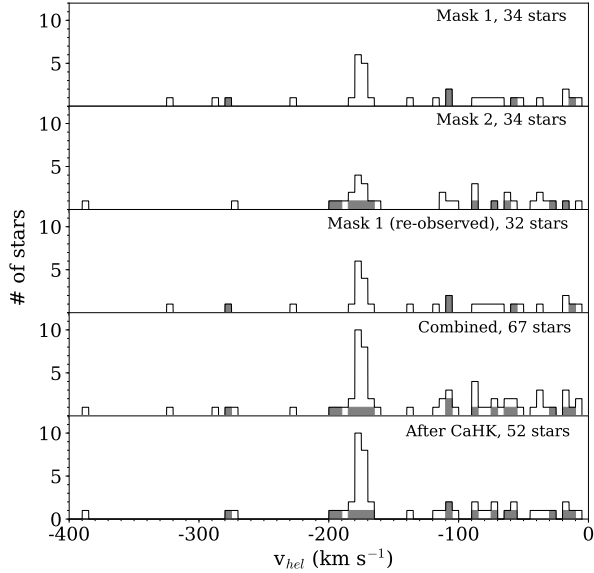
Figure 8. Heliocentric velocity histograms for the three spectroscopic samples, only for stars with a radial velocity between -400 and $0\,\mathrm{km\,s^{-1}}$. The fourth panel shows the merging of all samples. The total number of stars in each mask is indicated in the top right corner of each panel. Two stars from mask 1 have large velocity uncertainties in the re-observation of mask 1 and were therefore discarded. Therefore, although the third panel represents a re-observation of mask 1, it does not have the same number of stars presented here. The grey histograms show the number of stars with a non-reliable photometric metallicity measurement in our sample that therefore cannot be filtered out by our technique. The peak of Sgr II stars around $-177\,\mathrm{km\,s^{-1}}$ is pronounced and the disc contamination, from 0 to $-100\ \mathrm{km\,s^{-1}}$, is also quite populated. The last panel shows the final spectroscopic catalog. "Metal-rich" stars have been filtered out using photometric metallicities based on our CaHK photometry. For stars with reliable photometric metallicities, the ones with $-4.0 < [\mathrm{Fe/H}]_{\mathrm{CaHK}} < -1.6$, i.e. compatible with Sgr II metallicity properties measured in section 3 and 5, are selected, while the others are discarded. Stars with mediocre quality CaHK measurement or $[\mathrm{Fe/H}]_{\mathrm{CaHK}}$ uncertainties are not discarded as their $[\mathrm{Fe/H}]_{\mathrm{CaHK}}$ is not reliable. Among the 84 stars with reliable $[Fe/H]_{\mathrm{CaHK}}$ in the full spectroscopic sample of 118 stars, 50 are identified as part of the more metal-rich contamination and are therefore discarded.

stars would have to be identified and discarded from the spectroscopic sample. Sgr II is an old and metal-poor system, as suggested by its CMD and confirmed in section 3, 4, and 5, whereas stars from the contaminating foreground are expected to be more metal-rich overall. Therefore, the contaminating stars could be discarded based on their metallicities. Since the spectroscopic $[\mathrm{Fe/H}]$ can only be reliably measured for the brightest stars in our sample with S/N ≥ 12, the Pristine $CaHK$ photometric metallicities will be used to discriminate between the MW foreground stars and the Sgr II population.

The Pristine colour-colour diagram of Sgr II is shown in Figure 10. Field stars, i.e. a randomly selected sample of all stars outside five half-light radii, are represented as small black dots and form a clear stellar locus. This diagram is con-
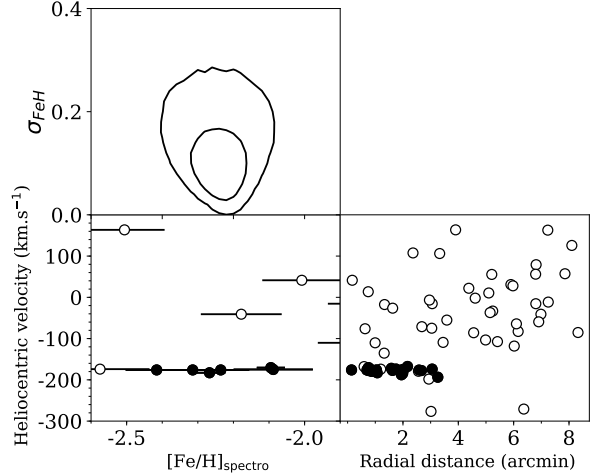
Figure 9. *Bottom right panel:* Radial distances to the center of Sgr II with respect to the heliocentric velocities. Open circles represent stars that are metal-poor using their photometric metallicities, or stars with non-reliable photometric metallicity measurements. Black-filled dots represent member stars. *Bottom left panel:* Spectroscopic metallicities with respect to the heliocentric velocities of all stars from the final spectroscopic data set with S/N $>= 12$. *Top panel:* Two-dimensional joint PDF of the systemic spectroscopic metallicity and metallicity dispersion. The contours represent the local 39%, 88% and 95% volume intervals. Sgr II comes out as a very metal-poor satellite, with $[\mathrm{Fe/H}]_{\mathrm{spectro}} = -2.23 \pm 0.05$ dex, and seems chemically enriched: $\sigma_{[\mathrm{Fe/H}]}^{\mathrm{spectro}} = 0.10^{+0.06}_{-0.04}$ dex.

structed so that the individual metallicity of a given star decreases from the bottom right to the top left. Stars observed with spectroscopy are colour-coded according to their heliocentric velocities, provided they have $\Delta[\mathrm{Fe/H}]_{\mathrm{CaHK}} < 0.5$ and $\delta_{\mathrm{CaHK}} < 0.1$. Stars that do not match these criteria are not discarded from the final spectroscopic sample because their photometric metallicity is too uncertain to be trusted. In section 4, we found that Sagittarius II has a systemic metallicity of $[\mathrm{Fe/H}]_{\mathrm{CaHK}}^{\mathrm{SgrII}} = -2.32 \pm 0.04$ dex and has a resolved metallicity dispersion. Therefore, within the subsample of stars that passed the CaHK photometry cuts discussed above, we choose to select only stars with $-4.0 < [\mathrm{Fe/H}]_{\mathrm{CaHK}} < -1.6$, as a Sgr II-like system would likely have a star formation history too short to produce significantly more metal-rich stars. The region of the diagram that corresponds to such a metallicity cut is represented by the two iso-metallicity green and red lines in Figure 10. Two cuts in $(g - i)_0$ are also applied in order to discard potential white dwarfs and metal-rich stars. The final spectroscopic velocity distribution is shown in the last panel of Figure 8. A significant number of MW stars with a reliable Pristine photometric metallicity measurements are cleaned out from the distribution as their metallicities are too high for them to be members of Sgr II, even if the satellite has a metallicity spread. In particular, one star in the immediate vicinity of the Sgr II velocity peak is identified as a more metal-rich contaminants using this technique ($[\mathrm{Fe/H}]_{\mathrm{CaHK}} = -1.11 \pm 0.25$ dex) and discarded.
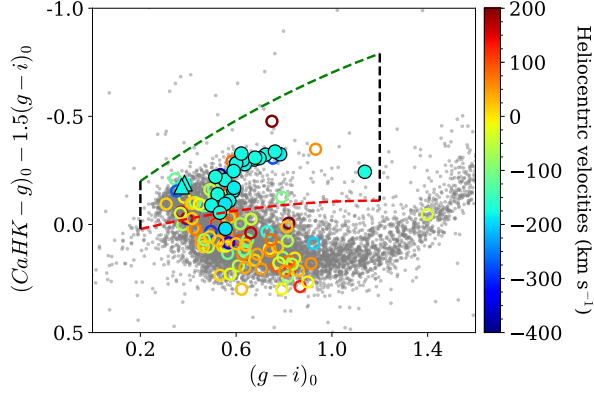
Figure 10. Pristine colour-colour diagram: the $(g-i)_0$ colour is represented on the x-axis, while the metallicity information is carried by the $(CaHK-g)_0 - 1.5*(g-i)_0$ colour on the y-axis. Grey dots stand for all field stars in a range between 5 and 8 half-light radii to Sgr II. Most of them are halo and disc stars and form a stellar locus of more metal-rich stars ($[Fe/H]_{CaHK}$ ~ 1 or above). Stars observed with spectroscopy are represented with circles colour-coded according to their heliocentric velocities. Among those, filled circles show the stars identified as spectroscopic members, while filled triangles stand for the HB stars in the spectroscopic data set. Above the grey stellar locus are located stars that become more and more metal-poor as we go towards the upper part of the diagram. Two iso-metallicity sequences are shown in red and green dashed lines, corresponding respectively to a photometric metallicity of $[Fe/H]_{CaHK} \sim -1.6$ and $[Fe/H]_{CaHK} \sim -4.0$. As expected, most of the stars in cyan, with a radial velocity compatible with Sgr II, are located in the metal-poor region enclaved by those two sequences. Hence, only stars within this region are selected for the final spectroscopic sample. Furthermore, we add a criterion on $(g-i)_0$ and discard all stars outside $0.2 < (g-i)_0 < 1.2$ in order to discard potential foreground white dwarfs.

The resulting velocity distribution is assumed to be the sum of three normally distributed populations: one for Sgr II stars, and two others corresponding to the MW foreground disc and halo stars. Each individual likelihood is weighted by its CMD and structural probability membership determined in section 5. One can write the individual likelihood of the k-th star as

$$\mathcal{L}(\langle v_{SgrII}\rangle, \sigma_v, \langle v_{MWd}\rangle, \sigma_{vd}, \langle v_{MWh}\rangle, \sigma_{vh}|\{v_{r,k}, \delta_{v,k}\}) = \quad (8)$$
$$\prod_k ((1 - \eta_{MWd} - \eta_{MWh})P_{mem}G(\{v_{r,k}\}|\langle v_{SgrII}\rangle, \sigma_v)$$
$$+ (1 - P_{mem})(\eta_{MWd}G(\{v_{r,k}\}|\langle v_{MWd}\rangle, \sigma_{vd})$$
$$+ \eta_{MWh}G(\{v_{r,k}\}|\langle v_{MWh}\rangle, \sigma_{vh}))),$$

with $\sigma_v = \sqrt{(\sigma_v^{SgrII})^2 + \delta_{v,k}^2 + \delta_{thr,i}}$ and $\delta_{v,k}$ the individual velocity uncertainty of the k-th star, σ_v^{SgrII} the intrinsic velocity dispersion, δ_{thr} the systematic threshold derived in section 2.2. $\langle v_{SgrII}\rangle$ is the systemic velocity of Sgr II. η_{MWd} and η_{MWh} are the fractions of stars respectively in the MW disc and halo populations. σ_{vd} is defined as $\sigma_{vd} = \sqrt{(\sigma_v^{MWd})^2 + \delta_{v,k}^2 + \delta_{thr,i}}$, with σ_v^{MWd} the intrinsic velocity dispersion of the disc population. The correspond-
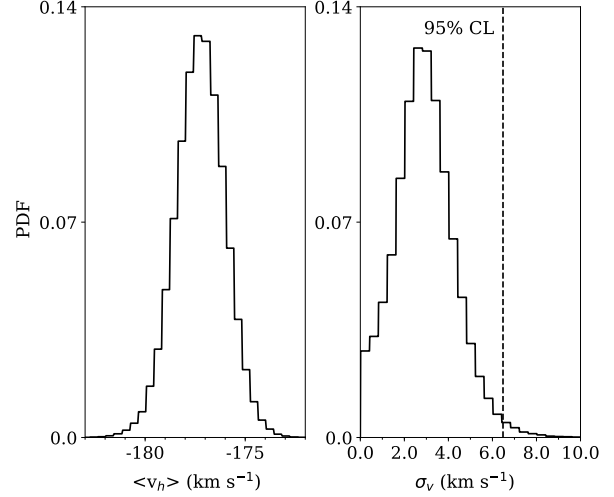
Figure 11. Marginalised PDFs for the systemic velocity (left) and its associated dispersion (right) for Sgr II. The satellite is found to be dynamically cold: the velocity dispersion is only marginally resolved: $\sigma_{vr} = 2.7^{+1.3}_{-1.0}$ km s^{-1}, reaching 6.5 km s^{-1} at the 95% confidence level.

ing quantity for the halo population is written σ_{vh}, while $\langle v_{MWd}\rangle$ is the systemic velocity of the disc population in the sample (resp. for the halo population). G is the usual one-dimensional normal distribution. We run a MCMC analysis and show the resulting marginalised 1D PDFs in Figure 11. At each iteration of the MCMC, the systematic threshold δ_{thr} is randomly drawn from its PDF. The favoured systemic velocity is $\langle v_{SgrII}\rangle = -177.3 \pm 1.2$ km s^{-1}. The velocity dispersion of Sgr II is $\sigma_v^{SgrII} = 2.7^{+1.3}_{-1.0}$ km s^{-1}, reaching 6.5 km s^{-1} at the 95% confidence interval, thus showing that Sagittarius II is a dynamically cold satellite. A similar analysis was performed for the inner (r < 1 arcmin) and outer (r > 1 arcmin) regions and no statistical difference was found in terms of velocity dispersion, with $\sigma_v^{inner} = 2.1^{+1.6}_{-1.4}$ km s^{-1} and $\sigma_v^{outer} = 2.9^{+2.1}_{-1.4}$ km s^{-1}. Using these inferences as well and taking into account the CMD and spatial models derived in section 3, 21 stars are identified as members of Sgr II.

5.2 Metallicity properties

To infer the metallicity properties of Sgr II from the spectroscopy, we create a subsample constituted of stars brighter than $i_0 = 20.5$ and a S/N ratio above 12 from our final spectroscopic sample, for a total of 26 stars. The spectroscopic metallicity is estimated using the calibration from Starkenburg et al. (2010) based on the Ca triplet. This method is originally calibrated for RGB stars above the horizontal branch, however, Leaman et al. (2013) showed that it can applied to stars up to two magnitudes fainter (see also Carrera et al. 2013).

The spectroscopic metallicity uncertainties have two sources. The first one is the uncertainty on the measurements of the equivalent widths (EWs) of the Calcium triplet lines by our pipeline, and the second one is the uncertainty inherent to the calibration of Starkenburg et al. (2010). The

latter uses the EWs of the Calcium triplet and an absolute magnitude. For each star, we assume that the uncertainty on each EW is gaussian. Therefore, a value of each EW is drawn from a normal distribution, with a mean being the favoured EW inferred from our pipeline, and a standard deviation corresponding to its uncertainty. The photometric and distance modulus uncertainties are also folded in the uncertainty of the absolute magnitude M_I used in the calibration. These randomly drawn EWs and M_I are then used to compute a spectroscopic metallicity. We perform this task 10,000 times to obtain a PDF of the spectroscopic metallicity for each star, and derive from there the favoured $[Fe/H]_{spectro}$ and its uncertainties. Six out of these 26 stars have a membership probability greater than 90 per cent and are also dynamical members of Sgr II. Among those six stars, the lowest S/N is 17. They constitute our final sample to infer the systemic metallicity of the satellite. The other twenty are discarded. The individual spectroscopic metallicities are reported in Table 2 under "$[Fe/H]_{spectro}$". The distribution of spectroscopic metallicities with respect to the radial velocity is shown in the bottom left panel of Figure 9, and shows the existence of a clump of stars at around $[Fe/H]_{spectro} \sim -2.3$ dex at the velocity of Sgr II.

To derive the systemic metallicity and metallicity dispersion of Sgr II, we assume that the spectroscopic metallicities of Sgr II stars are normally distributed and weigh each star with its CMD and structural probability membership, giving the following likelihood function:

$$\mathcal{L}(\langle[Fe/H]_{spectro}\rangle, \sigma_{[Fe/H]} | \{[Fe/H]_{spectro,k}, \delta_{[Fe/H],k}) = \quad (9)$$
$$P_{mem} \, G([Fe/H]_{spectro,k}, \delta_{[Fe/H],k} | \langle[Fe/H]_{spectro}\rangle, \sigma_{[Fe/H]}\}),$$

with $\sigma_{[Fe/H]} = \sqrt{\delta_{[Fe/H],k}^2 + (\sigma_{[Fe/H]}^{sgr})^2}$, $\delta_{[Fe/H],k}$ the individual uncertainty on the spectroscopic metallicity of the k-th star, and $\sigma_{[Fe/H]}^{sgr}$ the intrinsic metallicity dispersion of Sgr II. The 39, 88 and and 95 % volume intervals are represented by black solid lines on the resulting 2D PDFs in the top-left panel of Figure 9. Sgr II is confirmed to be metal-poor, with $[Fe/H]_{spectro}^{SgrII}$ = -2.23 ± 0.05 dex. Moreover, we find a metallicity dispersion of $\sigma_{spectro}^{[Fe/H]} = 0.10^{+0.06}_{-0.04}$ dex. This spread in metallicity is driven by the two brightest stars identified as members of Sgr II, for which the spectroscopic metallicity is accurately measured. They have a spectroscopic metallicity of -2.27 ± 0.04 dex and -2.10 ± 0.04 dex, respectively. Furthermore, since they are among the stars that were observed multiple times in our catalog, it is possible to infer their individual spectroscopic metallicities using the Ca triplet equivalent widths of each run separately. For both stars, the metallicities obtained from each spectroscopic run in which they were observed are consistent. The first star has been observed three times, with metallicity measurements of $[Fe/H]_{spectro}^1 = -2.36 \pm 0.07$, $[Fe/H]_{spectro}^2 = -2.25 \pm 0.08$ and $[Fe/H]_{spectro}^3 = -2.20 \pm 0.07$ dex. The second star has two metallicity measurements, $[Fe/H]_{spectro}^1 = -2.14 \pm 0.06$ and $[Fe/H]_{spectro}^2 = -2.05 \pm 0.06$ dex. This suggests that their final $[Fe/H]$ are not driven by one spurious equivalent widths measurement in one of the three spectroscopic samples. In addition with being consistent with the CMD of Sgr II and its systemic velocity, the two stars are also remarkably compatible with the satellite's proper motion
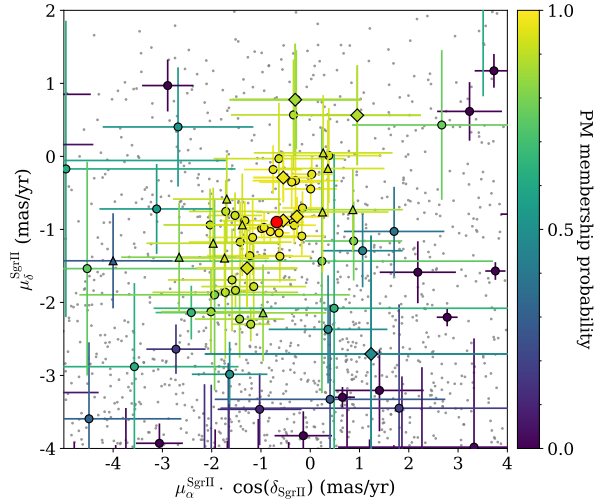
Figure 12. Distribution of the proper motions of MW contaminating stars in small grey dots, and our Sgr II-like population shown with dots colour-coded according to their proper motion membership probability, derived from a gaussian mixture model. The seven Sgr II members with a proper motion measurement in *Gaia* are represented with diamonds and the twelve HB stars with triangles. The systemic proper motion of Sgr II ($\mu_\alpha^* = -0.65^{+0.08}_{-0.10}$ mas.yr^{-1}, $\mu_\delta = -0.88 \pm 0.12$ mas.yr^{-1}) is represented with a large red dot.

inferred in section 6. Taken all together, we favour the fact that these two stars are indeed members of Sgr II, and that there is a spread in metallicity in the system.

The two independent measurements of the metallicity and dispersion of the satellite, using the $CaHK$ observations on the one hand and the spectra on the other are perfectly compatible. The results of both methods are then combined into one single measurement by performing the product of the two 2D joint PDFs. We show the corresponding 39, 88 and 95 % volume intervals as red thick line in Figure 7. This final measurement yields a systemic metallicity of $[Fe/H]_{SgrII}$ = -2.28 ± 0.03 dex and a metallicity dispersion of $\sigma_{[Fe/H]}^{SgrII} = 0.12^{+0.03}_{-0.02}$ dex.

6   *GAIA* DR2 PROPER MOTIONS AND ORBIT

To infer the orbit of Sgr II, we first build a sample of possible Sgr II stars based on the mask shown in the right panel of Figure 2. The proper motions of those stars are retrieved from the *Gaia* Data Release 2 (Gaia Collaboration et al. 2018a). All member stars identified as members from our spectroscopy and bright enough to have a proper motion measurement in *Gaia* are naturally present in this sample. Furthermore, the *Gaia* DR2 data are also cross-matched with the potential HB stars within two half-light radii of the satellite. Twelve HB stars have a proper motion measurement in *Gaia* and are added to the sample shown in Figure 12.
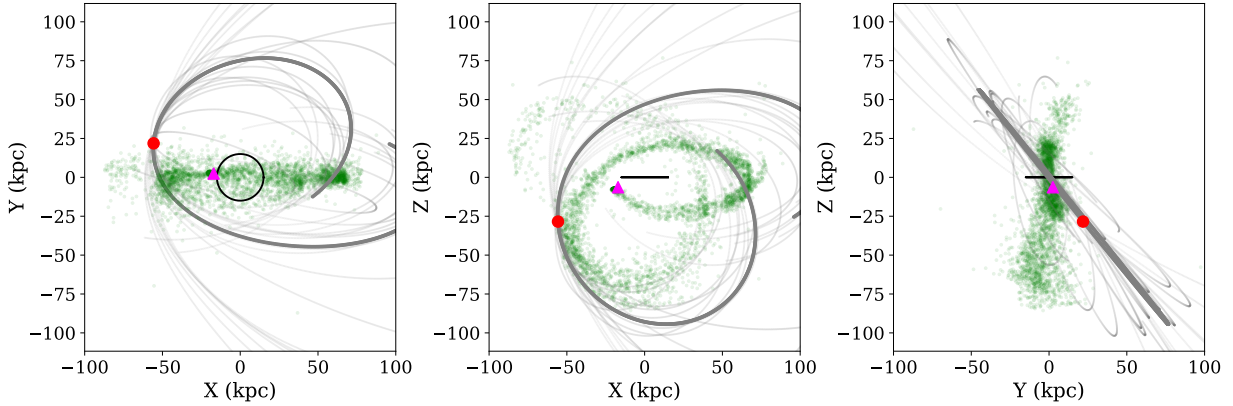
Figure 13. Projections of the orbit of Sgr II on the X-Y, X-Z and Y-Z planes backwards and forwards over 2.0 Gyr. Twenty-one orbits are shown here: the one based on the favoured position, distance, radial velocity and PMs of the satellite (as the thick, darker grey line), and twenty others using random realisations of those parameters (as thin, slightly transparent grey lines). The red circle is the current position of Sgr II, while the magenta triangle is the one of the Sgr dSph. A N-body simulation of the trailing arm of the Sgr stream (Law & Majewski 2010) is shown in green. The MW disk is shown in black, with a chosen radius of 15 kpc.

The inference of the Sgr II proper motion is performed through a gaussian mixture model. We assume that the sample can be modelled by the sum of two bivariate gaussians: one for the Sgr II population and another for the foreground MW contamination. The sets of parameters inferred from the analysis are composed of the proper motions in both directions, their dispersions and correlation c, for Sgr II ($\mathcal{P}_{\mathrm{SgrII}} = \langle\mu^*_{\alpha,\mathrm{SgrII}}\rangle, \langle\mu_{\delta,\mathrm{SgrII}}\rangle, \sigma_1, \sigma_2, c_{\mathrm{SgrII}}$) and for the contamination ($\mathcal{P}_{\mathrm{MW}} = \langle\mu^*_{\alpha,\mathrm{MW}}\rangle, \langle\mu_{\delta,\mathrm{MW}}\rangle, \sigma_3, \sigma_4, c_{\mathrm{MW}}$). The proper motion properties of the k-th star are defined as $\vec{d_k} = \{\mu^*_{\alpha,k}, \mu_{\delta,k}, \delta\mu^*_{\alpha,k}, \delta\mu_{\delta,k}\}$ with $\delta\mu^*_{\alpha,k}$ the uncertainty on the proper motion in the RA direction (respectively the DEC direction). The likelihood of the k-th star is

$$\mathcal{L}(\mathcal{P}_{\mathrm{SgrII}}, \mathcal{P}_{\mathrm{MW}}|\vec{d_k}) = \prod_k \eta P_{mem} \mathcal{M}_{\mathcal{G}}(\vec{d_k}|\mathcal{P}_{\mathrm{SgrII}}, \mathcal{P}_{\mathrm{MW}}) \quad (10)$$

$$+ (1-\eta)(1-P_{mem})\mathcal{M}_{\mathcal{G}}(\vec{d_k}|\mathcal{P}_{\mathrm{SgrII}}, \mathcal{P}_{\mathrm{MW}}),$$

where $\mathcal{M}_{\mathcal{G}}$ is a two-dimensional gaussian and η the fraction of Sgr II stars in the sample.

The gaussian mixture model gives a systemic proper motion of $\mu^{*,\mathrm{SgrII}}_{\alpha} = -0.65^{+0.08}_{-0.10}$ mas yr^{-1} and $\mu^{\mathrm{SgrII}}_{\delta} = -0.88 \pm 0.12$ mas yr^{-1} for Sgr II. These proper motions take into account the systematic error derived by Gaia Collaboration et al. (2018b). We also inferred the proper motion of the system using the HB and spectroscopic member stars only, and found a compatible result with $(\mu^*_{\alpha}, \mu_{\delta}) = (-0.55 \pm 0.13, -0.80 \pm 0.08)$ mas yr^{-1}.

Our estimate is discrepant from the one of Massari & Helmi (2018) who find a proper motion of $(\mu^*_{\alpha}, \mu_{\delta}) = (-1.18 \pm 0.14, -1.14 \pm 0.11)$ mas yr^{-1}. They rely on the convergence of the astrometric parameters through a 2.5σ clipping procedure, with an initial guess on those parameters based on the potential HB stars of Sgr II. However, our measurement based only on HB and spectroscopic member stars gives credit to the proper motion found in our work, and disfavours the estimate of the work of Massari & Helmi

(2018), which might be biased by the foreground contamination.

The orbit of the satellite can then be inferred using the GALPY package (Bovy 2015). The MW potential chosen to integrate the orbit is a modified "MWPotential14" constituted of three main components: a power-law, exponentially cut-off bulge, a Miyamoto-Nagai Disc, and a NFW DM halo with a virial mass of $1.2 \times 10^{12}\,\mathrm{M}_{\odot}$. Further details about this MW potential model can be found in Bovy (2015). We integrate 2000 orbits backwards and forwards, each time by randomly drawing a position, distance, radial velocity and proper motions from their respective PDFs, and extract for each realisation the pericenter, apocenter, and ellipticity of the orbit, integrated over 2 Gyr. The favoured orbit (i.e. the favoured position, distance, radial velocity, and proper motions) is shown in Figure 13 in the X–Y, X–Z, and Y–Z planes, along with the stream from the Sgr dwarf galaxy. Twenty other random realisations of Sgr II orbits are also shown in grey, partially transparent lines.

The analysis yields a pericenter of $54.8^{+3.3}_{-6.1}$ kpc, an apocenter of $118.4^{+28.4}_{-23.7}$ kpc and an orbital ellipticity of 0.44 ± 0.01. Moreover, Figure 13 shows that the orbit of Sgr II is compatible with the trailing arm of the Sgr stream, despite being slightly tilted from it, especially in the Y direction.

7 DISCUSSION

We used deep MegaCam broadband photometry, data from the narrow-band $CaHK$ Pristine survey, and DEIMOS spectroscopy to conduct a thorough study of the Milky Way satellite Sgr II. By performing a CMD and structural analysis, the satellite is found to have a half-light radius of $35.5^{+1.4}_{-1.2}$ pc, and is located at a distance of $73.1^{+1.1}_{-0.7}$ kpc based on the combination of BHB stars distances and a CMD fitting procedure. The favoured stellar population is old (12.0 ± 0.5 Gyr) and metal-poor. Using our spectroscopic
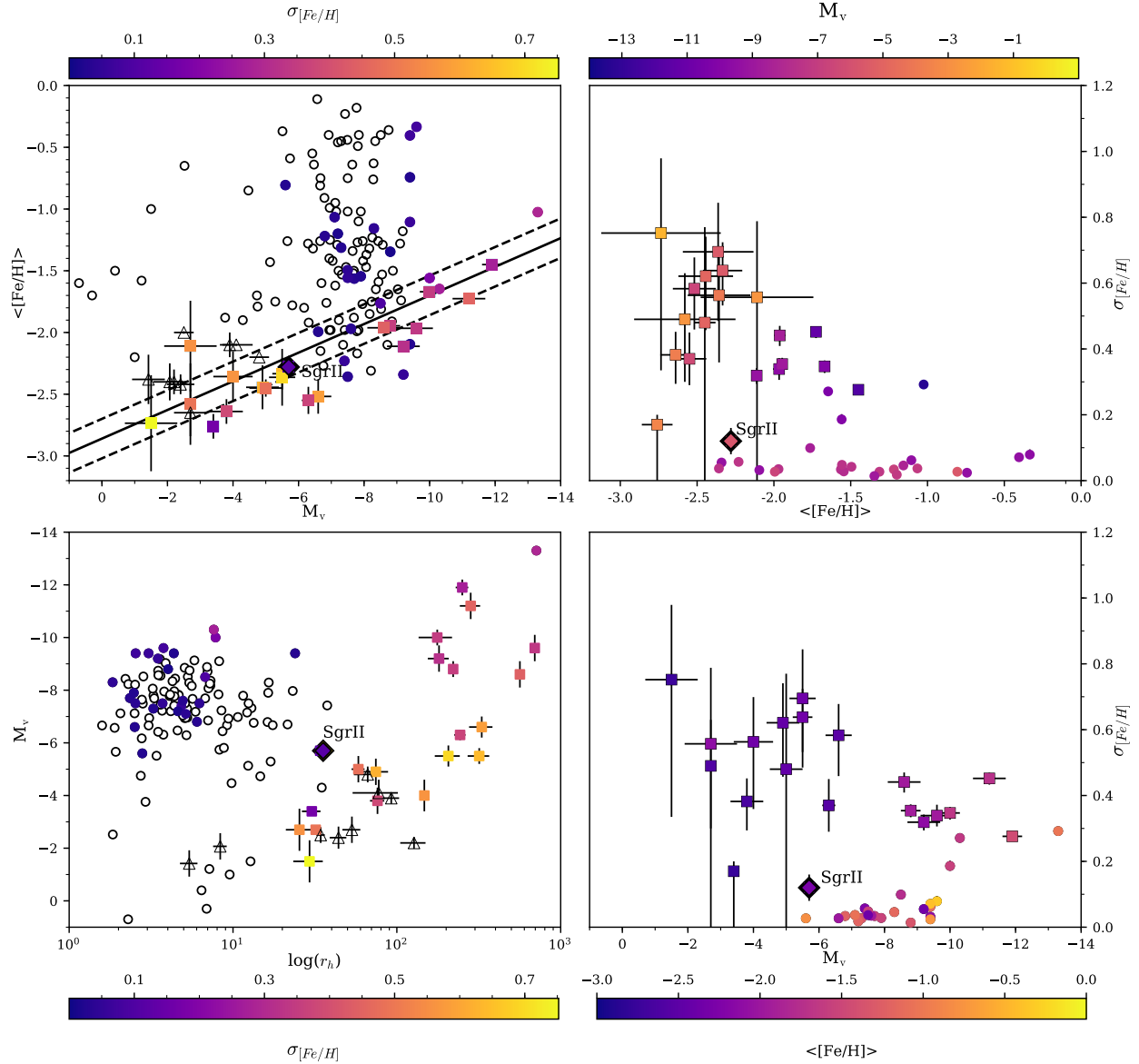
Figure 14. Comparison of Sgr II with other GCs and dwarf galaxies of the Milky Way. Squares represent dwarf galaxies while circles represent globular clusters, and the diamond corresponds to Sgr II. Triangles stand for recently discovered dwarf-galaxy candidates that await confirmation. Hollow markers correspond to systems for which no metallicity dispersion measurement can be found in the literature. The solid line in the top-left panel corresponds to the luminosity-metallicity relation of Kirby et al. (2013) for dwarf spheroidals and dwarf irregulars. Dashed lines represent the RMS about this relation, also taken from Kirby et al. (2013). Among the 123 globular clusters presented here, the properties of 116 were extracted from Harris (1996) catalog, revised in 2010. For the remaining ones (Kim 1, Kim 2, Kim 3, Laevens 1, Balbinot 1, Munoz 1 and SMASH 1) parameters of the discovery publications were used (Kim & Jerjen (2015), Kim et al. (2015), Kim et al. (2016), Laevens et al. (2014), Balbinot et al. (2013), Muñoz et al. (2012) and Martin et al. (2016b)). Globular cluster metallicity spread measurements are taken from Willman & Strader (2012) and references therein: Carretta et al. (2006, 2007, 2009, 2011), Cohen et al. (2010), Gratton et al. (2007), Johnson & Pilachowski (2010), and Marino et al. (2011). McConnachie (2012) and Willman & Strader (2012) are used to compile the properties of the dwarf galaxies represented here. The 18 dwarf galaxies represented here are: Bootes I (Belokurov et al. 2006; Norris et al. 2010), Canes Venatici I (Zucker et al. 2006b), Canes Venatici II (Sakamoto & Hasegawa 2006), Coma Berinices, Hercules, Leo IV and Segue I (Belokurov et al. 2007), Draco and Ursa Minor (Wilson 1955), Fornax (Shapley 1938b), Leo I and Leo II (Harrington & Wilson 1950), Pisces II (Belokurov et al. 2010), Sculptor (Shapley 1938a), Sextans (Irwin et al. 1990), Ursa Major I (Willman et al. 2005b), Ursa Major II (Zucker et al. 2006a), Willman I (Willman et al. 2005a). Their metallicity and metallicity spreads were drawn from Kirby et al. (2008), Kirby et al. (2010), Norris et al. (2010) and Willman et al. (2011). The dwarf galaxy candidates discovered recently and shown on this figure are Bootes II (Koch & Rich 2014), DES1 (Luque et al. 2016; Conn et al. 2018), Eridanus III (Bechtol et al. 2015; Conn et al. 2018; Koposov et al. 2015b), Hyades II (Martin et al. 2015), Pegasus III (Kim & Jerjen 2015), Reticulum II and Horologium I (Koposov et al. 2015a), Segue II (Belokurov et al. 2009), and the most significant candidates of Drlica-Wagner et al. (2015): Gru II, Tuc III, and Tuc IV.

catalog, we are able to find the systemic velocity of Sgr II to be $\langle v_{\text{SgrII}} \rangle = -177.3 \pm 1.3$ km s^{-1}. The velocity dispersion yields $\sigma_{\text{v}}^{\text{sgr}} = 2.7^{+1.3}_{-1.0}$ km s^{-1} and is smaller than 6.5 km s^{-1} at the 95% confidence interval. From the spectroscopic analysis, 21 stars are identified as members of the satellite and reported in Table 2. The individual photometric metallicities provided by the Pristine survey are used to show that Sgr II is a very metal-poor system, with $[\text{Fe/H}]^{\text{SgrII}}_{\text{CaHK}} = -2.32 \pm 0.04$ dex, and has a small but resolved metallicity dispersion: $\sigma^{\text{CaHK}}_{[\text{Fe/H}]} = 0.11^{+0.05}_{-0.03}$ dex. These two chemical properties are perfectly supported by our spectroscopic analysis of six RGB stars. We applied the Ca triplet calibration from Starkenburg et al. (2010) to member stars to derive the spectroscopic metallicity of Sgr II and its associated dispersion: $[\text{Fe/H}]^{\text{SgrII}}_{\text{spectro}} = -2.23 \pm -0.08$ dex and $\sigma^{\text{CaHK}}_{[\text{Fe/H}]} = 0.10^{+0.06}_{-0.04}$ dex. Combining the CaHK and spectroscopic measurements, we obtain refined estimates of both parameters: $[\text{Fe/H}]_{\text{SgrII}} = -2.28 \pm 0.04$ dex and $\sigma^{\text{SgrII}}_{[\text{Fe/H}]} = 0.12^{+0.03}_{-0.02}$ dex. Finally, using the *Gaia* DR2 data, the proper motion of Sgr II is inferred to be $(\mu^*_\alpha, \mu_\delta) = (-0.65^{+0.08}_{-0.10}, -0.88 \pm 0.12)$ mas yr^{-1}. This yields an apocenter and pericenter of $118.4^{+28.4}_{-23.7}$ and $54.8^{+3.3}_{-6.1}$ kpc respectively.

Sgr II is in perfect agreement with the luminosity-metallicity relation for dwarf galaxies (Kirby et al. 2013), as is shown in the top-left panel of Figure 14. Sgr II is however somewhat of an outlier in the $r_h - M_V$ plane (bottom-left panel of Figure 14), which led M18 to conclude that Sgr II is a globular cluster. However, the locus of dwarf galaxies in this plane becomes uncertain at low luminosities. The satellite is still more extended than the vast majority of MW globular clusters as shown in the bottom-left panel of Figure 14, although two of them have a comparable size: Crater (Belokurov et al. 2014; Laevens et al. 2014) and Terzan 5 (Terzan 1968). These two extended clusters do not, however, share the same metallicity properties as Sgr II: Terzan 5 is a bulge cluster with $[\text{Fe/H}] > -0.5$ and Crater is more metal-rich, with a systemic metallicity of $[\text{Fe/H}] \sim -1.65$ (Weisz et al. 2016). Our two estimates of the metallicity dispersion of Sgr II both yield similar results and suggest that the satellite was able to retain its gas and form successive generation of stars, thus suggesting the presence of a dark matter halo (Willman & Strader 2012). However, this result is driven by only two bright RGB stars that have significantly different metallicity measurements. If one of the two were misidentified as a Sgr II member, the claim of a metallicity dispersion would be weaker.

The question of the dynamical mass of Sgr II remains open. We can use the relation of Walker et al. (2009) to estimate the expected velocity dispersion of a purely baryonic system. Assuming a mass-to-light ratio of 2 for an old and metal-poor stellar population (McLaughlin & van der Marel 2005), Sgr II would have a velocity dispersion of ~ 1 km s^{-1}, which is not incompatible with our inference of $\sigma_{vr} = 2.7^{+1.3}_{-1.0}$ km s^{-1}. Nevertheless, taken at face value, our velocity dispersion measurement implies that Sgr II has a dynamical mass-to-light ratio of $23.0^{+32.8}_{-23.0}$ M$_\odot$ L$_\odot^{-1}$ and favours a slightly DM-dominated system under the usual assumption of dynamical equilibrium and sphericity. If this is confirmed, it would mean that Sgr II inhabits one of the lowest mass DM subhalos. Alternatively, this result could be driven by the compactness of the satellite, whose stars only probe the inner parts of the subhalo.

Taken together, these two pieces of evidence (marginally resolved metallicity dispersion and plausibly non-baryonic mass-to-light ratio) would indicate that Sgr II is more likely a dwarf galaxy rather than a cluster.

Before the submission of this work, a spectroscopic study of Sgr II was presented at the AAS iPoster[2] session (Simon et al. 2019). Using Magellan/IMACS spectroscopy, they found a systemic velocity and metallicity compatible to the ones in this work: $\langle v_r \rangle = -177.3 \pm 0.7$ km s^{-1} and $\langle [\text{Fe/H}] \rangle = -2.28$ dex. Their velocity dispersion is also consistent with ours: $\sigma_{vr} = 1.6 \pm 0.3$ km s^{-1}. Finally, the proper motion they derive for Sgr II $((\mu^*_\alpha, \mu_\delta) = (-0.63^{+0.08}_{-0.10}, -0.89 \pm 0.06)$ mas yr$^{-1})$ is also perfectly in agreement with our work. However, they estimate a very low metallicity dispersion, with $\sigma_{[\text{Fe/H}]} < 0.08$ dex at the 95 per cent confidence limit. Therefore, they conclude that the satellite is a globular cluster. Once the two data sets are made public, a thorough investigation is needed to understand the source of this discrepancy. Anyhow, it illustrates the difficulty of studying and understanding such faint systems.

Independently of the nature of Sgr II, the orbit we infer for the satellite is compatible with the trailing arm of the Sagittarius stream according to the model by Law & Majewski (2010) (Figure 13). However, we note that the agreement between the two orbits is not perfect and, in particular, that the position of Sgr II today and its favoured movement in the Y-Z galactocentric plane are slightly offset from the plane of the Sgr stream. Three hypotheses can be formulated to explain this discrepancy:

• The fact that the Sgr stream and the Sgr II orbits are compatible is purely coincidental.
• Sgr II is linked to the stream, and the discrepancy between Sgr II and the stream in the Y direction, if real, could be explained by the fact that Sgr dSph satellites were stripped first and with a different energy than that of stars represented in the simulation.
• Sgr II is linked to the stream and is also representative of its behaviour around the MW. No model is able to match all the observational constraints existing for the Sgr stream (Fardal et al. 2019) so the observed difference in the orbital plane of Sgr and Sgr II could suggest that the behaviour of the distant Sgr stream wrap that Sgr II would be associated to is not perfectly described by the Law & Majewski (2010) simulation.

If either the second or the third scenario is the valid one, it would mean that Sgr II is a new, exciting example of satellite of a satellite. Similarly to the Magellanic Clouds, the Sgr dSph would then have brought its own cohort of satellites that have now been deposited in the MW halo. Moreover, it would also bring some precious insights on the orbit of the Sgr stream in regions where it is poorly constrained.

---

[2] <https://aas233-aas.ipostersessions.com/default.aspx?s=E7-10-7C-92-5D-B1-84-24-1F-B5-07-1A-BF-2E-10-65>

REFERENCES

Balbinot E. et al., 2013, ApJ, 767, 101

Bechtol K. et al., 2015, ApJ, 807, 50

Belokurov V., Irwin M. J., Koposov S. E., Evans N. W., Gonzalez-Solares E., Metcalfe N., Shanks T., 2014, MNRAS, 441, 2124

Belokurov V. et al., 2010, ApJ, 712, L103

—, 2009, MNRAS, 397, 1748

—, 2007, ApJ, 654, 897

—, 2006, ApJ, 647, L111

Bernard E. J. et al., 2014, MNRAS, 442, 2999

Bertone G., Hooper D., Silk J., 2005, Phys. Rep., 405, 279

Boulade O. et al., 2003, 4841, 72

Bovy J., 2015, ApJSupp, 216, 29

Boylan-Kolchin M., Bullock J. S., Kaplinghat M., 2011, MNRAS, 415, L40

Bullock J. S., Boylan-Kolchin M., 2017, ARAA, 55, 343

Carrera R., Pancino E., Gallart C., del Pino A., 2013, MNRAS, 434, 1681

Carretta E., Bragaglia A., Gratton R. G., Leone F., Recio-Blanco A., Lucatello S., 2006, A&A, 450, 523

Carretta E. et al., 2009, A&A, 505, 117

—, 2007, A&A, 464, 967

Carretta E., Lucatello S., Gratton R. G., Bragaglia A., D'Orazi V., 2011, A&A, 533, A69

Chambers K. C. et al., 2016, arXiv:1612.05560

Cohen J. G., Kirby E. N., Simon J. D., Geha M., 2010, ApJ, 725, 288

Conn B. C., Jerjen H., Kim D., Schirmer M., 2018, ApJ, 852, 68

Deason A. J., Belokurov V., Evans N. W., 2011, MNRAS, 416, 2903

Dotter A., Chaboyer B., Jevremović D., Kostov V., Baron E., Ferguson J. W., 2008, ApJSupp, 178, 89

Drlica-Wagner A. et al., 2015, ApJ, 813, 109

Faber S. M. et al., 2003, 4841, 1657

Fardal M. A., van der Marel R. P., Law D. R., Sohn S. T., Sesar B., Hernitschek N., Rix H.-W., 2019, MNRAS, 483, 4724

Gaia Collaboration, Brown A. G. A., Vallenari A., Prusti T., de Bruijne J. H. J., Babusiaux C., Bailer-Jones C. A. L., 2018a, arXiv:1804.09365

Gaia Collaboration et al., 2018b, A&A, 616, A12

Geringer-Sameth A., Koushiappas S. M., Walker M., 2015, ApJ, 801, 74

Gratton R. G. et al., 2007, A&A, 464, 953

Harrington R. G., Wilson A. G., 1950, PASP, 62, 118

Harris W. E., 1996, AJ, 112, 1487

Hastings W. K., 1970, Biometrika, 97

Ibata R., Sollima A., Nipoti C., Bellazzini M., Chapman S. C., Dalessandro E., 2011, ApJ, 738, 186

Ibata R. A., Gilmore G., Irwin M. J., 1994, Nature, 370, 194

Irwin M., Lewis J., 2001, New Astronomy Review, 45, 105

Irwin M. J., Bunclark P. S., Bridgeland M. T., McMahon R. G., 1990, MNRAS, 244, 16P

Johnson C. I., Pilachowski C. A., 2010, ApJ, 722, 1373

Joo S.-J. et al., 2019, arXiv:1904.01599

Kim D., Jerjen H., 2015, ApJ, 799, 73

Kim D., Jerjen H., Mackey D., Da Costa G. S., Milone A. P., 2016, ApJ, 820, 119

Kim D., Jerjen H., Milone A. P., Mackey D., Da Costa G. S., 2015, ApJ, 803, 63

Kirby E. N., Cohen J. G., Guhathakurta P., Cheng L., Bullock J. S., Gallazzi A., 2013, ApJ, 779, 102

Kirby E. N. et al., 2010, ApJSupp, 191, 352

Kirby E. N., Simon J. D., Geha M., Guhathakurta P., Frebel A., 2008, ApJ, 685, L43

Koch A., Rich R. M., 2014, ApJ, 794, 89

Koposov S. E., Belokurov V., Torrealba G., Evans N. W., 2015a, ApJ, 805, 130

Koposov S. E. et al., 2015b, ApJ, 811, 62

—, 2011, ApJ, 736, 146

Koposov S. E., Yoo J., Rix H.-W., Weinberg D. H., Macciò A. V., Escudé J. M., 2009, ApJ, 696, 2179

Laevens B. P. M. et al., 2015a, ApJ, 813, 44

—, 2015b, ApJ, 802, L18

—, 2014, ApJ, 786, L3

Law D. R., Majewski S. R., 2010, ApJ, 714, 229

Leaman R. et al., 2013, ApJ, 767, 131

Longeard N. et al., 2018, MNRAS, 480, 2609

Luque E. et al., 2016, MNRAS, 458, 603

Marino A. F. et al., 2011, A&A, 532, A8

Martin N. F., Ibata R. A., Irwin M. J., Chapman S., Lewis G. F., Ferguson A. M. N., Tanvir N., McConnachie A. W., 2006, MNRAS, 371, 1983

Martin N. F. et al., 2016a, ApJ, 833, 167

—, 2016b, ApJ, 830, L10

—, 2015, ApJ, 804, L5

Massari D., Helmi A., 2018, A&A, 620, A155

Mateo M. L., 1998, ARAA, 36, 435

McConnachie A. W., 2012, AJ, 144, 4

McLaughlin D. E., van der Marel R. P., 2005, ApJSupp, 161, 304

Muñoz R. R., Geha M., Côté P., Vargas L. C., Santana F. A., Stetson P., Simon J. D., Djorgovski S. G., 2012, ApJ, 753, L15

Mutlu-Pakdil B. et al., 2018, ApJ, 863, 25

Navarro J. F. et al., 2010, MNRAS, 402, 21

Norris J. E., Wyse R. F. G., Gilmore G., Yong D., Frebel A., Wilkinson M. I., Belokurov V., Zucker D. B., 2010, ApJ, 723, 1632

Pawlowski M. S. et al., 2017, Astronomische Nachrichten, 338, 854

Pawlowski M. S., McGaugh S. S., Jerjen H., 2015, MNRAS, 453, 1047

Sakamoto T., Hasegawa T., 2006, ApJ, 653, L29

Schlafly E. F., Finkbeiner D. P., 2011, ApJ, 737, 103

Schlegel D. J., Finkbeiner D. P., Davis M., 1998, ApJ, 500, 525

Sesar B. et al., 2017, AJ, 153, 204

Shapley H., 1938a, Harvard College Observatory Bulletin, 908, 1

—, 1938b, Nature, 142, 715

Simon J., Fu S. W., Geha M., Kelson D. D., Alarcon Jara A. G., 2019, in American Astronomical Society Meeting Abstracts #233, American Astronomical Society Meeting Abstracts

Simon J. D., Geha M., 2007, ApJ, 670, 313

Starkenburg E. et al., 2010, A&A, 513, A34

—, 2017, MNRAS, 471, 2587

Terzan A., 1968, Academie des Sciences Paris Comptes Rendus Serie B Sciences Physiques, 267, 1245

Table 2. Properties of our spectroscopic sample. The Pristine metallicity of a given star is indicated only if $[\mathrm{Fe/H}]_{\mathrm{CaHK}} < -1.0$. The individual spectroscopic metallicity is reported for stars with S/N $>= 12$ and $g_0 > 20.5$ only. Stars with $P_{mem} > 0.8$ are systematically considered as members. Potential horizontal branch stars of Sgr II are marked as "HB" as the spectroscopic pipeline extracting the velocities is less reliable for those stars. Since our CMD fitting procedure described in section 4.1 does not account for the horizontal branch, their membership probability is not meaningful. Potential binary stars (as defined in section 2.2) are marked as "B". The systematic threshold δ_{thr} is not included in the velocity uncertainties presented in this table.

RA (deg)	DEC (deg)	g_0	i_0	$CaHK_0$	v_r (km s^{-1})	μ_α^* (mas.yr^{-1})	μ_δ (mas.yr^{-1})	S/N	$[\mathrm{Fe/H}]_{\mathrm{CaHK}}$	$[\mathrm{Fe/H}]_{\mathrm{spectro}}$	P_{mem}	Member
298.20599	−21.98790	18.53 ± 0.01	17.99 ± 0.01	19.44 ± 0.01	16.6 ± 1.3	2.949 ± 0.506	−6.861 ± 0.274	29.2	—	—	0.00	N
298.13158	−21.98583	19.00 ± 0.01	18.54 ± 0.01	19.77 ± 0.01	27.5 ± 1.5	−5.194 ± 0.738	−4.88 ± 0.384	22.5	—	—	0.00	N
298.13138	−21.98273	19.16 ± 0.01	18.50 ± 0.01	20.13 ± 0.01	−39.4 ± 2.2	0.336 ± 0.69	−7.317 ± 0.38	25.8	−1.39 ± 0.10	—	0.00	N
298.15508	−21.98054	19.34 ± 0.01	18.66 ± 0.01	20.52 ± 0.02	12.5 ± 1.7	1.159 ± 0.889	−8.058 ± 0.507	21.2	—	—	0.00	N
298.15097	−21.95283	19.46 ± 0.01	18.90 ± 0.01	20.39 ± 0.02	140.9 ± 1.7	−6.681 ± 1.002	0.739 ± 0.503	21.5	—	—	0.00	N
298.19072	−21.96758	19.88 ± 0.01	19.54 ± 0.01	20.19 ± 0.01	−118.1 ± 6.2	−0.867 ± 1.551	1.216 ± 0.81	14.4	−1.02 ± 0.15	−2.85 ± 0.23	0.00	N
298.18688	−21.97714	20.43 ± 0.01	19.87 ± 0.01	21.41 ± 0.03	−107.3 ± 2.8	−5.917 ± 2.251	−10.725 ± 1.175	12.6	−3.61 ± 0.17	−1.26 ± 0.13	0.00	N
298.18320	−21.96362	21.28 ± 0.01	20.73 ± 0.01	22.22 ± 0.06	−15.4 ± 3.5	— ± —	— ± —	5.6	—	—	0.30	N
298.13665	−21.97424	21.41 ± 0.01	20.90 ± 0.01	22.18 ± 0.06	−7.8 ± 7.4	— ± —	— ± —	4.7	−1.40 ± 0.30	—	0.04	N
298.19440	−21.99071	21.60 ± 0.01	21.22 ± 0.02	22.17 ± 0.06	−67.3 ± 3.8	— ± —	— ± —	3.9	−1.45 ± 0.35	—	0.00	N
298.19622	−21.93369	22.40 ± 0.02	21.66 ± 0.02	23.62 ± 0.18	−2.0 ± 13.4	— ± —	— ± —	2.8	−99.0 ± −99.0	—	0.00	N
298.16960	−22.17463	17.71 ± 0.01	16.94 ± 0.01	19.06 ± 0.01	89.7 ± 1.1	−3.409 ± 0.228	−5.191 ± 0.172	31.4	—	—	0.00	N
298.18001	−22.07175	17.90 ± 0.01	17.05 ± 0.01	19.32 ± 0.01	0.2 ± 0.9	1.896 ± 0.225	−7.431 ± 0.133	33.5	—	—	0.00	N
298.16810	−22.18830	18.27 ± 0.01	17.65 ± 0.01	19.27 ± 0.01	105.1 ± 1.3	−3.679 ± 0.287	−3.852 ± 0.18	37.2	−1.01 ± 0.11	—	0.00	N
298.19662	−22.14635	18.73 ± 0.01	18.31 ± 0.01	19.38 ± 0.01	29.2 ± 1.8	−0.708 ± 0.441	−4.393 ± 0.262	21.1	−1.30 ± 0.13	—	0.00	N
298.17484	−22.16606	18.82 ± 0.01	18.33 ± 0.01	19.65 ± 0.01	−54.0 ± 1.3	1.647 ± 0.507	−3.121 ± 0.37	27.6	—	—	0.00	N
298.19190	−22.19687	18.90 ± 0.01	18.34 ± 0.01	19.79 ± 0.01	65.8 ± 4.0	−1.137 ± 0.558	−3.422 ± 0.38	36.6	−1.15 ± 0.12	—	0.00	N
298.19827	−22.14498	18.94 ± 0.01	18.35 ± 0.01	19.77 ± 0.01	89.3 ± 1.3	−1.161 ± 0.478	−7.535 ± 0.281	25.3	−1.54 ± 0.13	—	0.00	N
298.16146	−22.08266	18.98 ± 0.01	18.20 ± 0.01	19.83 ± 0.01	−182.8 ± 0.9	−0.27 ± 0.46	−0.825 ± 0.269	26.3	−2.62 ± 0.13	−2.26 ± 0.04	0.98	Y
298.16120	−22.00829	19.04 ± 0.01	18.41 ± 0.01	20.13 ± 0.01	−85.1 ± 1.4	3.636 ± 0.626	−8.935 ± 0.343	26.7	—	—	0.00	N
298.15404	−22.11108	19.17 ± 0.01	18.71 ± 0.01	19.92 ± 0.01	51.4 ± 1.9	1.085 ± 0.593	−4.926 ± 0.335	17.5	−1.02 ± 0.15	—	0.00	N
298.15853	−22.05847	19.42 ± 0.01	18.93 ± 0.01	19.67 ± 0.01	−167.9 ± 9.5	0.865 ± 1.014	−0.73 ± 0.571	5.0	−99.0 ± −99.0	−0.44 ± 0.27	0.00	HB
298.15297	−22.02219	19.59 ± 0.01	18.93 ± 0.01	20.21 ± 0.01	122.6 ± 1.8	−0.935 ± 0.985	−1.78 ± 0.535	17.8	−1.39 ± 0.13	—	0.00	N
298.15097	−22.07939	19.56 ± 0.01	19.17 ± 0.01	19.94 ± 0.01	−174.0 ± 2.1	−1.205 ± 0.805	−0.816 ± 0.463	16.9	−3.16 ± 0.29	−2.57 ± 0.14	0.00	HB
298.17764	−22.04601	19.62 ± 0.01	19.83 ± 0.01	19.63 ± 0.01	−135.3 ± 4.2	−4.001 ± 1.206	−1.43 ± 0.651	11.1	−99.0 ± −99.0	−0.92 ± 0.27	0.00	HB
298.17252	−22.07411	19.66 ± 0.01	19.90 ± 0.01	19.67 ± 0.01	−76.1 ± 10.3	−0.958 ± 1.284	−2.143 ± 0.663	11.7	−99.0 ± −99.0	−0.03 ± 0.24	0.00	HB
298.12764	−22.17289	19.75 ± 0.01	19.37 ± 0.01	20.20 ± 0.01	−15.5 ± 2.6	2.824 ± 0.831	−6.75 ± 0.504	15.0	−2.38 ± 0.29	−1.77 ± 0.16	0.00	N
298.20524	−22.02751	19.83 ± 0.01	19.83 ± 0.01	21.05 ± 0.02	201.1 ± 3.4	−3.185 ± 1.126	−15.463 ± 0.607	17.8	−1.27 ± 0.13	—	0.00	N
298.18213	−22.05709	19.85 ± 0.01	19.04 ± 0.01	21.08 ± 0.03	28.4 ± 1.8	−0.533 ± 1.135	−6.337 ± 0.594	14.9	−1.24 ± 0.12	—	0.03	N
298.14821	−22.00248	19.89 ± 0.01	19.52 ± 0.01	20.39 ± 0.02	163.6 ± 1.9	0.014 ± 1.404	−4.599 ± 0.742	14.3	−1.82 ± 0.23	—	0.00	N
298.16397	−22.06350	19.94 ± 0.01	19.53 ± 0.01	20.46 ± 0.02	41.4 ± 2.0	3.398 ± 1.562	−8.363 ± 0.947	14.0	−2.04 ± 0.25	—	0.00	N
298.16217	−22.05441	19.96 ± 0.01	19.24 ± 0.01	20.72 ± 0.02	−176.0 ± 1.5	−1.281 ± 1.022	−1.531 ± 0.539	15.8	−2.65 ± 0.16	−2.24 ± 0.08	0.99	Y
298.14762	−22.18984	20.06 ± 0.01	19.67 ± 0.01	20.63 ± 0.02	−227.3 ± 3.3	−1.419 ± 1.191	−5.42 ± 0.742	11.3	−1.57 ± 0.18	—	0.00	N
298.19401	−22.08638	20.38 ± 0.01	19.70 ± 0.01	21.09 ± 0.03	−174.9 ± 2.3	−0.305 ± 1.333	0.776 ± 0.766	13.2	−2.59 ± 0.23	−2.09 ± 0.11	0.99	Y
298.19723	−22.12452	20.51 ± 0.01	19.94 ± 0.01	21.45 ± 0.03	−323.9 ± 2.6	−10.391 ± 1.957	−3.304 ± 1.107	12.0	—	—	0.01	N
298.14902	−22.02359	20.91 ± 0.01	20.49 ± 0.01	21.45 ± 0.03	−71.1 ± 3.6	— ± —	— ± —	7.2	−2.05 ± 0.31	—	0.00	N
298.18112	−22.06077	20.93 ± 0.01	20.29 ± 0.01	21.60 ± 0.04	−179.5 ± 2.4	— ± —	— ± —	9.7	−2.54 ± 0.28	—	1.00	Y
298.17318	−22.11584	21.10 ± 0.01	20.51 ± 0.01	21.83 ± 0.04	−173.9 ± 3.8	— ± —	— ± —	6.2	−2.06 ± 0.22	—	0.97	Y
298.14955	−22.10703	21.24 ± 0.01	20.62 ± 0.01	21.89 ± 0.05	−177.4 ± 3.7	— ± —	— ± —	6.2	−2.69 ± 0.45	—	0.99	Y
298.10564	−22.14928	21.27 ± 0.01	20.67 ± 0.01	21.89 ± 0.05	−176.3 ± 6.0	— ± —	— ± —	5.6	−2.67 ± 0.36	—	0.99	Y
298.15166	−22.14928	21.54 ± 0.01	21.13 ± 0.02	22.07 ± 0.05	10.6 ± 10.6	— ± —	— ± —	4.6	−1.82 ± 0.51	—	0.00	N
298.16335	−22.14322	21.60 ± 0.01	21.16 ± 0.02	22.27 ± 0.06	71.0 ± 4.9	— ± —	— ± —	4.0	−1.31 ± 0.36	—	0.00	N
298.16188	−22.05321	21.56 ± 0.01	20.99 ± 0.01	22.31 ± 0.07	−177.5 ± 7.8	— ± —	— ± —	5.7	−1.81 ± 0.37	—	1.00	Y
298.18229	−22.04275	21.61 ± 0.01	20.99 ± 0.01	22.22 ± 0.06	−177.1 ± 3.9	— ± —	— ± —	5.5	−2.96 ± 0.47	—	0.99	Y
298.19629	−22.18246	21.79 ± 0.01	21.30 ± 0.02	22.57 ± 0.08	−285.7 ± 12.8	— ± —	— ± —	4.2	−1.33 ± 0.37	—	0.02	N
298.13949	−22.1762	21.81 ± 0.01	21.41 ± 0.01	22.37 ± 0.07	174.5 ± 11.6	— ± —	— ± —	2.6	−1.49 ± 0.43	—	0.00	N
298.15003	−22.01742	21.77 ± 0.01	21.01 ± 0.01	22.59 ± 0.08	−276.5 ± 3.6	— ± —	— ± —	4.5	−2.68 ± 0.56	—	0.57	Y
298.14941	−22.17937	21.82 ± 0.01	21.21 ± 0.02	22.92 ± 0.11	−59.4 ± 5.6	— ± —	— ± —	4.1	−99.0 ± −99.0	—	0.00	N
298.16383	−22.18617	21.90 ± 0.01	21.11 ± 0.01	23.39 ± 0.16	−11.5 ± 5.2	— ± —	— ± —	3.3	−99.0 ± −99.0	—	0.00	N
298.16462	−22.09165	21.93 ± 0.01	21.41 ± 0.02	22.58 ± 0.08	−172.1 ± 4.5	— ± —	— ± —	3.7	−2.05 ± 0.41	—	1.00	Y
298.17171	−22.12262	22.32 ± 0.02	21.53 ± 0.02	23.38 ± 0.16	−109.2 ± 9.5	— ± —	— ± —	3.4	−1.74 ± 0.52	—	0.00	N
298.12891	−22.15738	22.55 ± 0.02	21.04 ± 0.01	22.81 ± 0.10	31.0 ± 6.0	— ± —	— ± —	4.8	−99.0 ± −99.0	—	0.00	N

Table 2. Properties of our spectroscopic sample - Part 2

RA (deg)	DEC (deg)	g_0	i_0	$CaHK_0$	v_r (km s^{-1})	μ_α^* (mas.yr^{-1})	μ_δ (mas.yr^{-1})	S/N	[Fe/H]$_{CaHK}$	[Fe/H]$_{spectro}$	P_{mem}	Member
298.13975	−22.02537	22.77 ± 0.02	22.02 ± 0.03	23.42 ± 0.16	642.6 ± 13.9	— ± —	— ± —	2.4	−99.0 ± −99.0	—	0.00	N
298.16238	−22.07748	17.50 ± 0.01	16.37 ± 0.01	18.97 ± 0.01	−170.4 ± 0.7	−0.548 ± 0.158	−0.878 ± 0.087	50.6	−99.0 ± −99.0	−2.09 ± 0.04	1.00	Y
298.16425	−22.16803	17.47 ± 0.01	16.68 ± 0.01	18.82 ± 0.01	−82.8 ± 1.1	14.405 ± 0.181	−4.936 ± 0.108	38.8	−99.0 ± −99.0	−1.39 ± 0.06	0.00	N
298.29535	−22.07591	18.37 ± 0.01	17.55 ± 0.01	19.82 ± 0.01	109.3 ± 2.6	−4.564 ± 0.37	−3.604 ± 0.22	32.2	—	—	0.00	N
298.26279	−22.10197	18.50 ± 0.01	17.87 ± 0.01	19.58 ± 0.01	66.3 ± 5.3	−3.609 ± 0.38	−9.306 ± 0.209	15.3	—	—	0.00	N
298.26702	−22.08326	19.00 ± 0.01	18.54 ± 0.01	19.80 ± 0.01	11.9 ± 1.6	3.988 ± 0.662	−6.709 ± 0.369	24.3	—	—	0.00	N
298.31595	−22.06792	19.21 ± 0.01	18.70 ± 0.01	19.84 ± 0.01	−85.3 ± 2.6	2.98 ± 0.722	−7.838 ± 0.438	26.2	−2.01 ± 0.15	−1.76 ± 0.08	0.00	N
298.26878	−22.02816	19.22 ± 0.01	18.54 ± 0.01	20.39 ± 0.02	42.9 ± 1.8	−5.562 ± 0.769	−9.669 ± 0.406	24.0	—	—	0.00	N
298.28164	−22.08366	19.48 ± 0.01	18.95 ± 0.01	20.34 ± 0.02	31.1 ± 2.3	−1.95 ± 0.912	−7.823 ± 0.498	22.5	−1.01 ± 0.14	—	0.00	N
298.30703	−22.09047	19.48 ± 0.01	18.62 ± 0.01	20.98 ± 0.02	33.2 ± 3.6	−4.498 ± 0.838	0.209 ± 0.47	30.8	—	—	0.00	N
298.28935	−22.06904	19.59 ± 0.01	19.18 ± 0.01	20.19 ± 0.01	17.8 ± 1.7	1.286 ± 1.111	−5.091 ± 0.609	22.4	−1.52 ± 0.18	—	0.00	N
298.29141	−22.07521	19.68 ± 0.01	19.31 ± 0.01	20.18 ± 0.01	−40.9 ± 2.0	−2.302 ± 1.145	−11.191 ± 0.665	22.0	−1.82 ± 0.22	−2.18 ± 0.11	0.00	N
298.26110	−22.03198	19.79 ± 0.01	19.16 ± 0.01	20.86 ± 0.02	−108.8 ± 2.2	4.747 ± 1.23	−6.477 ± 0.661	21.6	—	—	0.00	N
298.27998	−22.07672	20.40 ± 0.01	19.75 ± 0.01	21.44 ± 0.03	−111.5 ± 3.2	−5.707 ± 2.05	−4.735 ± 1.075	15.6	—	—	0.49	N
298.25045	−22.08093	20.39 ± 0.01	19.57 ± 0.01	21.80 ± 0.04	73.8 ± 2.4	−4.985 ± 1.811	−11.227 ± 0.907	18.1	—	—	0.00	N
298.25661	−22.0404	20.73 ± 0.01	20.19 ± 0.01	21.42 ± 0.03	−33.3 ± 4.3	5.009 ± 3.983	−5.137 ± 2.092	10.1	−1.93 ± 0.20	—	0.00	N
298.23870	−22.10072	21.06 ± 0.01	20.60 ± 0.01	21.83 ± 0.04	−85.8 ± 5.1	— ± —	— ± —	8.4	—	—	0.00	N
298.25472	−22.05189	21.49 ± 0.01	20.99 ± 0.01	22.09 ± 0.05	−103.4 ± 5.5	— ± —	— ± —	6.5	−2.30 ± 0.40	−2.8 ± 0.15	0.04	N
298.31195	−22.06705	21.50 ± 0.01	20.63 ± 0.01	23.09 ± 0.12	125.8 ± 6.7	— ± —	— ± —	8.5	−99.0 ± −99.0	−3.7 ± 0.33	0.00	N
298.29775	−22.10044	21.77 ± 0.01	21.15 ± 0.02	22.69 ± 0.08	67.2 ± 3.8	— ± —	— ± —	5.8	−1.36 ± 0.34	−2.42 ± 0.09	0.35	N
298.27070	−22.09640	22.06 ± 0.01	21.22 ± 0.02	23.49 ± 0.16	−64.3 ± 7.1	— ± —	— ± —	5.7	−99.0 ± −99.0	—	0.00	N
298.28685	−22.04170	22.40 ± 0.02	21.62 ± 0.02	−0.420 ± 0.00	217.5 ± 5.7	— ± —	— ± —	3.7	−99.0 ± −99.0	—	0.00	N
298.11755	−22.07704	18.09 ± 0.01	17.49 ± 0.01	19.07 ± 0.01	21.4 ± 1.5	−2.317 ± 0.273	−2.956 ± 0.152	28.9	—	—	0.00	N
298.21458	−22.09340	18.59 ± 0.01	18.06 ± 0.01	19.63 ± 0.01	9.5 ± 2.5	−1.798 ± 0.406	−3.73 ± 0.234	25.2	—	—	0.00	N
298.15560	−22.05778	19.22 ± 0.01	18.91 ± 0.01	19.58 ± 0.01	13.6 ± 2.3	−1.788 ± 0.74	−5.022 ± 0.38	20.8	−2.71 ± 0.29	—	0.00	N
298.12513	−22.04616	19.24 ± 0.01	18.87 ± 0.01	19.63 ± 0.01	−179.3 ± 4.2	9.328 ± 0.675	−6.482 ± 0.376	24.2	−3.08 ± 0.27	—	0.00	N
298.16299	−22.08244	19.38 ± 0.01	18.61 ± 0.01	20.18 ± 0.01	−176.0 ± 1.3	−0.547 ± 0.608	−0.29 ± 0.338	26.6	−2.73 ± 0.16	−2.42 ± 0.09	0.99	Y
298.22308	−22.03976	19.52 ± 0.01	18.78 ± 0.01	20.76 ± 0.02	60.9 ± 1.9	−5.413 ± 0.935	−5.874 ± 0.519	21.5	—	—	0.92	N
298.18333	−22.07023	19.79 ± 0.01	19.33 ± 0.01	20.41 ± 0.02	−110.3 ± 2.0	7.892 ± 0.932	4.142 ± 0.541	18.4	−1.79 ± 0.19	−1.87 ± 0.1	0.00	N
298.17679	−22.05594	19.98 ± 0.01	19.16 ± 0.01	21.27 ± 0.03	−63.7 ± 2.4	2.017 ± 0.904	−9.667 ± 0.501	21.1	—	—	0.00	N
298.16641	−22.06769	20.21 ± 0.01	19.51 ± 0.01	20.95 ± 0.02	−176.0 ± 2.6	0.954 ± 1.292	0.563 ± 0.684	17.2	−2.59 ± 0.14	−2.31 ± 0.12	1.00	Y
298.17500	−22.05421	20.70 ± 0.01	20.02 ± 0.01	21.41 ± 0.03	−174.6 ± 1.7	1.235 ± 3.375	−2.706 ± 1.621	13.1	−2.66 ± 0.30	—	0.99	Y
298.20856	−22.06174	21.18 ± 0.01	20.65 ± 0.01	21.80 ± 0.04	107.6 ± 5.3	— ± —	— ± —	8.4	−2.22 ± 0.29	—	0.57	N
298.20446	−22.05373	21.28 ± 0.01	20.55 ± 0.01	22.41 ± 0.07	−164.6 ± 6.1	— ± —	— ± —	8.1	−1.12 ± 0.25	—	0.00	N
298.15244	−22.06164	21.31 ± 0.01	20.72 ± 0.01	21.94 ± 0.05	−177.4 ± 2.6	— ± —	— ± —	7.8	−2.50 ± 0.41	—	1.00	Y
298.19704	−22.07148	21.65 ± 0.01	21.10 ± 0.02	22.28 ± 0.06	−173.9 ± 6.0	— ± —	— ± —	6.6	−2.45 ± 0.44	—	1.00	Y
298.14088	−22.04199	21.67 ± 0.01	21.08 ± 0.02	22.38 ± 0.07	−184.7 ± 3.7	— ± —	— ± —	5.7	−2.09 ± 0.44	—	1.00	Y
298.11370	−22.07934	21.75 ± 0.01	20.93 ± 0.01	23.21 ± 0.14	−74.9 ± 5.7	— ± —	— ± —	6.9	−99.0 ± −99.0	—	0.00	N
298.13356	−22.10374	21.98 ± 0.01	21.06 ± 0.01	23.45 ± 0.17	−198.2 ± 10.4	— ± —	— ± —	5.2	−99.0 ± −99.0	—	0.00	N
298.20068	−22.05972	22.05 ± 0.01	21.50 ± 0.02	22.79 ± 0.10	−187.7 ± 5.8	— ± —	— ± —	3.8	−1.73 ± 0.41	—	1.00	Y
298.10810	−22.07218	22.07 ± 0.01	21.51 ± 0.02	22.92 ± 0.11	−193.6 ± 8.6	— ± —	— ± —	4.4	−1.45 ± 0.60	—	0.99	Y
298.19912	−22.08466	22.15 ± 0.01	21.62 ± 0.02	22.90 ± 0.10	−167.6 ± 11.5	— ± —	— ± —	3.7	−1.63 ± 0.48	—	1.00	Y
298.18916	−22.07193	22.28 ± 0.02	21.83 ± 0.02	22.86 ± 0.10	−17.5 ± 14.9	— ± —	— ± —	3.3	−2.00 ± 0.73	—	1.00	Y
298.15436	−22.07078	22.30 ± 0.02	21.79 ± 0.02	22.85 ± 0.10	−171.8 ± 13.7	— ± —	— ± —	3.7	−2.72 ± 0.81	—	1.00	Y
298.14889	−22.04349	22.36 ± 0.02	21.78 ± 0.02	23.45 ± 0.17	−26.3 ± 13.5	— ± —	— ± —	3.1	−99.0 ± −99.0	—	0.99	N
298.08678	−22.10022	18.37 ± 0.01	17.60 ± 0.01	19.64 ± 0.01	18.0 ± 1.5	0.656 ± 0.279	−4.619 ± 0.163	28.0	—	—	0.00	N
298.06312	−22.0584	18.67 ± 0.01	18.19 ± 0.01	19.47 ± 0.01	16.8 ± 1.6	5.475 ± 0.404	−5.921 ± 0.228	28.9	−1.10 ± 0.12	—	0.00	N
298.08457	−22.0471	19.01 ± 0.01	18.37 ± 0.01	20.16 ± 0.01	39.1 ± 1.9	−2.449 ± 0.482	−2.806 ± 0.268	27.5	—	—	0.00	N
298.06152	−22.02591	19.30 ± 0.01	18.59 ± 0.01	20.56 ± 0.02	48.4 ± 2.4	−1.92 ± 0.559	−3.82 ± 0.317	22.1	—	—	0.01	N
298.08086	−22.0442	19.32 ± 0.01	18.79 ± 0.01	19.89 ± 0.01	−385.3 ± 1.6	−1.849 ± 0.609	−4.274 ± 0.343	23.4	−2.63 ± 0.21	−2.66 ± 0.09	0.00	N
298.08962	−22.02933	19.42 ± 0.01	18.67 ± 0.01	20.61 ± 0.02	80.2 ± 1.9	−1.374 ± 0.597	−5.162 ± 0.334	23.2	−1.03 ± 0.12	−1.03 ± 0.12	0.71	N
298.04697	−22.09121	19.76 ± 0.01	19.18 ± 0.01	20.34 ± 0.02	79.1 ± 2.4	−17.5 ± 0.76	−1.088 ± 0.455	22.5	−99.0 ± −99.0	−2.79 ± 0.15	0.00	N

Table 2. Properties of our spectroscopic sample - Part 3

RA (deg)	DEC (deg)	g_0	i_0	$CaHK_0$	v_r (km s^{-1})	μ_α^* (mas.yr^{-1})	μ_δ (mas.yr^{-1})	S/N	[Fe/H]$_{\mathrm{CaHK}}$	[Fe/H]$_{\mathrm{spectro}}$	P_{mem}	Member
298.07480	-22.08419	20.88 ± 0.01	19.95 ± 0.01	21.93 ± 0.05	55.5 ± 3.3	-10.032 ± 1.951	-18.831 ± 1.084	14.2	-2.62 ± 0.21	—	0.00	N
298.05488	-22.04129	20.87 ± 0.01	20.23 ± 0.01	21.93 ± 0.05	21.2 ± 5.4	1.271 ± 4.225	-12.49 ± 2.044	9.7	—	—	0.64	N
298.10189	-22.06900	20.94 ± 0.01	20.45 ± 0.01	21.52 ± 0.04	-55.2 ± 4.9	$- \pm -$	$- \pm -$	9.2	-2.27 ± 0.28	—	0.00	N
298.03362	-22.09989	20.97 ± 0.01	20.35 ± 0.01	21.89 ± 0.05	-85.2 ± 5.5	0.485 ± 3.664	-2.08 ± 2.111	15.5	-1.34 ± 0.21	—	0.35	N
298.05202	-22.07246	21.11 ± 0.01	20.76 ± 0.01	21.48 ± 0.04	-270.8 ± 7.6	$- \pm -$	$- \pm -$	7.0	-3.08 ± 0.45	—	0.00	N
298.07868	-22.07233	21.36 ± 0.01	20.79 ± 0.01	22.19 ± 0.06	21.9 ± 7.0	$- \pm -$	$- \pm -$	6.5	-1.53 ± 0.26	—	0.91	N
298.06683	-22.03142	21.36 ± 0.01	20.58 ± 0.01	22.71 ± 0.09	-36.9 ± 6.0	$- \pm -$	$- \pm -$	7.0	—	—	0.00	N
298.03617	-22.06643	21.75 ± 0.01	21.09 ± 0.01	22.78 ± 0.10	162.8 ± 6.8	$- \pm -$	$- \pm -$	4.6	-1.21 ± 0.45	—	0.01	N
298.02500	-22.06504	22.08 ± 0.01	21.27 ± 0.02	23.50 ± 0.18	57.2 ± 5.8	$- \pm -$	$- \pm -$	3.7	-99.0 ± -99.0	—	0.00	N
298.05970	-22.05248	22.40 ± 0.02	21.46 ± 0.02	-0.460 ± 0.00	27.9 ± 6.5	$- \pm -$	$- \pm -$	4.1	-99.0 ± -99.0	—	0.00	N
298.04913	-22.03305	17.50 ± 0.01	16.59 ± 0.01	19.05 ± 0.01	56.1 ± 1.6	4.746 ± 0.162	0.185 ± 0.092	40.1	-99.0 ± -99.0	-1.31 ± 0.08	0.00	N
298.07669	-22.08716	17.29 ± 0.01	15.89 ± 0.01	19.34 ± 0.01	-37.0 ± 1.5	-1.479 ± 0.125	-5.347 ± 0.069	44.1	-99.0 ± -99.0	-1.18 ± 0.08	0.00	N
298.21893	-22.07197	17.44 ± 0.01	16.54 ± 0.01	19.05 ± 0.01	-6.6 ± 1.7	3.183 ± 0.205	-7.464 ± 0.116	37.3	-99.0 ± -99.0	-1.18 ± 0.09	0.00	N

Table 3. Velocities and individual metallicities for all stars observed more than once, per mask. Mask 1 was observed on the 2015-09-12 and re-observed on the 2015-09-18, and mask 2 on the 2015-09-08. (respectively 2457283.760868, 2457277.742083, and 2457273.738102 in Julian dates). The systematic threshold δ_{thr} is not included in the velocity uncertainties presented in this table. The individual spectroscopic metallicity is reported for stars with S/N >= 12 and $g_0 > 20.5$ only.

RA (deg)	DEC (deg)	Mask	$v_r\,(\mathrm{km\,s^{-1}})$	$[\mathrm{Fe/H}]_{\mathrm{spectro}}$
298.18001	-22.07175	Combined	0.2 ± 0.9	—
		Mask 1	0.2 ± 1.6	—
		Mask 2	1.1 ± 1.7	—
		Mask 1 (re-observed)	-0.5 ± 1.4	—
298.16146	-22.08266	Combined	-182.8 ± 0.9	-2.26 ± 0.04
		Mask 1	-182.4 ± 1.8	-2.36 ± 0.07
		Mask 2	-183.1 ± 1.4	-2.25 ± 0.08
		Mask 1 (re-observed)	-182.8 ± 1.4	-2.2 ± 0.07
298.18213	-22.05709	Combined	28.4 ± 1.8	—
		Mask 1	29.4 ± 5.6	—
		Mask 2	29.6 ± 2.4	—
		Mask 1 (re-observed)	25.7 ± 3.3	—
298.20599	-21.98790	Combined	16.6 ± 1.3	—
		Mask 1	17.4 ± 1.7	—
		Mask 1 (re-observed)	15.1 ± 2.2	—
298.13158	-21.98583	Combined	27.5 ± 1.5	—
		Mask 1	27.1 ± 2.0	—
		Mask 1 (re-observed)	28.0 ± 2.4	—
298.13138	-21.98273	Combined	-39.4 ± 2.2	—
		Mask 1	-44.0 ± 2.8	—
		Mask 1 (re-observed)	-31.4 ± 3.6	—
298.15508	-21.98054	Combined	12.5 ± 1.7	—
		Mask 1	12.0 ± 2.9	—
		Mask 1 (re-observed)	12.7 ± 2.1	—
298.15097	-21.95283	Combined	140.9 ± 1.7	—
		Mask 1	140.8 ± 2.1	—
		Mask 1 (re-observed)	141.1 ± 3.1	—
298.19072	-21.96758	Combined	-118.1 ± 6.2	-2.85 ± 0.22
		Mask 1	-116.0 ± 10.1	-3.01 ± 0.26
		Mask 1 (re-observed)	-119.4 ± 7.9	-2.46 ± 0.41
298.18688	-21.97714	Combined	-107.3 ± 2.8	-1.25 ± 0.13
		Mask 1	-114.2 ± 5.4	-1.29 ± 0.18
		Mask 1 (re-observed)	-104.7 ± 3.3	-1.21 ± 0.18
298.18320	-21.96362	Combined	-15.4 ± 3.5	—
		Mask 1	-9.8 ± 7.3	—
		Mask 1 (re-observed)	-17.1 ± 4.0	—
298.13665	-21.97424	Combined	-7.8 ± 7.4	—
		Mask 1	-1.4 ± 9.9	—
		Mask 1 (re-observed)	-16.3 ± 11.3	—
298.19440	-21.99071	Combined	-67.3 ± 3.8	—
		Mask 1	-64.4 ± 7.0	—
		Mask 1 (re-observed)	-68.5 ± 4.5	—
298.18154	-21.96963	Combined	30.1 ± 16.0	—
		Mask 1	26.3 ± 20.0	—
		Mask 1 (re-observed)	37.0 ± 26.9	—
298.19622	-21.99369	Combined	-2.0 ± 13.4	—
		Mask 1	-4.6 ± 17.6	—
		Mask 1 (re-observed)	1.6 ± 20.5	—
298.16960	-22.17463	Combined	89.7 ± 1.1	—
		Mask 1	88.5 ± 1.7	—
		Mask 1 (re-observed)	90.5 ± 1.5	—
298.16810	-22.18830	Combined	105.1 ± 1.3	—
		Mask 1	104.8 ± 1.5	—
		Mask 1 (re-observed)	105.9 ± 2.5	—
298.19662	-22.14635	Combined	29.2 ± 1.8	—
		Mask 1	30.8 ± 2.4	—
		Mask 1 (re-observed)	27.1 ± 2.8	—
298.17484	-22.16606	Combined	-54.0 ± 1.3	—
		Mask 1	-54.2 ± 1.9	—
		Mask 1 (re-observed)	-53.9 ± 1.7	—
298.19827	-22.14498	Combined	89.3 ± 1.3	—
		Mask 1	91.0 ± 2.4	—
		Mask 1 (re-observed)	88.5 ± 1.6	—

Table 3. Velocities and individual metallicities for all stars observed more than once, per mask. - Part 2

298.16120	-22.00829	Combined	-85.1 ± 1.4	—
		Mask 1	-82.0 ± 2.1	—
		Mask 1 (re-observed)	-87.5 ± 1.9	—
298.15404	-22.11108	Combined	51.4 ± 1.9	—
		Mask 1	51.2 ± 3.3	—
		Mask 1 (re-observed)	51.5 ± 2.4	—
298.15853	-22.05847	Combined	-167.9 ± 9.5	-0.46 ± 0.28
		Mask 1	-161.0 ± 23.3	-1.23 ± 0.77
		Mask 1 (re-observed)	-169.3 ± 10.4	-0.34 ± 0.31
298.19297	-22.02219	Combined	122.6 ± 1.8	—
		Mask 1	123.3 ± 2.8	—
		Mask 1 (re-observed)	122.0 ± 2.5	—
298.17764	-22.04601	Combined	-135.3 ± 4.2	-0.92 ± 0.28
		Mask 1	-177.0 ± 4.9	-1.26 ± 0.4
		Mask 1 (re-observed)	-12.9 ± 8.4	-0.6 ± 0.39
298.17252	-22.07411	Combined	-76.1 ± 10.3	-0.07 ± 0.24
		Mask 1	-82.6 ± 18.3	-0.07 ± 0.35
		Mask 1 (re-observed)	-73.1 ± 12.5	-0.08 ± 0.32
298.12764	-22.17289	Combined	-15.5 ± 2.6	-1.79 ± 0.16
		Mask 1	-13.7 ± 3.4	-1.77 ± 0.2
		Mask 1 (re-observed)	-17.9 ± 4.0	-1.81 ± 0.25
298.20524	-22.02751	Combined	201.1 ± 3.4	—
		Mask 1	212.3 ± 4.9	—
		Mask 1 (re-observed)	190.9 ± 4.7	—
298.14821	-22.00248	Combined	163.6 ± 1.9	-2.5 ± 0.12
		Mask 1	163.3 ± 2.4	-2.43 ± 0.15
		Mask 1 (re-observed)	164.1 ± 3.4	-2.62 ± 0.2
298.16397	-22.06350	Combined	41.4 ± 2.0	-2.02 ± 0.11
		Mask 1	42.2 ± 3.0	-2.01 ± 0.16
		Mask 1 (re-observed)	40.7 ± 2.8	-2.02 ± 0.16
298.16217	-22.05441	Combined	-176.0 ± 1.5	-2.24 ± 0.08
		Mask 1	-176.4 ± 1.8	-2.2 ± 0.11
		Mask 1 (re-observed)	-175.1 ± 2.7	-2.26 ± 0.1
298.14762	-22.18984	Combined	-227.3 ± 3.3	—
		Mask 1	-229.5 ± 7.4	—
		Mask 1 (re-observed)	-226.8 ± 3.7	—
298.19401	-22.08638	Combined	-174.9 ± 2.3	-2.09 ± 0.11
		Mask 1	-174.8 ± 2.7	-2.11 ± 0.15
		Mask 1 (re-observed)	-175.1 ± 4.4	-2.07 ± 0.15
298.19723	-22.12452	Combined	-323.9 ± 2.6	—
		Mask 1	-320.8 ± 3.7	—
		Mask 1 (re-observed)	-326.8 ± 3.6	—
298.14902	-22.02359	Combined	-71.1 ± 3.6	—
		Mask 1	-68.0 ± 4.1	—
		Mask 1 (re-observed)	-80.9 ± 7.3	—
298.18112	-22.06077	Combined	-179.5 ± 2.4	—
		Mask 1	-179.9 ± 3.4	—
		Mask 1 (re-observed)	-179.2 ± 3.5	—
298.17318	-22.11584	Combined	-173.9 ± 3.8	—
		Mask 1	-157.7 ± 6.4	—
		Mask 1 (re-observed)	-182.8 ± 4.7	—
298.12500	-22.11766	Combined	-179.7 ± 16.8	—
		Mask 1	-97.2 ± 42.3	—
		Mask 1 (re-observed)	-195.1 ± 18.3	—
298.14955	-22.10703	Combined	-177.4 ± 3.7	—
		Mask 1	-180.8 ± 6.1	—
		Mask 1 (re-observed)	-175.5 ± 4.7	—
298.18245	-22.10564	Combined	-176.3 ± 6.0	—
		Mask 1	-172.9 ± 11.1	—
		Mask 1 (re-observed)	-177.7 ± 7.1	—
298.16335	-22.14322	Combined	71.0 ± 4.9	—
		Mask 1	75.7 ± 6.8	—
		Mask 1 (re-observed)	65.8 ± 7.0	—
298.16188	-22.05321	Combined	-177.5 ± 7.8	—
		Mask 1	-178.1 ± 12.5	—
		Mask 1 (re-observed)	-177.1 ± 9.9	—
298.18229	-22.04275	Combined	-177.1 ± 3.9	—
		Mask 1	-180.6 ± 6.3	—
		Mask 1 (re-observed)	-175.0 ± 5.0	—

Table 3. Velocities and individual metallicities for all stars observed more than once, per mask. - Part 3

298.19593	-22.13295	Combined	22.0 ± 6.6	—
		Mask 1	-497.1 ± 14.1	—
		Mask 1 (re-observed)	166.5 ± 7.4	—
298.13949	-22.17620	Combined	174.5 ± 11.6	—
		Mask 1	142.2 ± 24.7	—
		Mask 1 (re-observed)	183.7 ± 13.2	—
298.15003	-22.01742	Combined	-276.5 ± 3.6	—
		Mask 1	-273.9 ± 7.0	—
		Mask 1 (re-observed)	-277.5 ± 4.2	—
298.14941	-22.17937	Combined	-59.4 ± 5.6	—
		Mask 1	-52.7 ± 6.8	—
		Mask 1 (re-observed)	-73.5 ± 9.8	—
298.16383	-22.18617	Combined	-11.5 ± 5.2	—
		Mask 1	-6.4 ± 6.4	—
		Mask 1 (re-observed)	-21.4 ± 9.0	—
298.16462	-22.09165	Combined	-172.1 ± 4.5	—
		Mask 1	-164.5 ± 5.5	—
		Mask 1 (re-observed)	-189.6 ± 8.2	—
298.20290	-22.03570	Combined	-177.4 ± 7.9	—
		Mask 1	-181.2 ± 10.3	—
		Mask 1 (re-observed)	-171.9 ± 12.3	—
298.17171	-22.12262	Combined	-109.2 ± 9.5	—
		Mask 1	-112.2 ± 17.1	—
		Mask 1 (re-observed)	-107.9 ± 11.4	—
298.16051	-22.10941	Combined	-51.8 ± 8.5	—
		Mask 1	-12.1 ± 9.9	—
		Mask 1 (re-observed)	-171.3 ± 17.1	—
298.16816	-22.18472	Combined	62.8 ± 14.7	—
		Mask 1	48.7 ± 16.5	—
		Mask 1 (re-observed)	116.8 ± 32.3	—
298.17825	-22.01529	Combined	341.2 ± 10.5	—
		Mask 1	375.7 ± 10.9	—
		Mask 1 (re-observed)	-85.7 ± 38.3	—
298.20325	-22.11921	Combined	268.2 ± 8.4	—
		Mask 1	737.8 ± 29.0	—
		Mask 1 (re-observed)	225.0 ± 8.8	—
298.12891	-22.15738	Combined	31.0 ± 6.0	—
		Mask 1	32.6 ± 7.5	—
		Mask 1 (re-observed)	28.1 ± 9.9	—
298.18128	-22.11434	Combined	-15.4 ± 10.0	—
		Mask 1	-15.8 ± 14.1	—
		Mask 1 (re-observed)	-15.0 ± 14.2	—
298.12620	-22.16308	Combined	-100.2 ± 7.3	—
		Mask 1	-92.8 ± 7.9	—
		Mask 1 (re-observed)	-141.3 ± 18.6	—
298.19941	-22.10216	Combined	332.5 ± 8.3	—
		Mask 1	-238.7 ± 19.6	—
		Mask 1 (re-observed)	457.9 ± 9.2	—
298.13975	-22.02537	Combined	642.6 ± 13.9	—
		Mask 1	574.9 ± 20.1	—
		Mask 1 (re-observed)	704.6 ± 19.2	—
298.17350	-22.09813	Combined	37.3 ± 8.2	—
		Mask 1	724.5 ± 15.4	—
		Mask 1 (re-observed)	-238.5 ± 9.8	—
298.19098	-22.08826	Combined	-305.3 ± 16.6	—
		Mask 1	-622.7 ± 20.8	—
		Mask 1 (re-observed)	257.3 ± 27.6	—
298.14785	-22.05035	Combined	461.1 ± 10.1	—
		Mask 1	537.3 ± 26.9	—
		Mask 1 (re-observed)	448.6 ± 10.9	—
298.15192	-22.02911	Combined	126.0 ± 30.7	—
		Mask 1	139.2 ± 43.3	—
		Mask 1 (re-observed)	112.6 ± 43.6	—
298.16238	-22.07748	Combined	-170.4 ± 0.7	-2.09 ± 0.04
		Mask 1	-173.2 ± 1.2	-2.14 ± 0.06
		Mask 1 (re-observed)	-169.0 ± 0.9	-2.05 ± 0.06
298.16425	-22.16803	Combined	-82.8 ± 1.1	-1.39 ± 0.05
		Mask 1	-83.0 ± 1.7	-1.44 ± 0.08
		Mask 1 (re-observed)	-82.6 ± 1.5	-1.34 ± 0.08

The Dark Energy Survey Collaboration, 2005, arXiv:astro-ph/0510346

Tonry J. L. et al., 2012, ApJ, 750, 99

Tulin S., Yu H.-B., 2017, arXiv:1705.02358

Walker M. G., Mateo M., Olszewski E. W., Peñarrubia J., Wyn Evans N., Gilmore G., 2009, ApJ, 704, 1274

Weisz D. R. et al., 2016, ApJ, 822, 32

Willman B. et al., 2005a, AJ, 129, 2692

—, 2005b, ApJ, 626, L85

Willman B., Geha M., Strader J., Strigari L. E., Simon J. D., Kirby E., Ho N., Warres A., 2011, AJ, 142, 128

Willman B., Strader J., 2012, AJ, 144, 76

Wilson A. G., 1955, PASP, 67, 27

Wolf J., Martinez G. D., Bullock J. S., Kaplinghat M., Geha M., Muñoz R. R., Simon J. D., Avedo F. F., 2010, MNRAS, 406, 1220

York D. G. et al., 2000, The Astronomical Journal, 120, 1579

Youakim K. et al., 2017, MNRAS, 472, 2963

Zucker D. B. et al., 2006a, ApJ, 650, L41

—, 2006b, ApJ, 643, L103

Detailed study of the Milky Way globular cluster Laevens 3
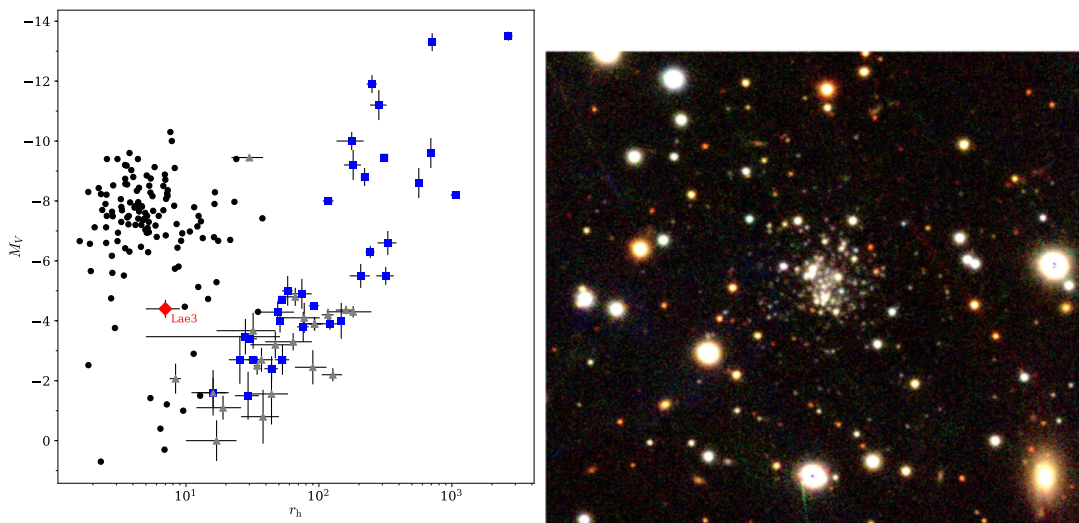
Figure 5.1: *Left plot*: Same plot as Figure 3.1, for Lae 3. Lae 3 is represented as a red diamond, with the r_h and M_V shown here both taken from L15. The system occupies, at the time of its discovery, a location unambiguously corresponding to globular clusters. *Right plot*: RGB image of Lae 3 in PS1, from L15. The satellite immediately appears as a very dense system.

This chapter presents my study on the faint MW satellite Lae 3 (Longeard et al., 2019a). The system was also discovered in 2015 by L15 and was found to be very compact, so much so that crowding effects at the center made the usual extraction of the photometric information challenging in PS1. Thanks to the presence of one RR-Lyrae at 0.6 arcminutes of the center of Lae 3, L15 estimated its distance to be of 67 ± 3 kpc. The RR Lyrae also allowed them to find that the systemic metallicity of Lae 3 should be between -1.9 and -1.6 dex. Given its metallicity, size and absolute magnitude ($M_V \sim -4.4$ mag), L15 concluded that Lae 3 was a globular cluster. Its distance placed the satellite in the outer halo, where only a few clusters are known, which made the system interesting to study in greater details. Therefore, to refine its properties and confirm its nature, deep MegaCam photometry and one run of spectroscopic observations with Keck II/DEIMOS were taken for Lae 3 a year later, leading to the study below.

Detailed study of the Milky Way globular cluster Laevens 3

Nicolas Longeard,[1]* Nicolas Martin,[1,2] Rodrigo A. Ibata,[1] Michelle L. M. Collins [ID],[3] Benjamin P. M. Laevens,[4] Eric Bell[5] and Dougal Mackey[6]

[1]*CNRS, Observatoire astronomique de Strasbourg, Université de Strasbourg, UMR 7550, F-67000 Strasbourg, France*
[2]*Max-Planck-Institut für Astronomie, Königstuhl 17, D-69117 Heidelberg, Germany*
[3]*Department of Physics, University of Surrey, Guildford, GU2 7XH Surrey, UK*
[4]*Institute of Astrophysics, Pontificia Universidad Católica de Chile, Av. Vicuña Mackenna 4860, 7820436 Macul, Santiago, Chile*
[5]*Department of Astronomy, University of Michigan, 500 Church St., Ann Arbor, 48109 MI, USA*
[6]*Research School of Astronomy and Astrophysics, Australian National University, Canberra, 2611 ACT, Australia*

ABSTRACT

We present a photometric and spectroscopic study of the Milky Way satellite Laevens 3. Using MegaCam/Canada–France–Hawaii Telescope g and i photometry and Keck II/DEIMOS multi-object spectroscopy, we refine the structural and stellar properties of the system. The Laevens 3 colour–magnitude diagram shows that it is quite metal-poor, old ($13.0 \pm 1.0\,\mathrm{Gyr}$), and at a distance of $61.4 \pm 1.0\,\mathrm{kpc}$, partly based on two RR Lyrae stars. The system is faint ($M_V = -2.8^{+0.2}_{-0.3}\,\mathrm{mag}$) and compact ($r_h = 11.4 \pm 1.0\,\mathrm{pc}$). From the spectroscopy, we constrain the systemic metallicity ($[\mathrm{Fe/H}]_{\mathrm{spectro}} = -1.8 \pm 0.1\,\mathrm{dex}$) but the metallicity and velocity dispersions are both unresolved. Using Gaia DR2, we infer a mean proper motion of $(\mu_\alpha^*, \mu_\delta) = (0.51 \pm 0.28, -0.83 \pm 0.27)\,\mathrm{mas\,yr^{-1}}$, which, combined with the system's radial velocity ($\langle v_r \rangle = -70.2 \pm 0.5\,\mathrm{km\,s^{-1}}$), translates into a halo orbit with a pericenter and apocenter of $40.7^{+5.6}_{-14.7}$ and $85.6^{+17.2}_{-5.9}\,\mathrm{kpc}$, respectively. Overall, Laevens 3 shares the typical properties of the Milky Way's outer halo globular clusters. Furthermore, we find that this system shows signs of mass segregation that strengthens our conclusion that Laevens 3 is a globular cluster.

Key words: Local Group.

1 INTRODUCTION

In recent years, the faint regime of Milky Way (MW) satellites has been explored under the impulsion of large photometric surveys. Among those, we can cite the Sloan Digital Sky Survey (York et al. 2000), the Panoramic Survey Telescope and Rapid Response System 1 (Chambers et al. 2016), or the Dark Energy Survey (The Dark Energy Survey Collaboration 2005). These surveys led to numerous discoveries of faint satellites. Several old and metal-poor faint systems have been identified as globular clusters (GCs; Balbinot et al. 2013; Laevens et al. 2014; Kim & Jerjen 2015; Kim et al. 2016), although some of them require confirmation (Martin et al. 2016c). Because of their old stellar populations, they can be considered as the witnesses of the formation of their host galaxy (Strader et al. 2005) and bring insights on low-mass galaxy formation. Furthermore, the chemodynamics of those GCs can also trace some of the current properties of their host (Pota et al. 2013). GCs can also be useful to constrain stellar population models (Chantereau, Charbonnel & Meynet 2016). The fact that these diffuse and small satellites survived for several billion years can also bring more information on their formation and internal processes (Baumgardt & Makino 2003; Renaud, Agertz & Gieles 2017).

The GCs associated with the MW span a wide range of luminosities, metallicities, and distances (Harris 2010), but only a few have been discovered in the outer reaches of the halo ($R_{\mathrm{gal}} > 50\,\mathrm{kpc}$). This specific group of clusters is in fact suspected to not have formed *in situ*, but rather as companions in nearby dwarf galaxies and accreted at later times in the MW history (Mackey et al. 2010; Dotter, Sarajedini & Anderson 2011). While clusters like Pal 14 (Arp & van den Bergh 1960, $d_{\mathrm{gal}} \sim 71\,\mathrm{kpc}$) or AM-1 (Madore & Arp 1979, $d_{\mathrm{gal}} \sim 125\,\mathrm{kpc}$) have been known for decades, only a handful of fainter outer halo clusters was discovered in recent photometric surveys. Laevens 1/Crater (Belokurov et al. 2014; Laevens et al. 2014) and Kim 2 (Kim et al. 2015) fall in this category. Such faint satellites often lie in the so-called 'valley of ambiguity' where the frontier between dwarf galaxies and old stellar clusters is not clearly defined (Gilmore et al. 2007). Laevens 1 is a great illustration of that, as its very nature was disputed at the time of its discovery. Indeed, while Laevens et al. (2014) identified the system as a cluster, Belokurov et al. (2014) proposed that the satellite could have been a tidally disrupted dwarf galaxy. This example only accentuates the hardship of studying these faint, distant stellar systems. In such an extreme regime, the combination of photometric, chemical, and kinematics data is needed to both classify and understand those systems.

* E-mail: nicolas.longeard@astro.unistra.fr

Laevens 3 (Lae 3) is a system first discovered in the Pan-STARRS 1 (PS1; Chambers et al. 2016) data by Laevens et al. (2015). At the time, it was found to be compact ($r_h = 7 \pm 2$ pc) and the existence of an RR Lyrae star in this region, probably belonging to the system, allowed to constrain the distance to the system (64 ± 3 kpc). Using this distance, Laevens et al. (2015) found that the main sequence of Lae 3 was compatible with a stellar population of 8 Gyr, and a metallicity of [Fe/H] = −1.9. From these properties, the authors concluded that the system is a faint MW GC.

In this work, we undertake a careful refinement of the properties of the satellite through deep broad-band photometry with Canada–France–Hawaii Telescope (CFHT)/MegaCam, as well as the first spectroscopic follow-up of the system using Keck/DEIMOS (Faber et al. 2003). Section 2 discusses the technical aspects of our observations. Section 3 details the photometric analysis that derives the structural and colour–magnitude diagram (CMD) properties of the satellite. In Section 4, we present the dynamics of Lae 3 using multi-object spectroscopy, while Section 5 details the orbital properties of the satellite obtained with the Gaia Data Release 2 data. Finally, the nature and main properties of Lae 3 are discussed in Section 6.

2 OBSERVATIONS

2.1 Photometry

The photometry used in this work consists of multi-exposures MegaCam broad-band g- and i-band images. The exposure times are of 3×480 s for g and 3×540 s for i. The observations were conducted in service mode by the CFHT crew during the night of 2015 July 18, under excellent seeing conditions (~ 0.3 arcsec), and the data reduced following the procedure detailed in Longeard et al. (2018; L18). We use the Cambridge Astronomical Survey Unit (CASU; Irwin & Lewis 2001) pipeline flags to perform the star/galaxy separation. CASU also indicates all saturated sources. The calibration of the MegaCam photometry (Boulade et al. 2003) is performed on to the Pan-STARRS 1 (PS1) photometric system similar to L18. We first cross-identified all unsaturated point sources between PS1 and MegaCam. Only stars with photometric uncertainties below 0.05 in both catalogues are then considered for the calibration. We assume that the transformation between the PS1 and MegaCam photometry can be reliably modelled by a second-order polynomial, with a 3σ clipping procedure.

All stars saturated in the MegaCam photometry are directly imported from the PS1 catalog, for a total of 51 759 stars. Finally, the catalogue is dereddened using the 2D dust map from Schlegel, Finkbeiner & Davis (1998) to determine the line-of-sight extinction and Schlafly & Finkbeiner (2011) for the extinction coefficients.

2.2 Spectroscopy

The spectroscopic run for Lae 3 was performed on the night of 2015 September 7 (Julian date of 2457272.5) using Keck II/DEIMOS. The targets were selected based on their distance to Lae 3 and their location on the CMD, using the PS1 photometry presented in Laevens et al. (2015). A total of 51 stars were observed using the OG550 filter and the 1200 lines mm^{-1} grating. The typical central wavelength resolution is $R \sim 8500$, covering the spectral range from 6500 to 9000 Å. The spectra were then processed using the IRAF SIMULATOR package from the Keck Observatories and

the pipeline detailed in Ibata et al. (2011). Stars with a signal-to-noise ratio below 3 as well as the ones with radial velocity uncertainties above 15 km s^{-1} are discarded from the spectroscopic catalogue. The resulting catalogue consists of 44 stars for which the spatial and CMD distributions are shown in Fig. 1. Finally, the instrumental systematic velocity uncertainty is chosen to be the same as in Longeard et al. (2019), with $\delta_{\text{thr}} = 1.8^{+0.3}_{-0.2}$ km s^{-1}.

3 BROAD-BAND PHOTOMETRY ANALYSIS

The region including Lae 3 is shown in the left-hand panel of Fig. 1, with the stars observed spectroscopically colour-coded by their velocities. The central region of the system is densely populated. The CMD within two half-light radii of Lae 3 is shown in the right-hand panel of Fig. 1. The great depth of the MegaCam photometry allows us to probe the system two magnitudes below the main sequence turn-off and clearly reveals the main sequence of Lae 3. Our spectroscopic sample extends all the way down to the sub-giant branch, and suggests that Lae 3 possesses at least a few red giant branch (RGB) stars. Four RR Lyrae stars are located in the vicinity of the satellite according to the catalogue of Sesar et al. (2017). Among those, only stars with an RRab classification score greater than 90 per cent are selected, as the distance modulus measurement of RRc stars can be biased. Two stars pass this criterion and have a $m - M$ of 18.87 ± 0.06 and 18.89 ± 0.06 mag, respectively. By doing the mean of these two distance moduli, we obtain a distance modulus estimate of 18.88 ± 0.04 mag for Lae 3 ($59.7^{+0.2}_{-1.0}$ kpc in physical distance).

3.1 Structural and CMD fitting

We aim to derive the structural and stellar population properties of Lae 3. As such, we rely on the technique presented in Martin et al. (2016b) and L18. The stellar population parameters that we aim to infer are the age A, metallicity [Fe/H]$_{\text{CMD}}$, the α abundance ratio [α/Fe], and the distance modulus $m - M$. The structural properties that are determined are the spatial offsets of the centroid from the literature values ($\alpha = +316.72635°$, $\delta = +14.98000°$) X_0 and Y_0, the ellipticity ϵ,[1] the half-light radius r_h, the position angle of the major axis θ, and the number of stars $N*$ of the system within the data set.

To derive the structural parameters, the satellite is assumed to follow an exponential radial density profile, while the spatial density of the background is assumed to be constant over the field. The stellar characteristics are determined by assuming that the CMD of the satellite can be considered as the sum of two components: a unique stellar population for Lae 3, and a contamination from the foreground stars. Given the appearance of the Lae 3 sequence in Fig. 1, these assumptions are reasonable as the differences between isochrones in the metal-poor regime are not significant, except in the case of important spreads in both age and metallicity. The modelling of the CMD contamination is done empirically, by selecting all stars outside $5r_h$ of the system. The CMD of this sub-sample is further binned and smoothed by a Gaussian kernel of 0.1 in both colour and magnitude. The Lae 3 stellar population is, on the other hand, modelled using old and metal-poor isochrones from the Darmouth library (Dotter et al. 2008). The Lae 3 likelihood model is built by convolving each isochrone track by the typical photometric

---

[1] The ellipticity is defined as $\epsilon = 1 - \frac{a}{b}$, with a and b the major and minor axes of the ellipse, respectively.
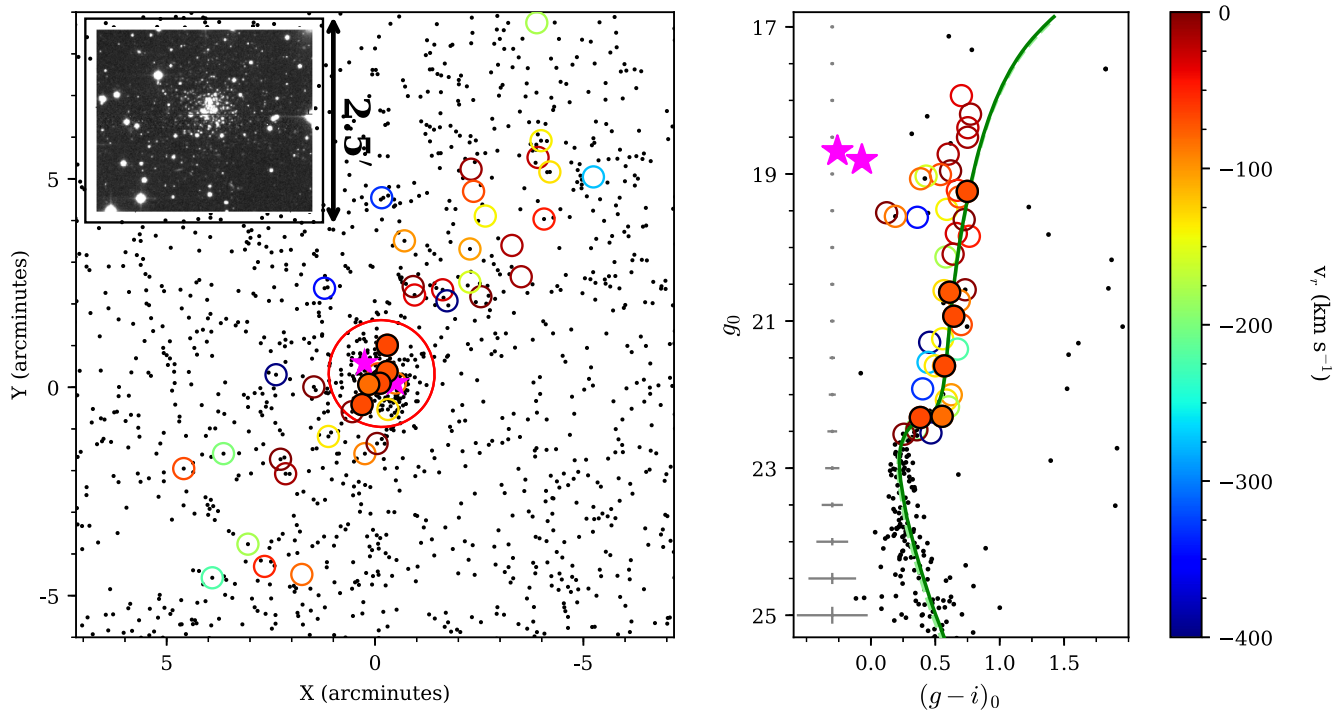
Figure 1. *Left-hand panel:* Spatial distribution of the Lae 3-like stellar population in the field of view. The CFHT image of the 2.5 arcmin × 2.5 arcmin region around Lae 3 in the *i* band is shown in the upper left-hand corner. The red circle represents the two half-light radii ($r_h \sim 0.64$ arcmin) region of Lae 3. The two RR Lyrae identified in the system are shown as the magenta stars. The spectroscopic data set is represented by the circles, colour-coded according to their heliocentric velocities. The filled circles stand for stars identified as Lae 3 members. *Right-hand panel:* CMD within two half-light radii of Lae 3. The best-fitting isochrone derived in Section 3.1 is represented as a solid green line, while the stellar population inferred without any distance or metallicity priors is represented by the light green dashed line. Photometric uncertainties are reported as the grey error bars on the left-hand side of the plot.

uncertainties of the data at a given (g_0, i_0). This model is then weighted by both the luminosity function of the track considered, and the completeness of the data at a given (g_0, i_0). This method is discussed in further details in L18.

The distance inferred using the RR Lyrae in the field can be used as a prior for our analysis. Moreover, and anticipating on Section 4, the spectroscopic analysis of three bright Lae 3 member stars allows us to infer the metallicity of the satellite to be $< [\mathrm{Fe/H}]_\mathrm{spectro} > = -1.8 \pm 0.1$ dex. The Probability Distribution Function (PDF) of this result can also be used as a prior.

The structural and CMD parameters are inferred all together and the results are displayed in Table 1, while the PDFs are shown in Fig. 2. We find that Lae 3 is spherical, with a half-light radius of 0.64 ± 0.05 arcmin that translates into a physical r_h of 11.4 ± 1.0 pc. The measured half-light radius is larger than that of the discovery paper (Laevens et al. 2015; ~ 0.4 arcmin). To investigate this discrepancy, the sample is split between bright ($15.0 < g_0 < 23.5$) and faint ($24.0 < g_0 < 25.0$) stars, and the structural properties of Lae 3 are derived in both cases. A significant difference arises in terms of half-light radius as shown in Fig. 3: the sample of bright stars yields a more compact size than with the faint end of the population. Such a discrepancy would naturally arise in a satellite in which a mass-segregation process has already occurred, and could explain the difference between this work and Laevens et al. (2015), who analysed the system with the shallower PS1 data. To test this, the structural analysis is performed using directly the PS1 data. The resulting PDF is shown as the dashed line in Fig. 3. The half-light radius inferred with this procedure is similar to the one obtained by L15, suggesting that the larger size derived from the MegaCam data is driven by less massive

stars below $g < 22.5$ mag and that Lae 3 is mass segregated. We compute the relaxation time of Lae 3 using the equations of Koposov et al. (2007) and references therein to confirm that the satellite had enough time to mass segregate. We choose a mass-to-light ratio of 2 expected from old GCs (Bell & de Jong 2001), a total luminosity of $1125\,\mathrm{L}_\odot$ determined below, and an average star mass of $0.6\,\mathrm{M}_\odot$. The resulting half-light relaxation time is around 2.2 Gyr, largely smaller than our inference of the age of the satellite (13.0 ± 1.0 Gyr).

Two favoured stellar populations are presented in Fig. 2: with and without using the priors on the metallicity and distance modulus coming, respectively, from the spectroscopic analysis of Section 4 and the two RR Lyrae in the system. Without those priors, Lae 3 is found to be old (13.0 ± 1.0 Gyr) and metal-poor ($< [\mathrm{Fe/H}]_\mathrm{CMD} > = -2.0 \pm 0.1$ dex). The abundance ratio in α elements is $[\alpha/\mathrm{Fe}] = 0.2 \pm 0.2$ dex, while the distance modulus is $m - M = 19.05^{+0.02}_{-0.10}$ mag, i.e. a physical distance of $64.4^{+0.6}_{-3.0}$ kpc. This model is represented as a dashed light green line in Fig. 1 and nicely follows the sequence of the satellite and the spectroscopic members identified in the next section. The favoured model, i.e. the one based on the metallicity and distance priors, is similar. The structural properties, age, metallicity, and α abundance ratio are compatible. However, the satellite is found to be closer ($m - M = 18.94^{+0.05}_{-0.02}$ mag, which translates in a physical distance of $61.4^{+1.2}_{-1.0}$ kpc) in this case. This population, represented as a solid green line in Fig. 1, also follows the features of Lae 3 in the CMD. The two isochrones are barely distinguishable and the last model is the one used in the rest of this work since it is based on a spectroscopic measurement of the metallicity of the system. Using the favoured model, two quantities are defined: a 'CMD probability membership' that assigns a probability to a given star solely based

Table 1. Inferred properties of Lae 3.

Parameter	Unit	Prior	Favoured model	Uncertainties
RA α	deg	–	316.72938021	± 0.00076375
			21:06:55:05	
DEC δ	deg	–	+14.98439985	± 0.00077118
			+ 14:59:03:84	
l	deg	–	63.598	± 0.001
b	deg	–	-21.176	± 0.001
r_h	arcmin	> 0	0.64	± 0.05
r_h	pc	> 0	11.4	± 1.0
θ	deg	[0,180]	72	$^{+24}_{-17}$
ϵ	–	> 0	0.11	$^{+0.09}_{-0.11}$
Distance modulus	mag	$G(18.88, 0.04)$	18.94	$^{+0.05}_{-0.02}$
Distance	kpc		61.4	$^{+1.2}_{-1.0}$
Age	Gyr	[8.0,13.5]	13.0	± 1.0
[Fe/H]$_{\rm spectro}$	dex	–	-1.8	± 0.1
[α/Fe]	dex	[-0.2,0.6]	0.0	± 0.2
M_V	mag	–	-2.8	$^{+0.2}_{-0.3}$
μ_0	mag arcsec^{-2}	–	25.0	± 0.3
$< v_r >$	km s^{-1}	–	-70.2	± 0.5
μ_α^*	mas yr^{-1}	–	0.51	± 0.28
μ_δ	mas yr^{-1}	–	-0.83	± 0.27
Apocenter	kpc	–	85.6	$^{+17.2}_{-5.9}$
Pericenter	kpc	–	40.7	$^{+5.6}_{-14.7}$
$e_{\rm orbit}$	–	> 0	0.60	$^{+0.04}_{-0.06}$
U	km s^{-1}	–	13.1	$^{+64.2}_{-56.4}$
V	km s^{-1}	–	-187.3	$^{+45.1}_{-28.4}$
W	km s^{-1}	–	-211.8	$^{+59.0}_{-46.0}$
L$_z$	km s^{-1} kpc	–	793	$^{+4010}_{-3442}$
E	km^2 s^{-2}	–	20819	$^{+14822}_{-9163}$

on its compatibility with the favoured stellar population of Lae 3 and a 'CMD and spatial probability membership' that also takes the spatial location of a given star into account.

Using this CMD membership probability, we search for potential tidal structures. To do so, the field of view is spatially binned with 0.2 arcmin bins. The CMD probability of all stars falling in a given bin are then added. This procedure therefore assigns higher values to bins that contain stars compatible with the stellar population of Lae 3. The result is shown in Fig. 4. This analysis shows that the satellite is highly spherical and that there is no tidal feature in the field of view compatible with the CMD properties of Lae 3.

The luminosity of the satellite is estimated following the method detailed in Martin et al. (2016a) that consists in simulating thousands of CMDs with the stellar and structural properties of Lae 3 derived earlier, and compute their resulting luminosities. This procedure yields a luminosity of $L_V = 1125^{+221}_{-129} \, {\rm L}_\odot$, translating into an absolute magnitude of $M_V = -2.8^{+0.2}_{-0.3}$ mag. This result is roughly one magnitude fainter than that found by Laevens et al. (2015) in the discovery paper of Lae 3. We observed a similar trend for another faint satellite discovered by Laevens et al. (2015): Draco II (Dra II). In L18, the inferred luminosity was significantly lower than found in the 2015 paper, and we concluded that it is most likely due to the overestimation of the number of giants in the system, probably due to the shallowness of the PS1 data used for the discovery of both Lae 3 and Dra II. Though Lae 3 is clearly brighter than Dra II, it is also significantly more distant, and the same overestimation effect might have affected the result of Laevens et al. (2015), as using the same technique for a brighter MW satellite (Longeard et al. 2019) did not yield such an effect.

4 SPECTROSCOPIC ANALYSIS

The distribution of the heliocentric velocities for all stars in our spectroscopic sample is shown in the top panel of Fig. 5, along with their radial distances and spectroscopic metallicities (if possible). The properties of the entire sample are described in Table 2.

4.1 Dynamical properties

The Lae 3 population is not prominent, and its systemic velocity overlaps that of the foreground MW stars (Fig. 5). Our approach is similar to L18: the velocity distribution is assumed to be the sum of the contamination (halo and disc stars) and the Lae 3 population, both modelled with different normal distributions. To highlight Lae 3's population in the spectroscopic data set, the individual likelihood of each star is weighted by its spatial and CMD probability estimated from the favoured structural model of Section 3 (Collins et al. 2010). This analysis yields a systemic radial velocity of $< v_r >= -70.2 \pm 0.5$ km s^{-1}. The 1D marginalized PDFs of the velocity parameters are represented in the left-hand panels of Fig. 6. As a consequence to the low number of Lae 3 stars, the velocity dispersion is unresolved. Finally, six stars with a dynamical, structural, and CMD membership probability greater than 90 per cent are identified as Lae 3 members and shown as the filled circles in Fig. 5.

4.2 Spectroscopic metallicity

The individual metallicities of stars observed with spectroscopy can be estimated using the calibration of the Calcium triplet (Starken-
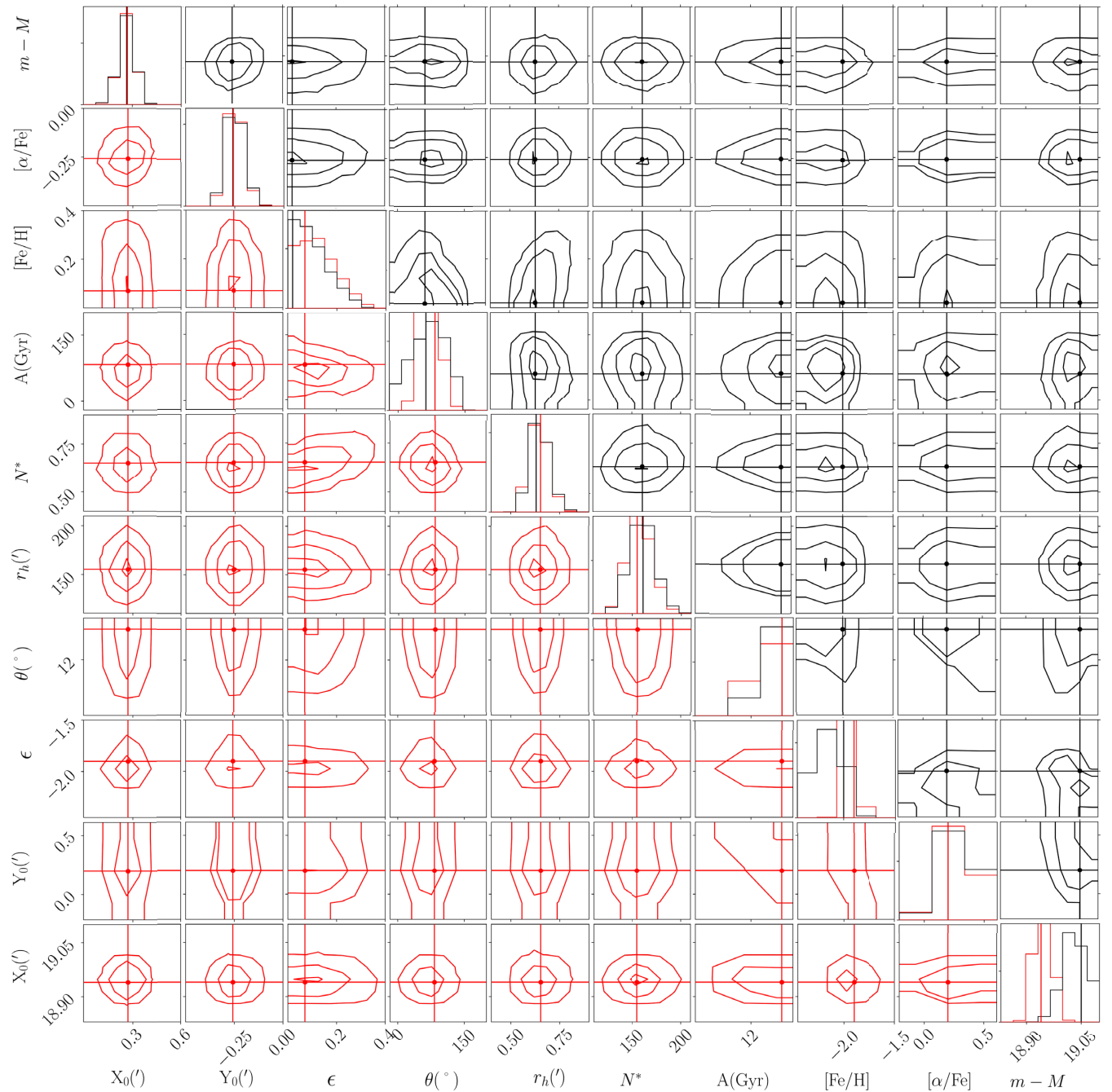
Figure 2. 1D and 2D posterior PDFs of the structural and CMD parameters of Lae 3, inferred using the method described in Section 3.1. Contours correspond to the usual 1σ, 2σ, and 3σ confidence intervals in the case of a 2D Gaussian. The red solid lines correspond to the analysis using both the distance and metallicity priors described in Section 3, while the black lines represent the case without any prior applied. The black and red dots correspond to the favoured model in each case.

burg et al. 2010) for RGB stars, and shown in Fig. 5. Member stars fainter than 21 in the *g* band, and with S/N < 10 are further discarded from our spectroscopic catalogue. Only three stars are left to infer the systemic metallicity and metallicity dispersion of Lae 3, by assuming that the metallicities are normally distributed. This yields a spectroscopic metallicity of $[Fe/H]_{spectro} = -1.8 \pm 0.1$ dex. The same analysis is also performed using the calibration of Carrera et al. (2013) for metal-poor stars on the RGB and sub-RGB branch, and yields compatible results. Once more, low-number statistics has a direct consequence on our ability to constrain efficiently the metallicity dispersion, which is found to be unresolved,

with $\sigma_{[Fe/H]} < 0.5$ dex at the 95 per cent confidence level. The PDFs of both parameters are shown in the right-hand panels of Fig. 6.

5 GAIA DR2 PROPER MOTIONS AND ORBIT

To infer the orbital properties of Lae 3, we cross-match all spectroscopic members and RR Lyrae stars with the Gaia Data Release 2 (Gaia Collaboration 2018). Among those, four stars have a proper motion (PM) measurement in Gaia. Furthermore,
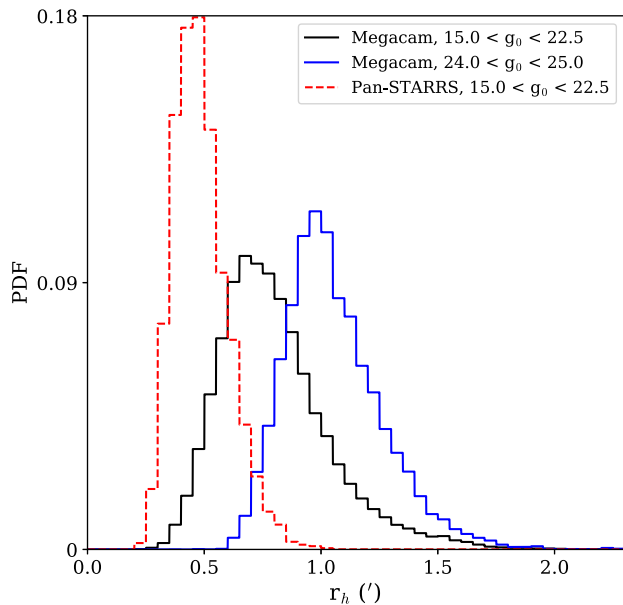
Figure 3. 1D PDFs of the half-light radius of Lae 3 in three cases: using stars with $15.0 < g_0 < 22.5$ in MegaCam (the solid black line), stars with $24.0 < g_0 < 25.0$ (the solid blue line) in MegaCam, and the PS1 catalog (the dashed red line). The magnitude ranges in the first two cases were chosen so that the inferred numbers of Lae 3 stars are similar. Lae 3 comes out as larger when considering lower mass stars than when the analysis is performed on a more massive sample, hinting at a mass-segregation process. The size of the satellite inferred by L15 is retrieved when using their data, indicating that this effect is not caused by a problem in our approach or a statistical fluke.

all stars in the Gaia catalog with a CMD and structural membership probability greater than 90 per cent are included. Six additional stars are retrieved through this procedure, and their PMs are compatible with those of the spectroscopic members, as shown in Fig. 7. The uncertainty-weighted average PM of Lae 3 yields $\mu_\alpha^{*,\mathrm{Lae3}} = \mu_\alpha^{\mathrm{Lae3}} \cos(\delta) = 0.51 \pm 0.28$ mas yr^{-1} and $\mu_\delta^{\mathrm{Lae3}} = -0.83 \pm 0.27$ mas yr^{-1}. These measurements take into account the systematic error of 0.035 mas yr^{-1} on the PMs for dSph as shown by Helmi et al. (2018). We point out that this choice of systematic error does not change our results, given the measured uncertainties on the PM of the satellite.

We use the GALPY package (Bovy 2015) to integrate the orbit of Lae 3. The MW potential chosen to integrate Lae 3 orbit is a variant of the 'MWPotential14' defined within GALPY, but updated with a halo mass of 1.2×10^{12} M$_\odot$ (Bland-Hawthorn & Gerhard 2016). A total of 5000 orbits are integrated backwards and forwards over 5 Gyr, each time by randomly drawing a position, distance, radial velocity, and PMs from their corresponding PDFs. Around 20 per cent of the resulting orbits are not bound to the MW. In the case where Lae 3 is bound to the MW, the pericenter is at $40.7^{+5.6}_{-14.7}$ kpc and the apocenter is at $85.6^{+17.2}_{-5.9}$ kpc. The favoured orbit of the satellite is shown as a solid blue line in Fig. 8 and corresponds to a typical outer halo orbit. In the unbound case, the apocenter is undefined and the pericenter is larger, at $59.1^{+0.7}_{-2.1}$ kpc.

6 DISCUSSION AND CONCLUSIONS

We present in this paper an analysis of the faint satellite Lae 3 using deep MegaCam/CFHT broad-band g- and i-band photometry of Lae 3 as well as multi-object spectroscopy observed with Keck
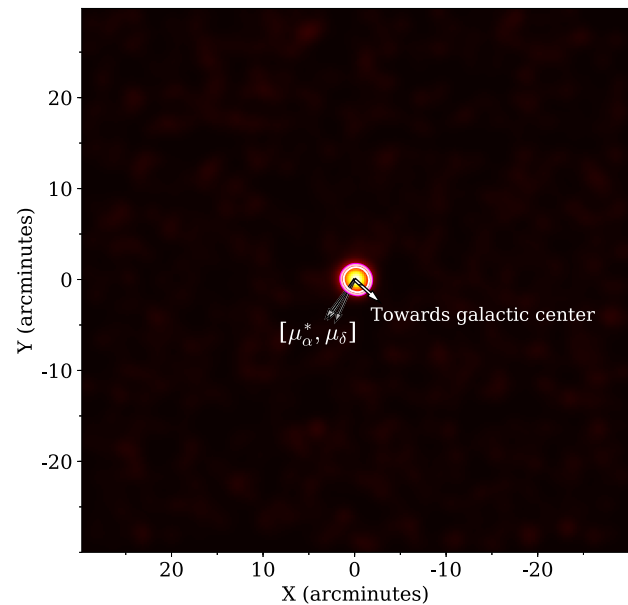
Figure 4. Density plot for all stars with $P_{\mathrm{mem}} > 0.01$ over the field of view. The magenta, pink, and white lines outline the regions with a density higher than 68, 95, and 99 per cent of the background pixel distribution. The proper motion of Lae 3 is shown with the grey arrows along with its uncertainties, while the direction towards the Galactic centre is indicated with a white arrow. No tidal features is detected in the vicinity of the satellite.
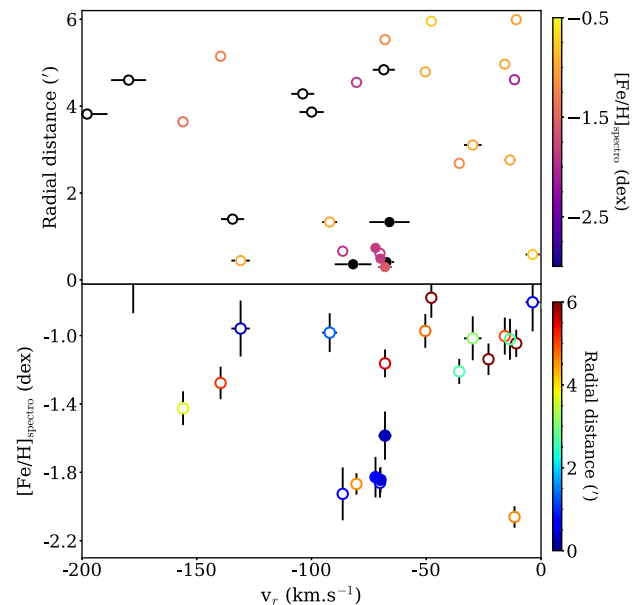
Figure 5. Heliocentric velocities versus radial distances (top panel) and spectroscopic metallicities (bottom panel). The coloured circles are non-HB stars with an S/N greater than 10, for which we are able to derive the spectroscopic metallicities. The colour maps stand for the metallicity (top) and radial distance (bottom). The spectroscopic members are shown as the filled dots.

II/DEIMOS. Lae 3 has a systemic velocity that overlaps with the MW foreground contamination: $\langle v_r \rangle = -70.2 \pm 0.5$ km s^{-1}, but an unresolved velocity dispersion. Using these results, six stars are unambiguously identified as Lae 3 members, and three are bright enough to be used to estimate the systemic metallicity of the satellite. Lae 3 comes out as a fairly metal-poor stellar

Table 2. Properties of our spectroscopic sample. Confirmed members are denoted by 'Y' and non-members by 'N'. The star denoted 'Y?' is a plausible member, as its position, spectroscopic metallicity, and velocity are compatible with those of Lae 3. However, it is not confirmed as it does not pass our membership probability cut ($P_{mem} \geq 90$ per cent).

RA (deg)	Dec. (deg)	g_0	i_0	v_r (km s^{-1})	μ_α^* (mas yr^{-1})	μ_δ (mas yr^{-1})	S/N	(Fe/H)$_{spectro}$	P_{mem}	Member
316.71305417	15.01271111	17.94 ± 0.01	17.23 ± 0.01	−35.6 ± 1.4	3.647 ± 0.221	−3.548 ± 0.242	39.3	−1.21 ± 0.07	0.00	N
316.68967917	15.06302222	18.19 ± 0.01	17.41 ± 0.01	−10.8 ± 1.4	−0.763 ± 0.239	−0.821 ± 0.254	36.3	−1.05 ± 0.08	0.00	N
316.67275417	15.03253056	18.73 ± 0.01	18.13 ± 0.01	−15.8 ± 1.7	−5.232 ± 0.413	−8.422 ± 0.403	22.1	−1.0 ± 0.11	0.00	N
316.68561250	15.01203889	18.96 ± 0.01	18.34 ± 0.01	8.1 ± 2.1	−2.672 ± 0.44	−6.607 ± 0.465	21.9	−1.15 ± 0.1	0.00	N
316.68863750	15.05416944	19.01 ± 0.01	18.47 ± 0.01	−68.0 ± 1.4	−1.407 ± 0.459	−2.176 ± 0.464	26.9	−1.16 ± 0.08	0.00	N
316.69020000	15.01787500	19.03 ± 0.01	18.60 ± 0.01	−156.0 ± 1.6	−2.898 ± 0.505	−7.339 ± 0.511	20.0	−1.43 ± 0.1	0.00	N
316.68378750	15.04429167	19.48 ± 0.01	18.89 ± 0.01	−139.6 ± 1.6	−2.633 ± 0.625	−13.336 ± 0.613	23.3	−1.28 ± 0.09	0.00	N
316.71363750	15.01609167	19.53 ± 0.01	19.41 ± 0.01	429.0 ± 2.6	−0.284 ± 0.873	−0.101 ± 0.927	20.8	−2.95 ± 0.14	0.00	N
316.75032500	15.01542778	19.59 ± 0.01	19.23 ± 0.01	−346.7 ± 1.6	−2.236 ± 0.853	−1.489 ± 0.947	24.0	−1.96 ± 0.08	0.00	N
316.70143333	15.01480278	19.81 ± 0.01	19.15 ± 0.01	−29.7 ± 3.8	−4.405 ± 0.758	−0.392 ± 0.796	18.5	−1.02 ± 0.13	0.01	N
316.69964167	15.01039167	21.29 ± 0.01	20.83 ± 0.01	−515.3 ± 3.0	− ± −	− ± −	9.1	− ± −	0.00	N
316.69013750	15.03111667	21.61 ± 0.01	21.05 ± 0.01	−103.8 ± 5.0	− ± −	− ± −	8.0	− ± −	0.01	N
316.72665833	15.05161389	21.92 ± 0.01	21.52 ± 0.01	−331.2 ± 3.6	− ± −	− ± −	5.4	− ± −	0.00	N
316.71725417	15.03437222	22.00 ± 0.01	21.38 ± 0.01	−99.9 ± 5.3	− ± −	− ± −	6.4	− ± −	0.01	N
316.72435000	14.99263333	22.31 ± 0.02	21.93 ± 0.02	−66.0 ± 8.8	− ± −	− ± −	4.3	− ± −	0.99	Y
316.66194583	15.06772222	18.37 ± 0.01	17.62 ± 0.01	−229 ± 1.4	1033 ± 0.276	0.696 ± 0.289	30.0	−1.14 ± 0.09	0.00	N
316.66891250	15.02001944	18.50 ± 0.01	17.75 ± 0.01	−11.5 ± 1.1	1.047 ± 0.322	−1.302 ± 0.317	29.3	−2.06 ± 0.06	0.00	N
316.65947083	15.04309444	19.85 ± 0.01	19.08 ± 0.01	−47.8 ± 1.9	−3.144 ± 0.76	−4.985 ± 0.724	20.7	−0.78 ± 0.12	0.00	N
316.66246667	15.12159167	20.13 ± 0.01	19.55 ± 0.01	−177.7 ± 2.8	0.483 ± 1.105	−6.195 ± 0.963	21.7	−0.61 ± 0.26	0.00	N
316.66070833	15.07443611	21.24 ± 0.01	20.68 ± 0.01	−138.4 ± 4.7	− ± −	− ± −	9.5	− ± −	0.00	N
316.63902917	15.05994444	21.56 ± 0.01	21.12 ± 0.01	−274.5 ± 11.8	− ± −	− ± −	5.9	− ± −	0.00	N
316.65706250	15.06192222	22.07 ± 0.01	21.49 ± 0.01	−131.8 ± 6.9	− ± −	− ± −	5.0	− ± −	0.00	N
316.80862500	14.94329722	21.05 ± 0.01	20.35 ± 0.01	−68.5 ± 4.8	− ± −	− ± −	12.2	− ± −	0.00	N
316.79680833	14.89063056	21.38 ± 0.01	20.71 ± 0.01	−221.0 ± 4.5	− ± −	− ± −	8.7	− ± −	0.00	N
316.79215417	14.94927500	22.47 ± 0.02	22.11 ± 0.02	−197.8 ± 8.9	− ± −	− ± −	3.3	− ± −	0.13	N
316.75973333	14.90096111	19.07 ± 0.01	18.68 ± 0.01	−80.4 ± 2.0	0.335 ± 0.641	−2.754 ± 0.557	26.2	−1.87 ± 0.06	0.00	N
316.77516250	14.90417500	19.22 ± 0.01	18.55 ± 0.01	−50.4 ± 1.9	−1.68 ± 0.596	−8.502 ± 0.498	27.5	−0.97 ± 0.1	0.00	N
316.72701667	14.97872778	19.24 ± 0.01	18.49 ± 0.01	−69.9 ± 1.6	1.565 ± 0.53	−1.232 ± 0.523	23.3	−1.84 ± 0.07	0.98	Y
316.72812500	14.98119167	19.31 ± 0.01	18.63 ± 0.01	−70.2 ± 1.4	0.31 ± 0.608	−0.609 ± 0.592	22.5	−1.86 ± 0.09	0.36	Y?
316.72099583	14.97752500	19.58 ± 0.01	19.39 ± 0.01	−86.4 ± 2.1	0.758 ± 0.852	2.285 ± 0.871	20.0	−1.93 ± 0.15	0.00	N
316.76855417	14.94703889	19.62 ± 0.01	18.90 ± 0.01	2.9 ± 1.8	−4.84 ± 0.79	−3.869 ± 0.784	25.6	−0.83 ± 0.1	0.16	N
316.76643750	14.94122778	20.09 ± 0.01	19.45 ± 0.01	−13.5 ± 2.3	−2.702 ± 1.02	−5.581 ± 1.006	19.0	−1.02 ± 0.12	0.02	N
316.73886667	14.96605556	20.57 ± 0.01	19.84 ± 0.01	−3.6 ± 3.1	−1.88 ± 1.572	−1.143 ± 1.61	15.6	−0.81 ± 0.17	0.45	N
316.72408750	14.96693889	20.59 ± 0.01	20.02 ± 0.01	−130.9 ± 4.0	1.839 ± 2.395	−0.506 ± 1.892	14.5	−0.96 ± 0.16	0.63	N
316.72444583	14.98208333	20.61 ± 0.01	20.00 ± 0.01	−72.1 ± 1.7	−0.0 ± 2.13	0.456 ± 2.024	15.0	−1.83 ± 0.12	0.99	Y
316.73362500	14.94926389	20.72 ± 0.01	20.04 ± 0.01	−92.1 ± 3.2	−0.211 ± 2.05	−3.577 ± 2.068	14.5	−0.98 ± 0.11	0.86	Y
316.73480000	14.96889167	20.93 ± 0.01	20.29 ± 0.01	−68.0 ± 2.9	− ± −	− ± −	13.3	−1.59 ± 0.14	1.00	Y
316.74872917	14.95614167	21.61 ± 0.01	21.11 ± 0.01	−134.4 ± 5.1	− ± −	− ± −	8.2	− ± −	0.09	N
316.72737500	14.97743611	21.61 ± 0.01	21.04 ± 0.01	−67.4 ± 3.4	− ± −	− ± −	7.5	− ± −	1.00	Y
316.78203333	14.91307778	22.17 ± 0.01	21.56 ± 0.01	−179.7 ± 7.6	− ± −	− ± −	5.3	− ± −	0.00	N
316.73203333	14.97697778	22.30 ± 0.02	21.74 ± 0.02	−81.9 ± 8.0	− ± −	− ± −	4.5	− ± −	1.00	Y
316.72857917	14.95332778	22.48 ± 0.02	22.12 ± 0.02	60.1 ± 9.2	− ± −	− ± −	3.5	− ± −	1.00	Y
316.77040833	14.98083611	22.52 ± 0.02	22.05 ± 0.02	−437.6 ± 3.9	− ± −	− ± −	4.1	− ± −	0.07	N
316.75475417	14.97596389	22.54 ± 0.02	22.28 ± 0.02	738.4 ± 15.1	− ± −	− ± −	3.2	− ± −	1.00	N
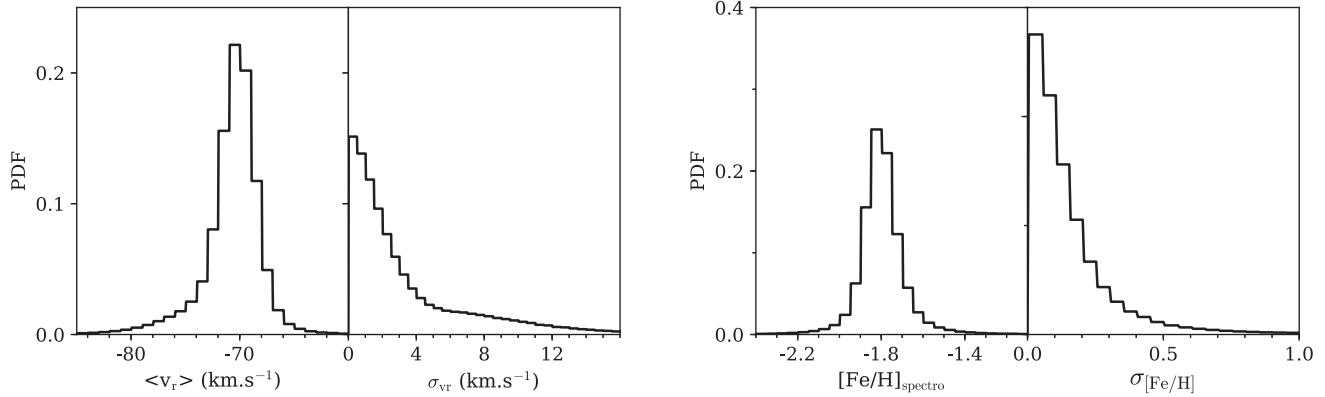
Figure 6. *Left-hand panels:* 1D marginalized PDFs of the systemic velocity and its associated dispersion. *Right-hand panels:* 1D marginalized PDFs of the systemic metallicity and its associated dispersion. The two measurements of the dispersions are unresolved.
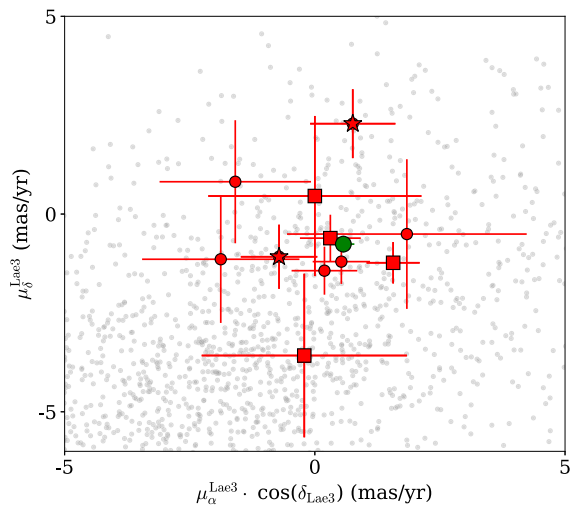
Figure 7. PMs of all stars within $15'$ of Lae 3. The grey transparent dots show the PMs of field stars. The measurements of the four spectroscopic members with PM in Gaia DR2 are represented as the squares, while the red stars and the dots, respectively, show the PMs of the RR Lyrae stars as well as the spatially and CMD selected stars. The large green dot marks the combined PM measurement of Lae 3.

system: $\langle[\mathrm{Fe/H}]_{\mathrm{spectro}}\rangle = -1.8 \pm 0.1$ dex that places Lae 3 far off the luminosity–metallicity relation of dwarf galaxies (Kirby et al. 2013) as shown in Fig. 9. The metallicity dispersion is also unresolved. Similar to Laevens et al. (2015), two RR Lyrae stars are used to estimate the distance of Lae 3, and yield a distance modulus of 18.88 ± 0.04 mag. Using these results as priors, we derive the structural and CMD properties and find a half-light radius of 11.4 ± 1.0 pc, a marginally resolved ellipticity and a final distance modulus measurement of $18.94^{+0.05}_{-0.02}$ mag. A discrepancy between the half-light radius of Lae 3 derived using bright and faint stars hints that the satellite is mass segregated. This hypothesis is strengthened by the relaxation time of the satellite of ~ 2.2 Gyr, much smaller than the age of the satellite found to be 13.0 ± 1.0 Gyr by our CMD fitting procedure. The sphericity of Lae 3 and an analysis of the density of Lae 3-like stars in the field show no clear sign of tidal features that might hint at a perturbation of the system and therefore its ability to mass segregate. The favoured stellar population is metal-poor, not particularly enriched in α elements, and at a distance of $61.4^{+1.2}_{-1.0}$ kpc. Finally, the orbit calculation yields an outer halo orbit, with a pericenter of $40.7^{+5.6}_{-14.7}$ kpc and an apocenter of $85.6^{+17.2}_{-5.9}$ kpc.

Lae 3 shows the main characteristics of MW GCs: the satellite is fairly spherical and is at the same time more compact and metal-rich than DGs of the same luminosity (McConnachie 2012; Kirby et al. 2013), such as Ret II ($M_V \sim -2.7$), Hor I ($M_V \sim -3.4$)
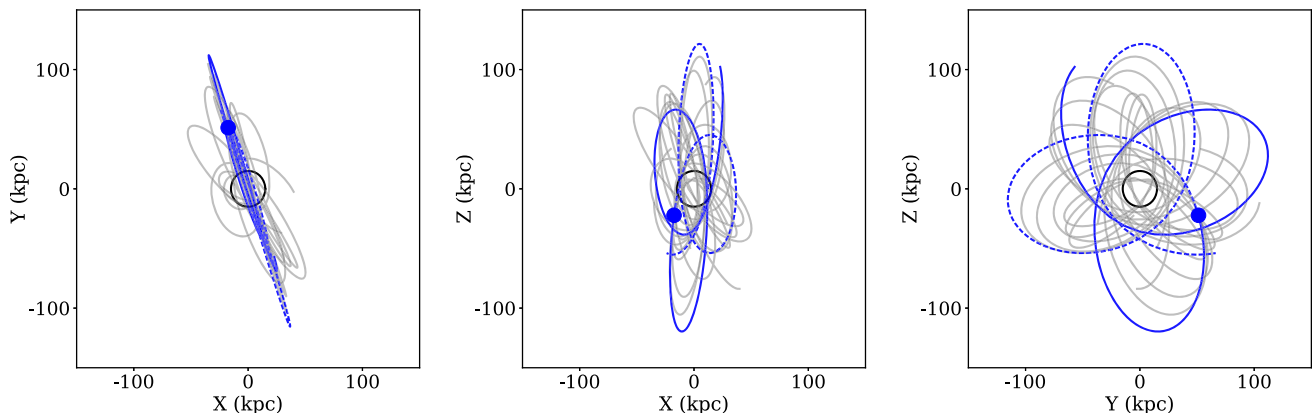
Figure 8. Orbits of Lae 3 in the X–Y, X–Z, and Y–Z planes integrated over 5 Gyr. The blue line is the orbit for the favoured distance, radial velocity, position, and proper motion. The grey, transparent lines are random realizations of the orbit. The MW is represented by the black circle ($R_{\mathrm{MW}} = 15$ kpc), while the blue dot indicates the location of Lae 3 at present day.
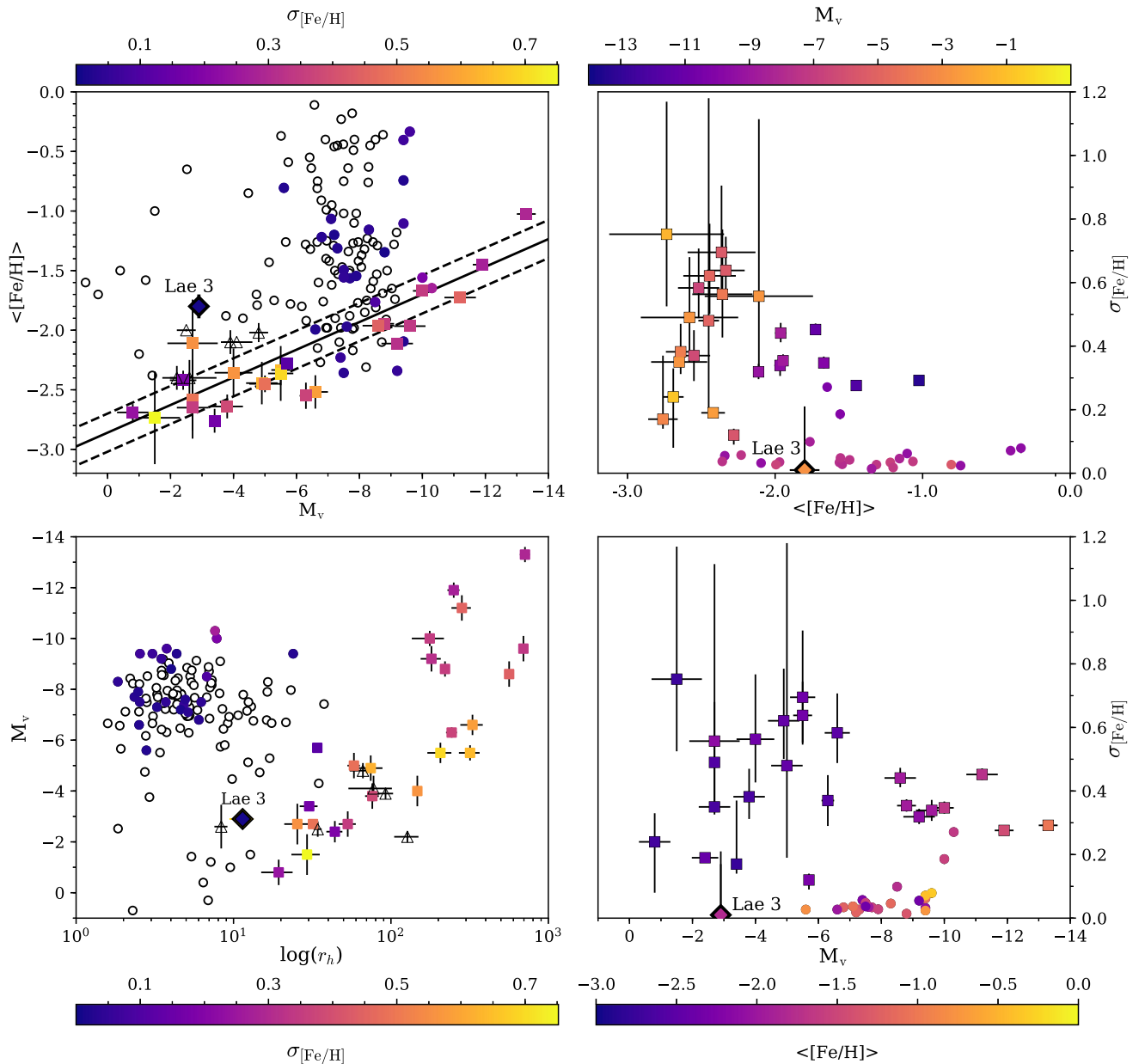
Figure 9. Comparison of Lae 3 with other GCs and dwarf galaxies of the Milky Way. The squares represent dwarf galaxies, while the circles represent globular clusters, and the diamond corresponds to Lae 3. The triangles stand for recently discovered dwarf-galaxy candidates that await confirmation. The hollow markers correspond to systems for which no metallicity dispersion measurement can be found in the literature. The solid line in the top left-hand panel corresponds to the luminosity–metallicity relation of Kirby et al. (2013) for dwarf spheroidals and dwarf irregulars. The dashed lines represent the RMS about this relation, also taken from Kirby et al. (2013). Among the 123 globular clusters presented here, the properties of 116 were extracted from Harris (1996) catalogue, revised in 2010. For the remaining ones (Kim 1, Kim 2, Kim 3, Laevens 1, Balbinot 1, Munoz 1, and SMASH 1), parameters of the discovery publications were used (Kim & Jerjen 2015, Kim et al. 2015, Kim et al. 2016, Laevens et al. 2014, Balbinot et al. 2013, Muñoz et al. 2012, and Martin et al. 2016c). Globular cluster metallicity spread measurements are taken from Willman & Strader (2012) and references therein: Carretta et al. (2006), Carretta et al. (2007), Carretta et al. (2009), Carretta et al. (2011), Cohen et al. (2010), Gratton et al. (2007), Johnson & Pilachowski (2010), and Marino et al. (2011). McConnachie (2012) and Willman & Strader (2012) are used to compile the properties of the dwarf galaxies represented here. The 18 dwarf galaxies represented here are Bootes I (Belokurov et al. 2006; Norris et al. 2010), Canes Venatici I (Zucker et al. 2006b), Canes Venatici II (Sakamoto & Hasegawa 2006), Coma Berinices, Hercules, Leo IV and Segue I (Belokurov et al. 2007), Draco and Ursa Minor (Wilson 1955), Fornax (Shapley 1938b), Leo I and Leo II (Harrington & Wilson 1950), Pisces II (Belokurov et al. 2010), Sculptor (Shapley 1938a), Sextans (Irwin et al. 1990), Ursa Major I (Willman et al. 2005b), Ursa Major II (Zucker et al. 2006a), and Willman I (Willman et al. 2005a). Their metallicity and metallicity spreads were drawn from Kirby et al. (2008), Kirby et al. (2010), Norris et al. (2010), and Willman et al. (2011). The dwarf galaxy candidates discovered recently and shown on this figure are Bootes II (Koch & Rich 2014), DES1 (Luque et al. 2016; Conn et al. 2018), Eridanus III (Bechtol et al. 2015; Koposov et al. 2015b; Conn et al. 2018), Hyades II (Martin et al. 2015), Pegasus III (Kim & Jerjen 2015), Reticulum II and Horologium I (Koposov et al. 2015a), Segue II (Belokurov et al. 2009), and the most significant candidates of Drlica-Wagner et al. (2015): Gru II, Tuc III, and Tuc IV.

or Boo II ($M_V \sim -2.7$) as shown in the bottom left-hand panel of Fig. 9. Regarding the size and Galactocentric distance of the satellite, Lae 3 can be compared to SMASH 1 (Martin et al. 2016c). SMASH 1 has a size of $9.1^{+5.9}_{-3.4}$ pc, and is lying at ~ 57 kpc of the centre of the Galaxy. The location and distance of SMASH 1 imply that it may be a satellite of the Large Magellanic Cloud. However, Lae 3 is brighter (-2.8 versus -1.0 mag) and is more metal-rich (-1.8 versus -2.2 dex). The top left-hand panel of Fig. 9 shows that the systemic metallicity of Lae 3 is offset by ~ 0.7 dex from the metallicity–luminosity relation of dwarf galaxies (Kirby et al. 2013). We have to turn to Pal 1 or Pal 13 (Harris 2010) to find a cluster with a luminosity comparable to the one of Lae 3 (respectively, of ~ -2.5 and ~ -3.8 mag). Still, these two GCs are much more compact, with a size of the order of the parsec.

Both the velocity and metallicity dispersions of Lae 3 are unresolved, although the small number of member stars in our spectroscopic data set does not give stringent enough constraints to rule out a dynamically hot system or that it is chemically enriched (right-hand panels of Fig. 9). Lae 3 is possibly mass segregated, which implies that its internal dynamics is ruled by purely baryonic two-bodies interactions (Kim et al. 2015) and it is statistically incompatible with the luminosity–metallicity relation of DGs. We therefore conclude that Lae 3 likely is an MW outer halo GC.

REFERENCES

Arp H., van den Bergh S., 1960, PASP, 72, 48
Balbinot E. et al., 2013, ApJ, 767, 101
Baumgardt H., Makino J., 2003, MNRAS, 340, 227
Bechtol K. et al., 2015, ApJ, 807, 50
Bell E. F., de Jong R. S., 2001, ApJ, 550, 212
Belokurov V. et al., 2006, ApJ, 647, L111
Belokurov V. et al., 2007, ApJ, 654, 897
Belokurov V. et al., 2009, MNRAS, 397, 1748
Belokurov V. et al., 2010, ApJ, 712, L103
Belokurov V., Irwin M. J., Koposov S. E., Evans N. W., Gonzalez-Solares E., Metcalfe N., Shanks T., 2014, MNRAS, 441, 2124
Bland-Hawthorn J., Gerhard O., 2016, ARA&A, 54, 529
Boulade O. et al., 2003, SPIE, 4841, 72
Bovy J., 2015, ApJS, 216, 29
Carrera R., Pancino E., Gallart C., del Pino A., 2013, MNRAS, 434, 1681
Carretta E., Bragaglia A., Gratton R. G., Leone F., Recio-Blanco A., Lucatello S., 2006, A&A, 450, 523
Carretta E. et al., 2007, A&A, 464, 967
Carretta E. et al., 2009, A&A, 505, 117
Carretta E., Lucatello S., Gratton R. G., Bragaglia A., D'Orazi V., 2011, A&A, 533, A69
Chambers K. C. et al., 2016, preprint (arXiv:1612.05560)
Chantereau W., Charbonnel C., Meynet G., 2016, A&A, 592, A111
Cohen J. G., Kirby E. N., Simon J. D., Geha M., 2010, ApJ, 725, 288
Collins M. L. M. et al., 2010, MNRAS, 407, 2411
Conn B. C., Jerjen H., Kim D., Schirmer M., 2018, ApJ, 852, 68
Dotter A., Chaboyer B., Jevremović D., Kostov V., Baron E., Ferguson J. W., 2008, ApJS, 178, 89
Dotter A., Sarajedini A., Anderson J., 2011, ApJ, 738, 74
Drlica-Wagner A. et al., 2015, ApJ, 813, 109
Faber S. M. et al., 2003, SPIE, 4841, 1657
Gaia Collaboration, 2018, A&A, 616, A1
Gilmore G., Wilkinson M. I., Wyse R. F. G., Kleyna J. T., Koch A., Evans N. W., Grebel E. K., 2007, ApJ, 663, 948
Gratton R. G. et al., 2007, A&A, 464, 953
Harrington R. G., Wilson A. G., 1950, PASP, 62, 118
Harris W. E., 1996, AJ, 112, 1487
Harris W. E., 2010, preprint (arXiv:1012.3224)
Helmi A., Babusiaux C., Koppelman H. H., Massari D., Veljanoski J., Brown A. G. A., 2018, Nature, 563, 85
Ibata R., Sollima A., Nipoti C., Bellazzini M., Chapman S. C., Dalessandro E., 2011, ApJ, 738, 186
Irwin M., Lewis J., 2001, New Astron. Rev., 45, 105

Irwin M. J., Bunclark P. S., Bridgeland M. T., McMahon R. G., 1990, MNRAS, 244, 16P

Johnson C. I., Pilachowski C. A., 2010, ApJ, 722, 1373

Kim D., Jerjen H., 2015, ApJ, 799, 73

Kim D., Jerjen H., Milone A. P., Mackey D., Da Costa G. S., 2015, ApJ, 803, 63

Kim D., Jerjen H., Mackey D., Da Costa G. S., Milone A. P., 2016, ApJ, 820, 119

Kirby E. N., Simon J. D., Geha M., Guhathakurta P., Frebel A., 2008, ApJ, 685, L43

Kirby E. N. et al., 2010, ApJS, 191, 352

Kirby E. N., Cohen J. G., Guhathakurta P., Cheng L., Bullock J. S., Gallazzi A., 2013, ApJ, 779, 102

Koch A., Rich R. M., 2014, ApJ, 794, 89

Koposov S. et al., 2007, ApJ, 669, 337

Koposov S. E., Belokurov V., Torrealba G., Evans N. W., 2015a, ApJ, 805, 130

Koposov S. E. et al., 2015b, ApJ, 811, 62

Laevens B. P. M. et al., 2014, ApJ, 786, L3

Laevens B. P. M. et al., 2015, ApJ, 813, 44

Longeard N. et al., 2018, MNRAS, 480, 2609

Longeard N. et al., 2019, preprint (arXiv:1902.02780)

Luque E. et al., 2016, MNRAS, 458, 603

Mackey A. D. et al., 2010, ApJ, 717, L11

Madore B. F., Arp H. C., 1979, ApJ, 227, L103

Marino A. F. et al., 2011, A&A, 532, A8

Martin N. F. et al., 2015, ApJ, 804, L5

Martin N. F. et al., 2016a, MNRAS, 458, L59

Martin N. F. et al., 2016b, ApJ, 833, 167

Martin N. F. et al., 2016c, ApJ, 830, L10

McConnachie A. W., 2012, AJ, 144, 4

Muñoz R. R., Geha M., Côté P., Vargas L. C., Santana F. A., Stetson P., Simon J. D., Djorgovski S. G., 2012, ApJ, 753, L15

Norris J. E., Wyse R. F. G., Gilmore G., Yong D., Frebel A., Wilkinson M. I., Belokurov V., Zucker D. B., 2010, ApJ, 723, 1632

Pota V. et al., 2013, MNRAS, 428, 389

Renaud F., Agertz O., Gieles M., 2017, MNRAS, 465, 3622

Sakamoto T., Hasegawa T., 2006, ApJ, 653, L29

Schlafly E. F., Finkbeiner D. P., 2011, ApJ, 737, 103

Schlegel D. J., Finkbeiner D. P., Davis M., 1998, ApJ, 500, 525

Sesar B. et al., 2017, AJ, 153, 204

Shapley H., 1938a, Harvard College Observatory Bulletin, 908, 1

Shapley H., 1938b, Nature, 142, 715

Starkenburg E. et al., 2010, A&A, 513, A34

Strader J., Brodie J. P., Cenarro A. J., Beasley M. A., Forbes D. A., 2005, AJ, 130, 1315

The Dark Energy Survey Collaboration, 2005, preprint (astro-ph/0510346)

Willman B., Strader J., 2012, AJ, 144, 76

Willman B. et al., 2005a, AJ, 129, 2692

Willman B. et al., 2005b, ApJ, 626, L85

Willman B., Geha M., Strader J., Strigari L. E., Simon J. D., Kirby E., Ho N., Warres A., 2011, AJ, 142, 128

Wilson A. G., 1955, PASP, 67, 27

York D. G. et al., 2000, AJ, 120, 1579

Zucker D. B. et al., 2006a, ApJ, 650, L41

Zucker D. B. et al., 2006b, ApJ, 643, L103

This paper has been typeset from a TEX/LATEX file prepared by the author.

Summary and perspectives **6**

6.1 Summary

My three years of PhD were mainly dedicated to the study and the understanding of three faint satellites of the MW: Dra II, Sgr II and Lae 3. I will now briefly summarise the results of my work.

▶ Chapter 3 is dedicated to the detailed study of the faint MW satellite Dra II (Longeard et al., 2018) discovered by L15. The intriguing satellite was the target of deep Mega-Cam/CFHT photometric and Keck II/DEIMOS spectroscopic observations. Furthermore, Dra II was also specifically targeted by the *Pristine* survey with the metallicity-sensitive CaHK photometry, centred on the CaII H and K doublet lines. First of all, I re-estimated the structural (half-light radius, centroid, ellipticity, position angle and number of stars) and CMD (age, metallicity, $[\alpha/\text{Fe}]$ abundance ratio and distance modulus) properties of the satellite. To do so, I designed my own code that infers all these properties through a Monte Carlo Markov Chain (MCMC) algorithm. Assuming an exponential radial profile on one hand, and by constructing a series of CMD likelihoods for a variety of simulated stellar populations, to find which corresponds the best to the CMD of Dra II on the other, I found that Dra II has a size of $19.0^{+4.5}_{-2.6}$ pc, contains 127 ± 20 stars down to $g = 24.5$ mag, and is slightly elliptical ($\epsilon = 0.23 \pm 0.15$). The satellite is old (13.5 ± 0.5 Gyr), and its CMD corresponds to that of a metal-poor system ($[\text{Fe/H}]_{\text{CMD}} \sim -2.4$ dex) sitting at 21.5 ± 0.4 kpc away from the Sun. Then, using these results, I estimated the luminosity of Dra II to be of 180^{+124}_{-72} L$_\odot$ and showed that the system could in fact be affected by the strong tidal field of the MW. Using the photometric metallicities provided by *Pristine*, I confirmed the metal-poor nature of the satellite suggested by its CMD ($[\text{Fe/H}]_{\text{CaHK}} = -2.7 \pm 0.1$ dex) but was not able to constrain its metallicity dispersion.

The radial velocities of 51 stars were determined. Using *Pristine* to isolate the most metal-poor stars of the spectroscopic sample that should belong to Dra II, I was able to identify 14 member stars of the satellite. From this small population, I constrained the systemic velocity of the system to be $<v_r> = -342.5^{-1.2}_{+1.1}$ km s^{-1}. The velocity dispersion, directly linked to the dynamical mass of the satellite and therefore to the mass of its potential dark matter halo, is still unresolved. I find σ_{vr} to be less than 5.9 km s^{-1} at the 95% confidence limit, which

is not informative regarding the mass of the halo. Finally, using the proper motion from the Gaia DR2 and the GALPY python package (Bovy, 2015), the distance and the radial velocity of Dra II, I computed the orbit of the satellite. Dra II can dangerously approach the MW, with a pericenter of $21.3^{+0.7}_{-1.0}$ kpc. In doing so, it would not be surprising for the satellite to be affected by tides, which coud naturally explain the tidal features detected with the photometry.

Dra II is still a puzzling satellite. While no definitive assessment of its nature has been made, its ability to survive for more than 10 Gyr along its orbit, its size and metallicity favours the galactic nature, potentially making Dra II one of the faintest dwarf galaxy known to date.

► Chapter 4 details the study of the faint MW satellite Sgr II (Longeard et al., 2019b), also discovered by L15. Benefiting from deep MegaCam and *Pristine* photometry as well as three spectroscopic runs with DEIMOS, the satellite is spherical (< 0.12 at the 95% confidence limit), has a size of $r_h = 35.5^{+1.4}_{-1.2}$ pc and an absolute magnitude of -5.7 ± 0.1 mag. These first results already are puzzling, as it places Sgr II in a unique place of the M_V-r_h plane, too compact to be unambiguously identified as a dwarf, but more extended than most globular clusters. Furthermore, the satellite is old (~ 12 Gyr) and a combination of BHB calibration and CMD fitting methods are used to measure the distance of Sgr II ($d = 73.1^{+1.1}_{-0.7}$ kpc). Despite the identification of 21 member stars, the velocity dispersion of Sgr II marginally favours the existence of a dark matter halo ($\sigma_{vr} = 2.7^{+1.3}_{-1.0}$ km s^{-1} vs. ~ 1 km s^{-1} in a Sgr II-like purely baryonic system). The spectroscopic metallicities of 6 RGB stars with a S/N ratio greater than 12 were derived. We confirm the metallicity of the satellite, with $[\text{Fe/H}]_{\text{spectro}} = -2.28 \pm 0.03$ dex, well within the metallicity-luminosity relation of dwarf galaxies of Kirby et al. (2013b). The metallicity dispersion is small but resolved, with $\sigma_{[\text{Fe/H}]} = 0.12^{+0.03}_{-0.02}$ dex. This result is similar to the one obtained with the *Pristine* photometric metallicities and is mainly driven by two bright RGB stars with discrepant metallicity measurements. This indicates that Sgr II was able to retain its gas against supernovae wind and suggests at the presence of a dark matter halo and therefore that Sgr II may be a dwarf galaxy. The orbit of Sgr II is similar to the one of the trailing arm of the Sgr stream based on the Law & Majewski (2010) simulation, except in the Y-Z plane where the orbital plane of Sgr II is slightly tilted compared to the plane of the stream. However, the uncertainties on the orbit of Sgr II and on some parts of the stream makes this tilt not a critical issue, and the orbital properties of the system still suggest that it was in fact a former satellite of the Sgr dSph that was stripped from its influence by the tides of the MW.

► Chapter 5 describes my analysis of Lae 3, yet another faint MW satellite discovered by L15 (Longeard et al., 2019a). Although the globular cluster nature of Lae 3 was clear for L15, deep MegaCam photometry and one Keck II/DEIMOS spectroscopic run were taken as it was one of the most distant MW cluster at the time of its discovery. The portrait painted by my analysis is the one of a slightly more complex satellite than previously anticipated. Indeed, the first striking result is the size of Lae 3, larger than the one drawn from the

shallower PS1 data (11.4 ± 1.0 vs. 7 ± 2 pc), making Lae 3 more extended than most globular clusters. By a careful re-analysis of the PS1 data, I conclude that this discrepancy could be the sign that Lae 3 is mass-segregated. This process only takes place in systems for which the internal dynamics is driven by two-body interactions, i.e. without any massive dark matter halo. The smaller size found by L15 might have been mostly driven by the fact that the brightest Lae 3 stars are more centrally concentrated than the faint ones. The satellite is otherwise spherical ($\epsilon < 0.26$ at the 95 per cent confidence limit) and does not seem to suffer from tidal interactions, indicating that the larger size of Lae 3 in the deep MC photometry is not driven by low surface brightness tidal structures in the field of view. Nevertheless, given its absolute magnitude ($M_v = -2.8\pm0.3$ mag), Lae 3 appears too compact to be a dwarf galaxy. This conclusion is strengthened by the spectroscopic metallicity of the satellite, [Fe/H] $= -1.8\pm0.1$ dex, undoubtedly too large to correspond to a system of galactic nature. However, the six stars identified as members do not allow for tight constrains on the velocity dispersion, unresolved, or the metallicity dispersion, found to be less than 0.5 dex at the 95% confidence interval. The orbital properties of Lae 3 confirm that it belongs to the outer halo of the galaxy, with a pericenter of $40.7^{+5.6}_{-14.7}$ kpc and an apocenter of $85.6^{+17.2}_{-5.9}$ kpc.

6.2 Perspectives

6.2.1 Effective spectroscopic campaigns

If there is one thing that comes out of my PhD work, it is the ever-ending need for more data. The astronomer is hungry for data, but in order to understand the faint satellites already discovered in the last few years, or the ones yet to come, the combination of deep photometry and spectroscopy is absolutely mandatory.

Chapter 3 and 4 make it perfectly clear that *Pristine* is particularly effective in identifying the metal-poor stars in a spectroscopic dataset, and therefore in weeding out the foreground contamination of the MW. Therefore, an interesting project would be to go over most of the literature related to the spectroscopy of faint satellites and re-analyse their spectroscopic samples in the light of the *Pristine* Survey. By cross-matching the available catalogues with *Pristine*, it would be possible to determine which stars are metal-poor and therefore likely to be members (if these stars do not have a spectroscopic metallicity already measured) and determine what would be the impact, if any, on the dynamics of these satellites. In other words, revising the spectroscopy with the CaHK and check if the published dynamical masses and the resulting mass-to-light ratios of the known faint satellites are affected by a more reliable selection of their members. Of course, with the current and upcoming Gaia data releases, this analysis could also greatly impact the orbits of these satellites.

Moreover, an already ongoing project is to gather new spectroscopic data selected a priori from the *Pristine* Survey. The very first of those datasets has already been observed for Sgr II with FLAMES at the VLT, but is not yet analysed. On this basis, I also plan to submit ESO proposals for FORS and/or MUSE on the VLT for the next semester in order to study in greater details the faint dwarfs in *Pristine* and accessible from the southern hemisphere.

6.2.2 A systematic inference of the metallicity properties of the satellites in the *Pristine* survey

One aspect that was not anticipated when I started my PhD was how powerful the *Pristine* survey revealed itself to be. Chapters 3 and 4, in particular, show that the photometric metallicities allow to estimate the systemic metallicities of M 15, M 92 and Sgr II in a very satisfying manner (Figure 14 of Chapter 3 and 7 of Chapter 4). In all these three cases, the metallicity and metallicity dispersions drawn from the *Pristine* data are compatible with the ones inferred from spectroscopy, whether mine or previous studies from the literature (Carretta et al. 2009a, Carretta et al. 2009b). The first measurement of the metallicity of Dra II was also provided by this method when the spectroscopy was almost not informative. Therefore, a natural project to carry on from there is to perform the same type of analysis on all the remaining systems in *Pristine*. This would be useful on two different fronts:

- Since 18 out of the 22 dwarf galaxies observed in *Pristine* have their systemic metallicity and metallicity dispersion measured with spectroscopy, such a project would be ideal to test extensively the method itself. It could also provide independent measurements for these quantities in cases when the [Fe/H] and/or $\sigma_{[Fe/H]}$ are not well constrained. This is the case, for example, of Boo II, that was studied spectroscopically by Koch et al. (2009) and Ji et al. (2016b) but for which the metallicity dispersion is still unresolved ($\sigma_{[Fe/H]}^{BooII} < 0.35$ at the 90% confidence limit).

- Test whether or not the photometric metallicities can be used to model the entire MDF of metal-poor systems. This, however, would be possible for the classical dSphs in *Pristine* (Dra and UMi) and for faint dwarfs that have been heavily studied, and hence for which the shape of the MDF is known, such as Boo I (Kirby et al. 2011, Lai et al. 2011).

If this endeavour is successful on either of this two fronts, it would demonstrate the importance of re-observations of the most ambiguous satellites with the *Pristine* filter in order to increase the number of photometric metallicities available, and therefore tighten the constraints on their metallicity properties. It would also give even more weight to a possible extension of the survey, by installing a similar CaHK filter in the southern hemisphere. Of course, such an endeavour requires quite an important funding, constructing the filter alone is expensive, but the benefits would, without any doubt, be substantial.

6.2.3 The next generation of telescopes

The calendar of the astronomers studying dwarf galaxies is already quite busy. Nine faint systems discovered in the last few years have not been under the scope of spectroscopy yet (Cet II, Cet III, DESJ0225+0304, Gru II, Ind II, Pic I, Pic II, Tuc IV, Tuc V). And there is still quite a lot to do with the confirmed ones: identifying even more members, constraining their MDFs, studying in details the abundances of their stars with medium and high-resolution spectroscopy, constraining their orbits, etc.. Moreover, the census of
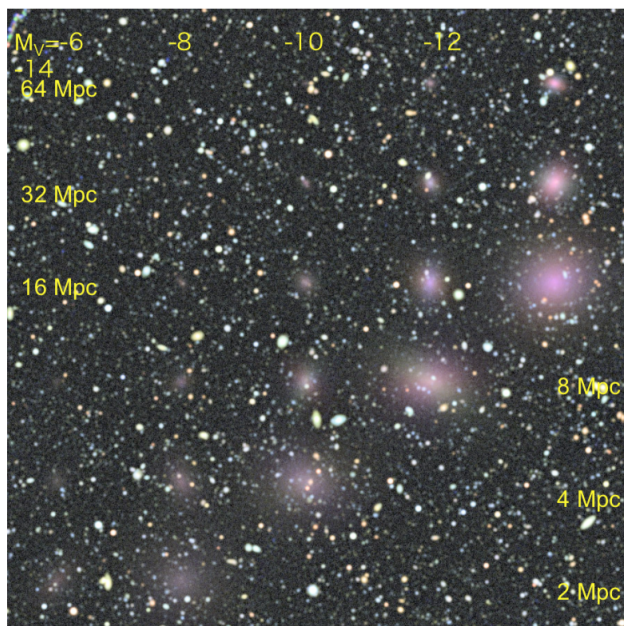
Figure 6.1: Plot taken from Ferguson et al. (2009) illustrating the ability of the LSST to detect faint stellar systems, for a field observed ~ 1500 seconds. The background corresponds to an image from the GOODS survey, while the galaxies shown here are simulated LSST images.

dwarf galaxies is not complete yet, and there will undoubtably be discoveries of new, faint satellites of the MW in the years to come. In order to conduct all these various studies, the next generation of instruments and telescopes will be extremely helpful.

One of the best representative of the future of astronomy is the Large Synoptic Survey Telescope (Ivezic et al., 2008, LSST), a 10 years mission that will cover over 18.000 deg^2 in the southern hemisphere. The survey consists into two visits of 15 sec per night and per field. The telescope itself has a diameter of 8.4 meters with a 3.5° field of view, and is equipped with six different filters ($ugrizy$) that are planned to reach the final respective depths of (26.3,27.5,27.7,27.0,26.2,24.9) mag (Rich, 2018). This corresponds to the ability to resolve the main sequence turn-off (MSTO) of systems at ~ 500 kpc away from the MW. Furthermore, the 10 years basetime of the LSST and their observational strategy will lead to the detection of RR Lyrae within 400 kpc. The combination of these two aspects of the survey alone will most likely heavily contribute to the census of dwarf galaxies of the MW (Tollerud et al., 2008). The detection ability of the LSST is illustrated in Figure 6.1. It will also have an astrometry as precise as Gaia, but for targets ~ 3-4 mag fainter, thus providing proper motions with a 0.2 mas yr^{-1} precision for r ~ 21 mag, and 1 mas yr^{-1} for r ~ 24 mag. The beginning of the LSST is set for 2023, and its outstanding precision will only be achieved 10 years from there, if not even later if some delays come in the way. Nonetheless, the perspectives brought by the LSST are exciting.

However, there are reasons why we should approach the recent and future discoveries of
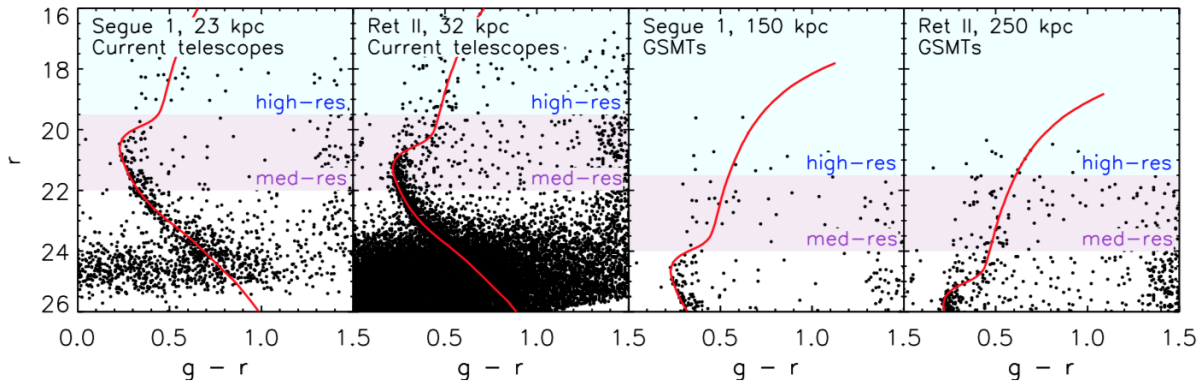
Figure 6.2: Plot taken from Simon (2019) showing the CMDs of Segue 1 and Ret II at their current distances (first two panels from the left) and shifted respectively at 150 and 250 kpc (last two panels). The blue-shaded areas correspond to what can be achieved for high-resolution spectroscopy with the current telescopes, and with 30-m class telescopes. A similar picture is shown for med-resolution spectroscopy in purple.

fainter/more distant systems with care, and those reasons were heavily highlighted throughout this thesis. Indeed, if we are already struggling to characterise the dwarf-galaxy candidates that are already known, what about the systems that will be unveiled by observations such as the ones what will be carry out by the LSST ? The key here is to maintain a balance between the spectroscopic and photometric capabilities of the observatories around the world, but it is easier said than done. The next generation of spectrograph will have to be high-performing and be mounted on 30-m class telescope in order to efficiently complement the upcoming discoveries of satellites. Figure 6.2 shows the capabilities of the current telescopes used for spectroscopy of dwarf galaxies, such as the Keck telescope. Figure 6.2 makes it clear that our current means will not be sufficient to probe the faintest/most distant systems. A Segue 1-like system at 150 kpc would almost not be accessible, except maybe for a few of its RGB stars. Of course, systems like Draco II sitting a few tens of kpc further than its current location, probably lacking RGB stars, is absolutely out of the question.

One of the best existing solution to probe extremely faint/distant systems is the VLT that can provide velocities for stars down to $V \sim 22$ mag with a few hours of observations, using instruments such as the FOcal Reducer and low dispersion Spectrograph (FORS), the Multi Unit Spectroscopic Explorer (MUSE) or FLAMES (Voggel et al. 2016, Fritz et al. 2019). However, several caveats can be addressed here, the first one being that the VLT is a southern instrument. As such, they can only observe up to a declination of $\sim +30°$, leaving behind a cohort of interesting satellites, including the mysterious Draco II. The second major problem is the reduced field of view (FoV) and capabilities of some of these spectrographs. For example, MUSE's FoV is one arcminute, but is extremely efficient by design at taking spectra of most of the targets observed. For most dwarf galaxies, this means that several

fields are necessary to cover the entire system. FORS has a larger FoV but ~ 10 stars can be observed at the same time in small systems of a few arcminutes. The last major caveat is that since the VLT is currently the only facility able to perform this kind of observations, the pressure for time proposals is quite high, and the field would largely benefit from having several other facilities with similar performances.

One of the next big thing is, of course, the Extremely Large Telescope (ELT), the first 40-m class telescope in history, for which first light is planned for 2025. The giant beast will be able to reach the MSTO of old systems ~ 2 Mpc away (Gullieuszik et al., 2014). Needless to say that, for dwarf galaxies of the MW located much closer, it will be possible to probe their stellar populations to a depth never seen before. Furthermore, it will allow deep med and high-resolution spectroscopy. The pressure to obtain time for the ELT will undoubtedly be extremely high, but it will also lessen the pressure on the VLT. Other projects, such as the Giant Magellan Telescope (GMT) will join the realm of 30/40-m class telescopes and be invaluable science-wise. However, both these facilites will be located in Chile, in the southern hemisphere.

In that regard, the MaunaKea Spectroscopic Explorer (MSE, The MSE Science Team et al. 2019) is a beacon of hope for the study of all systems in the northern hemisphere. Designed to be the successor of the CFHT in Hawaii, the MSE is a 11-m telescope, with a wide FoV (1.5°) that aims to extract more than 4000 spectra per exposure. It will drastically increase the number of member stars in each systems and allow to study their dynamics and abundances. If a 1.5° FoV can seem overkill to study the faintest dwarf galaxies and dwarf-galaxy candidates, it has the advantage to be able to detect potential tidal features around those systems, features that some of them are already showing signs of (for example Tucana III or Draco II). WEAVE (Dalton et al. 2014, Dalton 2016) will also be useful to study the northern hemisphere. With 1000 fibres on the WHT (4.2m) and a FoV of 2°, WEAVE will determine the radial velocities and metallicities of stars with $16 < V < 20$ (R ~ 5000) and abundances of stars with $12 < V < 17$ (R ~ 20000). Therefore, it will be possible for the spectrograph to obtain the radial velocities and [Fe/H] of the RGB stars of most MW faint satellites known.

The next two decades will therefore provide astronomers new telescopes and instruments with performances never seen before, that will push even further the boundaries and deliver some invaluable pieces of informations on our knowledge of dwarf galaxies, both regarding their census and the complete characterisation of their stellar populations. They might also mark a turning point in the study of dwarfs if the spectroscopy fails to efficiently follow the photometric capabilities of the next generation of telescopes, marking a significant transformation of the field in 10 or 15 years. Nonetheless, the exciting science surrounding the faintest dwarf galaxies will still be there, waiting for us to grasp it.

Bibliography

Abel T., Bryan G. L., Norman M. L., 2000, ApJ, 540, 39

Aguado D. S., González Hernández J. I., Allende Prieto C., Rebolo R., 2017, A&A, 605, A40

Aguado D. S. et al., 2019, MNRAS, 2271

Allende Prieto C., Beers T. C., Wilhelm R., Newberg H. J., Rockosi C. M., Yanny B., Lee Y. S., 2006, ApJ, 636, 804

Alpher R. A., Bethe H., Gamow G., 1948, Physical Review, 73, 803

Arentsen A. et al., 2019, arXiv e-prints, arXiv:1910.06337

Balbinot E. et al., 2013, ApJ, 767, 101

Barnard E. E., 1931, Publications of the Yerkes Observatory, 6, 1

Battaglia G., Helmi A., Tolstoy E., Irwin M. J., 2007, in Astronomical Society of the Pacific Conference Series, Vol. 374, From Stars to Galaxies: Building the Pieces to Build Up the Universe, Vallenari A., Tantalo R., Portinari L., Moretti A., eds., p. 273

Baumgardt H., Kroupa P., Parmentier G., 2008, MNRAS, 384, 1231

Bechtol K. et al., 2015, ApJ, 807, 50

Beers T. C., Christlieb N., 2005, ARAA, 43, 531

Beers T. C., Preston G. W., Shectman S. A., 1985, AJ, 90, 2089

—, 1992, AJ, 103, 1987

Bellazzini M. et al., 2008, AJ, 136, 1147

Belokurov V. et al., 2008, ApJ, 686, L83

—, 2010, ApJ, 712, L103

—, 2009, MNRAS, 397, 1748

—, 2007, ApJ, 654, 897

—, 2006, ApJ, 647, L111

Bernard E. J. et al., 2014, MNRAS, 442, 2999

Bertone G., Hooper D., Silk J., 2005, Phys. Rep., 405, 279

Bland-Hawthorn J., Karlsson T., Sharma S., Krumholz M., Silk J., 2010, ApJ, 721, 582

Bonifacio P., Hill V., Molaro P., Pasquini L., Di Marcantonio P., Santin P., 2000, A&A, 359, 663

Boulade O. et al., 2003, 4841, 72

Bovy J., 2015, ApJSupp, 216, 29

Boylan-Kolchin M., Bullock J. S., Kaplinghat M., 2011, MNRAS, 415, L40

Bradford J. D. et al., 2011, ApJ, 743, 167

Brown T. M. et al., 2012, ApJ, 753, L21

—, 2014, ApJ, 796, 91

Bullock J. S., Boylan-Kolchin M., 2017, ARAA, 55, 343

Caffau E. et al., 2011, Nature, 477, 67

Caldwell N. et al., 2017, ApJ, 839, 20

Cannon R. D., Hawarden T. G., Tritton S. B., 1977, MNRAS, 180, 81P

Carretta E., Bragaglia A., Gratton R., D'Orazi V., Lucatello S., 2009a, A&A, 508, 695

Carretta E., Bragaglia A., Gratton R. G., Leone F., Recio-Blanco A., Lucatello S., 2006, A&A, 450, 523

Carretta E. et al., 2010, ApJ, 714, L7

—, 2009b, A&A, 505, 117

—, 2007, A&A, 464, 967

Carretta E., Lucatello S., Gratton R. G., Bragaglia A., D'Orazi V., 2011, A&A, 533, A69

Chambers K. C. et al., 2016, arXiv:1612.05560

Chiti A., Frebel A., Ji A. P., Jerjen H., Kim D., Norris J. E., 2018, ApJ, 857, 74

Christlieb N., Wisotzki L., Graßhoff G., 2002, A&A, 391, 397

Cohen J. G., Kirby E. N., Simon J. D., Geha M., 2010, ApJ, 725, 288

Collins M. L. M. et al., 2013, ApJ, 768, 172

Collins M. L. M., Rich R. M., Ibata R., Martin N., Preston J., PAndAS Collaboration, 2017, in IAU Symposium, Vol. 321, Formation and Evolution of Galaxy Outskirts, Gil de Paz A., Knapen J. H., Lee J. C., eds., pp. 16–18

Conn B. C., Jerjen H., Kim D., Schirmer M., 2018, ApJ, 852, 68

Cui X.-Q. et al., 2012, Research in Astronomy and Astrophysics, 12, 1197

Dalton G., 2016, in Astronomical Society of the Pacific Conference Series, Vol. 507, Multi-Object Spectroscopy in the Next Decade: Big Questions, Large Surveys, and Wide Fields, Skillen I., Balcells M., Trager S., eds., p. 97

Dalton G. et al., 2014, in Society of Photo-Optical Instrumentation Engineers (SPIE) Conference Series, Vol. 9147, Proceedings of the SPIE, p. 91470L

Dawson K. S. et al., 2013, AJ, 145, 10

de Jong R. S. et al., 2016, in Society of Photo-Optical Instrumentation Engineers (SPIE) Conference Series, Vol. 9908, Ground-based and Airborne Instrumentation for Astronomy VI, p. 99081O

Deason A. J., Belokurov V., Evans N. W., 2011, MNRAS, 416, 2903

Dehnen W., Odenkirchen M., Grebel E. K., Rix H.-W., 2004, AJ, 127, 2753

Drlica-Wagner A. et al., 2016, ApJ, 833, L5

—, 2015, ApJ, 813, 109

Famaey B., McGaugh S., Milgrom M., 2018, MNRAS, 480, 473

Ferguson H. et al., 2009, in astro2010: The Astronomy and Astrophysics Decadal Survey, Vol. 2010, p. 79

Flores R. A., Primack J. R., 1994, ApJ, 427, L1

Fosbury R. A. E., Mebold U., Goss W. M., Dopita M. A., 1978, MNRAS, 183, 549

Frebel A., Simon J. D., Geha M., Willman B., 2010, ApJ, 708, 560

Fritz T. K., Battaglia G., Pawlowski M. S., Kallivayalil N., van der Marel R., Sohn T. S., Brook C., Besla G., 2018, ArXiv e-prints

Fritz T. K., Carrera R., Battaglia G., Taibi S., 2019, A&A, 623, A129

Fu S. W., Simon J. D., Alarcón Jara A. G., 2019, arXiv:1901.00594

Gaia Collaboration, Brown A. G. A., Vallenari A., Prusti T., de Bruijne J. H. J., Babusiaux C., Bailer-Jones C. A. L., 2018a, arXiv:1804.09365

Gaia Collaboration et al., 2018b, A&A, 616, A12

BIBLIOGRAPHY

Gatto A., Fraternali F., Read J. I., Marinacci F., Lux H., Walch S., 2013, MNRAS, 433, 2749

Geha M., Willman B., Simon J. D., Strigari L. E., Kirby E. N., Law D. R., Strader J., 2009, ApJ, 692, 1464

Geisler D., Smith V. V., Wallerstein G., Gonzalez G., Charbonnel C., 2005, AJ, 129, 1428

Gennaro M. et al., 2018, ApJ, 855, 20

Geringer-Sameth A., Koushiappas S. M., Walker M., 2015, ApJ, 801, 74

Gratton R. G., Carretta E., Bragaglia A., 2012, A&A Rv, 20, 50

Gratton R. G. et al., 2007, A&A, 464, 953

Grcevich J., Putman M. E., 2009, ApJ, 696, 385

Gullieuszik M., Greggio L., Falomo R., Schreiber L., Uslenghi M., 2014, A&A, 568, A89

Gustafsson B., Edvardsson B., Eriksson K., Jørgensen U. G., Nordlund A., Plez B., 2008, A&A, 486, 951

Hargis J. R., Willman B., Peter A. H. G., 2014, ApJ, 795, L13

Harrington R. G., Wilson A. G., 1950, PASP, 62, 118

Harris W. E., 1996, AJ, 112, 1487

—, 2010, eprint arXiv:1012.3224

Henden A. A., Welch D. L., Terrell D., Levine S. E., 2009, in American Astronomical Society Meeting Abstracts, Vol. 214, American Astronomical Society Meeting Abstracts #214, p. 407.02

Hernitschek N. et al., 2016, ApJ, 817, 73

Hirano S., Hosokawa T., Yoshida N., Umeda H., Omukai K., Chiaki G., Yorke H. W., 2014, ApJ, 781, 60

Høg E. et al., 2000, A&A, 355, L27

Homma D. et al., 2019, arXiv e-prints, arXiv:1906.07332

—, 2016, ApJ, 832, 21

—, 2018, PASJ, 70, S18

Hopkins P. F., Quataert E., Murray N., 2012, MNRAS, 421, 3522

Howes L. M. et al., 2015, Nature, 527, 484

Ibata R. A., Bellazzini M., Malhan K., Martin N., Bianchini P., 2019, Nature Astronomy

Ibata R. A., Gilmore G., Irwin M. J., 1994, Nature, 370, 194

Ibata R. A. et al., 2013, Nature, 493, 62

—, 2017, ApJ, 848, 128

Irwin M., Lewis J., 2001, New Astronomy Review, 45, 105

Irwin M. J. et al., 2007, ApJ, 656, L13

Irwin M. J., Bunclark P. S., Bridgeland M. T., McMahon R. G., 1990, MNRAS, 244, 16P

Ishigaki M. N., Aoki W., Arimoto N., Okamoto S., 2014, A&A, 562, A146

Ivezic Z. et al., 2008, Serbian Astronomical Journal, 176, 1

Ivezić Ž. et al., 2008, ApJ, 684, 287

Jethwa P., Erkal D., Belokurov V., 2016, MNRAS, 461, 2212

Ji A. P., Frebel A., Bromm V., 2015, MNRAS, 454, 659

Ji A. P., Frebel A., Simon J. D., Chiti A., 2016a, ApJ, 830, 93

Ji A. P., Frebel A., Simon J. D., Geha M., 2016b, ApJ, 817, 41

Ji A. P., Simon J. D., Frebel A., Venn K. A., Hansen T. T., 2019, ApJ, 870, 83

Johnson C. I., Pilachowski C. A., 2010, ApJ, 722, 1373

Kadla Z. I., 1972, SvA-AJ, 15, 601

Kallivayalil N. et al., 2018, ApJ, 867, 19

Kang X., Mao S., Gao L., Jing Y. P., 2005, A&A, 437, 383

Keller S. C. et al., 2014, Nature, 506, 463

—, 2007, PASA, 24, 1

Kim D., Jerjen H., 2015a, ApJ, 799, 73

—, 2015b, ApJ, 808, L39

Kim D., Jerjen H., Mackey D., Da Costa G. S., Milone A. P., 2016, ApJ, 820, 119

Kim D., Jerjen H., Milone A. P., Mackey D., Da Costa G. S., 2015, ApJ, 803, 63

Kirby E. N., Boylan-Kolchin M., Cohen J. G., Geha M., Bullock J. S., Kaplinghat M., 2013a, ApJ, 770, 16

Kirby E. N., Bullock J. S., Boylan-Kolchin M., Kaplinghat M., Cohen J. G., 2014, MNRAS, 439, 1015

Kirby E. N., Cohen J. G., Guhathakurta P., Cheng L., Bullock J. S., Gallazzi A., 2013b, ApJ, 779, 102

Kirby E. N., Cohen J. G., Simon J. D., Guhathakurta P., Thygesen A. O., Duggan G. E., 2017, ApJ, 838, 83

Kirby E. N., Cohen J. G., Smith G. H., Majewski S. R., Sohn S. T., Guhathakurta P., 2011, ApJ, 727, 79

Kirby E. N. et al., 2010, ApJSupp, 191, 352

Kirby E. N., Martin C. L., Finlator K., 2011, ApJ, 742, L25

Kirby E. N., Simon J. D., Cohen J. G., 2015, ApJ, 810, 56

Kirby E. N., Simon J. D., Geha M., Guhathakurta P., Frebel A., 2008, ApJ, 685, L43

Kleyna J. T., Wilkinson M. I., Evans N. W., Gilmore G., 2005, ApJ, 630, L141

Klypin A., Kravtsov A. V., Valenzuela O., Prada F., 1999, ApJ, 522, 82

Koch A., Grebel E. K., Gilmore G. F., Wyse R. F. G., Kleyna J. T., Harbeck D. R., Wilkinson M. I., Evans N. W., 2008a, AJ, 135, 1580

Koch A., McWilliam A., Grebel E. K., Zucker D. B., Belokurov V., 2008b, ApJ, 688, L13

Koch A., Rich R. M., 2014, ApJ, 794, 89

Koch A. et al., 2009, ApJ, 690, 453

Koposov S. E., Belokurov V., Torrealba G., Evans N. W., 2015a, ApJ, 805, 130

Koposov S. E. et al., 2015b, ApJ, 811, 62

—, 2011, ApJ, 736, 146

—, 2018, MNRAS, 479, 5343

Küpper A. H. W., Balbinot E., Bonaca A., Johnston K. V., Hogg D. W., Kroupa P., Santiago B. X., 2015, ApJ, 803, 80

Laevens B. P. M. et al., 2015a, ApJ, 813, 44

—, 2015b, ApJ, 802, L18

—, 2014, ApJ, 786, L3

Lai D. K., Lee Y. S., Bolte M., Lucatello S., Beers T. C., Johnson J. A., Sivarani T., Rockosi C. M., 2011, ApJ, 738, 51

Law D. R., Majewski S. R., 2010, ApJ, 714, 229

Leaman R., 2012, AJ, 144, 183

Lépine S., Koch A., Rich R. M., Kuijken K., 2011, ApJ, 741, 100

Li T. S. et al., 2018, ApJ, 857, 145

Libeskind N. I., Frenk C. S., Cole S., Helly J. C., Jenkins A., Navarro J. F., Power C., 2005, MNRAS, 363, 146

Lokhorst D. et al., 2016, ApJ, 819, 124

Longeard N., Martin N., Ibata R. A., Collins M. L. M., Laevens B. P. M., Bell E., Mackey D., 2019a, MNRAS, 2229

Longeard N. et al., 2018, MNRAS, 480, 2609

—, 2019b, arXiv:1902.02780

Luque E. et al., 2017, MNRAS, 468, 97

—, 2016, MNRAS, 458, 603

Lynden-Bell D., 1976, MNRAS, 174, 695

Lynden-Bell D., Lynden-Bell R. M., 1995, MNRAS, 275, 429

Magg M., Hartwig T., Agarwal B., Frebel A., Glover S. C. O., Griffen B. F., Klessen R. S., 2018, MNRAS, 473, 5308

Magrini L. et al., 2012, MNRAS, 427, 1075

Malhan K., Ibata R. A., 2019, MNRAS, 486, 2995

Marcolini A., D'Ercole A., Brighenti F., Recchi S., 2006, MNRAS, 371, 643

Marino A. F. et al., 2011, A&A, 532, A8

Martin N. F., Collins M. L. M., Longeard N., Tollerud E., 2018, ApJ, 859, L5

Martin N. F., de Jong J. T. A., Rix H.-W., 2008, ApJ, 684, 1075

Martin N. F. et al., 2016a, MNRAS, 458, L59

Martin N. F., Ibata R. A., Chapman S. C., Irwin M., Lewis G. F., 2007, MNRAS, 380, 281

Martin N. F. et al., 2016b, ApJ, 818, 40

Martin N. F., Ibata R. A., McConnachie A. W., Mackey A. D., Ferguson A. M. N., Irwin M. J., Lewis G. F., Fardal M. A., 2013, ApJ, 776, 80

Martin N. F. et al., 2016c, ApJ, 830, L10

—, 2015, ApJ, 804, L5

Massari D., Helmi A., 2018, A&A, 620, A155

Mateo M. L., 1998, ARAA, 36, 435

McConnachie A. W., 2012, AJ, 144, 4

McConnachie A. W., Côté P., 2010, ApJ, 722, L209

McConnachie A. W. et al., 2018, ApJ, 868, 55

—, 2009, Nature, 461, 66

McGaugh S. S., Rubin V. C., de Blok W. J. G., 2001, AJ, 122, 2381

McLaughlin D. E., Anderson J., Meylan G., Gebhardt K., Pryor C., Minniti D., Phinney S., 2006, ApJSupp, 166, 249

McLaughlin D. E., van der Marel R. P., 2005, ApJSupp, 161, 304

McNamara B. J., Harrison T. E., Anderson J., 2003, ApJ, 595, 187

Metz M., Kroupa P., Jerjen H., 2007, MNRAS, 374, 1125

Mo H., van den Bosch F. C., White S., 2010, Galaxy Formation and Evolution

Monaco L., Bellazzini M., Bonifacio P., Ferraro F. R., Marconi G., Pancino E., Sbordone L., Zaggia S., 2005, A&A, 441, 141

Muñoz R. R., Carlin J. L., Frinchaboy P. M., Nidever D. L., Majewski S. R., Patterson R. J., 2006, ApJ, 650, L51

Muñoz R. R., Geha M., Côté P., Vargas L. C., Santana F. A., Stetson P., Simon J. D., Djorgovski S. G., 2012, ApJ, 753, L15

Muñoz R. R., Geha M., Willman B., 2010, AJ, 140, 138

Navarro J. F., Eke V. R., Frenk C. S., 1996, MNRAS, 283, L72

Navarro J. F. et al., 2010, MNRAS, 402, 21

Nordlander T., Amarsi A. M., Lind K., Asplund M., Barklem P. S., Casey A. R., Collet R., Leenaarts J., 2017, A&A, 597, A6

Norris J. E., Wyse R. F. G., Gilmore G., Yong D., Frebel A., Wilkinson M. I., Belokurov V., Zucker D. B., 2010, ApJ, 723, 1632

Oñorbe J., Boylan-Kolchin M., Bullock J. S., Hopkins P. F., Kereš D., Faucher-Giguère C.-A., Quataert E., Murray N., 2015, MNRAS, 454, 2092

Orban C., Gnedin O. Y., Weisz D. R., Skillman E. D., Dolphin A. E., Holtzman J. A., 2008, ApJ, 686, 1030

Pace A. B., Li T. S., 2019, ApJ, 875, 77

Pawlowski M. S., McGaugh S. S., Jerjen H., 2015, MNRAS, 453, 1047

Peñarrubia J., Navarro J. F., McConnachie A. W., 2008, ApJ, 673, 226

Perryman M. A. C. et al., 1997, A&A, 500, 501

Planck Collaboration et al., 2016, A&A, 594, A13

Pritzl B. J., Venn K. A., Irwin M., 2005, AJ, 130, 2140

Read J. I., Agertz O., Collins M. L. M., 2016, MNRAS, 459, 2573

Read J. I., Erkal D., 2019, MNRAS, 1615

Read J. I., Gilmore G., 2005, MNRAS, 356, 107

Read J. I., Walker M. G., Steger P., 2018, MNRAS, 481, 860

Rees, Richard F. J., 1992, AJ, 103, 1573

Revaz Y., Jablonka P., 2018, A&A, 616, A96

Rich R. M., 2018, in IAU Symposium, Vol. 334, Rediscovering Our Galaxy, Chiappini C., Minchev I., Starkenburg E., Valentini M., eds., pp. 233–241

Richstone D. O., Tremaine S., 1986, AJ, 92, 72

Robin A. C., Reylé C., Derrière S., Picaud S., 2003, A&A, 409, 523

Sakamoto T., Hasegawa T., 2006, ApJ, 653, L29

Sanders J. L., Evans N. W., Dehnen W., 2018, MNRAS, 478, 3879

Sawala T. et al., 2016, MNRAS, 457, 1931

Schaye J. et al., 2015, MNRAS, 446, 521

Schlaufman K. C., Casey A. R., 2014, ApJ, 797, 13

Schörck T. et al., 2009, A&A, 507, 817

Sestito F. et al., 2019, MNRAS, 484, 2166

Shapley H., 1938a, Harvard College Observatory Bulletin, 908, 1

—, 1938b, Nature, 142, 715

Shetrone M. D., Bolte M., Stetson P. B., 1998, AJ, 115, 1888

Shetrone M. D., Côté P., Sargent W. L. W., 2001, ApJ, 548, 592

Simon J. D., 2018, ApJ, 863, 89

—, 2019, ARAA, 57, 375

Simon J. D., Bolatto A. D., Leroy A., Blitz L., Gates E. L., 2005, ApJ, 621, 757

Simon J. D., Geha M., 2007, ApJ, 670, 313

Simon J. D. et al., 2011, ApJ, 733, 46

—, 2017, ApJ, 838, 11

Skrutskie M. F. et al., 2006, AJ, 131, 1163

Sohn S. T., Anderson J., van der Marel R. P., 2012, ApJ, 753, 7

Springel V. et al., 2008, MNRAS, 391, 1685

Stacy A., Bromm V., 2014, ApJ, 785, 73

Starkenburg E. et al., 2017, MNRAS, 471, 2587

Steinmetz M. et al., 2006, AJ, 132, 1645

Strigari L. E., Bullock J. S., Kaplinghat M., Simon J. D., Geha M., Willman B., Walker M. G., 2008, Nature, 454, 1096

Tammann G. A., 1994, in European Southern Observatory Conference and Workshop Proceedings, Vol. 49, European Southern Observatory Conference and Workshop Proceedings, Meylan G., Prugniel P., eds., p. 3

Tassis K., Abel T., Bryan G. L., Norman M. L., 2003, ApJ, 587, 13

The Dark Energy Survey Collaboration, 2005, arXiv:astro-ph/0510346

The MSE Science Team et al., 2019, arXiv:1904.04907, arXiv:1904.04907

Thomas G. F. et al., 2018, MNRAS, 481, 5223

Tinsley B. M., 1979, ApJ, 229, 1046

Tollerud E. J., Bullock J. S., Graves G. J., Wolf J., 2011, ApJ, 726, 108

Tollerud E. J., Bullock J. S., Strigari L. E., Willman B., 2008, ApJ, 688, 277

Tolstoy E. et al., 2006, The Messenger, 123

Tolstoy E., Hill V., Tosi M., 2009, ARAA, 47, 371

Torrealba G. et al., 2018, MNRAS, 475, 5085

—, 2019, MNRAS, 1548

Torrealba G., Koposov S. E., Belokurov V., Irwin M., 2016a, MNRAS, 459, 2370

Torrealba G. et al., 2016b, MNRAS, 463, 712

van der Marel R. P. et al., 2014, in Astronomical Society of the Pacific Conference Series, Vol. 480, Structure and Dynamics of Disk Galaxies, Seigar M. S., Treuthardt P., eds., p. 43

van Dokkum P. et al., 2018, Nature, 555, 629

van Dokkum P. G., Abraham R., Merritt A., Zhang J., Geha M., Conroy C., 2015, ApJ, 798, L45

van Leeuwen F., 2009, A&A, 497, 209

Vargas L. C., Geha M., Kirby E. N., Simon J. D., 2013, ApJ, 767, 134

Vasiliev E., 2019, MNRAS, 484, 2832

Vogelsberger M. et al., 2014, MNRAS, 444, 1518

Voggel K., Hilker M., Baumgardt H., Collins M. L. M., Grebel E. K., Husemann B., Richtler T., Frank M. J., 2016, MNRAS, 460, 3384

Walker M. G. et al., 2016, ApJ, 819, 53

Walker M. G., Mateo M., Olszewski E. W., Peñarrubia J., Wyn Evans N., Gilmore G., 2009, ApJ, 704, 1274

Watkins L. L., Evans N. W., An J. H., 2010, MNRAS, 406, 264

Watkins L. L., van der Marel R. P., Sohn S. T., Evans N. W., 2019, ApJ, 873, 118

Webster D., Sutherland R., Bland-Hawthorn J., 2014, ApJ, 796, 11

White S. D. M., Rees M. J., 1978, MNRAS, 183, 341

Wilkinson M. I., Kleyna J. T., Evans N. W., Gilmore G. F., Irwin M. J., Grebel E. K., 2004, ApJ, 611, L21

Willman B. et al., 2005a, AJ, 129, 2692

—, 2005b, ApJ, 626, L85

Willman B., Geha M., Strader J., Strigari L. E., Simon J. D., Kirby E., Ho N., Warres A., 2011, AJ, 142, 128

Willman B., Strader J., 2012, AJ, 144, 76

Wilson A. G., 1955, PASP, 67, 27

Wisotzki L., Christlieb N., Bade N., Beckmann V., Köhler T., Vanelle C., Reimers D., 2000, A&A, 358, 77

Wolf C. et al., 2018, PASA, 35, e010

Wolf J., Martinez G. D., Bullock J. S., Kaplinghat M., Geha M., Muñoz R. R., Simon J. D., Avedo F. F., 2010, MNRAS, 406, 1220

Wright E. L. et al., 2010, AJ, 140, 1868

Yanny B. et al., 2009, AJ, 137, 4377

York D. G. et al., 2000, The Astronomical Journal, 120, 1579

Youakim K. et al., 2017, MNRAS, 472, 2963

BIBLIOGRAPHY

Zentner A. R., Kravtsov A. V., Gnedin O. Y., Klypin A. A., 2005, ApJ, 629, 219

Zhao G., Zhao Y.-H., Chu Y.-Q., Jing Y.-P., Deng L.-C., 2012, Research in Astronomy and Astrophysics, 12, 723

Zucker D. B. et al., 2006a, ApJ, 650, L41

—, 2006b, ApJ, 643, L103

Appendix A: Tracing the formation of the Milky Way through ultra metal-poor stars
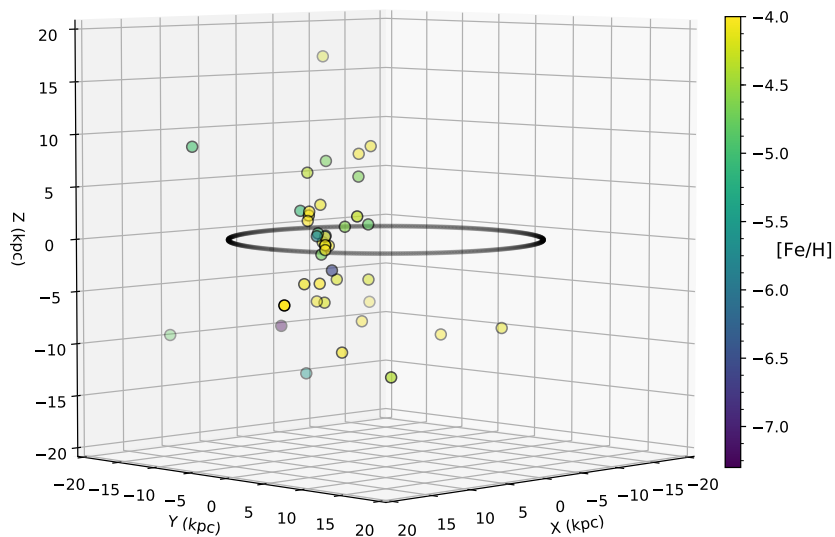
Figure A.1: Full sample of stars studied in Sestito et al. (2019), colour-coded according to their metallicity. The black circle represents the outer limit of the MW disk at 15 kpc. Most of them form a compact group around X ∼ 8 kpc because the sample is mostly constituted of stars in the solar neighbourhood.

The following study is led by Federico Sestito and consists into the determination and analysis of the orbital properties of the 42 known UMP stars ([Fe/H] < −4.0 dex) as of the end of 2018, represented in Figure A.1. These stars being among the oldest ones in the universe, they can greatly contribute to our understanding of the formation and evolution of the MW. However, to determine the orbit of these stars, their tridimensional motion, their

position and their distance are needed. This last property is particularly tricky: if isochrones are used, at least as a first approach, to estimate the distance of a stellar system, using them on a single star is much more difficult without any information on the properties of the star, in particular on its metallicity. One of the advantage of the Gaia DR2 is its ability to measure parallaxes, i.e. distances, for all stars surveyed. However, in a lot of cases, the parallax provided by Gaia is not informative, spanning a wide range of possible distances. That is why, in this article, Sestito et al. (2019) devise a procedure that is able to estimate the distance PDF of stars using their metallicities and isochrone tracks, and apply it on the UMP sample.

My contribution in this study resides in the determination of all the orbits of these 42 stars. While Federico Sestito created and tested the algorithm mentionned before, I used the Galpy Python library that implements various functions to determine the orbits of stars. My work consisted in integrating this library into a more global code that would take the position, tridimensional motion and the distances PDFs provided by the algorithm to estimate the orbital properties of the 42 UMPs.

Tracing the formation of the Milky Way through ultra metal-poor stars

Federico Sestito,[1,2]★ Nicolas Longeard,[1] Nicolas F. Martin,[1,3] Else Starkenburg,[2] Morgan Fouesneau [ORCID],[3] Jonay I. González Hernández,[4,5] Anke Arentsen,[2] Rodrigo Ibata,[1] David S. Aguado,[6] Raymond G. Carlberg,[7] Pascale Jablonka,[8,9] Julio F. Navarro,[10] Eline Tolstoy[11] and Kim A. Venn[10]

[1]*Observatoire astronomique de Strasbourg, CNRS, UMR 7550, F-67000 Strasbourg, France*
[2]*Leibniz Institute for Astrophysics Potsdam (AIP), An der Sternwarte 16, D-14482 Potsdam, Germany*
[3]*Max-Planck-Institut für Astronomie, Königstuhl 17, D-69117 Heidelberg, Germany*
[4]*Instituto de Astrofisica de Canarias, Vía Láctea, E-38205 La Laguna, Spain*
[5]*Departamento de Astrofísica, Universidad de La Laguna, Tenerife, E-38206 La Laguna, Spain*
[6]*Institute of Astronomy, University of Cambridge, Madingley Road, CB3 0HA Cambridge, UK*
[7]*Department of Astronomy and Astrophysics, University of Toronto, Toronto, ON M5S 3H4, Canada*
[8]*GEPI, Observatoire de Paris, Université PSL, CNRS, Place Jules Janssen, F-92190 Meudon, France*
[9]*Institute of Physics, Laboratoire d'astrophysique, École Polytechnique Fédérale de Lausanne (EPFL), Observatoire, CH-1290 Versoix, Switzerland*
[10]*Department of Physics and Astronomy, University of Victoria, PO Box 3055, STN CSC, Victoria BC V8W 3P6, Canada*
[11]*Kapteyn Astronomical Institute, University of Groningen, Landleven 12, NL-9747AD Groningen, the Netherlands*

ABSTRACT

We use *Gaia DR2* astrometric and photometric data, published radial velocities and MESA models to infer distances, orbits, surface gravities, and effective temperatures for all ultra metal-poor stars ([Fe/H] < -4.0 dex) available in the literature. Assuming that these stars are old (> 11 Gyr) and that they are expected to belong to the Milky Way halo, we find that these 42 stars (18 dwarf stars and 24 giants or sub-giants) are currently within ~ 20 kpc of the Sun and that they map a wide variety of orbits. A large fraction of those stars remains confined to the inner parts of the halo and was likely formed or accreted early on in the history of the Milky Way, while others have larger apocentres (> 30 kpc), hinting at later accretion from dwarf galaxies. Of particular interest, we find evidence that a significant fraction of all known UMP stars (~ 26 per cent) are on prograde orbits confined within 3 kpc of the Milky Way plane ($J_z < 100$ km s^{-1} kpc). One intriguing interpretation is that these stars belonged to the massive building block(s) of the proto-Milky Way that formed the backbone of the Milky Way disc. Alternatively, they might have formed in the early disc and have been dynamically heated, or have been brought into the Milky Way by one or more accretion events whose orbit was dragged into the plane by dynamical friction before disruption. The combination of the exquisite *Gaia DR2* data and surveys of the very metal-poor sky opens an exciting era in which we can trace the very early formation of the Milky Way.

Key words: stars: distances – Galaxy: abundances – Galaxy: disc – Galaxy: evolution – Galaxy: formation – Galaxy: halo.

1 INTRODUCTION

Ultra metal-poor (UMP) stars, defined to have [Fe/H][1] < -4 dex (Beers & Christlieb 2005), are extremely rare objects located mainly in the Milky Way (MW) halo. Because they are ultra metal-poor,

also relative to their neighbourhood, it is assumed that they formed from relative pristine gas shortly after the big bang (e.g. Freeman & Bland-Hawthorn 2002). As such, they belong to the earliest generations of stars formed in the Universe (Karlsson, Bromm & Bland-Hawthorn 2013). Because they are old, observable UMPs must be low-mass stars, however the minimum metallicity at which low-mass stars can form is still an open question (see Greif 2015; and references therein). The search for, and study of, stars with the lowest metallicities are therefore important topics to answer

★ E-mail: federico.sestito@astro.unistra.fr
[1][Fe/H] = $\log{(N_{Fe}/N_H)_\star} - \log{(N_{Fe}/N_H)_\odot}$, with N_X = the number density of element X.

questions on the masses of the first generation of stars and the universality of the initial mass function (IMF), as well as on the early formation stages of galaxies and the first supernovae (e.g. Frebel & Norris 2015; and references therein). Careful studies over many decades have allowed us to build up a catalogue of 42 UMP stars throughout the Galaxy. Many of these stars were discovered in survey programs that were or are dedicated to finding metal-poor stars using some special pre-selection through prism techniques (e.g. the HK and HES surveys; Beers, Preston & Shectman 1985; Christlieb, Wisotzki & Graßhoff 2002) or narrow-band photometry (such as for instance the SkyMapper and Pristine survey programmes; Starkenburg et al. 2017a; Wolf et al. 2018). Others were discovered in blind but very large spectroscopic surveys such as SDSS/SEGUE/BOSS (York et al. 2000; Yanny et al. 2009; Eisenstein et al. 2011) or LAMOST (Cui et al. 2012).

From the analysis of cosmological simulations, predictions can be made for the present-day distribution of such stars in MW-like galaxies. Since these predictions have been shown to be influenced by the physics implemented in these simulations, we can use the present-day distribution to constrain the physical processes of early star formation. For instance, a comparison between the simulations of Starkenburg et al. (2017b) and El-Badry et al. (2018) indicates a clear sensitivity of the present-day distribution on the conditions applied for star formation and the modelling of the ISM.

In an effort to refine the comparison with models and unveil the phase-space properties of these rare stars, we combine the exquisite *Gaia DR2* astrometry and photometry (Gaia Collaboration 2018) with models of UMP stars (MESA isochrones and luminosity functions; Paxton et al. 2011; Choi et al. 2016; Dotter 2016; waps.cfa.harvard.edu/MIST) to infer the distance, stellar properties, and orbits of all 42 known UMP stars.

This paper is organized as follows: Section 2 explains how we put our sample together while Section 3 presents our statistical framework to infer the distance, effective temperature, surface gravity, and orbit of each star in the sample using the *Gaia DR2* information (parallax, proper motion, and *G*, *BP*, and *RP* photometry). The results for the full sample are presented in Section 4 and we discuss the implications of the derived orbits in Section 5 before concluding in Section 6. We refer readers who are interested in the results for individual stars to Appendix A (available Online), in which each star is discussed separately.

2 DATA

We compile the list of all known ultra metal-poor ([Fe/H] < −4.0 dex), hyper metal-poor ([Fe/H] < −5.0 dex), and mega metal-poor ([Fe/H] < −6.0 dex) stars from the literature building from the Joint Institute of Nuclear Astrophysics catalogue (Abohalima & Frebel 2017), supplemented by all relevant discoveries. The literature properties for these stars are listed in Table 1. We crossmatch this list with the *Gaia DR2* catalogue[2] (Gaia Collaboration 2018) in order to obtain the stars' photometric and astrometric information. This is listed in Table 2.

Some stars were studied in more than one literary source, with different methods involving 1D or 3D models and considering the stellar atmosphere at Local Thermodynamic Equilibrium (LTE) or non-LTE, leading to dissimilar results on metallicity and stellar parameters. In this paper, when multiple results are available,

[2]https://gea.esac.esa.int/archive/

we report in Table 1 preferentially results including 3D stellar atmosphere and/or involving non-LTE modelling. If all results are in 1D LTE, we favour the most recent results.

When the UMP stars are recognized to be in binary systems and the orbital parameters are known (see Table 1), the reported radial velocity is the systemic value that is corrected for the binary orbital motion around the centre of mass.

Assuming that all stars in our sample are distant, we consider that all the extinction is in the foreground. Therefore, all stars are de-reddened using the Schlegel, Finkbeiner & Davis (1998) extinction map as listed in Table 1 and the Marigo et al. (2008) coefficients for the Gaia filters based on Evans et al. (2018), i.e.

$$G_0 = G - 2.664E(B - V), \tag{1}$$

$$BP_0 = BP - 3.311E(B - V), \tag{2}$$

$$RP_0 = RP - 2.021E(B - V). \tag{3}$$

Extinction values remain small in most cases (Table 1).

We assume that the distance between the Sun and the Galactic centre is 8.0 kpc, that the Local Standard of Rest circular velocity is $V_c = 239 \, \text{km s}^{-1}$, and that the peculiar motion of the Sun is $(U_0 = 11.10 \, \text{km s}^{-1}, V_0 + V_c = 251.24 \, \text{km s}^{-1}, W_0 = 7.25 \, \text{km s}^{-1})$ as described in Schönrich, Binney & Dehnen (2010).

3 INFERRING THE PROPERTIES OF STARS IN THE UMP SAMPLE

3.1 Distance inference

It is ill advised to calculate the distance to a star by simply inverting the parallax measurement (Bailer-Jones 2015), especially for large relative measurement uncertainties (e.g. $\delta\varpi/\varpi > 0.2$) and negative parallaxes. Therefore, we infer the probability distribution function (PDF) of the heliocentric distance to a star by combining its photometric and astrometric data with a sensible MW stellar density prior. Following Bayes' rule (Sharma 2017), the posterior probability of having a star at a certain distance given its observables Θ (e.g. photometry, metallicity, parallax) and a model $\mathcal{M}$ is characterized by its likelihood $\mathcal{L}(\Theta|\mathcal{M})$ and the prior $\mathcal{P}(\mathcal{M})$. The likelihood gives the probability of the set of observables Θ given model $\mathcal{M}$, whereas the prior represents the knowledge of the model used for the representation of a phenomenon. With these notations,

$$\mathcal{P}(\mathcal{M}|\Theta) \propto \mathcal{L}(\Theta|\mathcal{M})\mathcal{P}(\mathcal{M}). \tag{4}$$

In this work, the model parameters are $\mathcal{M} = \{\mu = 5\log(r) - 5, A\}$, with μ the distance modulus of the star, r the distance to the star, and A its age. The observables Θ can be split into the Gaia photometric observables $\Theta_{\text{phot}} = \{G_0, BP_0, RP_0, \delta_G, \delta_{BP}, \delta_{RP}\}$ and the Gaia astrometric (parallax) observables $\Theta_{\text{astrom}} = \{\varpi, \delta_\varpi\}$, with δx the uncertainty associated with measurement x. Assuming that the photometric and astrometric information on the star are independent, equation (4) becomes

$$\mathcal{P}(\mathcal{M}|\Theta) \propto \mathcal{L}_{\text{phot}}(\Theta_{\text{phot}}|\mathcal{M})\mathcal{L}_{\text{astrom}}(\Theta_\varpi|\mathcal{M})\mathcal{P}(\mathcal{M}). \tag{5}$$

Table 1. Physical parameters of the analysed UMPs found in literature. [Fe/H], [C/Fe], v_r, $T_{\rm lit}$, $\log(g)_{\rm lit}$ are from the articles listed in the column References. v_r and the binarity flag denoted with a are from Arentsen et al. (2018), the v_r values for binary systems denoted with a are the systemic radial velocities corrected for the binary orbital motion. v_r values for stars that are not known to be in a binary system and from the compilation of Arentsen et al. (2018) are calculated with a weighted average of all the v_r measurements. $E(B-V)$ is from Schlegel et al. (1998). In case the star is in a binary system, the binarity flag is equal to Y, while stars labelled with N are not in a binary system or the binarity is not known.

Identifier	α_{J2000} (deg)	δ_{J2000} (deg)	[Fe/H] (dex)	$\delta_{[Fe/H]}$ (dex)	[C/Fe] (dex)	$\delta_{[C/Fe]}$ (dex)	v_r (km s^{-1})	δ_{v_r} (km s^{-1})	$T_{\rm lit}$ (K)	$\delta_{T_{\rm lit}}$ (K)	$\log(g)_{\rm lit}$ (dex)	$\delta_{\log(g)_{\rm lit}}$ (dex)	E(B-V) (mag)	Binarity	References
HE 0020−1741	5.6869167	−17.4080944	−4.05	–	1.4	–	93.06	0.83	4630.0	150	0.95	0.3	0.021	N	Placco et al. (2016)
SDSS J0023+0307	5.80834363858	3.13284420892	<−6.6	–	<2.0	–	−195.5	1.0	6140	132	4.8	0.6	0.028	N	Aguado et al. (2018b)
HE 0044−3755	11.6508144643	−37.6593210379	−4.19	–	−0.3	–	48.3	2.5	4800	100	1.5	0.1	0.010	N	Cayrel et al. (2004)
HE 0057−5959	14.9749409617	−59.7249294278	−4.08	–	0.86	–	375.64a	1.00	5257	–	2.65	–	0.016	N	Norris et al. (2007), Norris et al. (2013)
HE 0107−5240	17.3714810637	−52.4095009821	−5.5	0.2	3.85	–	46.0a	2.0	5100	150	2.2	0.3	0.011	Ya	Christlieb et al. (2004)
HE 0134−1519	24.2724039774	−15.0729979538	−4.0	0.2	1.00	0.26	244	1	5500	100	3.2	0.3	0.016	N	Hansen et al. (2015)
SDSS J014036.21+234458.1	25.1509195676	23.7495011637	−4.0	0.3	1.1	0.3	−197a	1	5703	100	4.7	0.3	0.114	Ya	Yong et al. (2013)
BD+44 493	36.7072451683	44.9629239592	−4.3	0.2	1.2	0.2	−150.14	0.63	5430	150	3.4	0.3	0.079	N	Ito et al. (2013)
HE 0233−0343	39.1241380137	−3.50167460698	−4.7	0.2	3.48	0.24	64	1	6300	100	3.4	0.3	0.022	N	Hansen et al. (2015)
BPS CS 22963−0004	44.1940476203	−4.85483952327	−4.09	0.15	0.40	0.23	292.4	0.2	5060	42	2.15	0.16	0.045	N	Roederer et al. (2014)
SDSS J030444.98+391021.1	46.1874375223	39.1725764233	−4.0	0.2	0.7	–	87	8	5859	13	5.0	0.5	0.111	N	Aguado et al. (2017b)
SMSS J031300.36−670839.3	48.2515614545	−67.1442601577	<−6.53	–	4.5	0.2	298.5a	0.5	5125	–	2.3	–	0.032	N	Keller et al. (2014), Nordlander et al. (2017)
HE 0330+0148	53.158696449	1.96666957231	−4.0	0.1	2.6	–	−33.6a	1.0	4100	200	5.2	0.1	0.094	Y	Plez, Cohen & Meléndez (2005)
HE 0557−4840	89.6636087844	−48.6658029727	−4.8	0.2	1.65	–	211.9	0.8	4900	100	2.2	0.3	0.037	N	Norris et al. (2007)
SDSS J081554.26+472947.5	123.976115075	47.4965559814	<−5.8	–	>5.0	–	−95	23	6215	82	4.7	0.5	0.063	N	Aguado et al. (2018a)
SDSS J092912.32+023817.0	142.301366238	2.63806158906	−4.97	–	<3.91	–	388.3	10.4	5894	–	3.7	–	0.053	Y	Bonifacio et al. (2015), Caffau et al. (2016)
SDSS J094708.27+461010.0	146.784471294	46.1694746754	−4.1	0.2	1.0	0.4	−5	12	5858	73	5.0	0.5	0.013	N	Aguado et al. (2017a)
HE 1012−1540	153.722814524	−15.9314366402	−4.17	0.16	2.2	–	225.8a	0.5	5230	32	2.65	0.2	0.061	N	Roederer et al. (2014)
SDSS J102915+172927	157.313121378	17.4910907404	−4.99	0.06	<0.7	–	−35	4	5850	100	4.0	0.2	0.023	N	Caffau et al. (2011)
SDSS J103402.70+070116.6	158.511301205	7.02129528322	−4.01	0.14	–	–	153	3	6270	–	4.0	–	0.02	N	Bonifacio et al. (2018)
SDSS J103556.11+064143.9	158.983818359	6.6955582264	<−5	–	3.08	–	−45	6	6262	–	4	–	0.024	N	Bonifacio et al. (2015)
SDSS J105519.28+232234.0	163.830333515	23.3761158455	−4.00	0.07	<0.7	–	62	4	6232	28	4.9	0.1	0.015	N	Aguado et al. (2017b)
SDSS J120441.38+120111.5	181.172452065	12.019865284	−4.34	0.05	<1.45	–	51	3	5917	–	3	–	0.024	N	Placco et al. (2015)
SDSS J124719.46−034152.4	191.831114232	−3.69791795379	−4.11	0.18	<1.61	–	84	6	6332	–	4	–	0.022	N	Caffau et al. (2013b)
LAMOST J125346.09+075343.1	193.44189217	7.89526036289	−4.02	0.06	1.59	–	78.0	0.4	6030	135	3.65	0.16	0.025	N	Li et al. (2015)
SDSS J131326.89−001941.4	198.3620349838832	−0.3281488686298	−4.7	0.2	2.8	0.3	268	4	5525	106	3.6	0.5	0.024	Y	Allende Prieto et al. (2015), Frebel et al. (2015), Aguado et al. (2017b)
HE 1310−0536	198.379940261	−5.87014820763	−4.2	0.2	2.36	0.23	113.2	1.7	5000	100	1.9	0.3	0.037	N	Hansen et al. (2015)
HE 1327−2326	202.524748159	−23.6971386187	−5.96	–	3.78	–	64.4a	1.3	6200	100	3.7	0.3	0.066	N	Frebel et al. (2008)
HE 1424−0241	216.668044499	−2.90763517546	−4.05	–	<0.63	–	59.8	0.6	5260	–	2.66	–	0.055	N	Norris et al. (2013), Cohen et al. (2008)
SDSS J144256.37−001542.7	220.734907425	−0.26188939275	−4.09	0.21	<1.59	–	225	9	5850	–	4	–	0.036	N	Caffau et al. (2013a)
Pristine221.8781+9.7844	221.878064787	9.78436859397	−4.66	0.13	<1.76	–	−149.0	0.5	5792	100	3.5	0.5	0.020	N	Starkenburg et al. (2018)
SDSS J164234.48+443004.9	250.643694345	44.5013644484	−4.0	0.2	0.55	0.0	−136	4	6280	150	5.0	0.3	0.011	N	Aguado et al. (2016)
SDSS J173403.91+644633.0	263.516273652	64.7758235012	−4.3	0.2	3.1	0.2	−258	13	6183	78	5.0	0.5	0.028	N	Aguado et al. (2017a)
SDSS J174259.67+253135.8	265.748669215	25.526636261	−4.8	0.07	3.6	0.2	−221.93	10.00	6345	–	4	–	0.055	N	Bonifacio et al. (2015)
2MASS J18082002−5104378	272.083464041	−51.0771900644	−4.07	0.07	<0.5	–	16.54	0.12	5440	100	3.0	0.2	0.101	Y	Meléndez et al. (2016) Schlaufman et al. (2018)
BPS CS 22891−0200	293.829490257	−61.7067706698	−4.06	0.15	–	–	131	10	4490	33	0.5	0.1	0.068	N	Roederer et al. (2014)
BPS CS 22885−0096	305.213220651	−39.8917320574	−4.21	0.07	–	–	−248	10	4580	34	0.75	0.15	0.048	N	Roederer et al. (2014)
BPS CS 22950−0046	305.368323431	−13.2760006492	−4.12	0.14	–	–	111	10	4380	32	0.5	0.1	0.054	N	Roederer et al. (2014)
BPS CS 30336−0049	311.348055352	−28.7099758468	−4.04	0.09	−0.28	0.31	−236.6	0.8	4827	100	1.5	0.2	0.054	N	Lai et al. (2008)
HE 2139−5432	325.676864649	−54.3119357441	−4.02	–	–	–	105a	3	5457	44	2.0	0.2	0.017	Ya	Norris et al. (2013)
HE 2239−5019	340.611864594	−50.0669213083	−4.2	0.2	<1.7	–	368.7	0.5	6100	100	3.5	0.3	0.010	N	Hansen et al. (2015)
HE 2323−0256	351.62419731	−2.66612144628	−4.38	0.15	–	–	−125.8a	0.3	4630	34	0.95	0.13	0.043	N	Roederer et al. (2014)

3.1.1 $\mathcal{L}_{\rm phot}(\boldsymbol{\Theta}_{\rm phot}|\mathcal{M})$

In order to determine the photometric likelihood of a given star for a chosen μ and A, we rely on the isochrone models from the MESA/MIST library (Paxton et al. 2011; Choi et al. 2016; Dotter 2016), as they are the only set of publicly available isochrones that reach the lowest metallicity ([Fe/H] = −4.0 dex) and is therefore the most appropriate for our study.

Any isochrone, $\mathcal{I}$, of a given age, A, associated with a luminosity function[3] $\Phi(M_G|A)$, predicts the density distribution triplet of absolute magnitudes $p(M_G, M_{BP}, M_{RP}|\mathcal{I}, \Phi)$ in

[3]This associated luminosity function, Φ, assumes a Salpeter IMF (Salpeter 1955). The choice of the IMF is not very sensitive for the type of stars we analyse.

Table 2. Gaia properties of the stars. Coordinates at J2015.5, the dereddened G_0, BP_0, and RP_0 magnitudes, proper motion μ_α, μ_δ, and the parallax ϖ for the analysed sample of UMPs (https://gea.esac.esa.int/archive/ Gaia Collaboration 2016, 2018) are listed. G_0, BP_0, and RP_0 magnitudes are dereddened using the Schlegel et al. (1998) extinction map. The parallaxes ϖ are not corrected for the offset $\varpi_0 = -0.029$ mas.

Identifier	$\alpha_{J2015.5}$ (deg)	$\delta_{J2015.5}$ (deg)	Gaia id	G_0 (mag)	δ_G (mag)	BP_0 (mag)	δ_{BP} (mag)	RP_0 (mag)	δ_{RP} (mag)	μ_α (mas yr^{-1})	δ_{μ_α} (mas yr^{-1})	μ_δ (mas yr^{-1})	δ_{μ_δ} (mas yr^{-1})	ϖ (mas)	δ_ϖ (mas)
HE 0020−1741	5.68699047782	−17.40811466246	2367173119271988480	12.5609	0.00017	13.0699	0.0010	11.9040	0.0006	14.424	0.064	−4.546	0.043	0.1456	0.0384
SDSS J0023+0307	5.80835977813	3.132743082	2548541852945056896	17.5638	0.001	17.7947	0.0074	17.1246	0.0074	3.743	0.318	−13.912	0.187	0.2697	0.1406
HE 0044−3755	11.65089731416	−37.65935345272	5000753194373767424	11.6633	0.0003	12.1427	0.0009	11.0310	0.0009	15.234	0.061	−7.529	0.041	0.2152	0.0344
HE 0057−5959	14.97496136508	−59.72497472878	4903905598859396480	15.0507	0.0004	15.3857	0.0025	14.5292	0.0025	2.389	0.042	−10.522	0.041	0.1982	0.0254
HE 0107−5240	17.37149810186	−52.40951706252	4927204800008334464	14.9334	0.0003	15.3232	0.0019	14.3638	0.0019	2.414	0.033	−3.735	0.035	0.0789	0.0258
HE 0134−1519	24.27251527664	−15.07304490506	2453397508316944128	14.2270	0.0003	14.5501	0.0022	13.7181	0.0022	24.961	0.056	−10.905	0.039	0.3454	0.0299
SDSS J014036.21+234458.1	25.15092436121	23.74940873996	290930261314166528	15.0495	0.0006	15.3423	0.0034	14.5750	0.0034	1.019	0.176	−21.466	0.091	1.0482	0.0562
BD+44 493	36.70796538815	44.96278519908	341511064663637376	8.6424	0.0005	8.9634	0.0016	8.1758	0.0016	118.359	0.141	−32.229	0.105	4.7595	0.0660
HE 0233−0343	39.12435352835	−3.50172027632	2495327693479473408	15.2126	0.0005	15.4433	0.0027	14.8029	0.0027	49.962	0.073	−10.607	0.072	0.7925	0.0545
BPS CS 22963−0004	44.1941414394	−4.85485100336	5184426749232471808	14.6906	0.0005	14.9991	0.0024	14.1973	0.0024	21.712	0.058	−2.666	0.059	0.2220	0.0364
SDSS J030444.98+391021.1	46.18743595787	39.17249343121	142874251765330944	17.0085	0.0019	17.3215	0.0088	16.5085	0.0088	−0.282	0.336	−19.276	0.241	0.0752	0.1929
SMSS J031300.36−670839.3	48.25163934361	−67.14425547143	4671418400651900544	14.4342	0.0003	14.8379	0.0018	13.8545	0.0018	7.027	0.032	1.088	0.03	0.0981	0.0162
HE 0330+0148	53.15953261866	1.96344241611	3265069670684495744	13.0859	0.0004	13.8664	0.0032	12.2728	0.0032	194.093	0.453	−749.533	0.499	12.7174	0.2106
HE 0557−4840	89.66361346726	−48.66579980934	4794791782906532608	15.0976	0.0004	15.5156	0.0028	14.4984	0.0028	0.718	0.043	0.735	0.044	0.0389	0.0207
SDSS J081554.26+472947.5	123.97602487635	47.49645166114	931227322991970560	16.5417	0.0006	16.8056	0.0057	16.1052	0.0057	−14.154	0.135	−24.229	0.09	0.4441	0.0837
SDSS J092912.32+023817.0	142.30134736257	2.63804791153	3844818546870217728	17.8302	0.0023	18.1360	0.0316	17.3618	0.0316	−4.379	0.342	−3.177	0.364	0.1276	0.1872
SDSS J094708.27+461010.0	146.78455769932	46.16940656739	821637654725909760	18.7343	0.0021	19.0195	0.0221	18.2783	0.0221	13.898	0.317	−15.819	0.332	0.1989	0.2299
HE 1012−1540	153.7223563828	−15.93131552666	3751852536639575808	13.7019	0.0004	14.0084	0.0033	13.2135	0.0033	−102.32	0.046	28.13	0.04	2.5417	0.0280
SDSS J102915+172927	157.31307233934	17.49107327845	3890626773968983296	16.4857	0.0013	16.7665	0.0062	15.9976	0.0062	−10.863	0.146	−4.056	0.113	0.7337	0.0780
SDSS J103402.70+070116.6	158.51126738928	7.02126631404	3862721340654330112	17.1906	0.0018	17.4051	0.0227	16.7943	0.0063	−7.795	0.236	−6.728	0.291	0.2874	0.1367
SDSS J103556.11+064143.9	158.98383317025	6.69554785085	3862507691800855040	18.3472	0.0034	18.6230	0.0197	17.9584	0.0197	3.416	0.403	−2.41	0.369	−0.3912	0.3163
SDSS J105519.28+232234.0	163.83036912138	23.37606935407	3989873022818570240	17.5182	0.0025	17.7015	0.0317	17.1298	0.0317	7.591	0.291	−10.798	0.324	0.5909	0.1821
SDSS J120441.38+120111.5	181.17245380263	12.01984412118	3919025342543602176	16.0270	0.0005	16.3239	0.0043	15.5497	0.0043	0.395	0.11	−4.915	0.067	0.2454	0.0656
SDSS J124719.46−034152.4	191.83107728926	−3.69791015204	3681866216349964288	18.1908	0.0016	18.3958	0.0118	17.7716	0.0118	−8.562	0.439	1.812	0.226	0.3075	0.2098
LAMOST J125346.09+075343.1	193.44198364753	7.895007511	3737680786424022016	12.2280	0.0002	12.4603	0.0011	11.8239	0.0011	21.045	0.082	−58.727	0.049	1.4053	0.0378
SDSS J131326.89−001941.4	198.36201866349555	−0.32817714440715445	3687441358777986688	16.3560	0.0010	16.7237	0.0058	15.8183	0.0710	−3.790	0.160	−6.567	0.078	0.2976	0.0972
HE 1310−0536	198.37991838382	−5.8701554707	3635533208672382592	14.0256	0.0004	14.5363	0.0021	13.3649	0.0021	−5.054	0.053	−1.687	0.042	0.0078	0.0342
HE 1327−2326	202.52450119109	−23.69694272263	6194815228636688768	13.2115	0.0004	13.4500	0.0019	12.8012	0.0019	−52.524	0.04	45.498	0.035	0.8879	0.0235
HE 1424−0241	216.66802803117	−2.90764744641	3643332182086977792	15.0437	0.0007	15.3934	0.0046	14.5017	0.0046	−3.82	0.087	−2.85	0.066	0.1152	0.0469
SDSS J144256.37−001542.7	220.73490626598	−0.26186035888	3651420563283262208	17.5635	0.0023	17.8216	0.0277	17.1364	0.0277	−0.269	0.315	6.743	0.396	−0.3910	0.2981
Pristine221.8781+9.7844	221.87803086877	9.78436834556	1174522686140620672	16.1846	0.0009	16.4688	0.0053	15.7060	0.0053	−7.763	0.110	−0.058	0.116	0.1187	0.0940
SDSS J164234.48+443004.9	250.643641407	44.50138608236	1405755062407483520	17.4658	0.0012	17.6987	0.0112	17.0356	0.0112	−8.769	0.149	5.025	0.244	0.3122	0.0906
SDSS J173403.91+644633.0	263.51630029934	64.77581642801	1632736765377141632	19.1198	0.0038	19.3849	0.0465	18.7074	0.0465	2.638	0.44	−1.643	0.553	−0.1052	0.2702
SDSS J174259.67+253135.8	265.74864014534	25.52658646063	4581822389265279232	18.5115	0.0022	18.7628	0.0248	18.0991	0.0248	−6.093	0.248	−11.567	0.292	−0.1628	0.1870
2MASS J18082002−5104378	272.08342547713	−51.07724449784	6702907209758894848	11.4880	0.0003	11.7853	0.0024	11.0119	0.0024	−5.627	0.068	−12.643	0.058	1.6775	0.0397
BPS CS 22891−0200	293.82944462026	−61.70676742367	6445220927325014016	13.4478	0.0003	13.9306	0.0017	12.8053	0.0017	−5.024	0.053	0.754	0.036	0.1135	0.0342
BPS CS 22885−0096	305.21319576813	−39.89176180812	6692925538259931136	12.9385	0.0003	13.3482	0.0017	12.3514	0.0017	−4.434	0.038	−6.91	0.028	0.1708	0.0247
BPS CS 22950−0046	305.36833037469	−13.27600846442	6876806419780834048	13.7403	0.0002	14.2631	0.0011	13.0627	0.0011	1.57	0.045	−1.815	0.028	0.0587	0.0270
BPS CS 30336−0049	311.34804708033	−28.71001086007	6795730493933072128	13.5803	0.0002	14.0740	0.0013	12.9283	0.0013	−1.685	0.038	−8.132	0.027	0.0418	0.0227
HE 2139−5432	325.676883449	−54.31195504869	6461736966363075200	14.9386	0.0003	15.2991	0.0017	14.4000	0.0017	2.547	0.046	−4.484	0.041	−0.0067	0.0298
HE 2239−5019	340.61191653735	−50.06702317874	6513870718215626112	15.6038	0.0007	15.8336	0.0034	15.2107	0.0034	7.744	0.054	−23.66	0.076	0.2200	0.0545
HE 2323−0256	351.6242048175	−2.66612932812	2634585342263017984	13.9922	0.0004	14.4286	0.0031	13.3832	0.0031	1.742	0.062	−1.831	0.048	0.0038	0.0359

the Gaia photometric bands. After computing the likelihood $p(\mathbf{\Theta}_{\rm phot}|M_G, M_{BP}, M_{RP}, \mu)$, of these predictions shifted to a distance modulus μ, against the observed photometric properties of the star, $\mathcal{L}_{\rm phot}$ results from the marginalization along that isochrone:

$$\mathcal{L}_{\rm phot}(\mathbf{\Theta}_{\rm phot}|\mu, A, \Phi)$$
$$= \int_{\mathcal{I}} p(\mathbf{\Theta}_{\rm phot}|M_G, M_{BP}, M_{RP}, \mu)$$
$$\times p(M_G, M_{BP}, M_{RP}|\mathcal{I}, \Phi)p(\mathcal{I}|A)d\mathcal{I}, \qquad (6)$$

with

$$p(\mathbf{\Theta}_{\rm phot}|M_G, M_{BP}, M_{RP}, \mu)$$
$$= \mathcal{N}(G_0|M_G + \mu, \delta_G^2 + 0.01^2)$$
$$\times \mathcal{N}((BP - RP)_0|M_{BP} - M_{RP}, \delta_{BP}^2 + \delta_{RP}^2 + 2 \times 0.01^2) \quad (7)$$

and $\mathcal{N}(x|m, s^2)$ the value of a Gaussian function of mean m and variance s^2 taken on x. In equation (7), a systematic uncertainty of 0.01 mag is added to the photometric uncertainties in each band to represent the uncertainties on the models.

For most stars, we expect to find two peaks in $\mathcal{L}_{\rm phot}(\mathbf{\Theta}_{\rm phot}|\mathcal{M})$, corresponding to the dwarf and giant solutions but stars close to the main sequence turnoff naturally yield a PDF with a single peak.

3.1.2 $\mathcal{L}_{\rm astrom}(\mathbf{\Theta}_\varpi|\mathcal{M})$

Gaia DR2 provides us with a parallax ϖ and its uncertainty δ_ϖ, which is instrumental in breaking the dwarf/giant distance degeneracy for most stars. The astrometric likelihood is trivially

defined as

$$\mathcal{L}_{\text{astrom}}(\varpi\,|\delta_\varpi,r) = \frac{1}{\sqrt{2\pi}\,\delta_\varpi} \exp\left(-\frac{1}{2}\left(\frac{\varpi - \varpi_0 - r^{-1}}{\delta_\varpi}\right)^2\right). \quad (8)$$

Here, $\varpi_0 = -0.029$ mas is the parallax zero-point offset measured by Lindegren et al. (2018).

Even in cases for which the parallax is small and the associated uncertainties are large, the Gaia data are often informative enough to rule out a nearby (dwarf) solution.

3.1.3 $\mathcal{P}(\mathcal{M})$

Prior on the distance and position $(r|\ell,\,b)$ — The prior on the distance and position to the star folds in our knowledge of the distribution of UMP stars around the MW. Since we expect those stars to be among the oldest stars of the MW and (likely) accreted, we first assume a halo profile. In particular, we use the RR Lyrae density power-law profile inferred by Hernitschek et al. (2018), $\rho(r) \propto r^{-3.4}$, since RR Lyrae stars are also expected to be old halo tracers.

From this stellar density profile, the probability density to have a star at distance r from the Sun along the line of sight described by Galactic coordinates $(\ell,\,b)$ is

$$\mathcal{P}_{\text{H}}(r|\ell,b) = \rho_0 r^2\left(\frac{D_{\text{GC}}(r|\ell,b)}{r_0}\right)^{-3.4}. \quad (9)$$

In this equation, $D_{\text{GC}}(r|\ell,b)$ is the distance of the star to the Galactic centre, while ρ_0 and r_0 are reference values for the density and the scalelength of the halo. For this work, the specific values of ρ_0 and r_0 will not affect the result because they will be simplified during the normalization of the posterior PDF.

Anticipating the results described in Section 4, we find that, even when using a pure halo prior, ~26 per cent of our sample remains confined to the MW plane and the distance inference for a small number of stars yields unrealistic (unbound) orbits. Hence we repeat the analysis described with a mixture of a thick disc and a halo prior to investigate if, and how, the choice of the prior affects our results. This alternative MW prior is defined as

$$\mathcal{P}_{\text{DH}}(r|\ell,b) = \eta\mathcal{P}_{\text{D,norm}}(r|\ell,b) + (1-\eta)\mathcal{P}_{\text{H,norm}}(r|\ell,b), \quad (10)$$

with $\eta = 1/2$ the mixture coefficient, $\mathcal{P}_{\text{H,norm}}(r|\ell,b)$ the normalized halo prior expressed in equation (9), and $\mathcal{P}_{\text{D,norm}}(r|\ell,b)$ the normalized thick disc prior defined by Binney & Tremaine (2008):

$$\mathcal{P}_{\text{D}}(r|\ell,b) = \frac{r^2\Sigma_{\text{T}}}{2z_{\text{T}}}\exp\left(-\frac{D_{\text{GC}}(r,\ell,b)}{D_{\text{T}}} - \frac{|z|}{z_{\text{T}}}\right), \quad (11)$$

with $\Sigma_{\text{T}} = 268.648\,\text{M}_\odot\,\text{pc}^{-2}$ the disc surface density, $D_{\text{T}} = 2\,\text{kpc}$ the radial scalelength for the density and $z_{\text{T}} = 0.9\,\text{kpc}$ the vertical scalelength (Bland-Hawthorn & Gerhard 2016).

Prior on the age A, $\mathcal{P}(A)$ — There is no well defined age constraint for UMP stars, but they are usually assumed to be very old (Starkenburg et al. 2017b). Hence we assume that all the stars studied here were formed at least 11.2 Gyr ago ($\log(A/\text{yr}) = 10.05$). Beyond this age, we assume a uniform prior on $\log(A)$ until 14.1 Gyr ($\log(A/\text{yr}) = 10.15$), which is the maximum value of the isochrone grid.

Finally, $\mathcal{P}(\mathcal{M}) = \mathcal{P}(r|\ell,b)\mathcal{P}(A)$.

3.1.4 Posterior PDF on distance r

So far, $\mathcal{M} = \{\mu, A\}$ but we aim to infer the PDF on the distance modulus (or the distance) to the star alone. In order to do so, we

simply marginalize over the age:

$$P(r = 10^{(\mu+5)/5}|\mathbf{\Theta}) = \int \mathcal{P}(\mathcal{M}|\mathbf{\Theta})dA, \quad (12)$$

assuming $\mu \geq 0$ mag ($r \geq 10\,\text{pc}$).

3.2 Effective temperature and surface gravity inference

For each point of the theoretical isochrones $\mathcal{I}(A,\mu)$ corresponds a value of the surface gravity, $\log(g)$, and a value of the effective temperature, T_{eff}. Marginalizing the likelihood and prior over distance modulus and age instead of over the isochrone as in equation (6), we can find the posterior probability as a function of $\log(g)$ and T_{eff}. In detail,

$$\mathcal{P}(\log(g), T_{\text{eff}}|\mathbf{\Theta}) = \iint P(\mathbf{\Theta}|\log(g), T_{\text{eff}}, \mathcal{I}(A), \mu)$$
$$\times\,\Phi(M(\log(g), T_{\text{eff}}, A))\mathcal{P}(r,\ell,b)\mathcal{L}_{\text{astrom}}(\varpi\,|r(\mu), \delta_\varpi)\,\text{dA}\,\text{d}\mu. \quad (13)$$

3.3 Orbital inference

Gaia DR2 provides proper motions in right ascension and declination with their associated uncertainties and covariance. Combining this with the distance inferred through our analysis, we can calculate the velocity vector PDF $P(\boldsymbol{v}) = P(v_r, v_\alpha, v_\delta)$ for all 42 stars in our UMPs sample. This PDF, in turn, allows us to determine the properties of the orbit of the stars for a given choice of Galactic potential. We rely on the `galpy`[4] package (Bovy 2015) and choose their *MWPotential14*, which is a MW gravitational potential composed of a power law, exponentially cut-off bulge, a Miyamoto Nagai Potential disc, and a Navarro, Frenk & White (1997) dark matter halo. A more massive halo is chosen for this analysis, with a mass of $1.2 \cdot 10^{12}\,\text{M}_\odot$ compatible with the value from Bland-Hawthorn & Gerhard (2016; versus $0.8 \cdot 10^{12}\,\text{M}_\odot$ for the halo used in *MWPotential14*).

For each star, we perform a thousand random drawings from the position, distance, radial velocity, and proper motion PDFs. In the case of the two components of the proper motion $(\mu_\alpha,\,\mu_\delta)$, we consider their correlation given by the coefficients in *Gaia DR2*, drawing randomly these two parameters according to a multivariate Gaussian function that takes into account the correlation. The possible correlation between coordinates and proper motions is not taken into account because it does not affect our result. For each drawing, we integrate this starting phase-space position backwards and forwards for 2 Gyr and extract the apocentre, r_{apo}, pericentre, r_{peri}, eccentricity, ε, energy E, the angular momentum L of the resulting orbit (note that in this frame of reference, $L_z > 0$ means a prograde orbit), and the action-angle vector $(J_r, J_\phi = L_z, J_z$, where the units are in $\text{km s}^{-1}\,\text{kpc}$).

4 RESULTS

Tables 3 and 4 summarize the results of the analysis and list the inferred stellar and orbital properties for all stars, respectively. In cases for which the (distance) PDF is double-peaked, we report the two solutions along with their fractional probability.

Fig. 1 shows the colour-magnitude diagram (CMD) and the temperature-surface gravity diagram for our UMP sample, plot-

---

[4] http://github.com/jobovy/galpy

Table 3. Inferred stellar parameters for the stars in the sample. Distances D, effective temperatures T_{eff} and surface gravities log(g) obtained in this work for the UMPs sample. If a second peak in the PDF is present, an estimate of the subtended area around the two peaks within $\pm 3\sigma$ is shown (Area= $\int_{d_1-3\sigma}^{d_1+3\sigma} P(r) \mathrm{d}r$). The column *Prior* indicates the MW prior used for inferring the parameters (i.e. H means halo prior, D+H indicates the disc+halo prior).

Identifier	D (kpc)	δ_D (kpc)	T_{eff} (K)	$\delta_{T_{eff}}$ (K)	log(g) (dex)	$\delta_{\log(g)}$ (dex)	Area	Prior
HE 0020−1741	10.3	0.4	4774	20	1.05	0.05		H
	10.3	0.4	4774	20	1.05	0.05		D+H
SDSS J0023+0307	2.710	0.139	6116	66	4.6	0.1	88%	H
	11.03	0.73	6047	146	3.4	0.1	12%	H
	2.693	0.136	6108	65	4.6	0.1	99.6%	D+H
	11.02	0.74	6050	154	3.4	0.1	0.4%	D+H
HE 0044−3755	5.70	0.25	4852	22	1.2	0.1		H
	5.65	0.26	4863	23	1.2	0.1		D+H
HE 0057−5959	6.80	0.71	5483	42	2.7	0.1		H
	6.50	0.72	5501	44	2.7	0.1		D+H
HE 0107−5240	14.3	1.0	5141	32	1.9	0.1		H
	14.2	1.0	5141	32	1.9	0.1		D+H
HE 0134−1519	3.75	0.33	5572	90	2.9	0.1		H
	3.61	0.30	5589	37	2.9	0.1		D+H
SDSS J014036.21+234458.1	0.762	0.022	5963	41	4.6	0.1		H
	0.761	0.022	5962	40	4.6	0.1		D+H
BD+44 493	0.211	0.003	5789	19	3.2	0.1		H
	0.211	0.003	5794	20	3.2	0.1		D+H
HE 0233−0343	1.090	0.043	6331	47	4.5	0.1		H
	1.088	0.043	6327	47	4.5	0.1		D+H
BPS CS 22963−0004	4.47	0.42	5589	42	2.9	0.1		H
	4.36	0.39	5601	43	3.0	0.1		D+H
SDSS J030444.98+391021.1	14.9	1.3	5547	39	2.8	0.1	99%	H
	1.505	0.071	5649	68	4.7	0.1	1%	H
	14.3	2.5	5548	74	2.8	0.2	79%	D+H
	1.503	0.071	5648	68	4.7	0.1	21%	D+H
SMSS J031300.36−670839.3	12.0	0.8	5111	31	1.8	0.1		H
	12.1	0.8	5111	32	1.8	0.1		D+H
HE 0330+0148	0.075	0.001	4454	1	5.0	0.1		H
	0.075	0.001	4460	1	5.0	0.1		D+H
HE 0557−4840	20.0	1.3	5017	28	1.6	0.1		H
	20.0	1.3	5018	30	1.6	0.1		D+H
SDSS J081554.26+472947.5	1.591	0.067	6034	56	4.6	0.1		H
	1.588	0.066	6031	56	4.6	0.1		D+H
SDSS J092912.32+023817.0	15.6	2.6	5708	124	3.1	0.2	68%	H
	2.398	0.205	5775	122	4.7	0.1	32%	H
	2.367	0.198	5756	120	4.7	0.1	95%	D+H
	15.5	2.6	5713	125	3.1	0.2	5%	D+H
SDSS J094708.27+461010.0	3.84	0.30	5854	110	4.7	0.1	82%	H
	21.9	2.0	5801	118	3.2	0.1	18%	H
	3.76	0.28	5823	55	4.7	0.1	98%	D+H
	21.9	2.0	5802	120	3.2	0.1	2%	D+H
HE 1012−1540	0.384	0.004	5872	16	4.7	0.1		H
	0.384	0.004	5870	16	4.7	0.1		D+H
SDSS J102915+172927	1.281	0.051	5764	57	4.7	0.1		H
	1.278	0.050	5761	56	4.7	0.1		D+H
SDSS J103402.70+070116.6	2.79	0.26	6366	110	4.5	0.1	89%	H
	8.28	0.64	6333	211	3.6	0.1	11%	H
	2.75	0.25	6330	110	4.5	0.1	99.4%	D+H
	8.18	0.65	6320	200	3.6	0.1	0.6%	D+H
SDSS J103556.11+064143.9	3.97	0.35	6144	110	4.6	0.1	67%	H
	15.6	1.2	6072	168	3.5	0.1	33%	H
	3.88	0.32	6114	106	4.6	0.1	95.5%	D+H
	15.6	1.2	6073	175	3.5	0.1	0.5%	D+H
SDSS J105519.28+232234.0	3.49	0.45	6452	147	4.5	0.1	96%	H
	8.84	0.94	6581	248	3.8	0.2	4%	H
	3.30	0.39	6387	138	4.5	0.1	99.7%	D+H
	8.79	0.99	6606	257	3.8	0.2	0.3%	D+H
SDSS J120441.38+120111.5	7.03	0.54	5679	56	3.1	0.1		H
	6.96	0.53	5686	59	3.1	0.1		D+H

Table 3 – *continued*

Identifier	D (kpc)	δ_D (kpc)	T_{eff} (K)	$\delta_{T_{eff}}$ (K)	log(g) (dex)	$\delta_{\log(g)}$ (dex)	Area	Prior
SDSS J124719.46−034152.4	4.17	0.32	6296	92	4.5	0.1	92%	H
	13.5	1.0	6256	196	3.6	0.1	8%	H
	4.09	0.30	6273	90	4.5	0.1	99%	D+H
	13.4	1.0	6263	205	3.6	0.1	1%	D+H
LAMOST J125346.09+075343.1	0.766	0.016	6598	52	3.8	0.1		H
	0.766	0.016	6608	52	3.8	0.1		D+H
SDSS J131326.89−001941.4	8.59	2.86	5649	171	3.1	0.3	99.96%	H
	1.765	0.248	6278	171	4.5	0.1	0.04%	H
	8.07	2.70	5687	185	3.1	0.3	96.85%	D+H
	1.707	0.227	6237	164	4.6	0.1	3.15%	D+H
HE 1310−0536	20.6	0.9	4788	20	1.0	0.1		H
	20.6	0.9	4764	21	1.0	0.1		D+H
HE 1327−2326	1.212	0.024	6581	52	3.8	0.1		H
	1.212	0.024	6591	51	3.8	0.1		D+H
HE 1424−0241	10.3	1.0	5308	40	2.3	0.1		H
	10.3	1.0	5308	40	2.3	0.1		D+H
SDSS J144256.37−001542.7	11.3	1.0	5993	165	3.4	0.1	87%	H
	2.683	0.266	6104	128	4.6	0.1	13%	H
	2.634	0.249	6079	124	4.6	0.1	84%	D+H
	11.3	1.0	5998	172	3.4	0.1	16%	D+H
Pristine221.8781+9.7844	7.36	0.55	5700	63	3.1	0.1		H
	7.28	0.52	5710	65	3.1	0.1		D+H
SDSS J164234.48+443004.9	2.66	0.16	6149	77	4.6	0.1	99%	H
	10.2	0.7	6126	163	3.5	0.1	1%	H
	2.64	0.16	6140	76	4.6	0.1	99.95%	D+H
	10.1	0.7	6148	172	3.5	0.1	0.05%	D+H
SDSS J173403.91+644633.0	5.46	1.02	6094	233	4.6	0.1	86%	H
	21.8	3.0	6131	297	3.5	0.2	14%	H
	5.05	0.79	5992	208	4.6	0.1	97%	D+H
	21.7	3.0	6134	302	3.5	0.2	3%	D+H
SDSS J174259.67+253135.8	4.46	0.52	6194	145	4.6	0.1	63%	H
	16.6	1.4	6115	198	3.5	0.1	37%	H
	4.34	0.48	6162	140	4.6	0.1	94%	D+H
	16.5	1.4	6118	206	3.5	0.1	6%	D+H
2MASS J18082002−5104378	0.647	0.012	6124	44	3.5	0.1		H
	0.647	0.012	6133	44	3.5	0.1		D+H
BPS CS 22891−0200	14.7	0.5	4789	2	1.2	0.1		H
	13.6	0.6	4836	22	1.2	0.1		D+H
BPS CS 22885−0096	6.65	0.22	5068	16	1.7	0.1		H
	6.61	0.38	5070	27	1.7	0.1		D+H
BPS CS 22950−0046	19.1	0.3	<4780	−	<1.0	−		H
	19.1	0.3	<4780	−	<1.0	−		D+H
BPS CS 30336−0049	15.5	0.7	4809	20	1.1	0.1		H
	15.5	0.7	4802	21	1.1	0.1		D+H
HE 2139−5432	11.0	0.9	5259	34	2.1	0.1		H
	11.0	0.9	5259	34	2.1	0.1		D+H
HE 2239−5019	4.19	0.28	6195	179	3.5	0.1		H
	4.13	0.16	6411	100	3.6	0.1		D+H
HE 2323−0256	14.2	0.6	4937	22	1.4	0.1		H
	14.2	0.6	4937	22	1.4	0.1		D+H

ted with three isochrones that cover the age range we considered ($\log(A/\mathrm{yr}) = 10.05, 10.10, 10.15$). For stars for which the dwarf/giant degeneracy is not broken, we show both solutions connected by a dot–dashed line, where the least probable solution is marked with a dot–dashed ellipse. Only results using a MW halo prior are shown here. As we can see, from the CMD plot (left-hand panel of Fig. 1), the method overall works well, except for the HE 0330+0148 ($(BP - RP)_0 \approx 1.6$ mag) that

lays outside the colour range of the available set of isochrones. This special case is discussed in more detail in section A13 (available Online). The distances and stellar parameters lead to the conclusion that 18 stars (∼43 per cent) are in the main sequence phase, and the other 24 are in the subgiant/giant phase (∼57 per cent). This is of course a result of the observing strategies of the multiple surveys that led to the discovery of these stars.

Table 4. Inferred orbital parameters of the stars in the sample. Position (X,Y,Z), the apocentre and pericentre distances in the galactocentric frame, the velocity (U,V,W) in the heliocentric frame, the eccentricity $\varepsilon = (r_{\rm apo} - r_{\rm peri})/(r_{\rm apo} + r_{\rm peri})$ of the orbit, the z-component of the angular momentum, the energy and the kind of orbit (IH = inner halo with $r_{\rm apo} < 30$ kpc, OH = outer halo with $r_{\rm apo} > 30$ kpc, P = close to the MW plane, S = possible Sgr stream member, ω = possible ωCen member) are listed. For the unbound orbits, all the orbital parameters and the kind of orbit are denoted by NB.

Identifier	X (kpc)	Y (kpc)	Z (kpc)	U (km s^{-1})	V (km s^{-1})	W (km s^{-1})	Apo (kpc)	Peri (kpc)	ε	Lz (km s^{-1} kpc)	E (km^2 s^{-2})	Orbit
HE 0020−1741	$7.909^{+0.0}_{-0.0}$	$1.84^{+0.0}_{-0.0}$	$-8.846^{+0.0}_{-0.0}$	$-428.7^{+0.0}_{-0.0}$	$-446.4^{+0.0}_{-0.0}$	$-192.2^{+0.0}_{-0.0}$	$295.8^{+0.0}_{-0.0}$	$12.0^{+0.0}_{-0.0}$	$0.92^{+0.0}_{-0.0}$	$-2311.5^{+0.0}_{-0.0}$	$63046.1^{+0.0}_{-0.0}$	IH
SDSS J0023+0307	$8.456^{+0.039}_{-0.026}$	$1.311^{+0.113}_{-0.075}$	$-2.375^{+0.133}_{-0.199}$	$76.8^{+3.9}_{-5.2}$	$-251.2^{+8.6}_{-12.9}$	$69.2^{+8.1}_{-5.4}$	$9.8^{+0.0}_{-0.0}$	$0.6^{+0.1}_{-0.1}$	$0.88^{+0.03}_{-0.04}$	$108.2^{+97.9}_{-65.3}$	$-68950.0^{+0.0}_{-0.0}$	IH
	NB	NB	NB	NB	NB	NB	NB	NB	NB	NB	NB	NB
HE 0044−3755	$7.353^{+0.028}_{-0.036}$	$-0.824^{+0.036}_{-0.045}$	$-5.61^{+0.246}_{-0.308}$	$-235.9^{+11.0}_{-12.9}$	$-397.1^{+17.8}_{-22.0}$	$-18.1^{+2.5}_{-2.9}$	$21.8^{+4.6}_{-3.0}$	$4.5^{+0.7}_{-0.7}$	$0.66^{+0.01}_{-0.01}$	$-885.7^{+102.1}_{-134.0}$	$-35273.2^{+6822.9}_{-5458.3}$	IH
HE 0057−5959	$6.077^{+0.187}_{-0.22}$	$-3.206^{+0.312}_{-0.367}$	$-5.839^{+0.568}_{-0.668}$	$206.5^{+10.9}_{-9.8}$	$-456.5^{+26.5}_{-29.9}$	$-129.0^{+20.5}_{-19.4}$	$31.3^{+10.2}_{-5.9}$	$9.0^{+0.4}_{-0.3}$	$0.56^{+0.07}_{-0.06}$	$-1947.5^{+229.5}_{-256.5}$	$-20642.9^{+9464.8}_{-6625.3}$	OH
HE 0107−5240	$5.255^{+0.167}_{-0.191}$	$-5.497^{+0.334}_{-0.382}$	$-12.877^{+0.782}_{-0.894}$	$12.5^{+2.4}_{-2.0}$	$-294.3^{+18.3}_{-19.5}$	$77.2^{+8.7}_{-7.7}$	$15.9^{+1.0}_{-0.9}$	$3.2^{+1.5}_{-1.0}$	$0.66^{+0.08}_{-0.1}$	$-354.3^{+98.9}_{-105.5}$	$-46879.6^{+3604.2}_{-3604.2}$	IH
HE 0134−1519	$9.025^{+0.103}_{-0.082}$	$0.244^{+0.025}_{-0.019}$	$-3.679^{+0.291}_{-0.369}$	$-302.5^{+18.8}_{-23.8}$	$-416.8^{+34.1}_{-43.2}$	$-197.1^{+3.7}_{-3.3}$	$70.2^{+49.3}_{-20.7}$	$4.1^{+5.9}_{-0.6}$	$0.87^{+0.02}_{-0.07}$	$-1555.1^{+313.6}_{-425.6}$	$2196.4^{+16677.9}_{-10006.7}$	OH
SDSS J014036.21+234458.1	$8.447^{+0.023}_{-0.025}$	$0.414^{+0.021}_{-0.023}$	$-0.473^{+0.027}_{-0.024}$	$132.8^{+3.6}_{-3.6}$	$-153.5^{+3.6}_{-4.3}$	$61.5^{+4.2}_{-4.7}$	$11.4^{+0.2}_{-0.1}$	$2.5^{+0.1}_{-0.1}$	$0.64^{+0.02}_{-0.02}$	$884.9^{+29.2}_{-30.8}$	$-61399.9^{+465.4}_{-413.7}$	P
BD+44 493	$8.157^{+0.005}_{-0.005}$	$0.131^{+0.004}_{-0.004}$	$-0.054^{+0.002}_{-0.002}$	$30.6^{+2.4}_{-2.6}$	$-184.5^{+2.7}_{-2.8}$	$51.8^{+0.4}_{-0.4}$	$8.3^{+0.0}_{-0.0}$	$1.5^{+0.2}_{-0.1}$	$0.69^{+0.01}_{-0.03}$	$549.6^{+21.8}_{-22.6}$	$-76078.3^{+236.5}_{-236.5}$	P
HE 0233−0343	$8.62^{+0.04}_{-0.04}$	$0.063^{+0.004}_{-0.004}$	$-0.913^{+0.061}_{-0.056}$	$-175.5^{+9.0}_{-8.6}$	$-209.8^{+13.8}_{-13.3}$	$27.5^{+5.0}_{-5.2}$	$11.9^{+0.5}_{-0.4}$	$1.0^{+0.3}_{-0.3}$	$0.85^{+0.04}_{-0.05}$	$344.6^{+119.0}_{-114.2}$	$-62501.0^{+1475.7}_{-1248.6}$	P
BPS CS 22963−0004	$10.739^{+0.268}_{-0.231}$	$-0.087^{+0.007}_{-0.008}$	$-3.62^{+0.304}_{-0.352}$	$-421.8^{+20.9}_{-24.0}$	$-359.1^{+29.5}_{-34.1}$	$-39.2^{+19.1}_{-16.6}$	$155.8^{+183.4}_{-55.0}$	$3.0^{+8.7}_{-1.1}$	$0.96^{+0.02}_{-0.01}$	$-1134.0^{+337.8}_{-391.2}$	$25397.6^{+15195.6}_{-11396.7}$	OH
SDSS J030444.98+391021.1	NB	NB	NB	NB	NB	NB	NB	NB	NB	NB	NB	NB
	$9.24^{+0.063}_{-0.059}$	$0.735^{+0.037}_{-0.035}$	$-0.435^{+0.021}_{-0.022}$	$-77.0^{+6.6}_{-7.0}$	$-33.8^{+5.1}_{-5.8}$	$-139.9^{+6.8}_{-6.1}$	$16.5^{+1.1}_{-1.0}$	$7.9^{+0.1}_{-0.1}$	$0.35^{+0.03}_{-0.03}$	$1960.2^{+38.6}_{-47.4}$	$-40260.6^{+1798.9}_{-1574.0}$	IH
SMSS J031300.36−670839.3	$5.821^{+0.134}_{-0.16}$	$-8.413^{+0.516}_{-0.619}$	$-8.566^{+0.526}_{-0.631}$	$-218.6^{+18.4}_{-19.5}$	$-459.4^{+16.2}_{-18.2}$	$-32.7^{+12.9}_{-12.2}$	$40.4^{+14.7}_{-7.8}$	$5.8^{+1.5}_{-1.5}$	$0.76^{+0.02}_{-0.01}$	$519.6^{+227.0}_{-176.6}$	$-14038.7^{+9814.5}_{-7633.5}$	OH
HE 0330+0148	$8.055^{+0.002}_{-0.002}$	$-0.003^{+0.0}_{-0.0}$	$-0.049^{+0.002}_{-0.002}$	$106.0^{+8.6}_{-9.1}$	$-240.9^{+9.1}_{-11.1}$	$-71.1^{+8.1}_{-8.1}$	$9.0^{+0.6}_{-0.5}$	$0.5^{+0.3}_{-0.2}$	$0.89^{+0.04}_{-0.06}$	$83.2^{+73.0}_{-89.8}$	$-72495.6^{+717.6}_{-717.6}$	P
HE 0557−4840	$12.281^{+0.27}_{-0.254}$	$-17.142^{+1.012}_{-1.075}$	$-9.58^{+0.566}_{-0.601}$	$-110.0^{+5.3}_{-5.9}$	$-203.0^{+2.8}_{-3.1}$	$-32.5^{+6.1}_{-4.4}$	$23.4^{+1.2}_{-1.1}$	$8.2^{+0.9}_{-0.7}$	$0.48^{+0.02}_{-0.03}$	$2273.1^{+186.3}_{-165.6}$	$-29646.0^{+2020.2}_{-2272.7}$	IH
SDSS J081554.26+472947.5	$9.332^{+0.082}_{-0.091}$	$0.185^{+0.011}_{-0.013}$	$0.892^{+0.055}_{-0.061}$	$-12.2^{+18.0}_{-18.0}$	$-176.1^{+12.1}_{-15.2}$	$-156.2^{+12.6}_{-15.2}$	$9.7^{+0.2}_{-0.2}$	$5.0^{+0.5}_{-0.5}$	$0.32^{+0.04}_{-0.04}$	$705.3^{+101.9}_{-92.2}$	$-59940.5^{+2067.3}_{-1447.1}$	IH
SDSS J092912.32+023817.0	$9.225^{+0.165}_{-0.064}$	$-1.502^{+0.203}_{-0.078}$	$1.401^{+0.189}_{-0.073}$	$-218.9^{+9.2}_{-5.2}$	$-275.2^{+13.3}_{-7.8}$	$178.3^{+1.6}_{-2.4}$	$23.5^{+2.6}_{-1.4}$	$2.7^{+0.3}_{-0.1}$	$0.79^{+0.04}_{-0.02}$	$91.4^{+71.5}_{-48.8}$	$-33988.5^{+3752.4}_{-2170.6}$	IH/S
	$16.138^{+0.072}_{-0.234}$	$-9.971^{+0.088}_{-0.287}$	$9.303^{+0.082}_{-6.944}$	$-321.7^{+9.5}_{-43.6}$	$-447.3^{+4.7}_{-35.4}$	$-102.6^{+1.1}_{-40.7}$	$193.7^{+17.6}_{-11.8}$	$21.1^{+0.1}_{-0.4}$	$0.8^{+0.02}_{-0.01}$	$-51.8^{+197.4}_{-928.4}$	$34372.9^{+3808.7}_{-2625.2}$	OH
SDSS J094708.27+461010.0	$10.521^{+0.216}_{-0.189}$	$0.326^{+0.028}_{-0.024}$	$2.941^{+0.251}_{-0.22}$	$205.0^{+18.6}_{-16.3}$	$-264.7^{+20.6}_{-22.1}$	$197.6^{+22.6}_{-18.8}$	$30.0^{+11.4}_{-5.7}$	$8.2^{+0.8}_{-0.8}$	$0.58^{+0.07}_{-0.05}$	$-71.0^{+198.5}_{-213.8}$	$-21786.8^{+9921.8}_{-7717.0}$	OH
	NB	NB	NB	NB	NB	NB	NB	NB	NB	NB	NB	NB
HE 1012−1540	$8.074^{+0.002}_{-0.002}$	$-0.316^{+0.008}_{-0.008}$	$0.207^{+0.005}_{-0.005}$	$-222.5^{+4.3}_{-4.6}$	$-191.1^{+0.4}_{-0.4}$	$49.0^{+1.9}_{-1.8}$	$14.0^{+0.3}_{-0.3}$	$1.3^{+0.1}_{-0.0}$	$0.83^{+0.0}_{-0.01}$	$552.7^{+3.7}_{-3.7}$	$-55562.1^{+850.4}_{-850.4}$	P
SDSS J102915+172927	$8.537^{+0.038}_{-0.033}$	$-0.481^{+0.03}_{-0.034}$	$1.062^{+0.075}_{-0.066}$	$-31.1^{+3.4}_{-3.6}$	$-23.7^{+2.7}_{-4.4}$	$-68.7^{+3.9}_{-4.4}$	$10.9^{+0.3}_{-0.2}$	$8.6^{+0.0}_{-0.0}$	$0.12^{+0.01}_{-0.01}$	$1952.3^{+15.6}_{-19.6}$	$-49546.0^{+552.3}_{-552.3}$	P
SDSS J103402.70+070116.6	$8.917^{+0.075}_{-0.094}$	$-1.482^{+0.122}_{-0.153}$	$2.209^{+0.181}_{-0.227}$	$-97.0^{+1.2}_{-3.4}$	$-178.5^{+6.2}_{-8.9}$	$35.4^{+7.0}_{-11.0}$	$10.2^{+0.1}_{-0.2}$	$2.3^{+0.2}_{-0.3}$	$0.63^{+0.03}_{-0.03}$	$775.0^{+41.4}_{-55.4}$	$-65816.8^{+49.8}_{-102.9}$	P
	$10.714^{+0.263}_{-0.02}$	$-4.385^{+0.425}_{-0.033}$	$6.535^{+0.633}_{-0.241}$	$-188.8^{+36.2}_{-1.5}$	$-366.7^{+24.4}_{-19.5}$	$-126.1^{+38.5}_{-0.8}$	$24.3^{+17.8}_{-0.0}$	$9.3^{+2.1}_{-0.1}$	$0.46^{+0.12}_{-0.0}$	$-426.0^{+81.6}_{-27.7}$	$-27566.6^{+17448.6}_{-82.0}$	IH
SDSSJ103556.11+064143.9	$9.26^{+0.121}_{-0.035}$	$-2.106^{+0.202}_{-0.058}$	$3.131^{+0.3}_{-0.087}$	$87.9^{+12.0}_{-2.3}$	$2.2^{+4.7}_{-6.3}$	$-20.0^{+4.8}_{-0.2}$	$22.2^{+1.0}_{-1.0}$	$7.1^{+0.2}_{-0.1}$	$0.52^{+0.03}_{-0.01}$	$2137.3^{+60.4}_{-50.3}$	$-32395.0^{+1110.9}_{-1568.4}$	IH
	$12.915^{+0.102}_{-0.061}$	$-8.218^{+0.171}_{-0.102}$	$12.216^{+0.254}_{-0.346}$	$300.8^{+42.6}_{-25.2}$	$-60.8^{+43.7}_{-31.4}$	$25.1^{+11.4}_{-13.5}$	$147.8^{+25.5}_{-11.8}$	$11.9^{+0.4}_{-0.2}$	$0.86^{+0.02}_{-0.01}$	$-99.4^{+873.1}_{-641.6}$	$25522.1^{+5791.8}_{-2555.6}$	OH
SDSS J105519.28+232234.0	$9.313^{+0.197}_{-0.173}$	$-0.922^{+0.119}_{-0.136}$	$3.204^{+0.481}_{-0.421}$	$155.4^{+29.0}_{-25.8}$	$-150.7^{+19.3}_{-19.3}$	$90.2^{+8.6}_{-5.4}$	$15.2^{+2.7}_{-2.7}$	$4.9^{+0.4}_{-0.2}$	$0.52^{+0.04}_{-0.05}$	$790.4^{+169.0}_{-236.6}$	$-45745.3^{+4608.7}_{-4608.7}$	IH
SDSS J120441.38+120111.5	$8.213^{+0.021}_{-0.016}$	$-2.304^{+0.168}_{-0.228}$	$6.814^{+0.678}_{-0.499}$	$92.3^{+9.6}_{-9.1}$	$-149.9^{+10.1}_{-13.8}$	$6.2^{+4.3}_{-5.2}$	$12.8^{+0.7}_{-0.6}$	$3.7^{+0.3}_{-0.3}$	$0.55^{+0.04}_{-0.04}$	$597.9^{+110.1}_{-169.3}$	$-53841.3^{+1714.2}_{-1142.8}$	IH
SDSS J124719.46−034152.4	$6.874^{+0.081}_{-0.108}$	$-1.879^{+0.135}_{-0.18}$	$3.581^{+0.351}_{-0.263}$	$-141.4^{+15.7}_{-19.6}$	$-102.9^{+5.2}_{-10.4}$	$88.2^{+6.9}_{-5.6}$	$9.9^{+2.9}_{-0.0}$	$5.0^{+0.3}_{-0.2}$	$0.41^{+0.05}_{-0.05}$	$1263.5^{+31.8}_{-31.8}$	$-55819.2^{+2448.5}_{-2448.5}$	IH
	NB	NB	NB	NB	NB	NB	NB	NB	NB	NB	NB	NB
LAMOST J125346.09+075343.1	$7.856^{+0.006}_{-0.005}$	$-0.208^{+0.008}_{-0.008}$	$0.723^{+0.028}_{-0.027}$	$188.3^{+6.8}_{-6.8}$	$-148.3^{+4.7}_{-4.9}$	$2.6^{+2.6}_{-2.7}$	$13.4^{+0.4}_{-0.3}$	$1.9^{+0.1}_{-0.2}$	$0.75^{+0.03}_{-0.02}$	$766.8^{+40.7}_{-42.5}$	$-56611.4^{+914.8}_{-774.1}$	P
SDSS J131326.89−001941.4	$4.472^{+0.866}_{-1.126}$	$-3.561^{+3.014}_{-1.136}$	$9.327^{+81.5}_{-2.318}$	$92.1^{+7.3}_{-6.7}$	$-443.7^{+33.6}_{-124.4}$	$99.5^{+33.6}_{-43.7}$	$20.4^{+39.8}_{-8.5}$	$8.5^{+3.3}_{-1.6}$	$0.41^{+0.26}_{-0.13}$	$-1256.6^{+383.5}_{-264.5}$	$-34000.2^{+35769.3}_{-16692.3}$	IH
HE 1310−0536	$0.259^{+0.29}_{-0.29}$	$-8.32^{+0.311}_{-0.311}$	$17.184^{+0.644}_{-0.644}$	$-284.9^{+13.2}_{-12.5}$	$-448.9^{+16.8}_{-15.2}$	$47.0^{+3.4}_{-3.2}$	$99.7^{+38.3}_{-26.0}$	$19.0^{+0.7}_{-0.7}$	$0.68^{+0.06}_{-0.07}$	$2216.2^{+238.5}_{-238.5}$	$15227.9^{+8052.8}_{-8052.8}$	OH
HE 1327−2326	$7.332^{+0.028}_{-0.022}$	$-0.686^{+0.028}_{-0.023}$	$0.755^{+0.025}_{-0.031}$	$-279.3^{+12.7}_{-10.7}$	$-68.7^{+1.4}_{-1.3}$	$287.8^{+8.5}_{-10.6}$	$91.4^{+18.5}_{-17.0}$	$7.4^{+0.0}_{-0.0}$	$0.85^{+0.02}_{-0.03}$	$1522.3^{+4.9}_{-5.6}$	$11193.7^{+5154.1}_{-6091.2}$	OH
HE 1424−0241	$1.915^{+0.468}_{-0.54}$	$-1.738^{+0.134}_{-0.154}$	$8.108^{+0.723}_{-0.627}$	$-26.0^{+5.5}_{-7.0}$	$-233.7^{+16.1}_{-22.8}$	$44.9^{+2.2}_{-2.1}$	$8.8^{+0.7}_{-0.6}$	$0.9^{+0.5}_{-0.3}$	$0.81^{+0.06}_{-0.09}$	$58.6^{+38.9}_{-23.9}$	$-71087.9^{+2804.7}_{-1869.8}$	IH
SDSS J144256.37−001542.7	NB	NB	NB	NB	NB	NB	NB	NB	NB	NB	NB	NB
	$6.366^{+0.089}_{-0.221}$	$-0.233^{+0.013}_{-0.032}$	$2.033^{+0.283}_{-0.113}$	$93.2^{+6.6}_{-7.6}$	$42.0^{+8.0}_{-6.4}$	$217.1^{+9.0}_{-9.0}$	$39.1^{+5.2}_{-2.6}$	$6.7^{+0.1}_{-0.1}$	$0.71^{+0.03}_{-0.02}$	$1832.0^{+27.4}_{-18.2}$	$-14290.8^{+3324.2}_{-1662.1}$	OH
Pristine 221.8781+9.7844	$3.941^{+0.29}_{-0.38}$	$0.432^{+0.041}_{-0.031}$	$6.4^{+0.602}_{-0.46}$	$-249.6^{+12.4}_{-18.2}$	$-194.4^{+12.6}_{-19.9}$	$-6.7^{+12.7}_{-8.7}$	$14.1^{+2.3}_{-1.1}$	$4.9^{+0.7}_{-0.5}$	$0.49^{+0.01}_{-0.01}$	$123.6^{+83.8}_{-119.7}$	$-47818.2^{+5527.2}_{-3684.8}$	IH/S
SDSS J164234.48+443004.9	$7.283^{+0.048}_{-0.072}$	$1.869^{+0.196}_{-0.13}$	$1.742^{+0.182}_{-0.121}$	$-124.6^{+6.1}_{-9.1}$	$-143.0^{+4.5}_{-6.1}$	$-6.7^{+8.7}_{-5.8}$	$9.2^{+0.0}_{-0.0}$	$1.6^{+0.2}_{-0.2}$	$0.72^{+0.03}_{-0.04}$	$539.8^{+82.0}_{-41.0}$	$-70959.7^{+2586.2}_{-0.0}$	P
SDSS J173403.91+644633.0	$8.374^{+0.131}_{-0.058}$	$4.823^{+1.691}_{-0.752}$	$3.089^{+1.083}_{-0.481}$	$66.2^{+25.0}_{-16.7}$	$-174.4^{+20.0}_{-15.0}$	$-200.0^{+16.2}_{-23.1}$	$13.0^{+5.5}_{-2.7}$	$7.7^{+1.8}_{-1.3}$	$0.33^{+0.07}_{-0.06}$	$980.4^{+414.3}_{-207.1}$	$-43731.4^{+9796.3}_{-7347.2}$	IH
	NB	NB	NB	NB	NB	NB	NB	NB	NB	NB	NB	NB
SDSS J174259.67+253135.8	$5.293^{+0.294}_{-0.336}$	$3.185^{+0.399}_{-0.349}$	$2.0^{+0.25}_{-0.219}$	$74.6^{+26.6}_{-21.6}$	$-348.1^{+23.9}_{-27.3}$	$-58.7^{+8.8}_{-7.6}$	$8.0^{+1.3}_{-0.7}$	$1.0^{+0.2}_{-0.2}$	$0.77^{+0.06}_{-0.04}$	$-227.0^{+71.9}_{-61.6}$	$-78634.3^{+5992.5}_{-3424.3}$	IH/ω/P
	NB	NB	NB	NB	NB	NB	NB	NB	NB	NB	NB	NB
2MASS J18082002−5104378	$7.40^{+0.02}_{-0.03}$	$-0.189^{+0.007}_{-0.008}$	$-0.163^{+0.006}_{-0.007}$	$2.19^{+0.53}_{-0.53}$	$-45.4^{+1.6}_{-1.7}$	$-5.2^{+0.2}_{-0.2}$	$7.6^{+0.1}_{-0.1}$	$6.3^{+0.1}_{-0.1}$	$0.091^{+0.006}_{-0.005}$	$1520.0^{+17.0}_{-18.4}$	$-64227.3^{+509.0}_{-509.0}$	P
BPS CS 22891−0200	$-2.803^{+0.469}_{-0.469}$	$-5.036^{+0.219}_{-0.219}$	$-6.553^{+0.285}_{-0.285}$	$255.7^{+11.1}_{-11.1}$	$-93.4^{+4.6}_{-4.9}$	$222.1^{+14.0}_{-12.5}$	$64.0^{+18.9}_{-11.1}$	$7.4^{+0.6}_{-0.6}$	$0.8^{+0.03}_{-0.02}$	$-1788.2^{+160.3}_{-171.0}$	$1304.9^{+7251.3}_{-6445.6}$	OH
BPS CS 22885−0096	$2.413^{+0.302}_{-0.302}$	$0.123^{+0.007}_{-0.007}$	$-3.701^{+0.2}_{-0.2}$	$-145.0^{+8.6}_{-8.1}$	$-241.8^{+12.1}_{-12.9}$	$223.8^{+7.2}_{-7.2}$	$9.3^{+0.6}_{-1.3}$	$3.6^{+0.3}_{-0.3}$	$0.44^{+0.06}_{-0.06}$	$5.2^{+36.0}_{-29.7}$	$-63004.7^{+2672.9}_{-2672.9}$	IH/S
BPS CS 22950−0046	$-6.594^{+0.353}_{-0.243}$	$8.665^{+0.144}_{-0.21}$	$-8.233^{+0.199}_{-0.137}$	$59.4^{+8.2}_{-7.7}$	$-70.6^{+5.8}_{-5.5}$	$-222.9^{+6.8}_{-5.6}$	$41.7^{+3.6}_{-3.2}$	$2.5^{+0.4}_{-0.4}$	$0.89^{+0.02}_{-0.02}$	$-572.2^{+56.5}_{-56.5}$	$-14149.5^{+2904.8}_{-2582.0}$	OH
BPS CS 30336−0049	$-4.037^{+0.507}_{-0.475}$	$3.41^{+0.135}_{-0.144}$	$-9.176^{+0.386}_{-0.362}$	$-31.8^{+6.6}_{-6.6}$	$-643.6^{+25.2}_{-23.2}$	$119.8^{+1.9}_{-2.4}$	$122.7^{+51.1}_{-41.4}$	$8.1^{+0.8}_{-0.8}$	$0.88^{+0.03}_{-0.03}$	$1489.5^{+305.3}_{-305.3}$	$19080.8^{+11833.4}_{-11833.4}$	OH
HE 2139−5432	$0.746^{+0.54}_{-0.607}$	$-2.466^{+0.183}_{-0.206}$	$-8.023^{+0.597}_{-0.672}$	$-48.5^{+11.6}_{-12.3}$	$-264.7^{+18.4}_{-20.7}$	$-113.8^{+8.5}_{-8.5}$	$9.8^{+1.1}_{-0.9}$	$1.1^{+0.5}_{-0.3}$	$0.79^{+0.05}_{-0.06}$	$87.2^{+37.9}_{-27.1}$	$-66571.3^{+4078.3}_{-3625.1}$	IH

Table 4 – *continued*

Identifier	X (kpc)	Y (kpc)	Z (kpc)	U (km s^{-1})	V (km s^{-1})	W (km s^{-1})	Apo (kpc)	Peri (kpc)	ε	L$_Z$ (km s^{-1} kpc)	E (km^2 s^{-2})	Orbit
HE 2239−5019	$5.857^{+0.137}_{-0.142}$	$-0.731^{+0.047}_{-0.049}$	$-3.406^{+0.217}_{-0.226}$	$125.2^{+4.6}_{-4.6}$	$-540.5^{+29.3}_{-30.5}$	$-248.0^{+3.9}_{-3.7}$	$52.9^{+16.6}_{-10.4}$	$6.8^{+0.0}_{-0.0}$	$0.77^{+0.05}_{-0.05}$	$-1792.6^{+141.3}_{-141.3}$	$-4551.9^{+7794.6}_{-7145.0}$	OH
HE 2323−0256	$6.687^{+0.076}_{-0.053}$	$7.11^{+0.29}_{-0.411}$	$-11.698^{+0.674}_{-0.476}$	$-53.7^{+4.4}_{-5.3}$	$-199.4^{+8.4}_{-6.1}$	$20.4^{+5.7}_{-4.2}$	$15.4^{+0.5}_{-0.6}$	$2.8^{+0.2}_{-0.2}$	$0.68^{+0.03}_{-0.03}$	$44.7^{+94.9}_{-78.1}$	$-48598.2^{+1025.7}_{-1172.2}$	IH
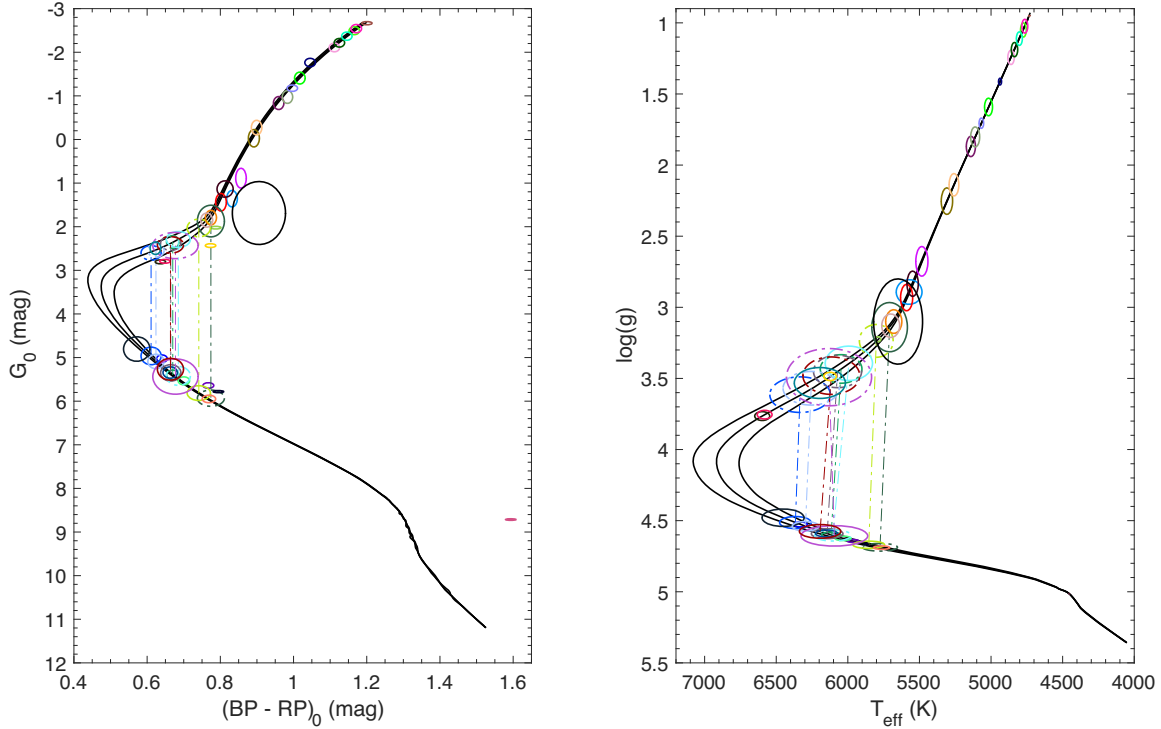
Figure 1. Position of the sample stars in the CMD (left) and the $\log(g)$ versus $T_{\rm eff}$ plane (right). The ellipses represent the position of the stars within 1σ and the black lines correspond to the three isochrones with $\log(A/\mathrm{yr}) = 10.05$, 10.10, 10.15 and metallicity [Fe/H] $= -4$ dex. If the dwarf–giant degeneracy is not broken, the two possible solutions are represented and connected by a dot–dashed line of the same colour code. Each colour represents a star and the colour-code is the same as the colour-code for the markers in Fig. 2 and the panel's titles in Figs A1–A42 (available Online). Solutions with integrated probability ($\int_{d-3\sigma}^{d+3\sigma} P(r)\mathrm{d}r$) lower than 5 per cent are not shown and solutions with integrated probability in the range [5 per cent, 50 per cent] are shown with dot–dashed ellipses.

For all 42 stars in our sample, we show the results of our analysis in Figs A1–A42 (available Online). In all figures, the top-left panel shows the distance likelihood functions and posterior PDFs, the top-middle panel presents the log(g) PDF, while the top-right panel shows the effective temperature PDF. The orbit of the star in Galactic Cartesian coordinates is presented in the bottom panels of the figures.

In the subsections of Appendix A (available Online), we discuss in detail the results for every star in the sample sorted by right ascension. Specifically, we focus on the inferred distances, stellar parameters, and orbits using a MW halo prior and, when it yields different results, we also discuss the use of the disc+halo prior. A global comparison between the inferred stellar parameters form our work and the values from the literature is described in Appendix B (available Online) and shown in the two panels of Fig. B1.

We did a comparison between the distances inferred in this work and the ones inferred by Bailer-Jones et al. (2018). These authors

use a posterior probability composed by the astrometric likelihood shown in equation (8) and a MW prior that is based on a Gaia-observed Galaxy distribution function accurately describing the overall distribution of all MW stars. This is naturally more biased to higher densities in the thin disc and thus results in closer distances for most of the stars.

Frebel et al. (2018) compiled a list of 29 UMP stars inferring orbital parameters starting from the MW prior described in Bailer-Jones et al. (2018), but fixing the length-scale parameter to $L = 0.5$. As both the initial assumptions and the focus of the analysis given in Frebel et al. (2018) significantly differ from the approach taken in this work, we refrain from a further qualitative comparison.

5 DISCUSSIONS

Our combined analysis of the *Gaia DR2* astrometry and photometry with stellar population models for low-metallicity stars allows us to infer the stellar parameters and orbital properties of the 42 known

UMP stars. We derive well constrained properties for most stars and, in particular, we are now in a position to unravel the possible origin of the heterogeneous sample of UMP stars found to date.

5.1 Insights on the orbits of UMP stars

Apart from two ambiguous cases, we can classify the orbits of the UMP stars within three loosely defined categories:

(i) 19 'inner halo' stars, arbitrarily defined as having apocentres smaller than 30 kpc.

(ii) 12 'outer halo' stars with apocentre larger than 30 kpc.

(iii) Strikingly, 11 stars that have 'MW plane' orbits, by which we mean that they stay confined close to the MW plane ($|Z| < 3.0$ kpc).

Fig. 2 attempts to show these different kind of orbits, displaying on the top panel the vertical component of the action-angle J_z versus the rotational component J_ϕ ($=L_z$) for all the UMP in our sample. In this space, the stars confined to the MW plane (denoted by a star marker) are constrained to the lower part of the diagram, while the halo stars have larger J_z. Stars that have a prograde motion have $J_\phi > 0$ and stars with retrograde orbits lie in the $J_\phi < 0$ part of the diagram. We note how the Caffau star (SDSS J102915+172927) and 2MASS J18082002−5104378 occupy a special place in this plane and they are the only stars on a quasi-circular orbit at large J_ϕ and low J_z.

It is appealing to assign a tentative origin to stars in these three categories. The 'inner halo' stars could well be stars accreted on to the MW during its youth, when its mass was smaller and therefore its potential well less deep than it is now. At that time, more energetic orbits would have been unbound and left the MW in formation. 'Outer halo' orbits tend to have very radial orbits in this sample (likely a consequence of the window function imparted by the various surveys that discovered these UMP stars; see below), which makes it easier to identify them. It is tempting to see those as being brought in through the accretion of faint dwarf galaxies on to the MW throughout the hierarchical formation of its halo. Although no UMP has been found in MW satellite dwarf galaxies yet, we know of many extremely metal-poor stars in these systems, down to [Fe/H] = −4 (e.g. Tafelmeyer et al. 2010) and UMP stars are expected to be present as well (Salvadori, Skúladóttir & Tolstoy 2015). We note that, among the two 'halo' categories, there is a distinct preference for prograde over retrograde orbits.

The 11 'MW plane' orbits are much more unexpected:

(i) 8 stars (SDSS J014036.21+234458.1, BD+44 493, HE 0233−0343, HE 0330+0148, HE 1012−1540, SDSS J103402.70+070116.6, LAMOST J125346.09+075343, SDSS J164234.48+443004.9) share similar rosette orbits within a wide range of angular momentum along the z axis ($83 \lesssim L_z \lesssim 885$ km s^{-1} kpc). These stars orbit close to the plane, but not on circular orbits.

(ii) SDSS J102915+172927 and 2MASS J18082002−5104378 (Figs A19 and A35 available Online), are on almost circular orbits close to the solar radius.

(iii) SDSS J174259.67+253135.8 (Fig. A34, available Online) is retrograde and more likely on an 'inner halo' orbit that remains close to the MW plane.

The first 10 of those stars, excluding SDSS J174259.67+253135.8, all have positive L_z and thus a prograde orbit, which is unlikely to be a random occurrence (< 1 per cent chance). It is worth noting that it is very unlikely the selection functions that led to the discovery of the UMP stars

biased the sample for/against prograde orbit. The origin of those stars is puzzling but we can venture three different hypothesis for their presence in the sample, all of which must account for the fact that this significant fraction of UMP stars, which are expected to be very old, appears to know where the plane of the MW is located, even though the MW plane was unlikely to be in place when they formed.

Scenario 1: The first obvious scenario is that these stars formed in the MW disc itself after the HI disc settled. In this fashion, the stars were born with a quasi-circular orbit and then the presence of a dynamical heating mechanism is mandatory to increase the eccentricity and the height from the plane as a function of time. We find that all the prograde 'MW plane' stars and few catalogued as inner halo stars that are confined within $Z_{max} < 15$ kpc and $d_{apo} < 25$ kpc (see Fig. 2) overlap in the parameters space (Z_{max}, d_{apo}, L_z, E) with a population of known stars at higher metallicity that Haywood et al. (2018) hypothesize to be born in the thick disc and then dynamical heated by the interaction between the disc and a merging satellite. However, the question is whether in a relatively well-mixed HI disc it is possible to form stars so completely devoid of metals.

Scenario 2: The second scenario is that these stars were brought into the MW by the accretion of a massive satellite dwarf galaxy. Cosmological simulations have shown that merger events are expected to sometimes be aligned with the disc. As a result, significant stellar populations currently in the disc might actually be merger debris (Gómez et al. 2017). Alternatively, Scannapieco et al. (2011), show that 5–20 per cent of disc stars in their simulated MW-like disc galaxies were not formed *in situ* but, instead, accreted early from now disrupted satellites on co-planar orbits. Additionally, it is well known that the accretion of a massive system on to the MW will see its orbit align with the plane of the MW via dynamical friction, as shown by Peñarrubia, Kroupa & Boily (2002) or Abadi et al. (2003). From these authors' simulations, one would expect orbits to become such that they would end up with larger eccentricities than the satellite's orbit at the start of the merging process and also aligned with the disc by dynamical friction and tidal interactions, which is compatible with our orbital inference for the remarkable UMP stars. If such an accretion took place in the MW's past, it could have brought with it a significant fraction of the UMP stars discovered in the solar neighbourhood. The accretion of the so-called Gaia-Enceladus satellite in the Milky Way's past (Belokurov et al. 2018; Haywood et al. 2018; Helmi et al. 2018) could be an obvious culprit, however Gaia-Enceladus was discovered via the mainly halo-like and retrograde orbit of its stars whereas the vast majority of the stars we find here are on prograde orbits. In fact, there is no evidence of a particular overdensity of stars in the top-left region of the J_z versus J_ϕ of Fig. 2 where Gaia-Enceladus stars are expected to be found. It would therefore be necessary to summon the presence of another massive or several less massive accretion events on to the MW if this scenario is valid.

Scenario 3: Finally, the third scenario that could explain the presence of this significant fraction of UMP stars that remain confined to the plane of the MW would be one in which these stars originally belonged to one or more of the building blocks of the proto-MW, as it was assembling into the MW that we know today. Fully cosmological simulations confirm that stars that are at the present time deeply embedded in our Galaxy do not need to have their origin in the proto-Galaxy. El-Badry et al. (2018) find in their cosmological simulations that of all stars formed before $z = 5$ presently within 10 kpc of the Galactic centre less than half were already in the main progenitor at $z = 5$. Over half of these extremely
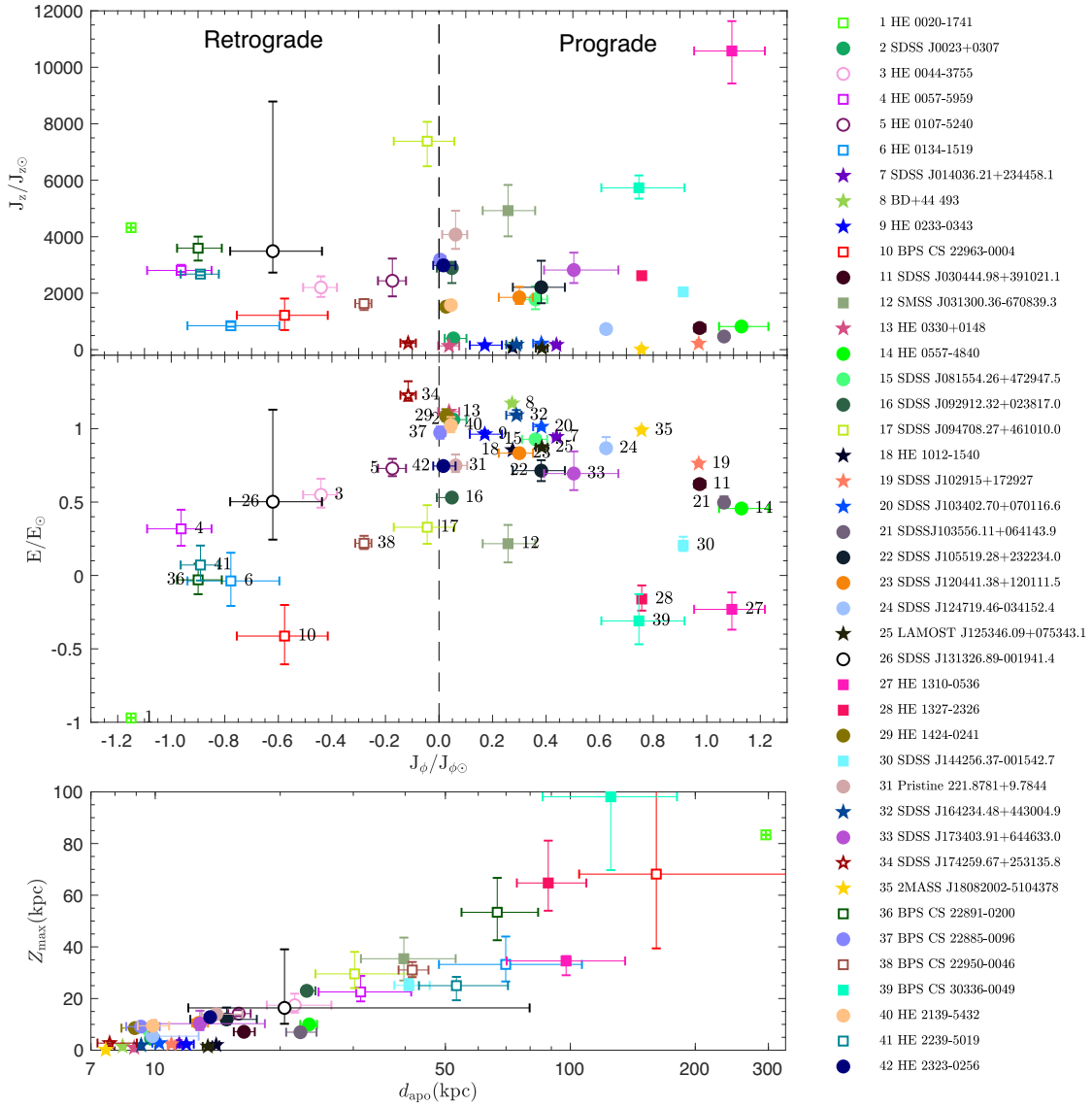
Figure 2. Position of the sample stars in the rotational action J_ϕ ($=L_z$) and vertical action J_z space (top panel), in the energy and rotational action space, and in the maximum height versus apocentre of the stars' orbits (bottom panel). The rotational and vertical action and the Energy are scaled by the Sun values respectively $J_{\phi\odot} = 2009.92\,\mathrm{km\,s^{-1}\,kpc}$, $J_{z\odot} = 0.35\,\mathrm{km\,s^{-1}\,kpc}$, and $E_\odot = -64943.61\,\mathrm{km^2\,s^{-2}}$. Stars within our 'MW planar' sample that are confined close to the MW plane are marked with a star symbols, while 'inner halo' and 'outer halo' stars are represented by circles and squares, respectively. Retrograde stars, which are located on the left side of the top and central panels ($J_\phi < 0\,\mathrm{km\,s^{-1}\,kpc}$) are denoted with empty marker, while prograde stars are shown with a filled marked. The colour-coding is the same as in Fig. 1 and as the title of Figs A1–A42 (available Online) and helps to differentiate the stars. The full legend is provided on the side of this figure. The number associated to each star also corresponds to the number of the subsection in the Appendix A (available Online) in which the individual results are discussed.

old stars would thus make their way into the main Galaxy in later merging events and find themselves at $z = 5$ inside different building blocks that are up to 300 kpc away from the main progenitor centre. In such a scenario, we can expect that whatever gas-rich blocks formed the backbone of the MW disc brought with it its own stars, including UMP stars. Yet, for such a significant number of UMP stars to align with the current MW plane, it is necessary to assume that the formation of the MW's disc involved a single massive event that imprinted the disc plane that is aligned with the orbit of its stars. The presence of many massive building blocks would have likely led to changes in the angular H I disc alignment. Similarly, the MW cannot have suffered many massive accretions since high redshift

or the disc would have changed its orientation (Scannapieco et al. 2009). This would be in line with expectations that the MW has had an (unusually) quiet accretion history throughout its life (Wyse 2001; Stewart et al. 2008).

5.1.1 The Caffau star and 2MASS J18082002−5104378

SDSS J102915+172927 (see Fig. A19, available Online), also known as 'the Caffau star' (Caffau et al. 2011), and 2MASS J18082002−5104378 (see Fig. A35, available Online) both have a disc-like prograde orbit but while the Caffau Star reaches a height of 2.3 kpc from the MW plane, the latter star is

confined within 0.166 kpc, confirming the results from Schlaufman, Thompson & Casey (2018). Both stars represent outliers inside the surprising sample of 'MW planar' stars that typically have more eccentric orbits. For these stars, scenario 3, as outlined above, might be an interesting possibility. A merging between the building blocks of the proto-MW could have brought in these UMP stars and their orbit circularized by dynamical friction.

5.1.2 Coincidence with the Sagittarius stream

We note that four of the 'halo' stars (SDSS J092912.32+023817.0, SDSS J094708.27+461010.0, Pristine221.8781+9.7844 and BPS CS 22885−0096) have orbits that are almost perpendicular to the MW plane (see Figs A16, A17, A31, and A37 available Online), coinciding with the plane of the stellar stream left by the Sagittarius (Sgr) dwarf galaxy as it as being tidally disrupted by the MW. We therefore investigate if these stars belong to the stream by comparing their proper motions and distances with the values provided by the N-body simulation of Law & Majewski (2010) (hereafter LM10; Fig. 3). It is clear that SDSS J094708.27+461010.0 has a proper motion that is incompatible with the simulation's particles. On the other hand, we find that SDSS J092912.32+023817.0, Pristine221.8781+9.7844, and BPS CS 22885−0096 have proper motions that are in broad agreement with those of the simulation. These stars could be compatible with the oldest wraps of the Sgr galaxy but we are nevertheless cautious in this assignment since only the young wraps of the stream were constrained well with observations in the Law & Majewski (2010) model. Older wraps rely on the simulation's capability to trace the orbit back in the MW potential that is itself poorly constrained and has likely changed over these time-scales, and the true 6D phase-space location the older warps could therefore easily deviate significantly from the simulation's expectations.

5.1.3 A connection between SDSS J174259.67+253135.8 and ω Centauri?

SDSS J174259.67+253135.8 is the only star of the 'MW planar' sample that has a retrograde motion and its orbital properties are, in fact, similar enough to those of the ω Centauri (ωCen) stellar cluster to hint at a possible connection between the two. It should be noted, however, that the L_z of ωCen's orbit is about twice that of this star. Nevertheless, given the dynamically active life that ωCen must have had in the commonly-held scenario that it is the nucleus of a dwarf galaxy accreted by the Milky Way long ago (e.g. Zinnecker et al. 1988; Mizutani, Chiba & Sakamoto 2003), the similarity of the orbits is intriguing enough to warrant further inspection.

5.2 Limits of the analysis and completeness

The heterogeneous UMP sample comes from multiple surveys conducted over the years, with their own, different window functions for the selection of the targets and it can thus by no means be called a complete or homogeneous sample. To reconstruct the full selection function of this sample is nearly impossible since it includes so many inherited window functions from various surveys and follow-up programs. As far as we can deduce, however, none of the programs would have specifically selected stars on particular orbits. We therefore consider the clear preference of the UMP star population for orbits in the plane of the MW disc a strong result of this work but we caution the reader not to consider the ratio of 'inner halo,'

'outer halo,' and 'MW plane' orbits as necessarily representative of the true ratios, which will require a more systematic survey to confirm.

We note that due to the different abundance patterns of these stars, [Fe/H] is not always a good tracer of the total metallicity [M/H]. However, not all stars in this sample are equally well-studied and therefore constraints on [M/H] are inhomogeneous. This has led us to nevertheless choose a cut on [Fe/H] as this is the common quantity measured by all the cited authors.

Another limitation of this work comes from the isochrones we use, which are the most metal-poor isochrones available in the literature at this time and have [Fe/H] = −4 dex with solar-scaled α-abundances. Beyond the fact that some stars in our sample are significantly more metal-poor than this, not all stars follow this abundance pattern and as a result their total metal-content can change, in turn affecting the colour of the isochrones. We estimate, however, that this will be a small effect at these low metallicities, as low-metallicity isochrones are relatively insensitive to small variations in metallicity, and take this into account adding a systematic uncertainty of 0.01 mag in quadrature to the model (see Section 3.1.1). This is unlikely to affect the final results on the evolutionary phase and the typology of the orbits. A final potential limitation of this work stems from the possible binary of some of the studied stars. If, unbeknownst to us, a star is in fact a binary system whose component are in the same or a similar evolutionary phase, their photometry would not be representative of their true properties and our distance inference would be biased. Similarly a binary star would like have its velocity be affected, leading to flawed orbital parameters. For known binary stars, we nevertheless take these effects into account and our distance and orbital inference should not be severely affected by this binarity issue.

5.3 Future outlook

As described in 5.2, the current sample and analysis of their dynamics is quite limited by an unknown and complicated selection function. With proper motion, parallax, and the exquisite photometry from *Gaia DR2*, we plan to apply the same bayesian framework described in Section 3 to all the EMP stars within the Pristine survey (Starkenburg et al. 2017a) to investigate their stellar properties and orbits. As the completeness and purity of this sample is very well understood (Youakim et al. 2017) and this sample is much larger, this will open up more quantitative avenues to explore the role of extremely metal-poor stars in the big picture of the accretion history of the MW.

6 CONCLUSIONS

Combining the *Gaia DR2* photometric and astrometric information in a statistical framework, we determine the posterior probability distribution function for the distance, the stellar parameters (temperature and surface gravity), and the orbital parameters of 42 UMPs (see Tables 3 and 4). Given that 11 of those stars remain confined close to the MW plane, we use both a pure halo prior and a combined disc+halo prior. Folding together distance posterior and orbital analysis we find that 18 stars are on the main sequence and the other 24 stars are in a more evolved phase (subgiant or giant).

Through the orbital analysis, we find that 11 stars are orbiting close to the plane of the disc, with maximum height above the disc within 3 kpc. We hypothesize that they could have once belonged to a massive building block of the proto-MW that formed the backbone of the MW disc, or that they were brought into
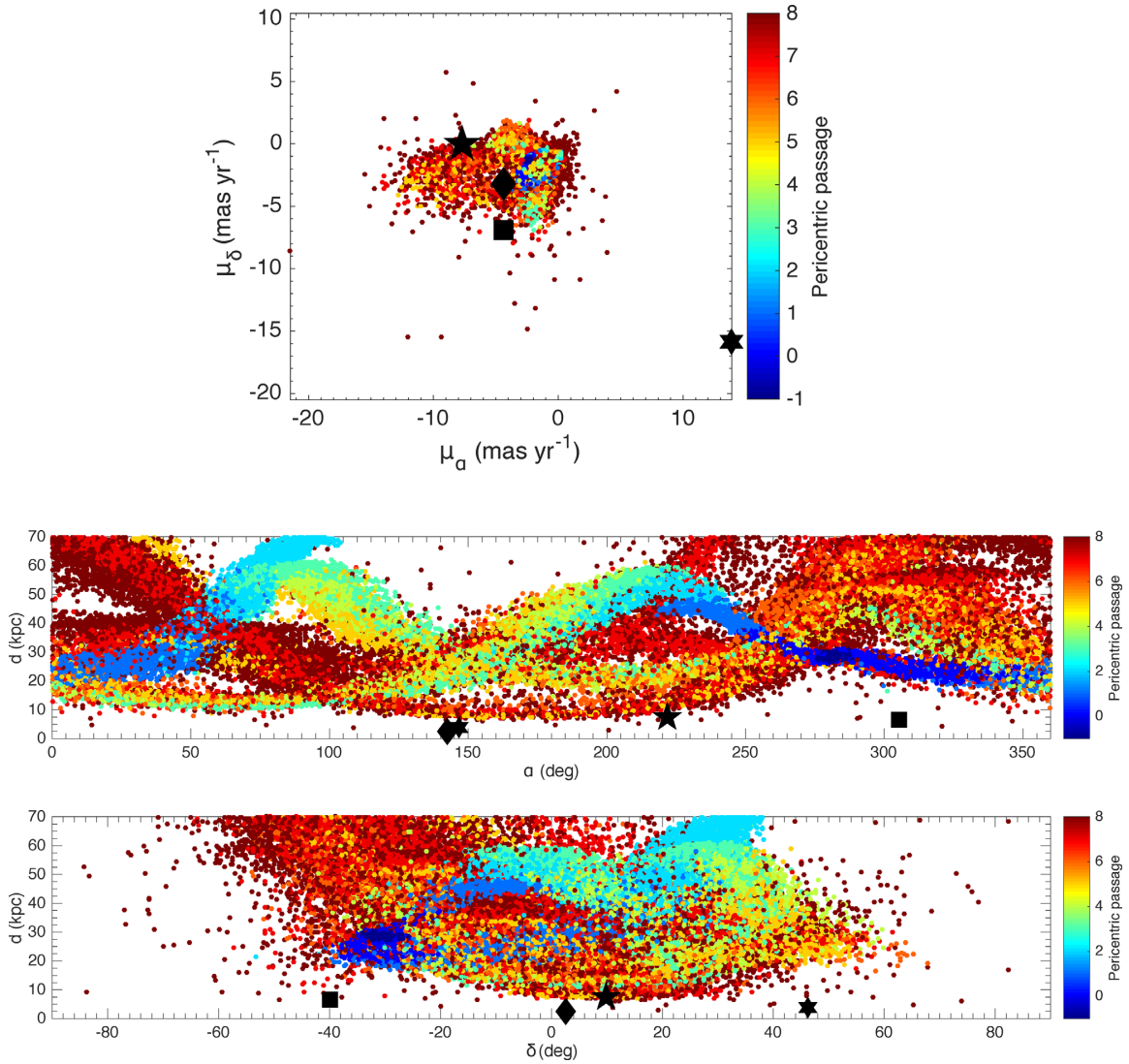
Figure 3. Top: proper motion space for the particles of the LM10 simulation (dots), and SDSS J092912.32+023817.0 (black diamond), SDSS J094708.27+461010.0 (black hexagram), Pristine221.8781+9.7844 (black pentagram), and BPS CS 22885−0096 (black square). The colour-code for the LM10 simulation indicates the pericentric passage on which the particle became unbound from Sgr. A pericentric passage value of −1 indicates debris which is still bound at the present day, while a value of 0 indicates debris stripped on the most recent pericentric passage of Sgr, and a value above 1 corresponds to successive pericentric passages. Centre: heliocentric distance d as a function of right ascension α for the LM10 simulation and the candidates. Bottom: heliocentric distance d as a function of declination δ for the LM10 simulation and the candidates. The LM10 simulation is shown within 70 kpc from the Sun for the centre and bottom panel.

the MW via a specific, massive hierarchical accretion event, or they might have formed in the early disc and have been dynamically heated. Another 31 stars are from both the 'inner halo' (arbitrarily defined as having $r_{apo} < 30\,\text{kpc}$) and were accreted early on in the history of the MW, or the 'outer halo' hinting that they were accreted on to the Galaxy from now-defunct dwarf galaxies. Of these halo stars, SDSS J092912.32+023817.0, Pristine221.8781+9.7844, and BPS CS 22885−0096, could possibly be associated with the Sagittarius stream, although they would need to have been stripped during old pericentric passages of the dwarf galaxy. SDSS J174259.67+253135.8 could also possibly be associated with ωCen as its progenitor.

The work presented here provides distances, stellar parameters, and orbits for all known UMP stars and, hence, some of the oldest stars known. To understand their position and kinematics within the

Galaxy it is very important to reconstruct the early formation of the MW and/or the hierarchical formation of some of its components. We foresee a statistical improvement of this first study with the arrival of homogeneous and large data sets of EMP stars, such as observed within the Pristine or SkyMapper surveys (Starkenburg et al. 2017a; Wolf et al. 2018). With these surveys, the window function and the selection criteria of the objects for which distances and orbits are derived will be much better known.

ACKNOWLEDGEMENTS

REFERENCES

Abadi M. G., Navarro J. F., Steinmetz M., Eke V. R., 2003, ApJ, 597, 21
Abohalima A., , Frebel A., 2018, ApJs, 238, 36
Aguado D. S., Allende Prieto C., González Hernández J. I., Carrera R., Rebolo R., Shetrone M., Lambert D. L., Fernández-Alvar E., 2016, A&A, 593, 13
Aguado D. S., Allende Prieto C., González Hernández J. I., Rebolo R., Caffau E., 2017a, A&A, 604, 7
Aguado D. S., González Hernández J. I., Allende Prieto C., Rebolo R., 2017b, A&A, 605, 10
Aguado D. S., González Hernández J. I., Allende Prieto C., Rebolo R., 2018b, ApJ, 852, 6
Aguado D. S., Allende Prieto C., González Hernández J. I., Rebolo R., 2018a, ApJ, 854, 4
Allende Prieto C. et al., 2015, A&A, 579, 6
Arentsen A., Starkenburg E., Shetrone M. D., Venn K. A., Depagne É., McConnachie A. W., 2019, A&A, 621, A108
Bailer-Jones C. A. L., Rybizki J., Fouesneau M., Mantelet G., Andrae R., 2018, AJ, 156, 58
Bailer-Jones C. A. L., 2015, PASP, 127, 994
Beers T. C., Christlieb N., 2005, ARA&A, 43, 531
Beers T. C., Preston G. W., Shectman S. A., 1985, AJ, 90, 2089
Belokurov V., Erkal D., Evans N. W., Koposov S. E., Deason A. J., 2018, MNRAS, 478, 611
Binney J., Tremaine S., 2008, Galactic Dynamics, 2nd edn. Princeton Univ. Press, Princeton
Bland-Hawthorn J., Gerhard O., 2016, ARA&A, 54, 529
Bonifacio P. et al., 2015, A&A, 579, 20
Bonifacio P. et al., 2018, A&A, 612, 10
Bovy J., 2015, ApJS, 216, 29
Caffau E. et al., 2011, Nature, 477, 67
Caffau E. et al., 2013a, A&A, 560, 7
Caffau E. et al., 2013b, A&A, 560, 9
Caffau E. et al., 2016, A&A, 595, 6
Cayrel R. et al., 2004, A&A, 416, 1117
Choi J., Dotter A., Conroy C., Cantiello M., Paxton B., Johnson B. D., 2016, ApJ, 823, 102
Christlieb N., Wisotzki L., Graßhoff G., 2002, A&A, 391, 397
Christlieb N., Gustafsson B., Korn A. J., Barklem P. S., Beers T. C., Bessell M. S., Karlsson T., Mizuno-Wiedner M., 2004, ApJ, 603, 708

Cohen J. G., Christlieb N., McWilliam A., Shectman S., Thompson I., Melendez J., Wisotzki L., Reimers D., 2008, ApJ, 672, 320
Cui X.-Q. et al., 2012, Res. Astron. Astrophys., 12, 1197
Dotter A., 2016, ApJS, 222, 8
Eisenstein D. J. et al., 2011, AJ, 142, 24
El-Badry K. et al., 2018, MNRAS, 480, 652
Evans D. W. et al., 2018, A&A, 616, 21
Frebel A., Norris J. E., 2015, ARA&A, 53, 631
Frebel A., Collet R., Eriksson K., Christlieb N., Aoki W., 2008, ApJ, 684, 588
Frebel A., Chiti A., Ji A. P., Jacobson H. R., Placco V. M., 2015, ApJ, 810, 7
Frebel A., Ji A. P., Ezzeddine R., Hansen T. T., Chiti A., Thompson I. B., Merle T., 2018, preprint (arXiv:1810.01228)
Freeman K., Bland-Hawthorn J., 2002, ARA&A, 40, 487
Gaia Collaboration, 2016, A&A, 595, 36
Gaia Collaboration, 2018, A&A, 616, A1
Gómez F. A. et al., 2017, MNRAS, 472, 3722
Greif T. H., 2015, Comput. Astrophys. Cosmol., 2, 36
Hansen T. et al., 2015, ApJ, 807, 17
Haywood M., Di Matteo P., Lehnert M. D., Snaith O., Khoperskov S., Gómez A., 2018, ApJ, 863, 113
Helmi A., , Babusiaux C., Koppelman H. H., Massari D., Veljanoski J., Brown A. G. A., 2018, Nature, 563, 85
Hernitschek N. et al., 2018, ApJ, 859, 32
Ito H., Aoki W., Beers T. C., Tominaga N., Honda S., Carollo D., 2013, ApJ, 773, 33
Karlsson T., Bromm V., Bland-Hawthorn J., 2013, Rev. Mod. Phys., 85, 809
Keller S. C. et al., 2014, Nature, 506, 463
Lai D. K., Bolte M., Johnson J. A., Lucatello S., Heger A., Woosley S. E., 2008, ApJ, 681, 1524
Law D. R., Majewski S. R., 2010, ApJ, 714, 229
Li H., Aoki W., Zhao G., Honda S., Christlieb N., Suda T., 2015, PASJ, 67, 84
Lindegren L. et al., 2018, A&A, 616, A2
Marigo P., Girardi L., Bressan A., Groenewegen M. A. T., Silva L., Granato G. L., 2008, A&A, 482, 883
Meléndez J., Placco V. M., Tucci-Maia M., Ramírez I., Li T. S., Perez G., 2016, A&A, 585, 5
Mizutani A., Chiba M., Sakamoto T., 2003, ApJ, 589, L89
Navarro J. F., Frenk C. S., White S. D. M., 1997, ApJ, 490, 493
Nordlander T., Amarsi A. M., Lind K., Asplund M., Barklem P. S., Casey A. R., Collet R., Leenaarts J., 2017, A&A, 597, 16
Norris J. E. et al., 2013, ApJ, 762, 16
Norris J. E., Christlieb N., Korn A. J., Eriksson K., Bessell M. S., Beers T. C., Wisotzki L., Reimers D., 2007, ApJ, 670, 774
Paxton B., Bildsten L., Dotter A., Herwig F., Lesaffre P., Timmes F., 2011, ApJS, 192, 3
Peñarrubia J., Kroupa P., Boily C. M., 2002, MNRAS, 333, 779
Placco V. M. et al., 2016, ApJ, 833, 13
Placco V. M., Frebel A., Lee Y. S., Jacobson H. R., Beers T. C., Pena J. M., Chan C., Heger A., 2015, ApJ, 809, 136
Plez B., Cohen J., Meléndez J., 2005, Hill V., Francois P., Primas F., Proceedings of The International Astronomical Union. p. 228
Roederer I. U., Preston G. W., Thompson I. B., Shectman S. A., Sneden C., Burley G. S., Kelson D. D., 2014, AJ, 147, 136
Salpeter E. E., 1955, ApJ, 121, 161
Salvadori S., Skúladóttir Á., Tolstoy E., 2015, MNRAS, 454, 1320
Scannapieco C., White S. D. M., Springel V., Tissera P. B., 2009, MNRAS, 396, 696
Scannapieco C., White S. D. M., Springel V., Tissera P. B., 2011, MNRAS, 417, 154
Schlaufman K. C., Thompson I. B., Casey A. R., 2018, ApJ, 867, 98
Schlegel D. J., Finkbeiner D. P., Davis M., 1998, ApJ, 500, 525
Schönrich R., Binney J., Dehnen W., 2010, MNRAS, 403, 1829
Sharma S., 2017, ARA&A, 55, 213
Starkenburg E. et al., 2017a, MNRAS, 471, 2587
Starkenburg E. et al., 2018, MNRAS, 481, 3838

Starkenburg E., Oman K. A., Navarro J. F., Crain R. A., Fattahi A., Frenk C. S., Sawala T., Schaye J., 2017b, MNRAS, 465, 2212

Stewart K. R., Bullock J. S., Wechsler R. H., Maller A. H., Zentner A. R., 2008, ApJ, 683, 597

Tafelmeyer M. et al., 2010, A&A, 524, 21

Wenger M. et al., 2000, A&AS, 143, 9

Wolf C. et al., 2018, PASA, 35, 29

Wyse R. F. G., 2001, in Funes J. G., Corsini E. M., eds, ASP Conf. Ser., Vol. 230, Galaxy Disks and Disk Galaxies. Astron. Soc. Pac., San Francisco, p. 71

Yanny B. et al., 2009, AJ, 137, 4377

Yong D. et al., 2013, ApJ, 762, 49

York D. G. et al., 2000, AJ, 120, 1579

Youakim K. et al., 2017, MNRAS, 472, 2963

Zinnecker H., Keable C. J., Dunlop J. S., Cannon R. D., Griffiths W. K., 1988, in Grindlay J. E., Philip A. G. D., eds, IAU Symposium, Vol. 126, The Harlow-Shapley Symposium on Globular Cluster Systems in Galaxies. Kluwer Academic Publishers, Dordrecht, p. 603

SUPPORTING INFORMATION

Supplementary data are available at *MNRAS* online.

Appendix A. Individual results.
Appendix B. Comparison with values from the literature.

Please note: Oxford University Press is not responsible for the content or functionality of any supporting materials supplied by the authors. Any queries (other than missing material) should be directed to the corresponding author for the article.

This paper has been typeset from a TEX/LATEX file prepared by the author.

Appendix B: Current Velocity Data on Dwarf Galaxy NGC 1052-DF2 do not Constrain it to lack dark matter
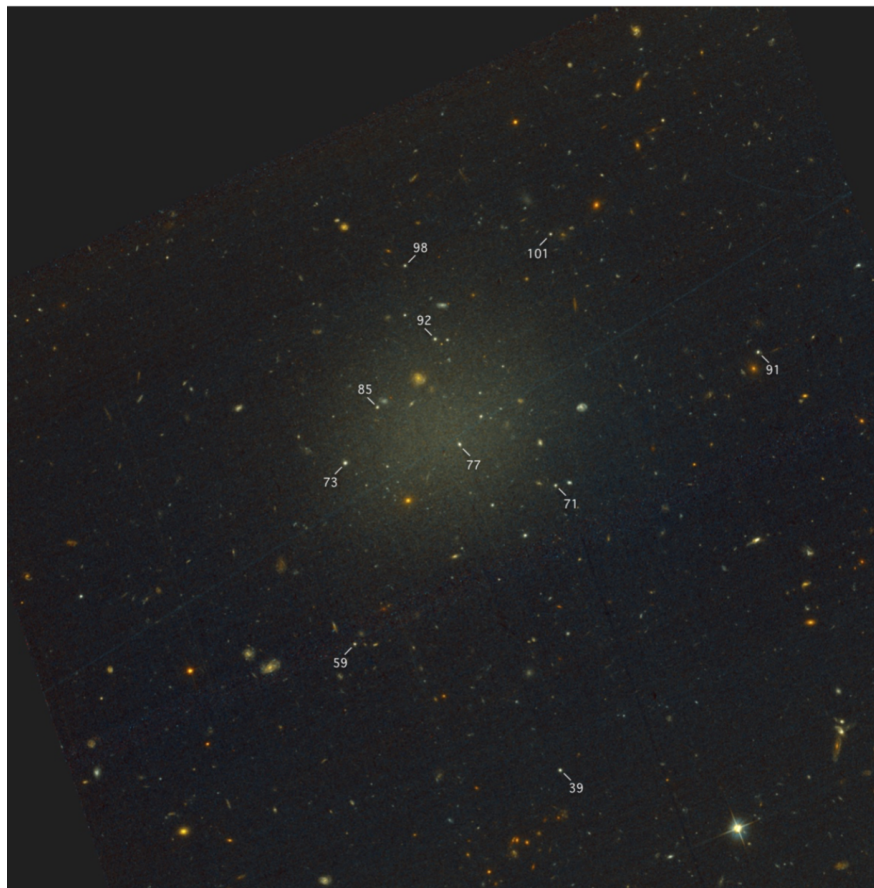
Figure B.1: $3.2' \times 3.2'$ HST/ACS image of NGC 1052-DF2 taken from VD18. The ten globular-cluster like objects, originally detected in the SDSS images and used to infer the dynamic of the system, are designated with numbers.

NGC 1052-DF2 is a very diffuse stellar system originally discovered by Fosbury et al. (1978). In SDSS, the system stood out as it appeared as a group of punctual sources, while appearing as a low surface brightness system in the images provided by the Dragonfly

Nearby Galaxy Survey (van Dokkum et al., 2015) and the HST, as shown in Figure B.1. This survey, based on the Dragonfly Telescope Array, benefits from a large field of view ($\sim$ six square degrees) and is specifically designed to detect low surface brightness structures in the local universe. Because of the exciting prospect that these punctual SDSS sources could be associated with NGC 1052-DF2, it was soon the target of a spectroscopic study to determine the mass of its dark matter halo by constraining its dynamics (van Dokkum et al., 2018, VD18). VD18 measured the radial velocities of objects in the field of NGC 1052-DF2, with the Keck II/DEIMOS and the Low-Resolution Imaging Spectrometer (LRIS) on the Keck telescope, including the globular-cluster like objects potentially associated to the system.
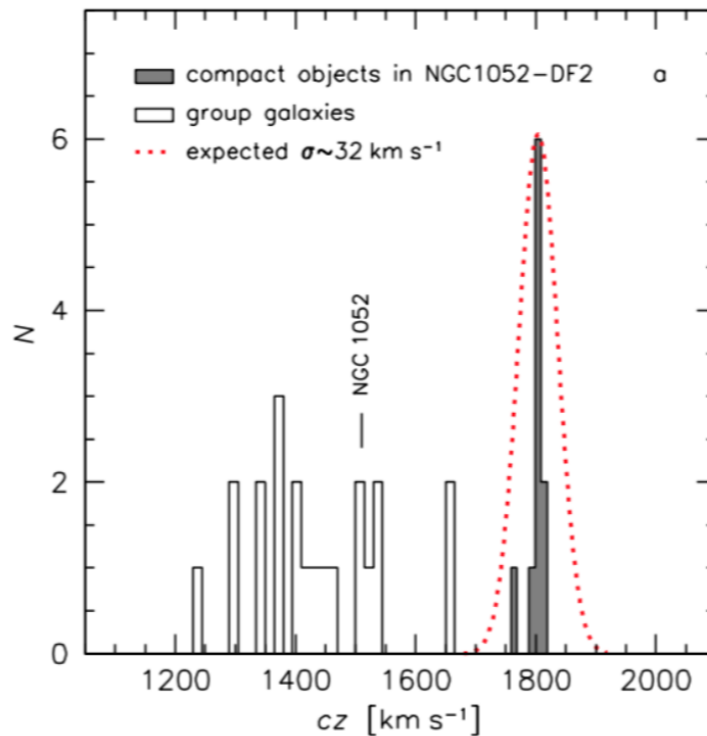
Figure B.2: Plot taken from VD18, showing their full spectroscopic sample. Two different populations can be distinguished here: a contaminant population spanning a wide range around 1400 km s^{-1}, and a narrow one centred on $\sim$ 1800 km s^{-1}. The objects considered as globular clusters of NGC 1052-DF2 are represented in grey, and the expected velocity distribution of a typical galaxy-like system with NGC 1052-DF2's size and luminosity is shown as a red dotted line.

The distribution of the radial velocity of the two spectroscopic samples is shown in Figure B.2, where 10 objects form a distinct, narrow group at $\sim$ 1800 km s^{-1}, that must therefore be part of a similar group and orbit NGC 1052-DF2. Using a biweight estimator on the ten globular-cluster like objects velocities, VD18 estimated the intrinsic velocity dispersion of the system to be $\sigma_{bi} = 3.2^{+5.5}_{-3.2}$ km s^{-1}, with a 90% confidence limit of 10.5 km s^{-1}. This was at odds with the $\sim$ 32 km s^{-1} expected from a galaxy with NGC 1052-DF2 structural properties. To estimate the dark matter halo mass, they then estimated the dynamical mass

enclosed within the distance to the most distant globular cluster-like object, i.e. at ~ 7.6 kpc from the center of NGC 1052-DF2, using the Tracer Mass Estimator method (TME, Watkins, Evans & An 2010). VD18 found a dynamical mass comparable with the stellar one, therefore indicating that NGC 1052-DF2 showed no sign of dark matter. At the 90% confidence limit, the mass of the dark matter halo was found to be of 1.5×10^8 M$_\odot$, which was still roughly 400 times less than the halo mass expected for such a system. Therefore, VD18 concluded that NGC 1052-DF2 is extremely deficient in dark matter. Furthermore, since a dark matter signature is expected in all galaxy-like systems in the MOdified Newtonian Dynamics (MOND) theory, VD18 claimed that the very existence of NGC 1052-DF2 may even falsify MOND.

The publication of this article in *Nature Astronomy* triggered a lot of reactions. The MOND part of VD18 was rapidly addressed by Famaey, McGaugh & Milgrom (2018), while the observational part was treated by following paper that I contributed to, Martin et al. (2018, M18). The main focus of M18 is the method used by VD18 to infer the intrinsic velocity dispersion of NGC 1052-DF2 and the subsequent conclusion that it contains little to no dark matter. Just like my work detailed in Chapters 3, 4 and 5, the spectroscopic study of the extended system is another case of trying to determine the dynamics with low-number statistics. VD18's method mainly relies on the assumption that one of the globular-like object is an outlier (because offset by ~ 60 km s^{-1} from the mean velocity) and on the use of the biweight estimator on such a sample. In an attempt to be closer to the data, we propose, in M18, to estimate the velocity dispersion of NGC 1052-DF2 in a purely Bayesian way, by not only considering only the plausible objects members of NGC 1052-DF2, but to model the entire spectroscopic sample by the sum of two Gaussian populations, one for NGC 1052-DF2, the other for the contamination. This method also has the advantage to naturally fold in the observational uncertainties in the analysis. For this work, my contribution has been to model the problem in this Bayesian way to test the conclusions of VD18, as well as being a part of the overall discussion around the paper.

Current Velocity Data on Dwarf Galaxy NGC 1052-DF2 do not Constrain it to Lack Dark Matter

Nicolas F. Martin[1,2] , Michelle L. M. Collins[3] , Nicolas Longeard[1], and Erik Tollerud[4]

[1] Université de Strasbourg, CNRS, Observatoire astronomique de Strasbourg, UMR 7550, F-67000 Strasbourg, France; nicolas.martin@astro.unistra.fr
[2] Max-Planck-Institut für Astronomie, Königstuhl 17, D-69117 Heidelberg, Germany
[3] Department of Physics, University of Surrey, Guildford, GU2 7XH, Surrey, UK
[4] Space Telescope Science Institute, 3700 San Martin Drive, Baltimore, MD 21218, USA

Abstract

It was recently proposed that the globular cluster system of the very low surface brightness galaxy NGC 1052-DF2 is dynamically very cold, leading to the conclusion that this dwarf galaxy has little or no dark matter. Here, we show that a robust statistical measure of the velocity dispersion of the tracer globular clusters implies a mundane velocity dispersion and a poorly constrained mass-to-light ratio. Models that include the possibility that some of the tracers are field contaminants do not yield a more constraining inference. We derive only a weak constraint on the mass-to-light ratio of the system within the half-light radius ($M/L_V < 6.7$ at the 90% confidence level) or within the radius of the furthest tracer ($M/L_V < 8.1$ at the 90% confidence level). This limit may imply a mass-to-light ratio on the low end for a dwarf galaxy, but many Local Group dwarf galaxies fall well within this contraint. With this study, we emphasize the need to reliably account for measurement uncertainties and to stay as close as possible to the data when determining dynamical masses from very small data sets of tracers.

Key words: galaxies: kinematics and dynamics – methods: statistical

1. Introduction

The dwarf galaxy NGC 1052-DF2 is a satellite of the elliptical NGC 1052 ($M_V \simeq -19.4$) discovered by Karachentsev et al. (2000) and later studied in detail by the Dragonfly experiment (van Dokkum et al. 2015). It is a very low surface brightness system, owing to its large half-light radius ($M_V \sim -15.3$; $r_{\rm half} \sim 2.2$ kpc; $\mu_0 = 24.4$ mag arcsec^{-2}; van Dokkum et al. 2018b). The presence of easily identified globular clusters in the system allowed van Dokkum et al. (2018b, hereafter vD18b) to explore the dynamics of this so-called "ultra-diffuse galaxy." From the velocities they obtained with LRIS and DEIMOS on the Keck telescopes, the authors isolate 10 likely member globular clusters (GCs), centered around $cz = 1803$ km s^{-1}. vD18b show that an rms estimate of the velocity dispersion of this sample yields $\sigma_{\rm rms} \sim 14.3$ km s^{-1}, while the use of a biweight dispersion (Beers et al. 1990) yields a smaller value $\sigma_{\rm rms} \sim 8.4$ km s^{-1}. This is expected, as this latter technique, which they favor, removes potential outliers to the distribution and produces a colder dispersion. After accounting for these uncertainties and under the hypothesis that the furthermost point (GC98) is an outlier, vD18b estimate an intrinsic velocity dispersion of $\sigma_{\rm int} = 3.2^{+5.5}_{-3.2}$ km s^{-1}.

However, it is well known that for such small samples of tracers that also have velocity uncertainties of order the measured velocity dispersion, results are extremely sensitive to the technique used and to the way the uncertainties are handled. This is a state of affairs that is, unfortunately, too common for the study of the dynamics of very faint dwarf galaxies in the Local Group for which samples are often restricted to 5–20 stars with velocities (e.g., Martin et al. 2007; Simon & Geha 2007). This community has converged on statistical methods that infer the velocity dispersion of a system by simply building a generative model for the data (e.g., Hogg et al. 2010; to measure a velocity dispersion, we would use a single Gaussian distribution, or the sum of a Gaussian

distribution with a simple contamination model that can handle outliers) and evaluating the posterior probability distribution. In favorable cases, the latter can potentially be summarized by its associated modes if it is well behaved.

In this Letter, we revise the estimation of the velocity dispersion of NGC 1052-DF2 by building such a generative model and sampling the posterior probability density function (PDF) of the intrinsic velocity dispersion. We show that the current data does not imply a vanishingly small velocity dispersion (and mass-to-light ratio) for NGC 1052-DF2 and that, in fact, it is compatible with expectations from dynamically hot (i.e., dark-matter dominated) Local Group dwarf galaxies.

2. Method and Results

We base our analysis on the sample of 10 GC velocities presented in van Dokkum et al. (2018a) and vD18b, with their associated uncertainties.

2.1. Model with no Contamination

We first assume that all 10 GCs are members of NGC 1052-DF2, with velocities v_i and velocity uncertainties $\delta_{v,i}$. In this case, our generative model is a simple Gaussian function with mean $\langle v \rangle$ and intrinsic dispersion, $\sigma_{\rm int}$. The likelihood function can be expressed as

$$\mathcal{L} = \prod_{i=1}^{i \leqslant 10} \frac{1}{\sqrt{2\pi}\,\sigma_{\rm obs}} \exp\left(-0.5\left(\frac{v_i - \langle v \rangle}{\sigma_{\rm obs}}\right)^2\right), \quad (1)$$

$$\text{with } \sigma_{\rm obs}^2 = \sigma_{\rm int}^2 + \delta_{v,i}^2. \quad (2)$$

Because the uncertainties $\delta_{v,i}$ provided by vD18b are asymmetric, we use the positive uncertainty when $v_i < \langle v \rangle$ and the negative one otherwise.
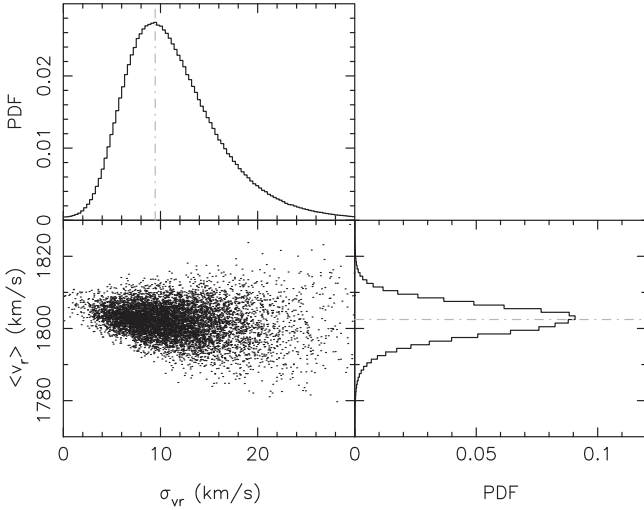
Figure 1. Joint PDF of the two-parameter Gaussian model (bottom left) and the marginalized PDF for the mean velocity $\langle v_r \rangle$ (right) and the velocity dispersion $\sigma_{\rm int}$ (top). This model yields $\sigma_{\rm int} = 9.5^{+4.8}_{-3.9}$ km s^{-1}.

We assume uniform priors on $\langle v \rangle$ and $\sigma_{\rm int}$ over the ranges 1750 to 1850 km s^{-1} and 0 to 30 km s^{-1}, respectively. We then sample the posterior PDF with our own Markov Chain Monte Carlo algorithm (Martin et al. 2016; Longeard et al. 2018). The resulting joint PDF is shown in Figure 1, along with the marginalized PDFs for the two parameters. The PDF on the intrinsic velocity dispersion of NGC 1052-DF2 is well behaved and yields a significantly higher dispersion than the one reported by vD18b: $\sigma_{\rm int} = 9.5^{+4.8}_{-3.9}$ km s^{-1} (<18.8 km s^{-1} at the 90% confidence level) versus $\sigma_{\rm int} = 3.2^{+5.5}_{-3.2}$ km s^{-1} (<10.5 km s^{-1} at the 90% confidence level). Note that our measurement is by design corrected for the velocity uncertainties, as those are specifically included in the model. Our inference is compatible with the rms estimate of vD18b ($\sigma_{\rm rms} \sim 12.2$ km s^{-1}); this is expected, as of all three methods used by vD18b, the rms estimate most closely resembles our formalism.

2.2. Priors

The inference described above assumes a uniform prior on $\sigma_{\rm int}$, but it is known that such a prior can be biased for small values. We also test the use of Jeffreys's prior, which does not suffer from this bias, but has the uncomfortable property of being improperly defined (i.e., the PDF does not integrate to unity) if it is not bound at the lower end. Doing so and forcing $\sigma_{\rm int} > 1$ km s^{-1} yields $\sigma_{\rm int} = 7.4^{+4.5}_{-3.3}$ km s^{-1} (<15.5 km s^{-1} at the 90% confidence level), which does not significantly change our inference. Alternatively, one can argue that, because the dynamical mass of NGC 1052-DF2 is the physical quantity we aim to constrain and because this quantity scales as $\sigma_{\rm int}^2$, it would be more appropriate to assume a uniform prior on $\sigma_{\rm int}^2$. Unsurprisingly, doing so yields larger value for the most likely intrinsic dispersion, with $\sigma_{\rm int} = 13.1^{+6.6}_{-4.5}$ km s^{-1} (<27.2 km s^{-1} at the 90% confidence level).

While changing the prior on $\sigma_{\rm int}$ does not change the main conclusion of this paper (the velocity dispersion of the NGC 1052-DF2 velocity sample is not very well constrained), the fluctuations on the constraint stemming from the choice of prior displays the poor constraining power of the data set.
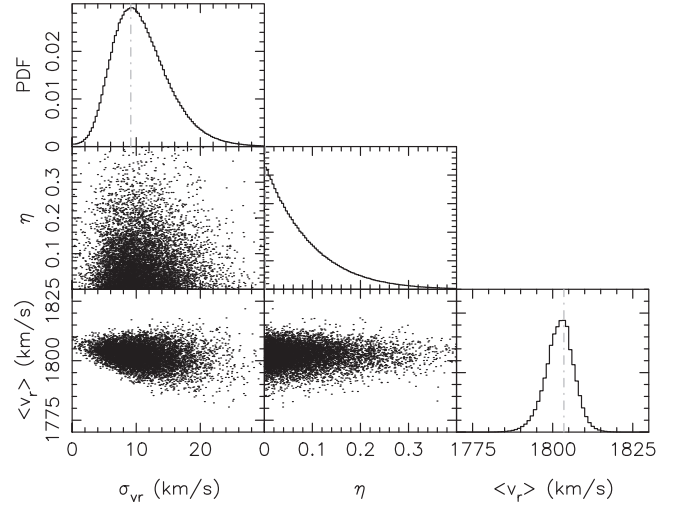
Figure 2. Joint PDF for the three-parameter model with a Gaussian component and a uniform contamination population. The marginalized PDF for the mean velocity $\langle v_r \rangle$, the fraction of contaminants η, and the velocity dispersion $\sigma_{\rm int}$ are also shown. Despite the contamination component, the PDF on the velocity dispersion remains similar to that of Figure 1, with $\sigma_{\rm int} = 9.2^{+4.8}_{-3.6}$ km s^{-1}.

2.3. Model with Contamination

A Kolmogorov–Smirnov test yields a high probability of 0.4 to 0.8 that the sparse data set is drawn from the range of models constrained in Section 2.1. It is therefore not possible to reject the simple Gaussian model as a bad model for this data set. Nevertheless, it is a priori possible that the sample of 10 GCs includes some contamination by field GCs (e.g., from the neighboring NGC 1052) and we now test a model that allows for contamination. We assume a uniform contamination model, $\mathcal{U}$ over the range $1750 < v_r < 1850$ km s^{-1}. With η the fraction of the data that is in the contamination, the likelihood function becomes

$$\mathcal{L} = \prod_{i=1}^{i \leqslant 10} \left[\eta \, \mathcal{U} + \frac{1-\eta}{\sqrt{2\pi}\,\sigma_{\rm obs}} \exp\left(-0.5 \left(\frac{v_i - \langle v \rangle}{\sigma_{\rm obs}} \right)^2 \right) \right], \quad (3)$$

with $\sigma_{\rm obs}$ as defined in Equation (2). The resulting PDFs are shown in Figure 2 for uniform priors. Interestingly, the inference on the intrinsic velocity dispersion of the GC sample remains unchanged, despite η reaching an upper limit of ~ 0.3. While this may seem surprising at first, it can easily be explained by the datum with the most discrepant velocity (GC98; $v = 1764^{+11}_{-14}$ km s^{-1}) having one of the largest velocity uncertainties. The model does not feel the need to separate this datum and fold it in the contamination model (indeed, that GC has the high probability of ~ 0.9 to belong to the dwarf galaxy part of the model). After marginalization, we infer $\sigma_{\rm int} = 9.2^{+4.8}_{-3.6}$ km s^{-1} (<17.3 km s^{-1} at the 90% level) for our baseline model with contamination. If we use a less-constraining contaminant model using a second Gaussian with only loose priors on the contamination (uniform from 1700 to 1900 km s^{-1} for the center and uniform between 100 and 200 km s^{-1} for the dispersion of this Gaussian representing the contamination), we get $\sigma_{\rm int} = 11.4^{+5.8}_{-4.5}$ km s^{-1}. Finally, even if we nevertheless decide to forego the outcome of the modeling with contamination and abruptly remove GC98 from the data
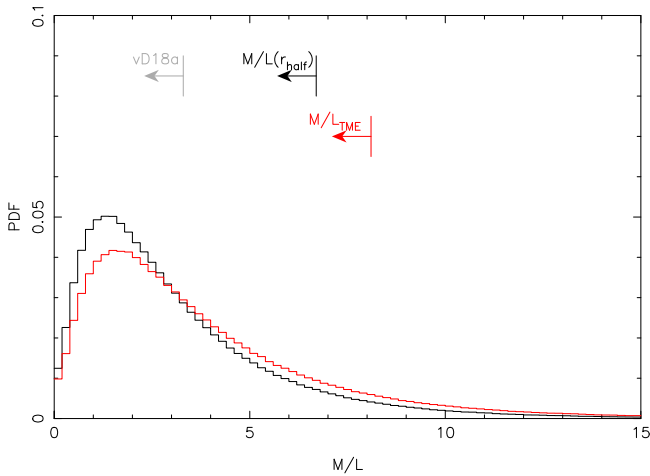
Figure 3. Mass-to-light ratio of NGC 1052-DF2 inferred from the marginalized velocity dispersion PDF of the model with contamination and for the Walker et al. (2009) mass estimator within the half-light radius (black) and the TME mass estimator of Watkins et al. (2010) favored by vD18b (red). In both cases, we infer a much less strict limit, as can be seen by the 90% confidence limits implied by our analysis (black and red limits and arrow) and that of vD18b (gray limit and arrow).

set (which is not advisable) to fit a single Gaussian model to the velocities of the remaining 9 GCs, we still only infer $\sigma = 7.1^{+3.6}_{-3.0}$ km s^{-1} (<14.3 km s^{-1} at the 90% confidence level). These variable results for different contamination assumptions highlight the challenges in interpreting such small-number data sets, while also demonstrating that these cases yield dispersions significantly higher than the vD18b limit.

In the following, we will use the model with the uniform contamination as our baseline model as it is among the most agnostic models discussed above.

2.4. Impact on the Mass-to-light Ratio

To infer the mass-to-light ratio of NGC 1052-DF2, we rely on the velocity dispersion from the model with contamination and use the mass estimator of Walker et al. (2009) that provides the mass within the half-light radius of the dwarf galaxy ($\sim$2.2 kpc) under the usual assumption of dynamical equilibrium and sphericity. This estimator yields $M(r_{\rm half}) < 3.7 \times 10^8 M_\odot$ at the 90% confidence level. Because this radius naturally includes half of the light of the system ($\sim$0.55 $\times 10^8 L_\odot$), we can infer the mass-to-light ratio $M/L(r_{\rm half}, V)$ within the half-light radius. The corresponding PDF is shown in black in Figure 3 and yields an upper limit of 6.7 at the 90% confidence level. Wolf et al. (2010) describe an alternate mass estimator to the one of Walker et al. (2009) that, beyond highlighting the difficulty of modeling the dynamical mass from a population of tracers, yields larger masses than the ones we give here ($M/L(r_{\rm half}, V) < 10.7$). The difference is driven by different choices for the profiles of the tracers, their (axi)symmetry and/or anisotropy assumption (see the discussion in Appendix C of Wolf et al. 2010). We focus on the Walker et al. (2009) estimator to allow for an easier comparison with vD18b, but recognize that the mass-to-light ratio limit of NGC 1052-DF2 would be even higher than the one we infer if we had used the Wolf et al. (2010) estimator.
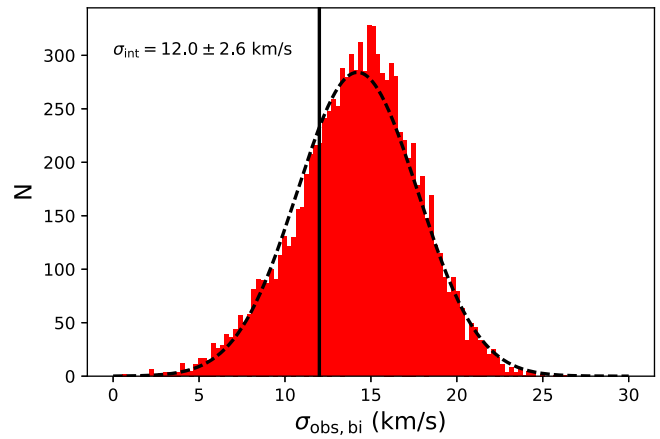
Figure 4. Results for measuring the observed biweight-midvairance dispersion from 10,000 resamples of the vD18b data set. Here, the original velocities are perturbed within their 1σ uncertainties as described in the text. The mean observed biweight for the sample comes out as $\sigma_{\rm obs,bi} = 14.3 \pm 3.5$ km s^{-1}, giving $\sigma_{\rm int,bi} = 12.0 \pm 2.5$ km s^{-1}, higher than the 90% upper limit from vD18b, and consistent with our MCMC analysis.

The mass estimator favored by vD18b and based on Watkins et al. (2010) gives the mass within the last datum, i.e., within 7.6 kpc for the sample of GCs.[5] The resulting mass-to-light ratio inference is similar but slightly less constrained (the red curve in Figure 3; $M/L_{\rm TME} < 8.1$ at the 90% confidence level).

Both mass estimators are therefore consistent with each other, and the data set is not strongly constraining, contrary to the finding of vD18b who found $M/L_{\rm TME,V} < 3.3$ at the 90% confidence level. It is also worth noting that folding in the uncertainties on $r_{\rm half}$ and L_V would make the constraint weaker, but vD18b unfortunately do not provide those for their measurement of the size and luminosity of NGC 1052-DF2. As such, the confidence limits provided here should only be seen as lower limits.

2.5. Additional Tests

2.5.1. Measuring the Velocity Dispersion by Resampling the Observed Data

Even though it amounts to making the data more noisy than they truly are and we do not recommend it, a common technique for measuring the dispersion from a small number of data points with significant uncertainties (i.e., similar to the size of the dispersion this is being measured), is to run a Monte Carlo resampling of the data. Here, we take the observed velocities of the vD18b sample and perturb them based on their uncertainties by randomly sampling from a Gaussian centered on the velocity measurement, with a dispersion equal to the uncertainties quoted by vD18b. We then follow their method for measuring the observed dispersion by recomputing the bi-weighted midvariance for this perturbed sample. We repeat this process 10,000 times, resulting in a distribution of values for $\sigma_{\rm obs,bi}$ (see Figure 4). From this process, we can use the mean and standard deviation of the distribution as a value for the observed dispersion, giving $\sigma_{\rm obs,bi} = 14.3 \pm 3.5$ km s^{-1} (very comparable with the observed r.m.s dispersion from vD18b). Following this, we must also correct for the effects of the observational uncertainties, which will inflate this

---

[5] Based on the structural parameters of NGC 1052-DF2 (vD18b), this radius includes 98% of the overall luminosity of the dwarf galaxy, or $\sim$1.08 $\times 10^8 L_\odot$.
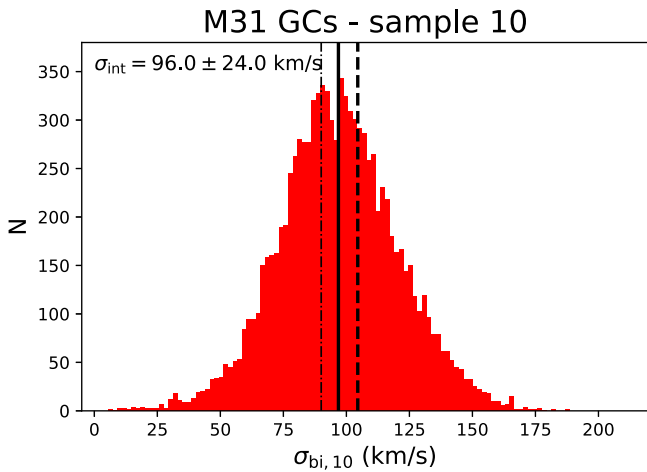
Figure 5. Results from randomly sampling 10 GCs from M31's outer cluster population, and measuring their dispersion from the biweight-midvariance, as in vD18. The mean of this analysis is shown as the solid line, while the value from the full sample of 74 clusters is shown as the dashed line. The value of the velocity dispersion from M31 halo stars is shown as the dashed–dotted line.

measurement. We follow the process of Pryor & Meylan (1993), using the average uncertainty from our 10,000 realizations, resulting in $\sigma_{int,bi} = 12.0 \pm 2.5$ km s^{-1}. This value is considerably higher than the $\sigma_{int} = 3.2^{+5.5}_{-3.2}$ km s^{-1} from vD18b, and lies above their proposed upper limit of $\sigma_{int} < 10.5$ km s^{-1}, but is consistent with the value we compute with our generative model (with or without contamination).

2.5.2. On the Reliability of Using Small Samples of Globular Clusters to Compute the "True" Dispersion

Two key issues with interpreting any measured velocity dispersion in this instance are (1) the small number of tracers available and (2) knowing whether these are truly relaxed tracers of the underlying dark-matter halo. For the latter, we know from observations of the outskirts of both the Milky Way and Andromeda that GCs are often associated with substructure at large radii (e.g., Mackey et al. 2010; Veljanoski et al. 2014). In Andromeda in particular, between 50% and 80% of all GCs at distances beyond 30 kpc show both spatial and kinematic correlations with stellar streams (Mackey et al. 2010), meaning that they are not fully relaxed mass tracers.

Given point (2), the effects of point (1) could be severe. Measuring a single dispersion from 10 tracers that may not be relaxed could lead to either a significant over- or under-estimate of the halo velocity dispersion. This can be straightforwardly demonstrated using the GC system of M31. We take the kinematics for 72 clusters from Veljanoski et al. (2014). As the globular cluster system of M31 is known to rotate, we use their rotation-corrected velocities to ensure we are not artificially inflating our measured mass. We then randomly draw 10 clusters and measure the biweight-midvariance of their velocity distribution, following the technique used by vD18b. This sample has a much larger intrinsic dispersion than DF2, but the data are of similar quality (mean velocity uncertainties of ∼10 km s^{-1}). Repeating this process 10,000 times gives us a distribution of observed velocity dispersions (see Figure 5) that we can compare to both the biweight from the full sample ($\sigma_{bi,all} = 105.0$ km s^{-1}; the dashed line in Figure 5), and the average velocity dispersion of the M31 halo from its stars ($\sigma_{M31_{stars}} \sim 90$ km s^{-1}, the dashed–dotted line; Gilbert et al. 2018).

The result here is clear: a single biweight dispersion measure from 10 GCs can give a huge range of dispersion measures. The mean value from this redraw gives $\sigma_{bi,10} = 96 \pm 24$ km s^{-1}, but the tails extend to far higher and smaller values. Such a large statistical uncertainty would mean that, from a sample of 10 GCs in M31, halo masses ranging from $0.2 < M < 1.2 \times 10^{12} M_{\odot}$ could be measured within the 90% confidence limit. Given that M31 has a stellar mass of ∼$10^{11} M_{\odot}$ (Sick et al. 2015; Williams et al. 2017), the mass-to-light ratio could also be compatible with no dark matter based on this analysis.

3. Discussion

It is evident from Figure 3 that the current velocity data set on NGC 1052-DF2 is not very constraining beyond pointing out that the dwarf galaxy is not massively dominated by dark matter. At the moment, it is not possible to rule out any mass-to-light ratio below $M/L < 6.7$ within the half-light radius or $M/L < 8.1$ within the radius covered by the tracers (at the 90% confidence level in both cases). Could NGC 1052-DF2 host no dark matter and its inferred mass (or mass-to-light ratio) be entirely consistent with an old stellar population ($M/L_V \sim 2$)? Certainly, but so could a much more mundane, dark-matter dominated mass-to-light ratio.

The mass-to-light ratio of NGC 1052-DF2 is compatible with that of other nearby dwarf galaxies. For instance, IC 1613 shares the luminosity of NGC 1052-DF2, has a radius that is only half as small and a velocity dispersion of $10.8^{+1.0}_{-0.9}$ km s^{-1} from which Kirby et al. (2014) inferred $M/L_V(r_{half}) = 2.2 \pm 0.5$. The M31 companions Cas III and Lac I, albeit somewhat fainter, share similar properties to those of NGC 1052-DF2: their large half-light radii (∼1.5 kpc; Martin et al. 2013) and velocity dispersion ∼10 km s^{-1} imply mass-to-light ratios ($M/L_V(r_{half}) = 8^{+9}_{-5}$ and 15^{+12}_{-9}, respectively; Martin et al. 2014) that are entirely compatible with the constraint on NGC 1052-DF2.[6] The well-studied Milky Way satellite dwarf galaxy, Fornax, also shares similar properties (Irwin & Hatzidimitriou 1995; Walker et al. 2009). Finally, NGC 1052-DF2's velocity dispersion and mass, despite being poorly constrained, fall perfectly on the Walker et al. (2009) universal mass profile proposed for Local Group dwarf galaxies. It also follows the locus of most dwarf galaxies in the M/L versus M plane, contrary to the peculiar dwarf galaxy Dragonfly 44, which appears as exceptionally massive (van Dokkum et al. 2016, their Figure 3). A conservative and cautious approach would therefore be to conclude that the mass-to-light ratio of NGC 1052-DF2 appears to be the low end of that measured for other dwarf galaxies, but share the properties of other local dwarf galaxies and relies on a noisy measurement. Other "ultra-diffuse dwarf galaxies" studied with data sets of similar quality also yield only weak constraints on the dark-matter content (Toloba et al. 2018). Significant additional proof is required before claiming a lack of dark matter in NGC 1052-DF2, even more so since rotation could also be present and its contribution to the dynamics of the galaxy could further increase its dynamical mass. An independent study by Laporte et al. (2018) shows that NGC 1052-DF2 can comfortably live in a dark-matter halo of $10^9 M_{\odot}$ or even $10^{10} M_{\odot}$ within the uncertainties.

The different conclusions reached by vD18b and this study show the difficulty in extracting information from a small

---

6 The fairly large uncertainties on $M/L_V(r_{half})$ for these two systems, despite being based on 100–200 tracers further imply that the 10 NGC 1052-DF2 tracers with velocities are unlikely to yield a strong constraint.

velocity data set, especially when the measurement uncertainties on the individual data points are of order the dispersion that is being inferred. In such cases, reverting back to the simplest model and techniques (using a generative model) yields more robust and tractable results.

ORCID iDs

Nicolas F. Martin ⓘ https://orcid.org/0000-0002-1349-202X
Michelle L. M. Collins ⓘ https://orcid.org/0000-0002-1693-3265
Erik Tollerud ⓘ https://orcid.org/0000-0002-9599-310X

References

Beers, T. C., Flynn, K., & Gebhardt, K. 1990, AJ, 100, 32
Gilbert, K. M., Tollerud, E., Beaton, R. L., et al. 2018, ApJ, 852, 128
Hogg, D. W., Bovy, J., & Lang, D. 2010, arXiv:1008.4686
Irwin, M., & Hatzidimitriou, D. 1995, MNRAS, 277, 1354
Karachentsev, I. D., Karachentseva, V. E., Suchkov, A. A., & Grebel, E. K. 2000, A&AS, 145, 415
Kirby, E. N., Bullock, J. S., Boylan-Kolchin, M., Kaplinghat, M., & Cohen, J. G. 2014, MNRAS, 439, 1015
Laporte, C. F. P., Agnello, A., & Navarro, J. F. 2018, arXiv:1804.04139
Longeard, N., Martin, N. F., Starkenburg, E., et al. 2018, MNRAS, submitted
Mackey, A. D., Ferguson, A. M. N., Irwin, M. J., et al. 2010, MNRAS, 401, 533
Martin, N. F., Chambers, K. C., Collins, M. L. M., et al. 2014, ApJL, 793, L14
Martin, N. F., Ibata, R. A., Chapman, S. C., Irwin, M., & Lewis, G. F. 2007, MNRAS, 380, 281
Martin, N. F., Ibata, R. A., Collins, M. L. M., et al. 2016, ApJ, 818, 40
Martin, N. F., Slater, C. T., Schlafly, E. F., et al. 2013, ApJ, 772, 15
Pryor, C., & Meylan, G. 1993, in ASP Conf. Ser. 50, Structure and Dynamics of Globular Clusters, ed. S. G. Djorgovski & G. Meylan (San Francisco, CA: ASP), 357
Sick, J., Courteau, S., Cuillandre, J.-C., et al. 2015, in IAU Symp. 311, Galaxy Masses as Constraints of Formation Models, ed. M. Cappellari & S. Courteau (Cambridge: Cambridge Univ. Press), 82
Simon, J. D., & Geha, M. 2007, ApJ, 670, 313
Toloba, E., Lim, S., Peng, E., et al. 2018, ApJL, 856, L31
van Dokkum, P., Abraham, R., Brodie, J., et al. 2016, ApJL, 828, L6
van Dokkum, P., Cohen, Y., Danieli, S., et al. 2018a, ApJL, 856, L30
van Dokkum, P., Danieli, S., Cohen, Y., et al. 2018b, Natur, 555, 629
van Dokkum, P. G., Abraham, R., Merritt, A., et al. 2015, ApJL, 798, L45
Veljanoski, J., Mackey, A. D., Ferguson, A. M. N., et al. 2014, MNRAS, 442, 2929
Walker, M. G., Mateo, M., Olszewski, E. W., et al. 2009, ApJ, 704, 1274
Watkins, L. L., Evans, N. W., & An, J. H. 2010, MNRAS, 406, 264
Williams, B. F., Dolphin, A. E., Dalcanton, J. J., et al. 2017, ApJ, 846, 145
Wolf, J., Martinez, G. D., Bullock, J. S., et al. 2010, MNRAS, 406, 1220

Résumé en français

C

C.1 Introduction

C.1.1 Contexte scientifique

Selon le modèle cosmologique standard, le modèle ΛCDM, de minuscules fluctuations (sur- et sous-densités) dans la distribution de matière dans les premiers instants de l'Univers ont grossi lentement au fil du temps sous l'effet de la gravité, pour former des halos de matière noire. Ces halos, toujours sous l'action de la gravité, ont attiré le gas autour d'eux et formé des régions denses. Parce qu'ils permettent la formation de ces environnements denses, les halos suffisamment massifs ont indirectement déclenché la formation des étoiles, qui elles-mêmes se sont assemblées pour former des galaxies. Les plus petits halos sont les premiers à se former, puis vont progressivement fusionné les uns avec les autres pour former des halos, et donc des galaxies, de plus en plus massives et lumineuses. Cependant, certains halos sont restés peu massifs et ont permis la formation de petites galaxies, peu massives et peu lumineuses, orbitant souvent autour de galaxies massives.

Ainsi, les galaxies sont une conséquence directe des propriétés sous-jacentes de l'Univers. Et donc, les paramètres cosmologiques qui décrivent notre Univers peuvent être contraints par l'étude de celles-ci. De plus, les galaxies ne doivent pas leur existence qu'aux halos de matière noire, mais également à de nombreux processus physiques, comme la formation des étoiles, par exemple. Ainsi, que ce soit pour des considérations cosmologiques ou pour la compréhension de la formation des galaxies, ces dernières sont de puissants outils pour tenter de lever un peu plus le voile sur les mystères de notre Univers.

Les galaxies naines sont particulièrement intéressantes, car, en plus d'être plus nombreuses, ce sont également elles qui se sont formées les premières. Mais parce qu'elles sont petites et peu lumineuses, elles ne sont pas toujours bien comprises et caractérisées. De plus, il en existe probablement plusieurs, orbitant autour de notre Voie Lactée, qui échappent, pour le moment, à nos téléscopes. Au cours des dernières années, le nombre de découverte de ces systèmes autour de la Voie Lactée a véritablement explosé, passant de 8 en 2004 à plus d'une cinquantaine de galaxies (confirmées ou candidates) de nos jours. Et ce, grâce à l'impulsion de grands relevés digitaux comme le Sloan Digital Sky Survey (SDSS), le Dark

Energy Survey (DES) ou encore le Panoramic Survey Telescop and Rapid Response System (PS1).

Le panneau gauche de la Figure C.1 montre la magnitude absolue et le rayon de demie-lumière de la plupart des amas globulaires connus (cercles), ainsi que des galaxies naines confirmées ou candidates (carrés). Le code couleur des galaxies correspond à leur année de découverte. Il est clair que les galaxies représentées en bleu, c'est-à-dire celles découvertes avant 2005, forment un groupe visuellement trés distinct de celui des amas. Ainsi, avant l'apparition des grand relevés photométriques, la classification galaxie/amas globulaire pouvait se faire aisément sur la base de la taille du système. Mais la Figure C.1 montre que lorsque l'on considère des objets de moins en moins lumineux, la distinction est de plus en plus compliquée à faire.

Le panneau droit, lui, représente la magnitude absolue et la métallicité systémique de tous ces systèmes et montre ainsi que les galaxies naines suivent une relation bien particulière dans cet espace des paramètres, représentée par la ligne noire (Kirby et al., 2013b). Une nouvelle fois, si dans cet espace, les galaxies les plus brillantes forment un groupe distinct des amas, ce n'est plus le cas dans un régime de luminosité plus faible. Si toutes les galaxies suivent la relation métallicité-luminosité représentée en noire, certains amas sont également compatibles avec celle-ci, rendant la frontière entre les deux types d'objets encore plus floue.

Ainsi, avec la multiplication des découvertes de systèmes à la nature ambigue est venu la nécessité de revenir à la définition d'une galaxie : elles résident au centre de halos de matière noire massifs. Afin de pouvoir effectuer la distinction galaxie/amas dans le régime de faible luminosité, il faut donc mettre en évidence l'existence d'un halo de matière noire.

Ceci peut se faire de différentes façons, mais deux méthodes sont le plus souvent utilisées:

- Étudier la dynamique des étoiles au sein du système. La masse importante du halo influe grandement sur le mouvement interne des étoiles d'une galaxie. Par spectroscopie, il est possible de mesurer les vitesses radiales individuelles d'un échantillon d'étoiles du système et d'en déduire une mesure de la dispersion de vitesse à l'intérieur dudit système. Cette dispersion de vitesse peut également être prédite théoriquement pour un système dépourvu de halo de matière noire. Ainsi, si la dispersion observée et celle prédite par le calcul dans le cas purement baryonique sont compatibles, cela signifie que la dynamique interne de l'objet étudié peut être expliquée sans faire appel à la matière noire. En revanche, si la dispersion de vitesses observée est bien supérieure, c'est que le système est dominé par la matière noire, et qu'il s'agit donc d'une galaxie.

- Étudier la métallicité des étoiles peuplant le système. Le panneau droit de la Figure C.1 montre que la majorité des galaxies confirmées suivent la relation métallicité-luminosité. Le fait que certains amas puissent également être compatibles avec cette relation implique que cette dernière n'est pas nécessairement un outil permettant d'affirmer qu'un système est effectivement une galaxie, mais peut être trés utile pour démontrer qu'il ne l'est pas, si l'objet a des propriétés trés éloignées de la relation. Il faudra, en revanche,
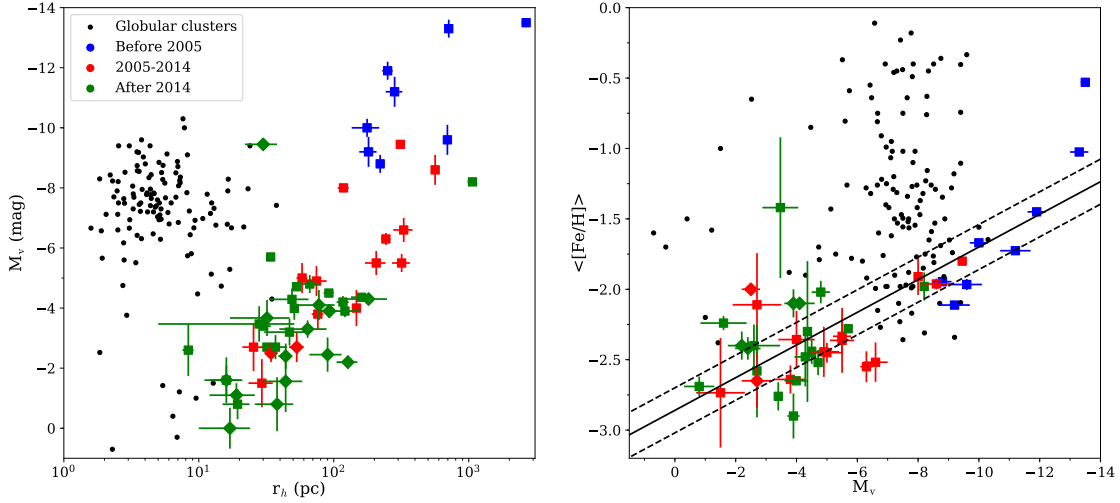
Figure C.1: Rayon de demie-lumière et magnitude absolue de la plupart des amas globulaires connus (cercles noirs), des galaxies naines confirmées (carrés de couleur) et des galaxies naines candidates (losanges de couleur) orbitant autour de la Voie Lactée. Pour les galaxies, il est également indiqué si elles ont été découvertes avant le SDSS, i.e. avant 2005 (bleu), entre 2005 et 2014 (rouge), ou aprés 2014 (vert). Les propriétés des galaxies les plus brillantes sont clairement différentes de celles des la majorité des amas. Les incertitudes sont seulement reportées pour les galaxies (confirmées ou candidates). La frontière entre galaxie et amas devient de moins en moins évidente à mesure que l'on considère des systèmes de moins en moins brillants. 124 amas globulaires sont représentés ici. Les propriétés de 116 d'entre eux sont issues du catalogue de Harris (1996), revisé en 2010. Pour les autres (Kim 1, Kim 2, Kim 3, Laevens 1, Balbinot 1, Munoz 1 et SMASH 1), les propriétés issues des articles de découvertes ont été utilisées (Kim & Jerjen (2015a), Kim et al. (2015), Kim et al. (2016), Laevens et al. (2014), Balbinot et al. (2013), Muñoz et al. (2012) et Martin et al. (2016c)). Les mesures de dispersion de métallicité des amas sont prises de Willman & Strader (2012) et des références associées: Carretta et al. (2006, 2007, 2009b, 2011), Cohen et al. (2010), Gratton et al. (2007), Johnson & Pilachowski (2010), et Marino et al. (2011). McConnachie (2012) et Willman & Strader (2012) sont utilisés pour les propriétés des galaxies naines représentées ici. Les 35 galaxies naines représentées sont: Aquarius II (Torrealba et al., 2016b), Bootes I (Belokurov et al., 2006; Norris et al., 2010), Canes Venatici I (Zucker et al., 2006b), Canes Venatici II (Sakamoto & Hasegawa, 2006), Carina (Cannon, Hawarden & Tritton, 1977), Carina II (Torrealba et al., 2018), Colomba I (Drlica-Wagner et al., 2015), Coma Berenices, Hercules, Leo IV et Segue I (Belokurov et al., 2007), Crater II (Torrealba et al., 2016a), Draco et Ursa Minor (Wilson, 1955), Eridanus II (Bechtol et al., 2015; Conn et al., 2018; Koposov et al., 2015b), Fornax (Shapley, 1938b), Grus I (Koposov et al., 2015a), Hydra II (Martin et al., 2015), Hydrus I (Koposov et al., 2018), Leo I et Leo II (Harrington & Wilson, 1950), Leo V (Belokurov et al., 2008), Leo T (Irwin et al., 2007), Phoenix II (Bechtol et al. 2015, Pisces II (Belokurov et al., 2010), Reticulum II et Horologium I (Koposov et al., 2015a), Sagittarius (Ibata, Gilmore & Irwin, 1994), Sextans (Irwin et al., 1990), Sculptor (Shapley, 1938a), Triangulum II (Laevens et al., 2015b), Tucana II (Bechtol et al., 2015), Ursa Major I (Willman et al., 2005b), Ursa Major II (Zucker et al., 2006a), Willman I (Willman et al., 2005a). Leur métallicité et dispersion de métallicité sont issues de Caldwell et al. (2017), Fritz et al. (2019), Kirby et al. (2008), Kirby et al. (2010), Kirby et al. (2017), Li et al. (2018), Martin et al. (2016b), Norris et al. (2010), Walker et al. (2016), Willman et al. (2011). Les galaxies naines candidates dćouvertes rćemment et montrées sur la figure sont Bootes II (Koch & Rich, 2014), Carina III, Cetus III (Homma et al., 2018), DES1 (Luque et al., 2016; Conn et al., 2018), DESJ0225+0304 (Luque et al., 2017), Horologium II (Kim & Jerjen, 2015b), Pegasus III (Kim & Jerjen, 2015a),Koposov et al. 2015a), Pictor I (Bechtol et al., 2015), Pictor II (Drlica-Wagner et al., 2016), Segue 2(Belokurov et al., 2009), les découvertes de Drlica-Wagner et al. (2015) qui attendent d'être confirmées: Cet II, Gru II, Indus II, Ret III, Tuc III, Tuc IV et Tuc V, et Virgo I (Homma et al., 2016)

145

s'assurer que l'objet étudié ne soit pas sujet à des effets de marées. L'existence de plusieurs populations stellaires au sein d'un même système de faible luminosité indique également l'existence d'un halo de matière noire. En effet, un système stellaire peu brillant, sans halo et la masse supplémentaire qu'il apporte, aura du mal à conserver son gaz lorsque les premières supernovae exploseront en son sein. Sans parvenir à conserver les ejecta de supernovae et son gaz, le système stellaire ne pourra plus former de nouvelles populations stellaires, qui auraient été enrichies en métaux par la génération précédente. La dispersion de métallicité dans un tel objet sera donc trés faible. C'est effectivement ce que l'on peut observer dans tous les amas de faible luminosité, alors que toutes les galaxies naines peu brillantes montrent des signes de populations multiples.

Ces deux méthodes reposent entièrement sur des observations spectroscopiques. Hors, moins un système stellaire est brillant, plus il sera difficile de réunir un échantillon suffisamment grand d'étoiles pour avoir des contraintes sur les propriétés dynamiques et de métallicité dudit système permettant de déterminer s'il est dominé par la matière noire. Ainsi, pour étudier efficacement les satellites peu brillants orbitant autour de la Voie Lactée, il devient nécessaire de disposer d'une méthode permettant d'identifier plus facilement les populations stellaires pauvres en métaux, spécifiques des galaxies naines candidates à priori et/ou à posteriori. Pour ce faire, j'ai utilisé, durant ma thèse, les données fournies par le relevé Pristine.

C.1.2   Le relevé Pristine

Le relevé Pristine (Starkenburg et al., 2017, S17) est un relevé photométrique mené par les Dr. Else Starkenburg et Dr Nicolas Martin. Il permet de trouver et d'étudier les étoiles pauvres en métaux individuellement, mais également les nombreuses sous-structures composées de ces populations de faible métallicité, que ce soit dans le halo Galactique ou au-delà. Pristine utilise l'instrument grand champ MegaCam basé au Canada France Hawai Telescope (Boulade et al., 2003, CFHT) et a observé plus de 6,000 degrés carrés jusqu'à présent, représentés sur la Figure C.2.

Le relevé se superpose avec le SDSS afin de pouvoir utiliser leurs magnitudes larges bandes (principalement g, i et r) ainsi que leurs observations spectroscopiques. Pristine contient également 22 galaxies naines et galaxies candidates.

Le coeur du relevé réside dans un filtre bande étroite centré sur le doublet du calcium H&K, qui possède la particularité d'être sensible à la métallicité des étoiles. Ainsi, la magnitude $CaHK$ déduite du flux reçu dans le filtre Pristine dépend de la métallicité d'une étoile. Parce qu'elle dépend également de la tempérture effective, il est également nécessaire d'avoir une estimation de celle-ci. Ceci est assuré par les bandes larges, comme celles du SDSS avec la couleur $g - i$. La Figure C.3 représente le diagramme coulour-couleur Pristine, avec le proxy de température $g - i$ sur l'axe x et une combinaison de magnitude contenant le $CaHK$ sur l'axe y. Sur un tel diagramme, les étoiles devraient donc être réparties en fonction de leur métallicité. Le code couleur, représentant la métallicité des étoiles issues d'observations spectroscopiques du SDSS, montre que c'est effectivement le cas : les étoiles de métallicité
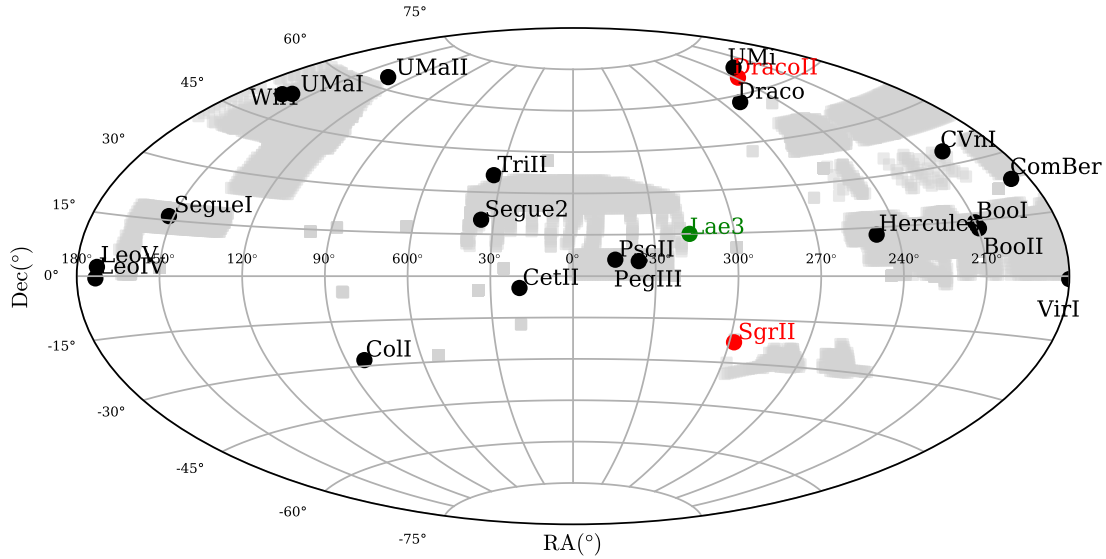
Figure C.2: Empreinte du relevé Pristine (Juillet 2019), superposé avec la position des 22 galaxies naines et galaxies naines candidates obserées par Pristine. Le relevé Pristine principal est représenté en gris. Les deux satellites en rouge, Draco II et Sagittaire II, ont fait l'objet d'observations plus profondes en *g* et *i* MegaCam/CFHT, et en *CaHK*. Les études de ces deux systèmes sont détaillées dans les chapitres 3 et 4. Les satellites restants, en noir, ont du *CaHK* moins profond et leur photométrie large bande est issue de relevé photométrique comme le SDSS ou PS1. Laevens 3, un amas du halo externe de la Voie Lactée, est montré en vert et fait l'objet de l'étude détaillée dans le chapitre 5. Cependant, celui-ci n'est pas dans Pristine.

solaire sont situées sur la partie basse du diagramme. Puis l'on trouve des étoiles de plus en plus faibles en métaux à mesure que l'on porte le regard plus haut dans le diagramme couleur-couleur. Grâce aux données spectroscopiques SDSS, il est donc possible de calibrer ce diagramme pour pouvoir déduire la métallicité de chaque étoile disposant de photométrie large bande et du *CaHK*. Tout ce travail de calibration est détaillé par S17. Le modèle ainsi obtenu permet donc de déduire la métallicité de n'importe quelle étoile dans le relevé Pristine, sans avoir besoin d'observations spectroscopiques. Les performances de Pristine, c'est-à-dire la faculté qu'a le relevé de qualitativement et quantitativement déterminer la métallicité des étoiles, détaillées par Youakim et al. (2017) et Aguado et al. (2019), sont excellentes.

L'application de Pristine aux galaxies naines de faible luminosité est naturelle. Puisque ces dernières sont peuplées par des populations stellaires pauvres en métaux et que Pristine est particulirèment efficace pour identifier ces mêmes populations, le relevé est donc un outil de choix pour optimiser la recherche des étoiles de systèmes stellaires peu brillants. D'une part, à priori, en sélectionnant les étoiles pauvres en métaux puis en les observant par spectrosopie, de l'autre, en nettoyant un jeu de données spectroscopiques existant pour éliminer la contamination galactique et ne garder que les étoiles de faible métallicité. C'est
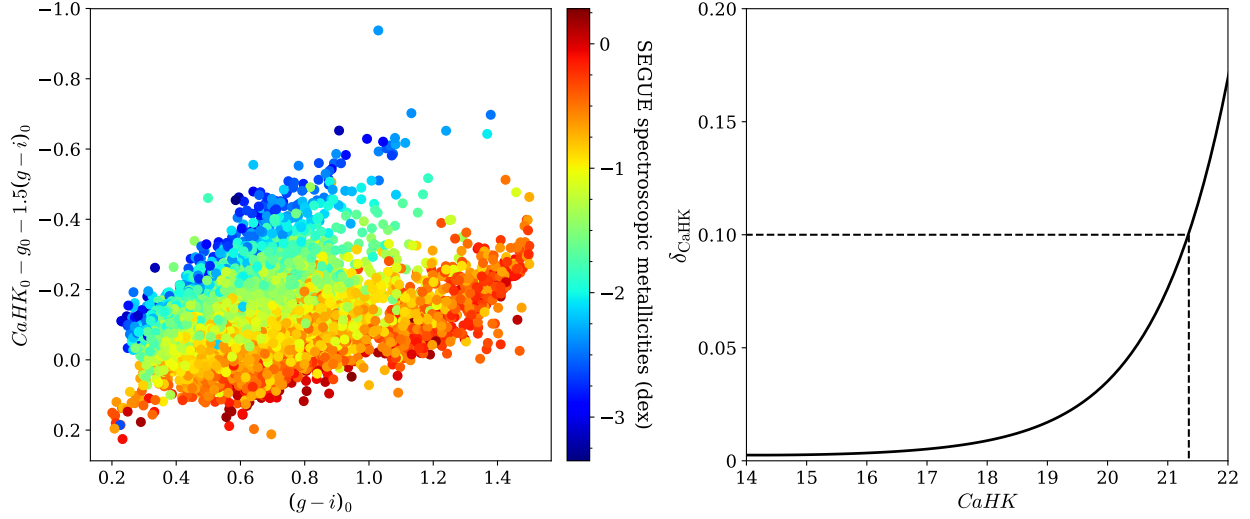
Figure C.3: *Panneau gauche :* Diagramme couleur-couleur Pristine. L'axe des x montre le proxy de température $(g-i)_0$, alors que l'axe des y contient l'information en métallicité avec la magnitude $CaHK$. Les étoiles sont colorées selon leur métallicités spectroscopiques provenant de SEGUE. Le pouvoir discriminatoire du filtre Pristine est illustré ici : les étoiles avec une métallicité solaire se situent dans la partie inférieure du diagramme, puis la métallicité diminue progressivement lorsque l'on considère des étoiles plus haut dans le diagramme. La métallicité photométrique de n'importe quelle étoile peut ainsi être déduite en connaissant sa position dans le diagramme Pristine. *Panneau droit :* Incertitudes typiques sur le $CaHK$ pour une région de deux degrés carrés représentatif du relevé principal. Une incertitude de ~ 0.1 est atteinte à $CaHK \sim 21.3$ mag.

dans ce cadre que j'ai effectué mon travail de thèse, présenté ci-aprés. Pendant trois ans, je me suis proposé d'étudier trois satellites de la Voie Lactée de faible luminosité : Draco II, Sagittaire II et Laevens 3, afin de déterminer leur nature respective.

C.2 Une étude photométrique et spectroscopique détaillée du satellite de trés faible métallicité Draco II

Draco II (Dra II) est un satellite de la Voie Lactée découvert par Laevens et al. (2015a, L15). Lors de de sa découverte, Draco II était une des galaxies candidates les moins brillantes. En effet, aucune branche horizontale ou branche des géantes ne ressortait clairement du diagramme couleur-magnitude du système. Avec sa taille et sa luminosité, L15 a penché pour une nature galactique concernant Dra II, mais a insisté sur la nécessité d'effectuer des observations spectroscopiques du système pour confirmer cette hypothèse. Ce fut chose faite avec Martin et al. (2016a, M16) qui a observé le satellite avec le spectrographe DEIMOS et le Keck. M16 a donc mesuré les vitesses de 34 étoiles dans la région de Dra II et a identifié 9 membres du satellite, pour une vitesse systémique fortement récessionelle de $-347^{+1.7}_{-1.8}$ km s^{-1}. Cependant, la dispersion de vitesse de Dra II n'a pas pu être suffisamment contrainte, avec une mesure de 2.9 ± 2.1 km s^{-1}, ce qui ne permet pas d'affirmer avec robustesse que le
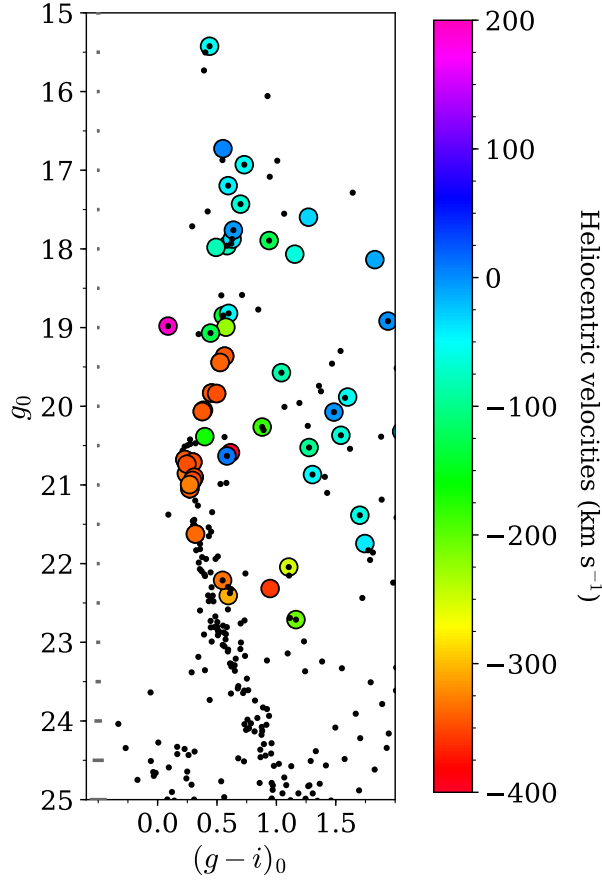
Figure C.4: Diagramme couleur-magnitude d'une région de 2 r$_h$ centrée sur Dra II. La position des étoiles observées spectroscopiquement sont également montrées ici, avec des cercles plus larges, colorés en fonction de leur vitesse radiale. La séquence principale de Dra II est facilement identifiable, ainsi que la plupart de ses membres en orange.

satellite baigne dans un halo massif de matière noire. De plus, les données de cette étude n'ont pas permis d'identifier d'étoiles de la branche des géantes ni de mesurer la métallicité du système par spectroscopie. Une analyse qualitative des spectres de plusieurs étoiles de Dra II suggè l'existence de populations multiples dans le satellite. Néanmoins, M16 a conclu de la nécessité d'observer encore Dra II avec de la spectropscopie.

Mon étude de Dra II (Longeard et al., 2018) s'inscrit donc à la suite de ces travaux. Pour tenter de percer les secrets de Dra II, je dispose d'observations photométriques larges bandes en g et i avec MegaCam, d'une nouvelle série d'observations spectroscopiques avec Keck/DEIMOS, et des données bandes étroites de Pristine.

Le diagramme couleur-magnitude de Draco II est montré avec la Figure C.4. Il est completé par la représentation des données spectroscopiques dans ce même diagramme. Si la photométrie trés profonde permet de mettre en évidence la séquence principale du satellite, ainsi que son turn-off, il est difficile de distinguer une quelconque branche des géantes ou

horizontale. Tout d'abord, je tire partie de la photométrie afin de redéterminer les propriétés structurelles de Dra II, à savoir son rayon de demie-lumière, son ellipticité, la position de son centre, son orientation, ainsi que le nombre d'étoiles dans le système jusqu'à une magnitude de $g = 24.5$ mag. Cette analyse est faite conjointement avec la détermination des caractéristiques principales de la population stellaire de Dra II: son âge, sa métallicité, son ratio d'abondance en éléments α et sa distance au soleil. Grâce à ces propriétés, je détermine également dans la foulée la luminosité totale du satellite. Avec un rayon de demie-lumière de $r_h = 19.0^{+4.5}_{-2.6}$ pc et une luminosité de $L_V = 180^{+124}_{-72}$ L$_\odot$, le système est plus étendu que les amas globulaires de même luminosité. De plus, il est situé à une distance de 21.5 ± 0.4 kpc, et son diagramme couleur-magnitude indique une métallicité de -2.40 ± 0.05 dex. Comme indiqué précédemment, si la taille de Dra II laisse penser qu'il s'agit d'une galaxie naine, la confirmation spectroscopique est nécessaire.

Afin de mesurer la métallicité de Dra II, j'ai utilisé les données Pristine. En effet, je dispose de la métallicité photométrique de plusieurs dizaines d'étoiles du satellite à l'intérieur de deux rayons de demie-lumière grâce au relevé. En supposant que les métallicités des étoiles dans Dra II sont distribuées suivant une gaussienne, et en tenant en compte de la contamination Galactique locale, j'obtiens une métallicité $[\mathrm{Fe/H}]_{\mathrm{CaHK}} = -2.7 \pm 0.1$ dex, ainsi qu'une dispersion de métallicité non résolue. Afin de vérifier du bien-fondé de la méthode, une analyse similaire est conduite sur deux amas globulaires observés dans Pristine, pour lesquelles les métallicités systémiques et dispersions de métallicité sont bien connues spectroscopiquement. En comparant les mesures de la littérature et celles obtenues uniquement par photométrie par mon analyse des données Pristine, on constate que les mesures concordent, indiquant que la méthode est fiable.

La deuxième partie de l'article se concentre sur l'analyse de la dynamique de Dra II grâce aux données DEIMOS. En combinant les données de M16 avec les nouvelles, l'échantillon spectroscopique pour Dra II compte désormais 57 étoiles avec une mesure de vitesse radiale. Cet échantillon est représenté dans les deux premiers panneaux de la Figure C.5. Si le pic de vitesse de Dra II est facilement identifiable aux alentours de -345 km s^{-1}, il y a tout même une contamination importante dans l'échantillon. Afin de s'en débarasser, j'utilise donc les données Pristine. En effet, la popultion stellaire de Dra II devrait être plus pauvres en métaux que celle de la contamination, qui est principalement constituée d'étoiles de la Voie Lactée (halo et disque). La Figure C.6 montre le diagramme couleur-couleur Pristine, avec des étoiles du champ en noir, et l'échantillon spectroscopique en points plus larges et colorés en fonction de leur vitesse radiale. La figure montre parfaitement que la majorité des étoiles compatibles avec la vitesse radiale de Dra II, en orange, forment un groupe distinct dans la partie du diagramme correspondant aux étoiles pauvres en métaux. A l'inverse, les autres étoiles sont plus riche en métaux. Ainsi, il est possible, dans le diagamme, de ne selectionner que les étoiles de faible métallicité selon Pristine afin de nettoyer l'échantillon spectroscopique. La sélection se fait suivant le polygone représenté par les lignes pointillées. L'histogramme des vitesses radiales des étoiles restantes est representé dans le dernier panneau de la Figure C.5.
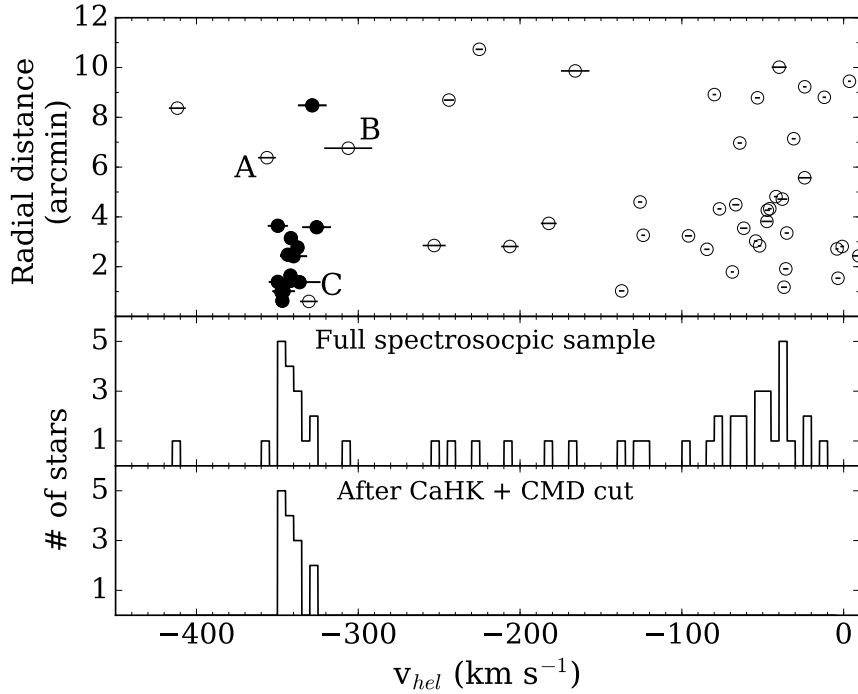
Figure C.5: *Panneau supérieur :* Distances au centre de Dra II vs. vitesses radiales pour toutes les étoiles observées spectroscopiquement. Les cercles noirs pleins représentent les membres de Dra II. *Panneau central :* Histogramme des vitesses radiales pour l'ensemble de l'échantillon spectroscopique. *Panneau inférieur :* Histogramme des vitesses radiales pour les membres seulement, obtenu en rejetant les étoiles qui ne sont pas suffisamment pauvres en métaux selon Pristine.

Avec cet échantillon spectroscopique final, j'estime ensuite la vitesse radiale et la dispersion de vitesse du satellite. La vitesse systémique de Dra II est de $-342.5^{+1.1}_{-1.2}$ km s^{-1}, et sa dispersion de vitesse n'est toujours pas résolue. Cependant, il est possible de la contraindre à être inférieure à 5.9 km s^{-1} à 95%. Ce résultat n'est cependant pas suffisamment décisif pour déterminer la nature du satellite.

Enfin, en s'appuyant sur les données Gaia, il est possible de déterminer le mouvement propre de Dra II: ($\mu^*_\alpha = 1.26 \pm 0.27, \mu_\delta = 0.94 \pm 0.28$) mas yr^{-1}. En combinant ces résultats avec la distance et la vitesse radiale déterminée précédemment, et sur le package python GALPY, l'orbite du satellite peut être d'terminée. Elle montre en particulier que le satellite est trés proche de son péricentre, qui est de $21.3^{+0.7}_{-1.0}$ kpc. S'approcher autant de la Voie Lactée devrait être dangereux pour Dra II qui devrait être affecté par des effets de marées. Si des structures étendues pouvant être le signe d'une telle intéraction sont effectivement observées dans le champ de Dra II, le fait que le satellite n'ait pas encore été détruit peut laisser un indice sur sa nature. Il serait en effet surprenant pour un amas d'avoir réussi à survivre aussi longtemps sur une telle orbite.
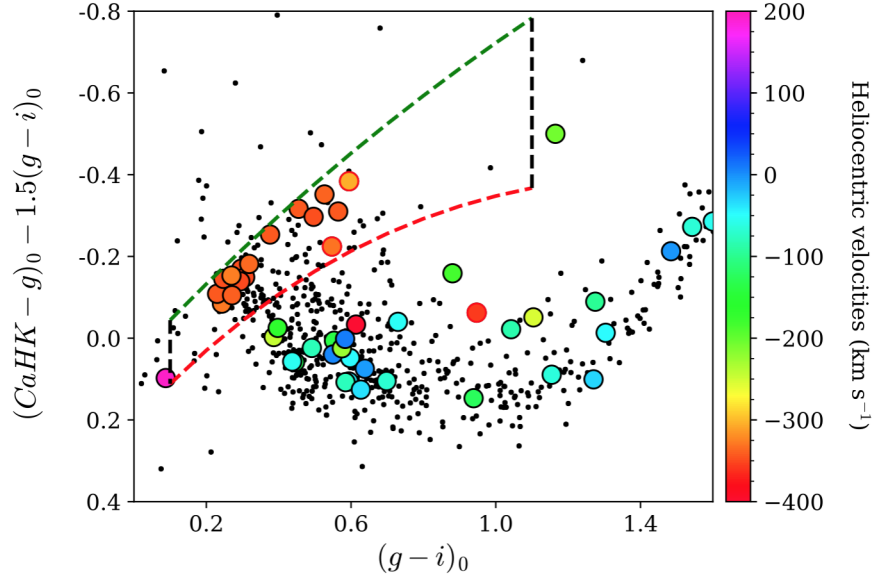
Figure C.6: Diagramme Pristine couleur-couleur. Le proxy de température $(g-i)_0$ est représenté sur l'axe des abcisses, alors que l'information en métallicité est portée par l'axe des ordonnées avec la couleur $CaHK - g_0 - 1.5*(g-i)_0$. Deux lignes d'iso-métallicité sont représentées ici, les lignes rouge ($[Fe/H] \sim -1.8$) et verte ($[Fe/H] \sim -3.5$). Les étoiles en orange, compatibles avec la vitesse radiale de Dra II, sont en majorité confirmées comme étant trés pauvres en métaux. À l'inverse, les étoiles clairement contaminantes car trop différentes dynamiquement, sont clairement plus riche en métaux. Ainsi, pour nettoyer l'échantillon spectroscopique de la contamination, une sélection est effectuée dans le diagramme : les étoiles particulièrement pauvres en métaux, c'est-à-dire celles à l'intérieur du polygone délimité par les lignes discontinues, sont conservées dans l'échantillon final et considérées comme membres de Dra II.

En conclusion, le cas de Dra II n'est toujours pas tranché. Le satellite est plus étendu que la majorité des amas de même luminosité. De plus, aucun amas à une métallicité inférieure à -2.5 dex n'a jamais été observé, et il serait étonnant pour un amas de cette taille, luminosité et orbite, de ne pas encore avoir été détruit. Ces éléments laissent penser que Dra II est de nature galactique. Cependant, il n'a pas été possible de contraindre suffisamment les dispersions de vitesse et de métallicité, et donc, de confirmer que Dra II est bel et bien une galaxie naine.

C.3   Étude observationnelle en profondeur du satellite de faible luminosité de la Voie Lactée Sagittaire II

Mon deuxième article porte sur l'étude de Sagittaire II (Sgr II), un autre satellite de la Voie Lactée découvert par L15. Tout comme pour Sgr II, L15 penchait pour une nature galactique pour Sgr II, mais soulignait l'importance d'observations spectroscopiques pour confirmer ceci. L15 a également remarqué la proximité sur le ciel, et en terme de distance, du satellite avec le courant de marée du Sagittaire, et a indiqué qu'un lien était envisageable entre les deux. Une nouvelle fois, des données relatives à la dynamique de Sgr II était
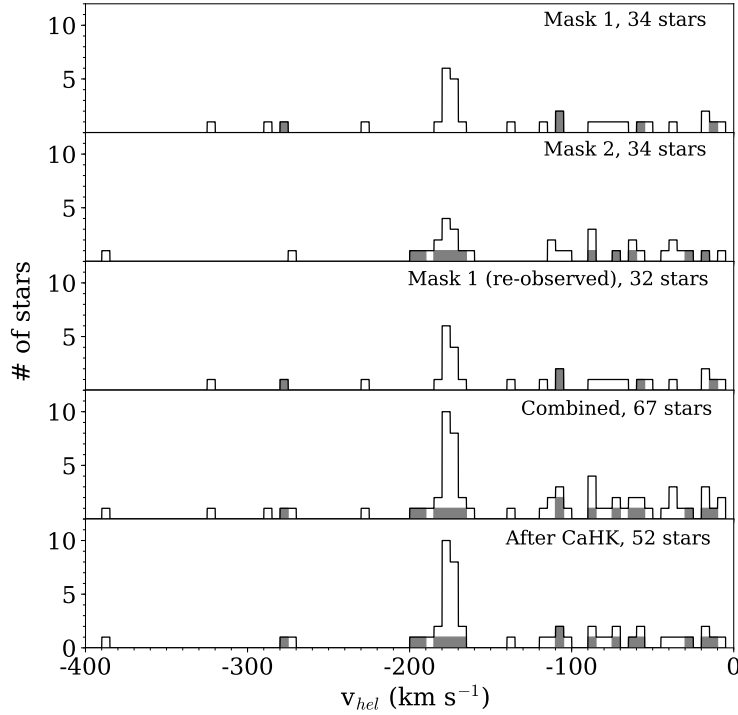
Figure C.7: Histogrammes des vitesses radiales pour les trois différents jeux d"observations spectroscopiques, pour toutes les étoiles entre -400 et 0 km s^{-1}. Le quatrième panneau représente la combinaison de toutes ces observations. Les histogrammes en gris montrent la distribution des étoiles ne disposant pas d'un *CaHK* de qualité suffisante ($\delta_{\mathrm{CaHK}} > 0.1$) pour donner une métallicité photométrique fiable. Ces étoiles sont donc de toute façon conservées dans l'échantillon final montré dans le dernier panneau. Le nettoyage du reste des données se fait de façon analogue à Dra II : les étoiles trop riches en métaux pour correspondre à la population stellaire de Sgr II sont rejetées.

nécessaire pour confirmer que les deux objets sont sur des orbites comparables.

Mon analyse du système (Longeard et al., 2019b) utilise des outils similaires à ceux de Longeard et al. (2018), et du même type d'observations : de la photométrie bande large MC/CFHT, de la photométrie bande étroite Pristine, ainsi que de trois jeux d'observations spectroscopiques différents avec Keck/DEIMOS. Tout d'abord, j'ai affiné les contraintes sur les propriétés structurelles du système: le rayon de demie-lumière de Sgr II est de $35.5^{+1.4}_{-1.2}$ pc, le système est quasiment sphérique et sa magnitude absolue est de -5.7 ± 0.1 mag. À cette taille et luminosité, Sgr II occupe une place bien particulière de l'espace r_h-M$_V$ vu dans la Figure C.1, à la fois plus compact que les galaxies naines connues à luminosité équivalente, tout en étant plus étendu que la majorité des amas globulaires de même M$_V$. L'étude des métallicités photométriques de Pristine permet de contraindre, uniquement par photométrie, la métallicité du système, donnant [Fe/H]CaHK $= -2.32 \pm 0.04$ dex, et une dispersion de métallicité faible mais résolue: $\sigma^{\mathrm{CaHK}}_{\mathrm{[Fe/H]}} = 0.11^{+0.05}_{-0.03}$ dex.
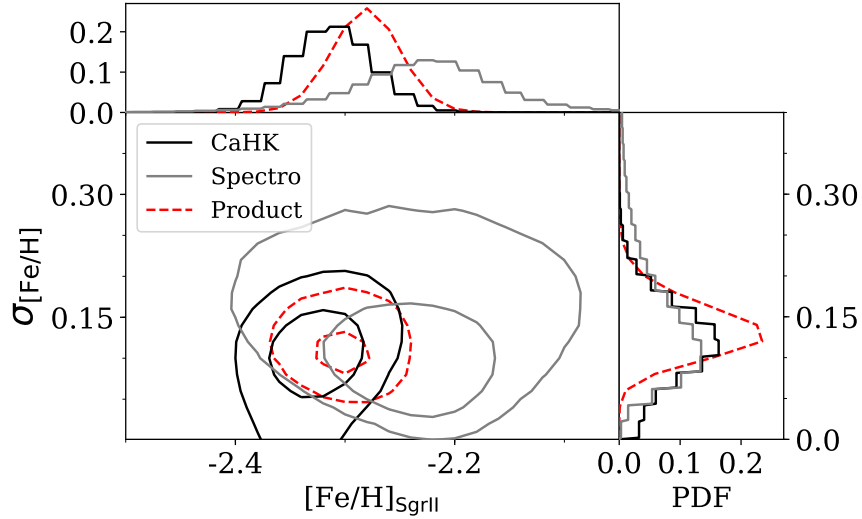
Figure C.8: Probability Distribution Functions (PDFs) 2D de la métallicité systémique et de la dispersion en métallicité de Sgr II, en utilisant uniquement les métallicités photométriques de Pristine (lignes noires) et les métallicities issues de la sectroscopie (lignes grises). Les deux mesures étant indépendantes, elles sont combinées en une seule représentée en ligne discontinue rouge. Les contours représentent les 39, 88 et 95% d'intervalle de confiance. Les PDFs 1D associées sont représentées dans les panneaux droits et supérieurs. Les deux méthodes sont en accord, que ce soit pour la métallicité systémique ou pour la dispersion.

Les trois échantillons spectroscopiques sont présentés en Figure C.7 dans les trois premiers panneaux. La combinaison de tous ces jeux de données est représentée dans le quatrième panneau. Une nouvelle fois, la population de Sgr II ressort assez clairement avec un pic de vitesse radiale autour de ~ -180 km s^{-1}. Cependant, tout comme Dra II, afin d'éviter d'être influencé par la contamination Galactique, j'utilise les données Pristine afin de déterminer quelles étoiles dans les observations spectroscopiques sont trop riches en métaux pour appartenir à Sgr II. Les étoiles restantes, probables membres de Sgr II, sont representées dans le dernier panneau. À partir de cet échantillon final, il est possible de déterminer que la vitesse radiale systémique du satellite est de $\langle v_r \rangle = -177.3 \pm 1.2$ km s^{-1}. La dispersion de vitesse de Sgr II est marginalement résolue, avec $\sigma_{vr} = 2.7^{+1.3}_{-1.0}$ km s^{-1}. Ce résultat favorise l'existence d'un halo de matière noire pour le système. Les observations spectroscopiques de Sgr II permettent également de mesurer ses propriétés de métallicité, et ce, de façon indépendante à celle utilisant les données Pristine. 6 étoiles ont un spectre avec un rapport signal-sur-bruit suffisant pour pouvoir mesurer leur métallicité. Avec la spectropscopie, j'obtiens $[Fe/H]_{spectro} = -2.23 \pm 0.05$ dex, ainsi qu'une dispersion de $\sigma^{spectro}_{[Fe/H]} = 0.10^{+0.06}_{-0.04}$ dex. Ces résultats sont compilés dans la Figure C.8. Les deux méthodes donnent des résultats tout à fait compatibles. En combinant les deux mesures, on obtient les mesures finales suivantes : $[Fe/H]_{SgrII} = -2.28 \pm 0.03$ dex et $\sigma^{SgrII}_{[Fe/H]} = 0.12^{+0.03}_{-0.02}$ dex.

Cette analyse favorise donc l'existence d'une dispersion de métallicité dans le système. Cependant, elle à ses limites. La première est qu'utiliser une autre calibration pour obtenir
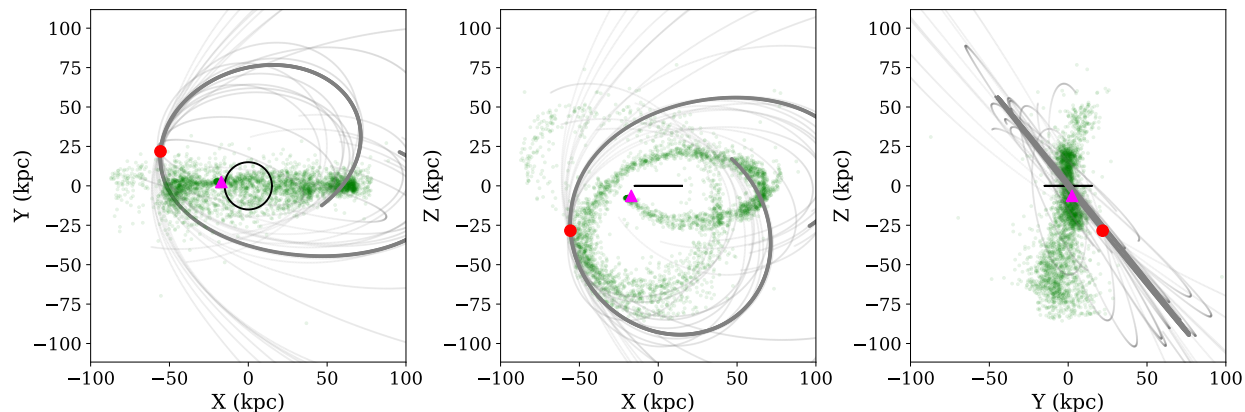
Figure C.9: Projections de l'orbite de Sgr II dans les plans X-Y, X-Z et Y-Z sur 2 Ga dans le passé et le futur. 21 orbites sont montrées ici : l'orbite privilégiée en ligne continue, 20 autres qui sont des réalisations aléatoires de l'orbite de Sgr II par tirage aléatoire du mouvement propre, vitesse radiale, distance et position. Ces orbites, reprsentées par des lignes grises partiellement transparentes, permettent de rendre compte de l'incertitude sur l'orbite du satellite. La position actuelle de Sgr II est montrée par le cercle rouge, tandis que la position actuelle de la galaxie naine sphéroidale du Sgr est montrée à l'aide du triangle magenta. Le courant de marée du Sgr, lui, est représenté par les points verts, selon la simulation de Law & Majewski (2010).

les métallicités spectroscopiques individuelles de chaque étoiles donne un résultat compatible mais légèrement différent, avec, en particulier, une plus grande dispersion de métallicité. Cela indique qu'il doit exister des erreurs systématiques inconnues dans cette analyse. De plus, cette inférence de la dispersion est surtout causée par l'identification de deux étoiles membres trés brillantes avec des métallicités non compatibles entre elles. Pour ces deux étoiles, la précision de mesure est de quelques centièmes de dex, ce qui est extrêmement précis pour une mesure de la métallicité basée sur une calibration empirique des raies du triplet du calcium. Encore une fois, une erreur systématique difficile à quantifier devrait rentrer en compte ici. Finalement, une étude spectroscopique de Sgr II, non publiée mais présentée lors d'une conférence , de Fu & Simon mesure une dispersion de métallicité dans le système extrêmement faible. Tous ces points indiquent que la valeur de la dispersion de métallicité de Sgr II de Longeard et al. (2019b) doit être prise avec précaution.

Tout comme Dra II, les données Gaia permettent, en combinant avec les inférences de distance et de vitesse radiale de Longeard et al. (2019b), d'obtenir l'orbite du satellite et de la comparer avec celle du courant de marée du Sagittaire. L'orbite de Sgr II ainsi obtenue est représentée sur la Figure C.9 avec la ligne continue grise. Le courant de marée du Sagittaire, lui, est issu de la simulation de Law & Majewski (2010). Des orbites aléatoires de Sgr II sont également montrées en lignes grises pointillées afin de rendre compte de l'incertitude sur l'orbite du satellite. L'orbite de Sgr II est compatible avec elle du courant de marée du Sagittaire, même les deux ne semblent pas être dans un même plan dans le plan Y-Z.

En conclusion, aucune affirmation ne peut être formulée sur la nature de Sgr II. La taille du satellite est bien particulière, à mi-chemin entre les amas et les galaxies naines de cette luminosité. La dispersion de vitesse favorise l'existence d'un halo de matière noire, bien que relativement peu massif. La dispersion de métallicité de Sgr II indique elle aussi l'existence d'un halo, mais les limites de l'analyse font que ce résultat doit être pris avec précaution. Néanmoins, la nature galactique reste favorisée pour Sgr II.

Finalement, l'orbite du système est compatible avec celle du courant de marée du Sagittaire, et laisse entendre que Sgr II serait un ancien satellite de la galaxie naine du Sagittaire, qui aurait été arraché de son influence par la Voie Lactée.

C.4   Étude détaillée de l'amas globulaire de la Voie Lactée Lavens 3

Encore un satellite découvert par L15, peu de doutes entourait la nature du satellite au moment de sa découverte. Laevens 3 (Lae 3) apparaissait comme trop compact ($r_h \sim 7$ pc) pour être une galaxie naine. Néanmoins, afin de le confirmer, des observations spectroscopiques ont été réalisées avec Keck/DEIMOS. Cependant, il n'y a pas de données Pristine pour ce système. Cette analyse constitue mon troisième article (Longeard et al., 2019a).

Une nouvelle fois, les paramètres structurels du satellite sont raffinés. Avec des données photométriques plus profondes, le rayon de demie-lumière de Lae 3 est plus important que celui trouvé par L15 (11.4 ± 1.0 vs 7.0 ± 2.0 pc). Afin d'expliquer cette différence, la taille de Lae 3 est redéterminée avec les données utilisées par L15, et donne le même résultat, à savoir un rayon autour de 7 pc. Puis, les données sont découpées en deux groupes : d'une part toutes les étoiles avec une magnitude en g comprise dans l'intervalle $15.0 < g_0 < 22.5$ mag, de l'autre les étoiles les moins brillantes de l'échantillon, dans l'intervalle $24.0 < g_0 < 25.0$. Pour chacun de ces deux groupes, le rayon de demie-lumière du satellite est redéterminé. Les résultats sont representés dans la Figure C.10. La taille du satellite varie suivant le groupe considéré : les étoiles les moins brillantes donnent un r_h plus important. Cela signifie que la différence de taille entre L15 et Longeard et al. (2019a) est causée principalement par les étoiles moins brillantes, qui ne se retrouvent pas dans les données photométriques moins profondes de L15. Une autre conclusion est que si les étoiles brillantes sont plus centralement concentrées que les autres, cela peut signifier que Lae 3 a subi une ségrégation de masse. Un tel phénomène est attendu chez les amas globulaires qui ont eu assez de temps pour se relaxer et qui ne sont pas affectés par d'eventuels effets de marée. Avec un temps de relaxation de ~ 2 Ga et aucune structure de marée observée dans le champ autour de Lae 3, il semble donc effectivement que de la ségrégation de masse ait eu lieu dans le satellite.

Les observations spectroscopiques de Lae 3 permettent de déterminer ses propriétés dynamiques et de métallicité. Tout d'abord, la vitesse radiale systémique du satellite est de $\langle v_r \rangle = -70.2$ km s^{-1}. Sa dispersion de vitesse n'est pas résolue. La métallicité de Lae 3, elle, est de $[\mathrm{Fe/H}] = -1.8 \pm 0.1$ dex. La dispersion de métallicité n'est également pas résolue.

Enfin, l'orbite de Lae 3 est celle d'un satellite du halo externe de la Voie Lactée, avec un péricentre de $40.7^{+5.6}_{-14.7}$ kpc et un apocentre de $85.6^{+17.2}_{-5.9}$ kpc.
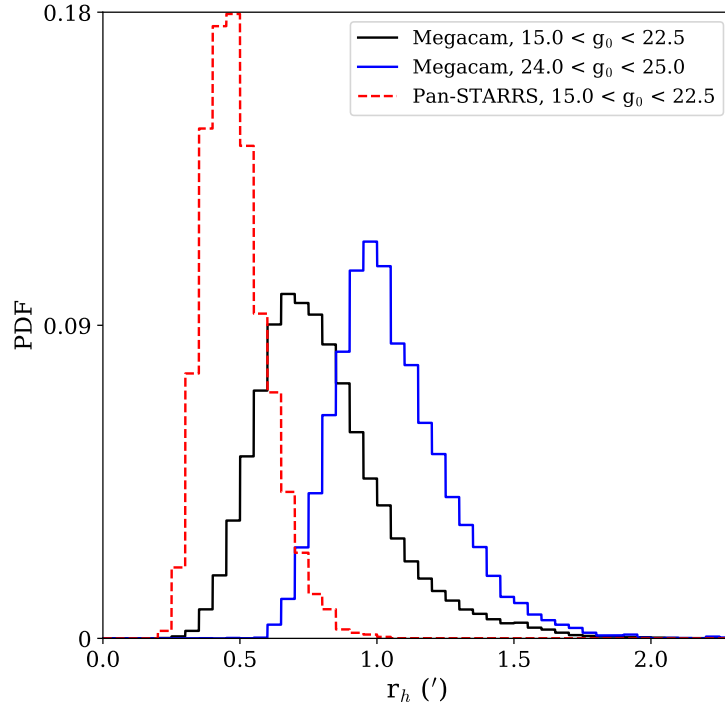
Figure C.10: PDFs 1D de la mesure du rayon de demie-lumière de Lae 3 dans trois cas : en utilisant les étoiles avec $15.0 < g_0 < 22.5$ dans MegaCam (ligne continue noire), les étoiles avec $24.0 < g_0 < 25.0$ (ligne continue bleue), et celles issues du catalogue PS1 (ligne discontinue rouge). Les intervalles de magnitude dans les deux premiers cas ont été choisi de tel sorte que le nombre d'étoiles trouvé pour Lae 3 aprés analyse des propriétés structurelles soit comparable dans les deux cas. Le rayon de demie-lumière de Lae 3 est plus grand en ne considérant que les étoiles de plus faible masse, ce qui suggère une ségrégation de masse dans le système. La même taille que L15 est retrouveée en utilisant les mêmes données, ce qui montrent que le résultat n'est pas du à un problème dans l'analyse.

En conclusion, malgré les dispersions de vitesse et de métallicité non résolues et peu contraintes, Lae 3 semble avoir subi une ségrégation de masse, processus attendu dans les amas mais pas les galaxies, et a une métallicité bien trop elevée pour être une galaxie naine, si l'on se réfère à la relation luminosité-métallicité des galaxies. Le satellite est donc un amas globulaire du halo externe de la Voie Lactée.

C.5 Conclusion

Une des principales conclusions de mon travail de thèse est l'absolue nécessité de combiner de la photométrie profonde et de la spectropscopie pour avoir une chance de réussir à décrire et comprendre les satellites de la Voie Lactée de trés faible luminosité. Sur les trois systèmes étudiés, seul un a vu sa nature déterminée avec confiance (Lae 3) et ce, malgré l'utilisation de données bande étroite issués du relevé Pristine.

Les perspectives d'avenir sont nombreuses. Tout d'abord, sur un plan personnel, je prévois de m'intéresser à l'ensemble des galaxies naines observées dans Pristine. Déja, pour mesurer de façon purement photométrique les propriétés de métallicité de tous ces satellites, voire tenter de construire leur fonction de distribution de métallicité complète pour les plus brillants et peuplés d'entre eux. Puis, pour effectuer une révision complète de la spectroscopie effectuée sur ces satellites au cours des années. En nettoyant la contamination Galactique avec Pristine, je redeterminerai leurs propriétés dynamiques afin de vérifier le potentiel impact de cette contamination sur les mesures de dispersion de vitesse des ces objets, et donc des masses de leurs halos.

De façon plus générale, l'arrivée de téléscopes de nouvelle génération risque, une fois de plus, de bouleverser le domaine. Parmi eux, le Large Synoptic Survey Telescope (Ivezić et al., 2008, LSST) va sans doute permettre de compléter le recensement des galaxies naines de la Voie Lactée en découvrant des systèmes impossibles à voir avec les moyens actuels, car trop peu brillants et/ou lointains. Si cette perspective est excitante, elle pose aussi des questions. S'il est déjà difficile de caractériser et comprendre les systèmes de faible luminosité que l'on connait, qu'en sera-t-il de ceux découverts par le LSST ? Il faudra que la technologie, aussi bien en photométrie qu'en spectroscopie, tienne la distance. Ou bien, serons-nous forcés de revoir notre façon d'étudier ces satellites. Quoiqu'il en soit, les galaxies naines de la Voie Lactée ont encore beaucoup de choses à dire sur notre Galaxie comme sur l'Univers.

Nicolas LONGEARD
An in-depth study of the faintest galaxies with dedicated spectroscopy based on the *Pristine* survey.

Université de Strasbourg

ECOLE DOCTORALE **pcp**

Observatoire astronomique de Strasbourg

Les galaxies naines sont des systèmes stellaires pauvres en métaux et peu lumineux, orbitant en général autour de galaxies plus massives. Elles peuvent être utiles pour contraindre la cosmologie autant que les processus de formation et d'évolution des galaxies. Cependant, les satellites peu brillants découverts récemment sont de nature ambiguë. Cette ambiguïté peut être levée par des observations spectroscopiques. Utiliser la spectroscopie à cette fin n'est efficace que si suffisamment d'étoiles membres de ces systèmes peuvent être identifiées, ce qui n'est pas toujours le cas pour ces satellites peu brillants.

Ma thèse présente les études détaillées de trois satellites de la Voie Lactée, Draco II, Sagittaire II et Laevens 3, visant à lever le voile sur leur nature par l'utilisation de photométrie profonde MegaCam à bande large et de spectroscopie multi-objet DEIMOS. À ces données s'ajoute de la photométrie bande étroite, sensible à la métallicité des étoiles, provenant du relevé Pristine. Celle-ci est complémentaire à la spectroscopie car elle permet d'identifier les populations pauvres en métaux typiques des galaxies naines. La taille de Draco II place le satellite dans le domaine des galaxies naines. Si la spectroscopie n'est pas informative dans ce cas, le relevé Pristine permet d'estimer la métallicité du système, celle-ci suggérant également une nature galactique. Les observations spectroscopiques et Pristine de Sagittaire II laissent également penser qu'il s'agit d'une galaxie naine, même si le satellite est légèrement plus compact qu'attendu pour une naine de cette luminosité. Son orbite, elle, suggère que c'est en fait un ancien satellite de la galaxie naine du Sagittaire, qui a été arraché de son influence par la Voie Lactée. Enfin, les propriétés de Laevens 3 montrent, sans ambiguïté, que le système est un amas globulaire du halo externe.

Mots-clés : Astronomie - Groupe Local - Galaxies naines - Photométrie - Spectroscopie

Dwarf galaxies are metal-poor, faint stellar systems orbiting in general around massive host galaxies. They can be used as cosmological probes as well as laboratories to constrain galaxy formation and evolution. However, most of the recently discovered faint satellites have an ambiguous nature. This ambiguity can be lifted with spectroscopy. But using spectroscopy to that end is only effective if enough stars members of these systems can be identified, which is not always the case given their faintness.

My thesis presents the detailed studies of three Milky Way satellites, Draco II, Sagittarius II and Laevens 3, that aim to unveil their nature using deep broadband MegaCam photometry and DEIMOS multi-object spectroscopy. These data are supplemented with the new narrow-band, metallicity-sensitive photometry provided by the Pristine survey that complements spectroscopy by identifying the typical metal-poor population of dwarf galaxies. The size of Draco II places the satellite in the realm of dwarf galaxies. If the spectroscopy is not informative in this case, the Pristine survey allows to estimate the metallicity of the system that also suggests a galactic nature. The spectroscopic and Pristine observations of Sagittarius II also marginally hint that it is a dwarf galaxy, although the satellite is slightly more compact than expected for a dwarf at that luminosity. Its orbit suggests that it is in fact a former satellite of the Sagittarius dwarf galaxy that was stripped from its influence by the Milky Way. Finally, the properties of Laevens 3 unambiguously show that it is an outer halo globular cluster.

Keywords: Astronomy - Local Group - Dwarf galaxies - Photometry - Spectroscopy